Compressive Residual Strength of Graphite/Epoxy Laminates After Impact

by

Teresa A. Guy

B. S. M. E. University of Washington
(1983)

Submitted in Partial Fulfillment of the
Requirements for the Degree of

MASTER OF SCIENCE

in

AERONAUTICS AND ASTRONAUTICS

at the

MASSACHUSETTS INSTITUTE OF TECHNOLOGY

June 1991

Signature of Author_____
Department of Aeronautics and Astronautics
May 10, 1991

Certified by_____
Prof. Paul A. Lagace
Thesis Supervisor

Accepted by_____
Prof. Harold Y. Wachman
Chairman, Departmental Graduate Committee

COMPRESSIVE RESIDUAL STRENGTH OF GRAPHITE/EPOXY LAMINATES AFTER IMPACT

by

Teresa A. Guy

Submitted to the Department of Aeronautics and Astronautics on May 10, 1991 in partial fulfillment of the requirements for the Degree of Master of Science.

ABSTRACT

The damage states and compressive residual strength behavior of AS4/3501-6 $[\pm 45/0]_{2S}$ graphite/epoxy laminates after impact was investigated experimentally using three different impacter masses at various velocities. Assessment of the state-of-the-art in predictive capabilities indicated that the need for basic understanding of the damage mechanisms governing compressive failure behavior still existed. Thus, the experimental program concentrated on answering three questions related to minimum compressive residual strength: one, what is the three-dimensional damage state that governs minimum compressive residual strength behavior; two, is this minimum compressive residual strength value dependent upon impact method; and three, how is this minimum compressive residual strength value related to impacter mass and velocity? The first question motivated an intensive damage evaluation program: three two-dimensional nondestructive damage evaluation methods (visual inspection, inspection by X-ray, and inspection by ultrasonic C-Scan) and three three-dimensional damage evaluation methods (nondestructive evaluation by time-of-flight ultrasonic C-Scan, destructive evaluation by cross-sectioning, and destructive evaluation by deply) were utilized. The minimum compressive residual strength is apparently independent of impact mass and method as all three impacter mass cases resulted in virtually identical minima. Impacter energy, a function of impacter mass and velocity, was not similar at these minima. Destructive evaluation of specimens impacted at the minimum compressive residual strength velocities resulted in similar three-dimensional damage states consisting of core damage and delamination. Predicted force and acceleration histories presented in this work were a good first approximation of potential similarities in the mechanics of the three impact events. Postmortem evaluation showed that the minimum compressive residual strength specimens exhibited similar failure mechanisms consisting of sublaminate buckling of ply 1 and fiber failure in the remaining plies. However, it was not possible to determine which damage mode or combination of damage modes controlled the compressive residual strength. Prediction of compressive residual strength must be based on the existing three-dimensional damage state as two-dimensional damage information determined by nondestructive evaluation was proven insufficient. Currently, an accurate assesment of the three-dimensional damage state can only be made by destructive evaluation. Thus, the need for improved three-dimensional nondestructive damage evaluation methods is indicated.

Thesis Supervisor: Paul A. Lagace

Title: Associate Professor, Department of Aeronautics and Astronautics, Massachusetts Institute of Technology

ACKNOWLEDGEMENTS

There are, of course, several people who I would like to acknowledge for aiding me in my pursuit of a greater understanding of composite material structural behavior. First of all, I would like to thank Ed Spier and Dr. Keith Kedward for inspiring me to expand my horizons by publishing papers, attending conferences, and continuing my formal education. I'd like to thank Ken Dawson, Bill Wennhold and my coworkers in Advanced Structures at General Dynamics Space Systems Division for encouraging me to take a leave of absence from my job responsibilities and pursue my Master of Science degree.

Once I made the decision to return to graduate school, I had to decide which one. Thanks goes to Prof. Ed Crawley for two important contributions made to this decision: his enticing description of the composite materials structures research and coursework in the M. I. T. Aeronautics and Astronautics Department, and for introducing me to Prof. Paul Lagace with whom my research interests matched.

The coursework at M. I. T. was exactly what I needed to enhance my job skills. I also appreciate the fact that the instructors placed the emphasis on learning and not on grades. This allowed me to concentrate on sponging knowledge from some very gifted individuals. I'd like to thank Prof. James Mar for trying to share his years of experience in 16.293, his open door policy to his M&M jar, and his interest in my well being (even though we did go to traditional rival high schools in Seattle). I'd like to thank Prof. Paul Lagace for his loud and clear teaching approach in 16.293 and for his ability to adjust his writing speed to his students capability. I'd like to thank Prof. John Dugundji for his patience and enthusiasm in

sharing his wealth of knowledge in 16.293 and 16.21. His thorough teaching approach earned my gratitude and respect. I'd like to thank Prof. Fred McGarry for his great sense of humor, his relaxed teaching approach in 3.90 and 3.92, and his inclusion of current topics of interest in his lectures. I'd also like to thank Prof. Michael Graves for bringing a little reality to the application of finite element analysis in 16.27, and the times I was able to reminisce about Seattle with someone who could truly appreciate the Pacific Northwest.

I have to express my overwhelming gratitude to my right hand man, Matt Beaumont. Matt was my UROP (undergraduate student) during the whole of my graduate studies. Matt was of invaluable help in completing my research. Not only did he help with the exhaustive literature search you'll see in Chapter 2, but he was responsible for a lot of the day-to-day lab work. His ability to learn quickly, his self-motivation, and his dependability earned my confidence to let him work with little to no supervision. This allowed me to concentrate on any analysis, technical reading, data reduction, and thesis writing that had to get done (though he did volunteer for these tasks as well!). John Woyak joined our team for the summer of 1990 and, under mainly Matt's supervision, provided an outstanding contribution to our effort. Matt and John were the ideal team of UROPers. They accomplished most of their tasks in record time and I was very pleased with the quality of their work. I should also thank Michael Clarke and Chantal Moore for their contributions as part time UROPers.

TELAC (the Technology Laboratory for Advanced Composites) was a wonderful environment to work in. Al Supple was always available to handle any crisis that arose (which was pretty often for Matt and I!). Thank you Al for fixing up the secondary vacuum system when we blew the

primary pump in the middle of a cure, your patience when we started testing, and your valued opinion on the many occasions I picked your brain for insight into problems I needed solved. Thanks to my fellow graduate students: Narendra Bhat, Randy Notestine, Claudia Ranniger, James Williamson, Wilson Tsang, Ed Wolf, Mary Mahler, Peter Dunn, Wai Tuck Chow, Yew-Poh Mak, Ken Bonello, Tom Wilson, and Adam Sawicki for help in the lab, help with my computer system, the great theoretical discussions, and the surprise birthday party.

Stuart Pekowsky, friend and electrical engineer extraordinaire, earned my everlasting gratitude with his offer to replace the outdated Air Gun electronic timing system with one that was easy to use and reliably accurate. The purchase of a timing system allowed me to spend my time elsewhere which expedited my experimental program and thus, my final departure date. (Which earned my husbands everlasting gratitude!)

And last, but certainly not least, I'd like to thank my thesis advisor, Prof. Paul Lagace. I appreciate his confidence and trust in my ability to find my own way and the conversations that often brought me back from industry concerns to academia. Of course, I also appreciate the free Red Sox tickets and access to the fish bowl of M&M's. Thanks Paul, for making my graduate student experience at M. I. T. one worth the sacrifices we both know I made.

FOREWORD

This work was conducted at TELAC (Technology Laboratory for Advanced Composites) in the Department of Aeronautics and Astronautics at the Massachusetts Institute of Technology under the supervision of Professor Paul A. Lagace on Naval Air Systems Command Contract No. N00019-89-C-0058.

DEDICATION

I'd like to dedicate this work to my husband, J. Kevan Guy, who was my greatest supporter during my graduate studies. Without his financial support, I truly would have felt like the typical "poor graduate student". His emotional support helped me maintain my sanity by providing a link to "the real world". But, most importantly, he kept reminding me of the value of my efforts for our future together as our present was spent commuting from San Diego to Boston. I will be forever grateful for his unselfish attitude, strength, and stability.

TABLE OF CONTENTS

TABLE OF CONTENTS

LIST OF FIGURES

LIST OF FIGURES

LIST OF FIGURES

LIST OF FIGURES

LIST OF FIGURES

LIST OF FIGURES

LIST OF FIGURES

LIST OF FIGURES

LIST OF FIGURES

LIST OF FIGURES

LIST OF FIGURES

LIST OF TABLES

LIST OF TABLES

NOMENCLATURE

a_o	characteristic distance for the average stress criterion
AS4/3501-6	graphite/epoxy material manufactured by Hercules, Inc.
°C	degrees Celsius
d_o	characteristic distance for the point stress criterion
DiB	1,4-Diiodobutane
EA-06-125AD-120	120 ohm strain gages manufactured by Micro Measurements
FM-123-2	film adhesive manufactured by American Cyanamid
FRED	Free Rolling Energy Device
g	gram
G_I	Mode I strain energy release rate
G_{Ic}	Mode I critical strain energy release rate
G_{II}	Mode II strain energy release rate
G_{III}	Mode III strain energy release rate
GPa	Giga (10^9) Pascals
Hg	mercury
J	joules
kg	kilogram
kV	kilovolts
LED	light-emitting diode
m	meter
min	minute

NOMENCLATURE

ml	millileter
mm	millimeter
mR	milliRad
MCRS	minimum compressive residual strength
MEK	methylethylketone
MHz	MegaHertz
MPa	MegaPascals
N	Newton
NDE	nondestructive evaluation
rpm	revolutions per minute
s	second
TELAC	Technology Laboratory for Advanced Composites

Chapter 1

INTRODUCTION

As the use of advanced composite materials for primary structure in the aerospace and aircraft industries increases, concerns involving their damage tolerance need to be addressed [1–11]. The "damage" in damage tolerance can be due to manufacturing defects and/or service events [1–5]. Manufacturing defects include such concerns as: porosity and voids, resin-rich areas, fiber kinks, inclusion of foreign materials, and poorly drilled holes. Damage due to service events includes such concerns as: cuts and scratches, delaminations, disbonds, hole elongation, edge damage, and penetration. Often, service-induced damage can occur due to impact from foreign objects. Possible impact events include tool drops, runway kickup, bird strikes, battle damage, and meteor debris.

The importance of the damage size and its location increases with the complexity of the applied stress field [2, 3, 12-14]. The most significant effects are due to damage in areas subject to high in-plane compression, shear stress, interlaminar stress, or out-of-plane bending moments [2, 4, 5, 12, 15]. Thus, out-of-plane load effects on delamination growth should be included when considering actual structural behavior due to defects or damage. Of the aforementioned complex stress fields, in-plane compression is one of the easier load conditions to apply at the coupon level.

Experimental evidence shows that a more severe reduction in compressive residual strength occurs from impact damage than due to the presence of an imbedded delamination with equal area (as determined by ultrasonic evaluation) [1, 3, 6–8, 16–18]. Impact damage may also result in a more severe reduction in compressive residual strength than a hole with

an equivalent diameter [3, 6, 15, 16, 19, 20]. It is thus important to test configurations with actual impact damage rather than "simulated" damage to get an accurate evaluation of the potential loss in compressive load-carrying ability. However, it is important to realize that coupon-level testing does not usually represent structural geometry or boundary conditions nor does it account for the multiple load path capability of structures. Thus, actual structure may be more damage tolerant than evidenced by coupon testing [1, 6–8, 21, 22].

Several available damage tolerant design concepts have been used with varying degrees of success [4, 8, 9, 12, 19, 23]. These include: increased number of ±45° plies; use of fastener rows, tear straps, buffer strips, adhesive interleaves, hybrid materials, fabric bonded reinforcement, stitching, braiding, stitched-woven fabrics, stiffeners, and multiple load paths. The most common approach for improving damage tolerance is to use a design allowable strain that is significantly less than the "A" allowable for the material [2, 4–6, 15]. (The "A" allowable is a statistically determined value of which at least 99% of the entire test population would exceed with a 95% confidence level [24].) This keeps manufacturing cost down by alleviating the need for complex designs and thus increased labor. However, system cost can drastically increase as additional weight may be added to the structure in areas not specifically requiring the reduced allowable. This approach reduces and sometimes eliminates the weight advantage of using composite materials instead of metals.

Although it is important to pursue damage tolerant design improvements, the need still exists to understand the effects of impact damage mechanisms on compressive residual strength. Also, understanding of these effects on compressive residual strength may allow

the use of increased design allowables through better confidence in predictive capabilities.

The overall objective of the current work is thus to understand the effects of damage mechanisms on compressive residual strength after impact. The approach was to start with previous work done in the area of damage tolerance of composite material structures and related issues, particularly as related to impact, as discussed in Chapter 2. This includes the separation of damage resistance and damage tolerance into two distinct issues. This leads to a discussion of the impact event and resulting damage states for various parameters and residual strength prediction methodologies under compressive loading.

The experimental procedures used in this research effort are discussed in Chapter 3. The impact test matrices are presented with justification for compressive residual strength tests or destructive damage evaluation. The specimen utilized is described and the manufacturing method used to fabricate and assemble the test specimen is discussed. Details of the experimental procedure used to impact specimens, perform damage evaluation, and test for compressive residual strength are also included. The details of manufacturing and testing should serve as a basis for duplication of the work by others interested in experimental and analytical correlation.

In Chapter 4, the nondestructive damage evaluation results, destructive damage evaluation results, and the compressive residual strength experimental results are presented. Comparisons of impact parameters affecting compressive residual strength and destructive and nondestructive damage evaluation methods are discussed in Chapter 5.

A summary of the present work, the conclusions drawn, and recommendations for future work are presented in Chapter 6. The recommendations include any limitations of the present work that may affect application of the conclusions in a general sense.

Chapter 2

PREVIOUS WORK

The objective of this study is to understand the effect of impact damage on the compressive residual strength of composite material laminates. The work related to this issue is discussed herein. However, before examining the residual strength of a composite laminate with damage due to impact, it is important to understand the impact event itself, specifically in terms of the damage produced.

2.1 Damage Resistance versus Damage Tolerance

Impact of a composite laminate by a foreign object is a complex event occurring over a very short period of time. The two areas of concern in an impact event are: one, the dynamic behavior and resulting stress field in a composite laminate, and two, the resulting damage in a composite laminate. The amount or types of damage in the composite laminate due to impact will vary for different material systems, layups, etc. This area of concern is referred to as *damage resistance*. The ability of a composite laminate to perform its design function (i.e., carry load or retain stiffness) after impact is referred to as *damage tolerance*. The separation of issues into the damage caused by impact (damage resistance) and the damage effect on residual strength (damage tolerance) has been recognized by several researchers [5, 23, 25–29].

The prediction of the damage state due to the impact event is not the purpose of the present work. Thus, the dynamic behavior and resulting stress field in a composite laminate due to impact is not of concern in the

current research. For damage tolerance, the important issue is not *how* the damage gets there, but *what* and *where* is the damage.

The discussion of previous work thus includes information on damage resistance in order to understand the effects on the resulting damage state. However, the main focus is on the analytical and experimental work on compressive residual strength in the presence of defects and damage.

2.2 Impact Damage

The possible damage due to impact includes: surface indentation, fiber splitting, delamination, fiber breakage, matrix cracking, fiber-matrix debonding, and fiber pull-out [4, 10, 12, 21, 25–27, 31, 33–37]. The three damage modes most commonly discussed are fiber breakage, matrix cracking, and delamination.

The damage state due to impact is a function of several parameters. A partial summary of these parameters includes: fiber/matrix system; tape or fabric construction; laminate stacking sequence and thickness; and projectile size, type, obliquity, and velocity [38]. Plate boundary conditions [25–28], impact specimen geometry [4, 21, 26, 27, 39], and the existence of preload should be added to this list [9, 15, 20, 25, 30, 40–43].

A significant amount of experimental work has been done on the effects of fiber, matrix and fiber/matrix combination on damage resistance. An increase in fiber strain-to-failure [44] or fiber volume content [45] resulted in significantly less front surface indentation damage under identical impact conditions. Isolating the effect of matrix on damage resistance, several researchers [3, 4, 9, 10, 30, 31, 33] found that a "tough"

matrix was more damage resistant than a "brittle" one. (A "tough" matrix has high strain-to-failure capability relative to a "brittle" matrix.) The visual and ultrasonic C-Scan indications of damage for the "brittle" system were significantly greater in diameter than the diameter of the "tough" system. When looking at fiber/matrix combinations and interactions, Elber [46] summed it up best for the work reviewed in this area [8, 25, 31, 32, 47]. He found that although the matrix properties are generally assumed to limit the impact resistance of composite laminates, an excessively tough or strong matrix can result in fiber-initiated impact failures. In thin laminates, high strain-to-failure fibers enhance impact resistance, not a tough matrix system. Also, in extreme cases of thin and especially thick laminates, matrix shear strength controls the onset of delamination damage while fiber ultimate strain controls the onset of penetration due to impact. He concluded that matrix toughness dominated the type and extent of impact damage in most cases.

The effect of tape versus fabric construction on impact resistance is not clear. Test results from Rhodes, Williams, and Starnes [40] shows no clear indication that one construction is more impact resistant than another. These tests included different material type combinations, different orientations, and modest thickness variations. This agrees with the supposition by Wilkins [12] that woven fabrics only remove the matrix cracking damage mode that he indicates is somewhat benign. However, these results appear inconsistent with the observations made in later work by Rhodes and Williams [9] where tape laminates show extensive delamination, while woven fabric exhibits limited delamination and no shear cracking. Challenger [8], and Bishop and Dorey [34] agree that direct

substitution of fabric for tape has a significant effect on the extent and shape of impact damage.

The effect of the laminate on damage resistance is separated into two categories: stacking sequence and thickness. Three important phenomena in the study of stacking sequence effects on impacted laminates have been consistently reported [2–4, 15, 34, 35, 40, 48, 49]. First, delaminations only occur where there is a change in ply orientation. Second, the larger the difference between the two ply angles, the larger the delamination. And third, delamination shape is oblong with the major axis nearly parallel to the fiber direction of the lower ply relative to the impact surface. As to laminate thickness effects, delamination area increases as a function of normalized ply thickness [27, 35] and total laminate thickness [35] for the same impact metrics. Increasing laminate thickness also increases laminate resistance to perforation [39]. (Perforation is the passage of the projectile through the laminate.) The concentration of delaminations moves from the back surface for thin laminates to the middle for thick laminates [21, 45, 49].

Several impacter parameters affect damage resistance: size, type, obliquity, and velocity. Impacter size affects the extent of damage as a function of impacter energy [45]. Most impacters which have been used were spherical or hemispherical in shape and the impact was normal to the laminate surface. Normal impact is the easiest to perform, but it is not the most likely to occur in service, nor is it known to be the most or least severe condition [21].

The impacter energy is a combination of impacter mass and velocity. Comparison of impact test results for the same material systems showed that the "low mass/high velocity" impacter resulted in greater damage than

the "high mass/low velocity" impacter at the same incident energy [8, 19, 32, 39]. The laminate can respond by bending at relatively low velocities. While at higher velocities, the laminate may be excited in higher dynamic modes that will result in different damage modes [4, 21, 39]. Test data from Cantwell and Morton [39] indicated that high velocity impact has a much lower first damage threshold energy than low velocity impact when thickness is constant (between 1 and 8 mm). However, for perforation threshold, high velocity and low velocity impact energies are similar at constant thickness (between 0.5 and 3 mm).

The significance of the additional parameters (boundary conditions, specimen geometry, and preload) are summarized here. The significance of boundary conditions on impact resistance depends upon the selected impact metrics [25, 27, 28]. The effect of beam length also depends upon the impact metrics. Beam length affects the low velocity impact resistance but not high velocity impact resistance [4, 21, 39]. Beam width is important when choosing an impact diameter. According to analysis by Ilcewicz, Dost, and Coggeshall [27], the resulting damage diameter from the chosen impacter should be less than 3/8 of the specimen width to avoid finite width effects in subsequent testing. As to the issue of preload, the extent of local damage increases with the magnitude of the preload because of the coupling between the applied axial load and local deformation due to impact [9, 15, 20, 25, 40–43].

2.3 Effects on Compressive Residual Strength

The issue of compressive residual strength in the presence of damage, introduced artificially or by impact, was summarized well in 1985

by Baker, Jones and Callinan [3]. The areas of concern include damage nature, damage size/extent, damage location, laminate-matrix type/state, laminate stacking sequence, laminate ply drop-offs, component size and geometry, component deformation geometry, applied stress field, environment, and prior service history.

A large part of the work reported in the literature on prediction of residual strength due to impact damage has focused on tensile loading. This is understandable as tensile loading of composite laminates is simpler and the number of possible structural failure modes is limited. Understanding the effects of impact damage on compressive residual strength becomes considerably more complicated as additional structural failure modes (i.e., stability of a composite sublaminate) become possible. Several tensile residual strength prediction methodologies have been modified for compressive loading.

The discussion of previous work considered for compressive residual strength prediction of composite laminates includes the effects of notches, imbedded delaminations, and combined damage. Understanding the effect of a combined damage state on compressive residual strength can only be accomplished by first understanding the effects of the individual damage states that constitute the combined state.

2.3.1 Notches

Prediction methodologies for compressive residual strength in the presence of a notch range in complexity from a stress concentration with smeared through-the-thickness properties to a detailed ply-by-ply finite

element analysis. A brief discussion of the two extreme cases and their relative success at predicting failure load follows.

The point stress criterion and average stress criterion of composite laminates with stress concentrations proposed for tension [50] have been applied to the compressive case. In the point stress criterion, it is assumed that failure occurs when the stress over a characteristic distance (d_0) away from the discontinuity is greater than or equal to the unnotched material strength. In the average stress criterion, it is assumed that failure occurs when the average stress over some distance (a_0) equals the unnotched material strength. In both approaches, the characteristic distance is assumed to be a material property independent of the laminate geometry and stress distribution. The average stress method was extremely successful in predicting the reduction in strength from unnotched compressive strength when applied to test results for both loaded and unloaded holes [51]. Modification of these criteria by Tan [52] resulted in an effective point stress model and an effective average stress model that assumed fracture was fiber-controlled and at least one ply had fibers in the principal load direction. Predicted results were within 20% of experimental results.

One example of a complex analysis approach is a progressive damage model to predict type and size of internal damage from initial loading to final failure [53]. The stresses and strains calculated using a nonlinear finite element model were based on the finite deformation theory considering material and geometric nonlinearities. A failure analysis that included criteria for matrix cracking, fiber-matrix shearing, and fiber buckling was used to predict damage type and size. Test results of coupons

with 12.7 mm diameter holes correlated very well to calculated strains and stresses and predicted damage types and sizes.

The less complex analyses may be easy to apply but result in predictions that vary from test results by as much as twenty percent. The more complex analyses are more accurate but can be time consuming and costly. Also, while these analyses may apply to the fiber breaks (notches) and matrix cracks due to impact, they do not take into account the probable surrounding delamination and its interaction with the notch.

2.3.2 Imbedded Delaminations

Much of the work done to develop prediction methodologies for compressive residual strength look at delamination as the sole damage state. To test a laminate with a delamination configuration of known size, shape, and quantity, a material like Teflon or Kapton is imbedded in the laminate during the manufacturing procedure. The most common configuration studied is an imbedded through-the-width delamination [11, 54–73]. The objective of a number of these authors was to correlate analysis of instability-related delamination growth to experiment, but the question of which growth criterion to use was difficult to answer [11, 54–62].

Whitcomb's [54] correlation of calculated G_I and G_{II} (strain energy release rate) values of imbedded through-the-width delaminations with experimentally-observed values showed Mode I to dominate delamination growth even though G_{II} could be numerically much larger than G_I. Whitcomb [55] then included the effects of initial imperfections and thermal loads. The use of the sublaminate buckling load as the upper bound on the allowable load was unconservative when initial imperfections were

present. Prediction of delamination growth required the strain energy release rate relationship to applied load, a growth criterion, and the critical values of G_I and G_{II}. The use of three different growth criteria resulted in a significant difference in prediction of critical load. Donaldson [56] showed a lower bound linear relationship between G_I and G_{II} was only slightly conservative for critical load prediction.

A number of authors found delamination length to be a significant parameter affecting the behavior of imbedded through-the-width delaminations under compressive loading [4, 54–58, 63–65, 74, 75]. Analysis done by Sallam and Simitses [63] to determine if delamination growth was possible used the energy release rate to determine if delamination growth was stable or unstable. For relatively small delamination lengths, the buckling load coincided with ultimate load. For relatively large delamination lengths, however, the plate could carry increased loads depending upon the critical strain energy release rate of the material.

Stacking sequence [11, 63, 64, 66, 74] and sublaminate depth [4, 41, 54–58, 64–67, 74, 75] are also significant parameters affecting compressive residual strength. Analysis shows that stacking sequence affects failure mode [11]. However, postbuckling effects can be important as the postbuckling axial load capability can be significantly greater than the buckling load for a relatively thin delamination [65]. For a short, relatively thick delamination, the sublaminate buckling load is a close lower-bound to ultimate axial load. Also, analysis showed that a short, relatively thick delamination grew predominantly under Mode I loading [57]. But a relatively long, thin delamination grew in a state of pure Mode II loading. An especially adverse effect to compressive residual strength occurs when

delamination is adjacent to a 0° ply near the surface [3, 8, 17, 36]. This results in a significant strength reduction as an adjacent delamination will increase the flexural strain in the 0° ply which is a main load-carrying member.

Chai, Babcock, and Knauss [41] compared thin film, thick beam, and general model predictions of strain energy release rate using a one-dimensional model. The thick beam model did not differ greatly from the thin film model when normalized strain energy release rates were calculated for the same delamination length per plate length. The general model resulted in significantly larger normalized strain energy release rates except when the loading strain to plate buckling strain ratio was 0.2 or less. The general model included buckling of the sublaminate and base plate and established the range of validity for the thin film model. This was important as the thin film model is easier to expand to two-dimensional delamination growth than the general model. The two-dimensional model [74] to predict compressive residual strength of a laminate with a near-surface defect used the Rayleigh-Ritz method to determine the postbuckling solution of the delamination. An energy balance criterion based on self-similar crack growth governed fracture. The parameters governing growth or arrest were fracture energy, disbond depth, and both laminate and sublaminate elastic properties.

The significance of material behavior assumptions and boundary conditions in the prediction of sublaminate buckling and compressive residual strength was studied by several authors. The inclusion of bending-stretching coupling [64] affects the critical buckling load for the global, local, and mixed modes of failure for simply-supported boundary conditions. Only the global mode of failure was affected for clamped

boundary conditions. The inclusion of transverse shear [75] causes a significant reduction in the critical load for mixed mode instability and an increase in the strain energy-release rate.

Large deflection behavior [67] results in a less stiff and more delamination growth-resistant laminate than earlier thin film approximations. However, large deflection model predictions of sublaminate buckling load were approximately twice actual test values. Also of interest, the thin film approximation could not distinguish between clamped or simply-supported boundary conditions. Thus, the effects of assumed boundary conditions on the critical buckling load of a delaminated sublaminate of a beam on an elastic foundation were compared [68]. For high values of foundation modulus, the end fixity has little effect on the critical load. However, for low values of foundation modulus, the simply-supported boundary case requires less load for instability. In a similar study, Vizzini and Lagace [59] found that clamped boundary conditions that automatically set deflections to zero at the delamination perimeter removed the possibility of interlaminar normal stresses. Thus, they used a model with clamped boundary conditions away from the delamination with an elastic foundation supporting the sublaminate up to the delamination perimeter. The basis of the growth criterion was a strength of materials approach dependent upon the interlaminar normal stress. Rothschilds, Gillespie, and Carlsson [57] also found that the assumption of clamped boundary conditions did not accurately represent the physical behavior.

Several analytical methods of predicting imbedded through-the-width delamination behavior have been presented but it is unclear which methods are appropriate. Jones and Callinan [22] assessed the suitability of finite element analysis combined with fracture mechanics in predicting

delamination-critical behavior. The strain energy density hypothesis and the energy release rate approach were both capable of predicting delamination buckling and growth. However, several experimental tests would be required to determine critical strain energy release rate parameters to apply these methods to determine flaw-criticality. Jones, Paul, and Broughton [69] used a three-dimensional finite element model and the strain energy density approach to assess delamination damage growth. Analytical failure predictions compared favorably with test data referenced and predicted a compressive residual strength asymptote with an increase in damage area. Williams, Stouffer, Illic, and Jones [70] used three independent methods to confirm that growth of an imbedded through-the-width delamination was dependent upon the stress field at the crack tip produced by buckling of the sublaminate: a model based on buckling and classical fracture mechanics, a finite element model of the crack tip, and an experimental study. The analytical model agreed with the finite element model and the experimental results in most cases.

While this information on analysis techniques and behavior of imbedded through-the-width delaminations is very interesting, the results may not be applicable to delamination configurations likely found in service [56, 60]. More common configurations include circular or elliptical shapes [17, 42, 52, 66, 71, 72, 74, 76–80] and possibly even rectangular shapes [18, 66, 69, 73, 81].

The large difference in G_{Ic} observed between the imbedded through-the-width case and axisymmetric case was attributed to the different secondary forces that generate strain energy release rate [71]. In this work, Whitcomb stated that an imbedded through-the-width delamination could be effectively transformed into an imbedded axisymmetric delamination by

the addition of tractions. However, the uniaxially-loaded imbedded delamination was much more complicated. Whitcomb [72] also performed a parametric study of delamination growth as affected by G_I, G_{II}, and G_{III}. Results show that a large gradient in strain energy release rate occurs along the delamination front; maximum G_I and G_{II} locations are dependent upon delamination shape and the applied strain; G_{III} is negligible for all cases considered; and for some cases G_I is greater than G_{II}, while for others the opposite was true.

Several researchers looked specifically at the case of axisymetrically loaded circular imbedded delaminations. If the original delamination has a radius greater than a certain value, delamination growth is stable for force-controlled or deformation-controlled testing [76]. Stable growth occurs for a smaller initial radius in the deformation-controlled testing. Yin disagreed [77] with the possibility of stable growth since the energy release rate grows monotonically with delamination radius. This leads to the conclusion that the growth of a circular thin film delamination under biaxial compressive strain is always catastrophic. However, the inclusion of buckling-induced deformation of the base laminate shows that stable growth is possible depending on delamination radius and boundary displacement conditions [78].

Research has been done comparing the effects of the imbedded delamination shape. The effects of delamination shape (elliptical, circular), orientation, material anisotropy, and sublaminate layup were investigated by Shivakumar and Whitcomb [66] using both finite element analysis and Rayleigh-Ritz analysis. The Rayleigh-Ritz analysis results agreed well with the finite element results except for the cases of the highly anisotropic sublaminates where bending-twisting and shear-extension

coupling were neglected. They then went on to apply the virtual crack closure technique to predict instability-related delamination growth of homogeneous, isotropic laminates with imbedded square and rectangular delaminations [73]. The square and rectangular delaminations did not experience self-similar crack growth due to the large variation of strain energy release rate along the delamination front. Delamination growth in the load direction or perpendicular to it depended upon the size of the delamination, its aspect ratio, and the strain level. An experimental study by Geier, Vilsmeier, and Weisgerber [81] shows imbedded rectangular delaminations cause a small loss in compressive strength at room temperature for a small delamination but a significant drop in strength as delamination size increases. At hot/wet conditions (120°C, moisture content of 1.1%) both small losses or gains in strength for a small delamination occur depending upon the delamination location while the strength decreases as delamination size increases. The influence of defect size on the compressive residual strength decreases as the defect location moved towards the center of the specimen.

The basis of the aforementioned analyses is a single imbedded delamination. As to the effect of multiple delaminations on the compressive residual strength of composite laminates, less work has been done due to the increased complexity of analysis [7, 17, 41, 61, 73]. The issues again include sublaminate buckling load and delamination growth initiation load; postbuckling response and delamination propagation; sublaminate(s) and base laminate interaction; and compressive residual strength. Experiments with one or two imbedded delaminations [61] show the second (and in this case smaller) delamination reduces the compressive residual strength of the single delamination specimen by as much as 40%.

This shows that the compressive residual strength of an impact-damaged specimen that contains multiple delaminations cannot be estimated by a single delamination of the same planar area. As the number of imbedded delaminations increases from one to three, compressive residual strength decreases further [7]. Still lower compressive residual strengths are observed for barely visible and visible impacts, where delaminations can occur at nearly every interface.

The use of a single imbedded delamination to approximate impact damage is obviously not appropriate. Assumed boundary conditions significantly affect the predicted sublaminate buckling load and therefore, the ultimate failure load. To predict compressive residual strength using multiple delaminations improves the approximation of damage due to impact. However, as the number of delaminations increases so does the complexity and cost of the analysis. Analysis of delamination behavior alone is probably not sufficient in accurately predicting compressive residual strength. The interaction with fiber breaks and matrix cracks needs to be addressed.

2.3.3 Combined Damage States

Experimental results from compression after impact test programs attempt to correlate parameters easily measured (i.e., two-dimensional damage size and impact metrics) with compressive residual strength. Several authors have found that compressive failure strain could not be correlated with in-plane damage area [8, 16, 27, 45, 49] though a few authors had partial success [30, 82]. Though correlation results of compressive failure strain to damage area were mixed, most curves

exhibited asymptotic behavior as damage area increased [8, 27, 30, 82]. Correlation of the compressive failure strain to impact energy also exhibited asymptotic behavior as impact energy increased [30–34, 43, 82].

This asymptotic behavior was seen in an undergraduate research project done in TELAC [83] with a slight deviation: an apparent minimum compressive residual strength (MCRS) below the asymptote. As impact velocity increases beyond the minimum point, damage around the penetration location becomes less extensive. Thus, compressive residual strength increases towards the open hole asymptotic value. The questions these results raised are of particular interest. What is the three-dimensional damage state that governs minimum compressive residual strength behavior?; Is this minimum compressive residual strength value dependent upon impact method?; and, How does this minimum compressive residual strength value relate to impacter mass and velocity?

Previous work on prediction methodologies of compressive residual strength after impact is very limited. Flanagan [17] had several difficulties applying a single delamination model to post-impact compressive strength data. The model assumed thin film behavior, clamped edges, self-similar growth, and sublaminate deflections determined by base laminate strain. Post-impact data did not always include delamination depth. Thus, a conservative approach assumed delamination at the smallest critical strain interface and that delaminations were initially circular. The model did not compare well to experiment for impact energies below 10 joules nor energies high enough to produce significant fiber damage or penetration.

A further step taken by Marshall, Sandorff, and Lauraitis [36] was to model impact by a circular sublaminate with a central through-the-thickness hole. A Rayleigh-Ritz analysis based on the Trefftz criterion with

a symmetric buckling shape about both axes of a uniaxially loaded laminate was used. The critical buckling stress was highly sensitive to damage parameter variations in the analysis but not in experiment. This led to the conclusion that this analysis alone could not successfully predict failure of impacted laminates. The need for a mixed-mode failure law was demonstrated as failure occurred by a combination of delamination growth and sublaminate buckling.

The only analysis approach that requires an accurate description of the characteristic damage state is presented by Dost, Ilcewicz, and Gosse [84]. In this work, the characteristic damage state consisted of a spiral array of transverse cracks and delaminations that formed 4-ply thick circular sublaminates in a "staircase" arrangement. Compressive residual strength tests were conducted on coupons fabricated from a "brittle" epoxy system and a "toughened" epoxy system with similar stiffness characteristics. The stability of the sublaminates depended upon the layup, stiffness, length, and thickness, but not the "toughness". Thus, the buckling predictions versus damage diameter for both systems were identical and that lead to identical compressive residual strength predictions for both systems. Experimental results correlated very well with analytical predictions. Finite width effects were modeled and found to have a significant effect on predicted compressive residual strength. This suggests that coupon results do not necessarily represent material behavior at the structural level. Results of a later study [27] show compressive residual strength can be dominated by fiber damage if the damage size is small due to an increase in buckling resistance of the sublaminate.

Though extensive work has been done in predicting compressive residual strength of composite laminates with known defects, the

extrapolation of most of this work to general impact damage has yet to be done successfully. The work of Dost, Ilcewicz, and Gosse [84] is the only truly successful analytical/experimental correlation of post-impact compressive behavior found in the literature. Though it is important to understand single delamination behavior, it is unlikely that an impact event would result in a single delamination. Multiple delaminations may not be a sufficient model depending upon the characteristic damage state of the laminate of interest. As Dost, et. al. [84] showed for the quasi-isotropic laminate, a single delamination or multiple delamination model would not have been appropriate. Therefore, before an appropriate analysis approach can be selected, a thorough understanding of the characteristic damage state of the laminate of interest must be determined.

Chapter 3

EXPERIMENTAL PROCEDURES

3.1 Approach Overview

The original purpose of the experimental program was twofold: to provide data for correlation to a preliminary predictive analysis method to be developed for compressive residual strength; and to answer the questions raised by the results of a previous research project concerning the existence of a minimum compressive residual strength [83]. A schematic of these results (Figure 3.1) shows that a minimum compressive residual strength (MCRS) apparently exists below the open hole value of the impacter diameter. These results raised the following three questions: one, what is the three-dimensional damage state that governs minimum compressive residual strength behavior; two, is this minimum compressive residual strength value dependent upon impact method; and three, how is this minimum compressive residual strength value related to impacter mass and velocity? As to the first purpose of the experimental program, assessment of the state-of-the-art in predictive capabilities, as discussed in Chapter 2, indicated that the need for basic understanding of the damage mechanisms governing compressive failure behavior still existed. Thus, the focus of the experimental program shifted to answering the questions on minimum compressive residual strength. It is hoped the detailed documentation of experimental results contained herein will allow for verification of compressive residual strength prediction methodologies later developed.

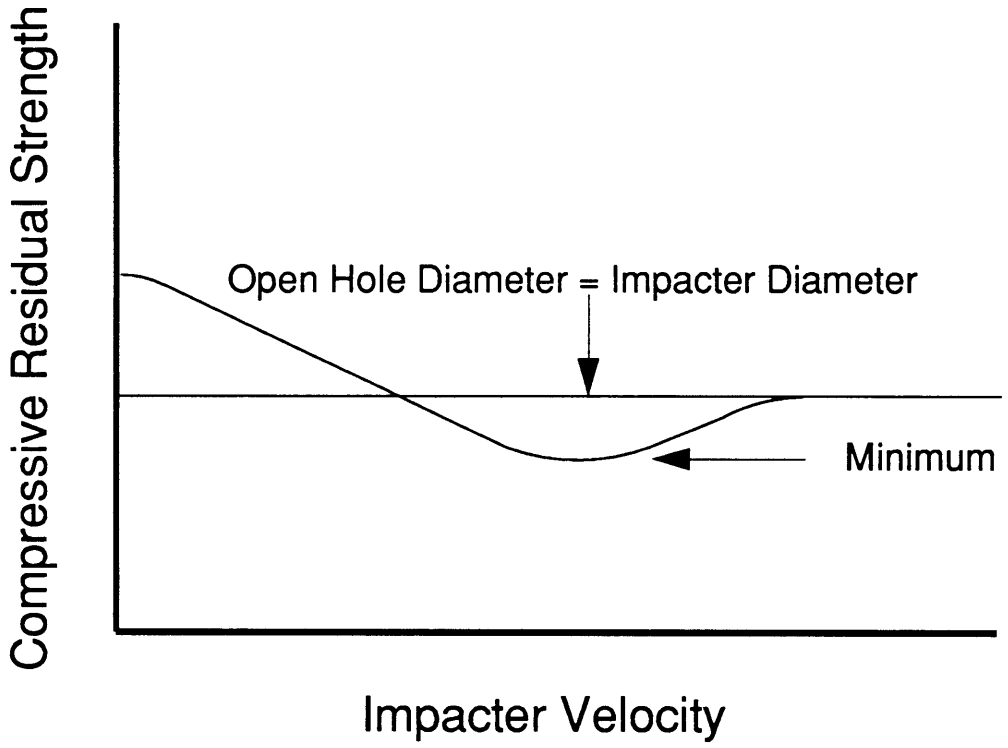

Figure 3.1 Schematic of Results of Previous Project [83] Indicating Existence of a Minimum Compressive Residual Strength.

3.2 Test Matrices

The test matrices were developed in response to the three questions enumerated in the previous section. Specimens were fabricated in a $[\pm 45/0]_{2S}$ laminate from AS4/3501-6 graphite/epoxy unidirectional tape manufactured by Hercules, Inc. This laminate orientation and material system were selected because of the extensive TELAC data base available on damage resistance and tensile residual strength [e.g., 25 and 29].

The questions involving impact method and impact metrics (mass and velocity) appeared easier to answer than the question on the three-dimensional damage state. Thus, the first item of the experimental program was the reproduction of the compressive residual strength versus impacter velocity curve (Figure 3.1) using a different set of impact metrics. The impact metrics for the minimum compressive residual strength obtained in Reference 83 were a mass of 8.4 g and velocity of approximately 57 m/s. This resulted in an impacter energy of approximately 13 J. The first impact device employed in the current work, as later described, makes it possible to impact with a heavier device more representative of a "tool drop." The impacter mass initially chosen was 1505 g.

Although it has been found [8, 19, 32, 39] that a "low mass/high velocity" impact method results in greater damage than the "high mass/low velocity" method for the same materials at identical incident energy, an initial estimate of the velocity at which a larger mass will create the damage necessary to achieve minimum compressive residual strength assumed impact energy was the controlling parameter. This resulted in a velocity of 4 m/s for the 1505 g impacter mass. Since damage is dependent upon the combination of impacter mass and velocity, a range of velocities

was then selected for impacting. The upper limit on velocity for the 1505 g impacter mass set by preliminary experiments showed impact at 6.3 m/s resulted in complete penetration of the tup into the coupon. Complete penetration is defined at the tip of the impacter progressing beyond the back surface of the laminate.

As a result of the preliminary experiments, the first desired impact test matrix consisted of fifteen coupons. Three coupons were to be impacted at each of the following velocities: 4.1, 4.6, 5.2, 5.7, and 6.3 m/s. The test matrix actually achieved, shown in Table 3.1, included the following velocities: 4.3, 4.8, 5.2, 5.5, 5.7, 6.0, 6.3, 7.1, and 8.6 m/s. (Why actual velocities deviate from desired is discussed in the section on impact apparatus operations.) All these impacted specimens were tested for compressive residual strength.

The compressive residual strength of impact-damaged specimens was compared to the compressive residual strength of undamaged specimens and specimens with open holes. Originally, five specimens in the undamaged state were selected from five cures for compressive residual strength tests. Three out of the five tests were unsuccessful as the upper hydraulic grip experienced spikes that crushed the specimens in the tab region. Once the source of the problem was determined, the pre-test setup procedure was modified to prevent this from reoccurring. The hole diameters tested are shown in Table 3.2. The 12.7 mm diameter hole is identical to the diameter of all impacters used in this work. Larger diameter holes were also tested to compare the compressive residual strength after impact to holes larger than the diameter of the impacter tup. The 25.4 mm diameter hole is the maximum size used in order to avoid finite width effects.

Table 3.1 Impact Test Matrix 1[a]

Impacter Velocity (m/s)	Test Type[b]		
	CRS	Section	Deply
4.3	1[c]	—	—
4.8	3	—	—
5.2	3	—	—
5.5	1	—	—
5.7	1	—	—
6.0	1	—	—
6.3	1	—	—
7.1	1	—	—
8.6	1	—	—

[a] Impacter Mass = 1505 g

[b] CRS – compressive residual strength test after impact
Section – destructive damage evaluation by cross-sectioning
Deply – destructive damage evaluation by deply technique

[c] Indicates number of coupons tested

Table 3.2 Undamaged and Open Hole Test Matrix

Hole Diameter (mm)	Test Type[a]		
	CRS	Section	Deply
0.0	2[b]	—	—
12.7	3	—	—
19.1	3	—	—
25.4	3	—	—

[a] CRS – compressive residual strength test after impact
Section – destructive damage evaluation by cross-sectioning
Deply – destructive damage evaluation by deply technique

[b] Indicates number of coupons tested

The experimental results of compressive residual strength versus impacter velocity for the specimens of Tables 3.1 and 3.2 pointed toward a minimum compressive residual strength around an impacter velocity of 6.3 m/s. This is where complete penetration of the tup occurred. A second impact matrix was thus designed to further characterize minimum compressive residual strength with three more specimens at each of the following velocities: 6.0, 6.3, and 6.7 m/s. The test matrix actually achieved is shown in Table 3.3. Again, all these impact-damaged specimens were tested for compressive residual strength.

The approach used to produce a minimum compressive residual strength curve with the 1505 g (or 1523 g) impacter mass (a steel rod) was successful. The same approach was used for a smaller impacter mass of 578 g (an aluminum rod). A third impact test matrix was designed to envelop the minimum compressive residual strength with impact of five coupons at each of the following desired velocities: 8.0, 8.6, 9.2, 10.0, and 10.9 m/s. The test matrix actually achieved is shown in Table 3.4.

After minimum compressive residual strengths were characterized for the three impacter masses of interest (one using previous work [83]), the focus shifted to defining the damage state at these minima. A fourth impact matrix was designed for damage definition of impact with the 1523 g mass. The intent was to impact seven specimens at three velocities (6.0, 6.3, and 6.7 m/s) encompassing the minimum compressive residual strength velocity previously determined. The choice of seven specimens at each velocity would allow four specimens to be destructively tested (3 for sectioning, 1 for deply) while the other three specimens would be tested for compressive residual strength. The impact test matrix achieved is shown in Table 3.5. The fifth and sixth impact matrices were designed with the

Table 3.3 Impact Test Matrix 2[a]

Impacter Velocity (m/s)	Test Type[b]		
	CRS	Section	Deply
5.5	1[c]	—	—
6.0	3	—	—
6.3	2	—	—
6.7	3	—	—
7.1	1	—	—
7.5	1	—	—

[a] Impacter Mass = 1505 (or 1523) g

[b] CRS – compressive residual strength test after impact
Section – destructive damage evaluation by cross-sectioning
Deply – destructive damage evaluation by deply technique

[c] Indicates number of coupons tested

Table 3.4 Impact Test Matrix 3[a]

Impacter Velocity (m/s)	Test Type[b]		
	CRS	Section	Deply
7.5	1[c]	—	—
8.0	1	—	—
8.6	2	—	—
9.2	6	—	—
10.0	7	—	—
10.9	3	—	—

[a] Impacter Mass = 578 g

[b] CRS – compressive residual strength test after impact
Section – destructive damage evaluation by cross-sectioning
Deply – destructive damage evaluation by deply technique

[c] Indicates number of coupons tested

Table 3.5 Impact Test Matrix 4[a]

Impacter Velocity (m/s)	Test Type[b]		
	CRS	Section	Deply
4.6	1[c]	—	—
5.2	1	—	—
5.5	1	1	—
5.7	2	3	1
6.0	—	2	—
6.3	1	3	1
6.7	—	2	—
7.5	1	1	—

[a] Impacter Mass = 1523 g

[b] CRS – compressive residual strength test after impact
Section – destructive damage evaluation by cross-sectioning
Deply – destructive damage evaluation by deply technique

[c] Indicates number of coupons tested

same intent for impact with 578 and 8.4 g masses, respectively. The test matrices achieved for impact with these two masses are shown in Tables 3.6 and 3.7, respectively. For all the specimens of Tables 3.5 through 3.7, nondestructive damage evaluation was conducted before destructive damage evaluation.

3.3 Specimen Description

The impact/open hole test coupon is 70 mm wide by 340 mm long as illustrated in Figure 3.2. One TELAC standard-sized laminate of 305 mm by 350 mm yields four such specimens. All coupons were made from AS4/3501-6 graphite/epoxy unidirectional tape manufactured by Hercules, Inc. in a $[\pm 45/0]_{2S}$ configuration.

The specimen used to determine compressive residual strength is a honeycomb sandwich specimen designed for compressive characterization of thin laminates [85]. Minor modifications to the planar geometry in Reference 84 result in a specimen width of 70 mm, length of 340 mm, and core thickness of 25.4 mm. Placement of the honeycomb core between the two facesheets prevents global buckling of the laminate as a possible failure mode. This core is a combination of low density (72 kg/m^3) and high density (352 kg/m^3) aluminum honeycomb. The high density core is located in the grip area to prevent crushing of the specimen when it is held in the test fixture. The core located in the test section is low density to virtually eliminate load-sharing with the facesheets. The impact coupon and an undamaged coupon are bonded to this aluminum honeycomb core after impact and nondestructive evaluation. Fiberglass end tabs are then bonded to the graphite/epoxy to provide an efficient load transfer mechanism. The

Table 3.6 Impact Test Matrix 5[a]

Impacter Velocity (m/s)	Test Type[b]		
	CRS	Section	Deply
7.5	1[c]	—	—
8.0	1	3	—
8.6	1	3	1
9.2	—	3	1
10.0	—	2	—
10.9	—	1	—
12.0	1	1	—

[a] Impacter Mass = 578 g

[b] CRS – compressive residual strength test after impact
Section – destructive damage evaluation by cross-sectioning
Deply – destructive damage evaluation by deply technique

[c] Indicates number of coupons tested

Table 3.7 Impact Test Matrix 6[a]

Impacter Velocity (m/s)	Test Type[b]		
	CRS	Section	Deply
55	2[c]	3	1
56	1	1	—
57	2	2	1
58	1	3	1
70	3	—	1

[a] Impacter Mass = 8.4 g

[b] CRS – compressive residual strength test after impact
Section – destructive damage evaluation by cross-sectioning
Deply – destructive damage evaluation by deply technique

[c] Indicates number of coupons tested

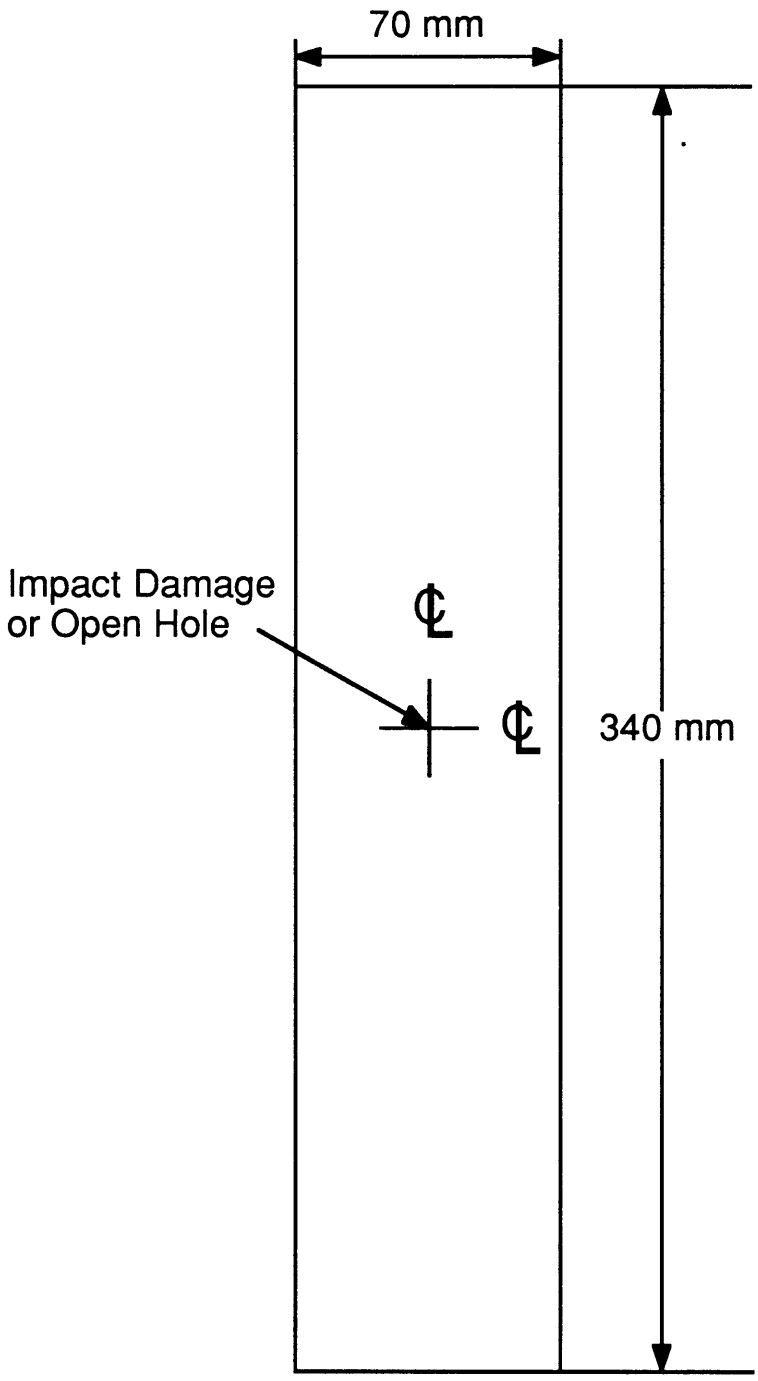

Figure 3.2 Impact/Open Hole Coupon Geometry.

resulting configuration is the compressive residual strength test specimen illustrated in Figure 3.3. Coupons with drilled holes instead of impact damage are also fabricated into identical compressive residual strength test specimens.

3.4 Manufacturing Procedures

The manufacturing procedure for the coupon consists of prepreg cutting, layup, cure, postcure, machining, and drilling. The manufacturing procedure for the compressive residual strength test specimen includes preparation of the honeycomb core and fiberglass tabs, bonding, and instrumentation. The procedures used were developed in TELAC [86], and are summarized herein.

3.4.1 Impact/Open Hole Coupon

Hercules AS4/3501-6 graphite/epoxy material was used in this investigation. This material consists of unidirectional AS4 graphite fibers in a 3501-6 thermoset matrix system. It is in a semi-cured (B-stage) state as preimpregnated (prepreg) tape and must be stored in a freezer in a tightly sealed bag at -18°C or colder. The prepreg roll is nominally 305 mm wide. Each roll has identification information including: lot number, spool number, areal weight, resin content, and date of manufacture. This information is recorded for traceability of material consistency from laminate to laminate (see Appendix A). Before prepreg cutting, the prepreg is taken out of the freezer and left sealed at room temperature for thirty minutes. This is to prevent water condensation on the material that could potentially result in a poor quality laminate.

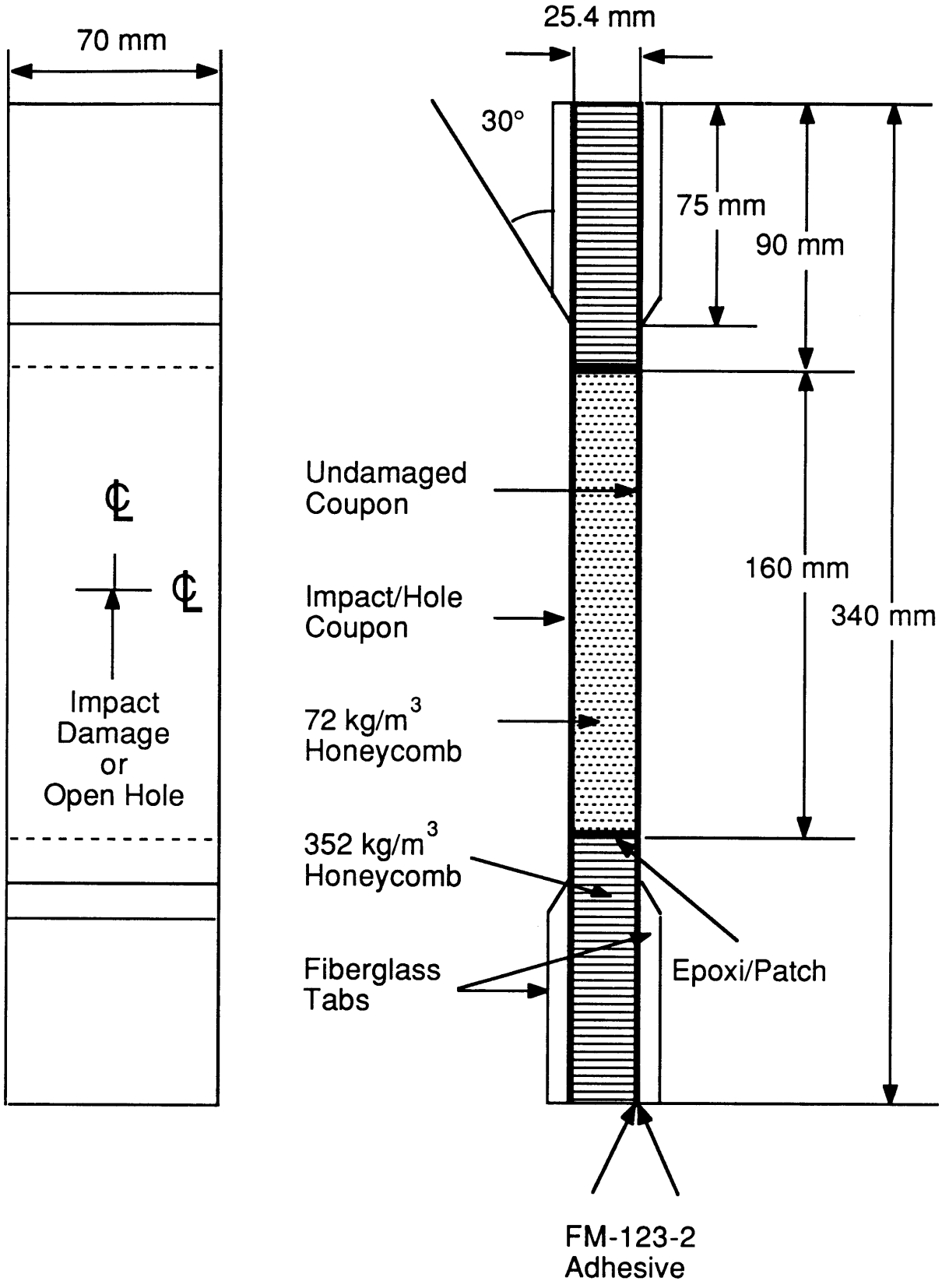

Figure 3.3 Compressive Residual Strength Test Specimen Geometry.

The prepreg is cut into appropriate shapes required for each ply orientation using aluminum templates covered with teflon and a sharp Stanley utility knife. Any section of prepreg with visible defects is not used. The 45° plies are cut into trapezoidal shapes that are placed together to form a 305 mm by 350 mm rectangle. These trapezoids are designed such that no fiber breaks exist in any ply. The joint where the two trapezoids meet is parallel to the fiber direction and becomes indistinguishable during the cure cycle. The 0° plies are made using a 305 mm by 350 mm rectangle. Each ply is laid up with the help of a corner jig to keep the angles properly aligned. A sheet of peel-ply, a nylon-like fabric that is porous to the epoxy, is applied to both sides of each laminate with the jig corner marked for future cure placement and machining reference.

Several materials are used in the curing process of a laminate as shown in Figure 3.4. The aluminum caul plate is covered by Mold Wiz® mold release, manufactured by Axel Plastics Research Laboratories, and nonporous teflon. The laminate (with peel-ply) is placed on the nonporous teflon with the marked corner in the corner of the aluminum T-dam. A sheet of porous teflon is placed on top of the laminate. Sheets of bleeder material are placed on top of the porous teflon to absorb excess epoxy as it flows out of the laminate during the cure. The number of bleeder sheets is half the number of plies of the laminate. In this case, six plies of bleeder are used. Aluminum top plates, wrapped in a high grade nonporous teflon, are placed on top of the bleeder material. The assembly butts up against an aluminum T-dam on two sides. On the remaining two sides, cork dams are built up around the laminate and top plate assembly to ensure that neither shifts during the cure.

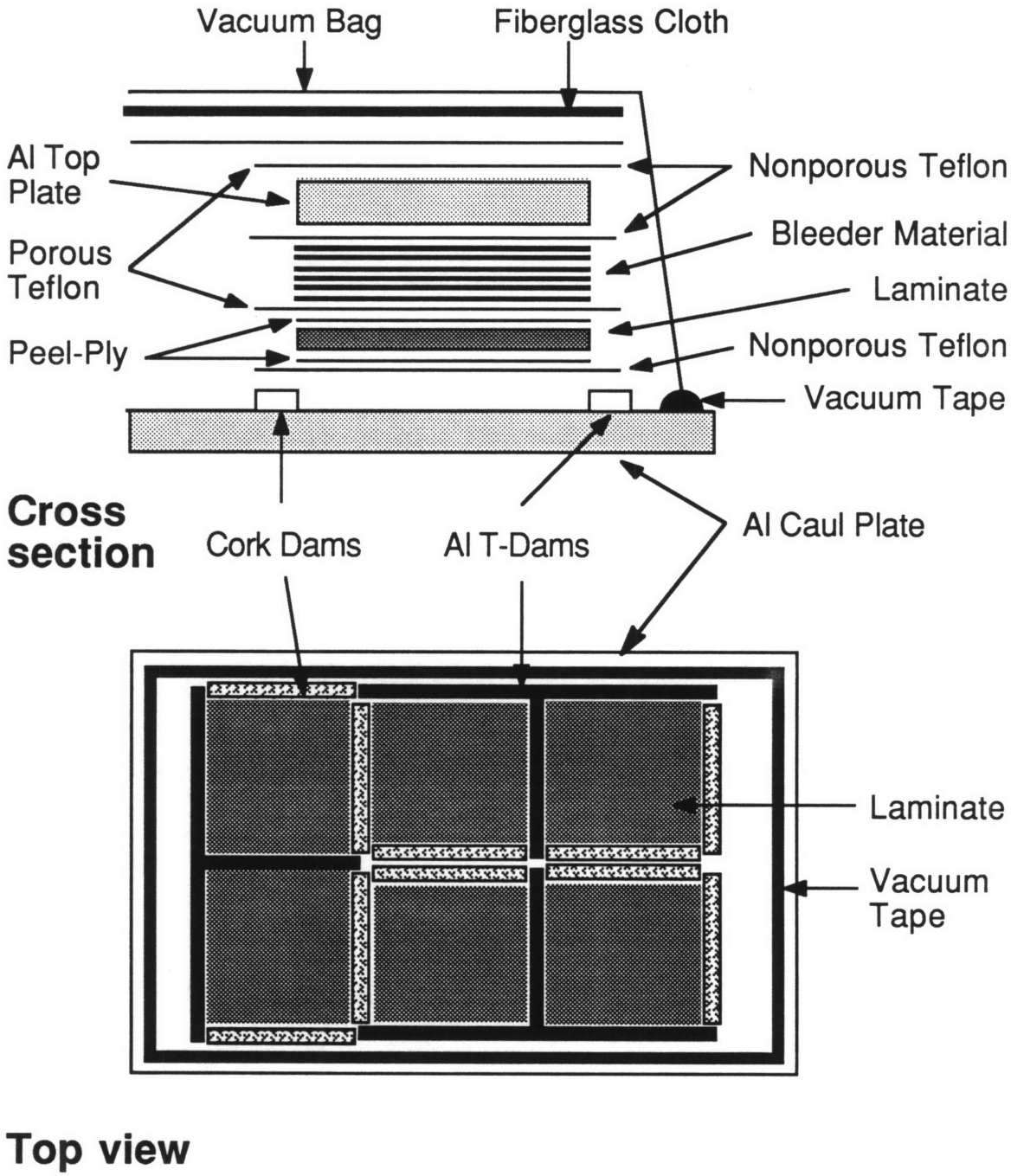

Figure 3.4 Illustration of Cure Assembly for Laminates.

Usually six laminates are cured at a time on one caul plate. The location at which the laminates are placed on the caul plate is illustrated in Figure 3.4. The entire assembly is covered with sheets of porous teflon, and a heavy fiberglass cloth serving as an air breather, and sealed with a high-temperature nylon bagging material and vacuum tape.

Once the cure plate is ready, a vacuum check is performed on the system. A vacuum of 760 mm Hg is applied. The inlet valve is shut off and the assembly sits for five minutes to determine if there are any leaks in the system. If more than 130 mm Hg is lost in those five minutes, the vacuum bag is repaired or replaced. When the vacuum check is successful, the assembly is rolled into the autoclave and the vacuum check is repeated.

After successful vacuum checks, the autoclave door is closed and pressure is applied up to 0.59 MPa and held. The heater is then turned on to raise autoclave temperature at a rate of 1–3°C per minute to 117°C. The temperature is held at 117°C for one hour. This is the flow stage when the epoxy is at its lowest viscosity. The temperature is again raised at a rate of 1–3°C per minute to 177°C. The temperature is held at 177°C for two hours. This is the set stage when the chemical cross-linking of the polymer chains occurs in the epoxy. The temperature is then lowered at a rate of 1–3°C per minute to 66°C and pressure is released. The vacuum is then released and the autoclave door is opened to vent the cure assembly to room temperature. This standard cure cycle is illustrated in Figure 3.5.

The assembly is rolled out of the autoclave and the laminates removed from all the surrounding materials except the peel-ply. The laminates (with peel-ply) are placed in an unpressurized oven for a postcure of eight hours at 177°C. The postcure drives the chemical cross-linking of the polymer chains in the epoxy to completion.

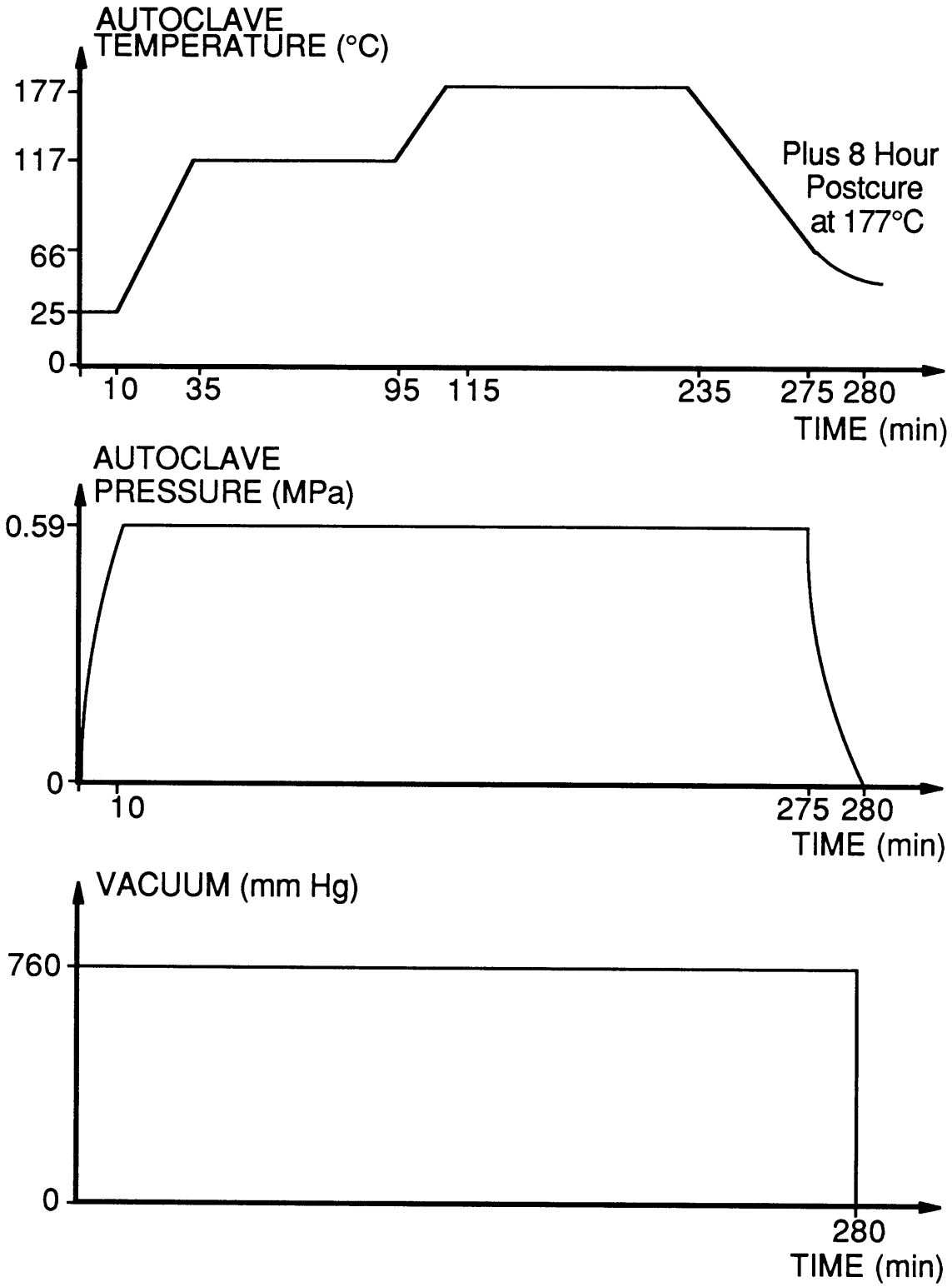

Figure 3.5 Standard Cure Cycle for AS4/3501-6 Graphite/Epoxy Laminates.

Out of the eleven standard cures attempted in this study, only the third cure did not follow the cycle illustrated in Figure 3.5. Twenty minutes into the one hour hold at 117°C, the vacuum gage read only 380 mm of Hg. The vacuum and pressure were released, the temperature was reduced, and the autoclave door was opened to vent the assembly to room temperature. The assembly was rolled out of the autoclave and one laminate was removed from all the surrounding materials. When this laminate was allowed to cool, it appeared partially cured. It was reheated with a blow dryer and became t. ky and pliable. Thus, the standard cure on the remaining five laminates was reattempted. The vacuum bag and tape on the assembly were replaced and a secondary vacuum pump attached to the autoclave. The vacuum checks were successful and the standard cure cycle was completed without any further mishap. Cure cycle numbers for all laminates fabricated in this study are referenced in Appendix A.

Four coupons are machined from each laminate to the proper dimensions (70 mm by 340 mm) starting at the marked corner. A water-cooled 152 mm diameter diamond grit cutting wheel is used on a milling machine at a spindle speed of 1100 rpm and a table feed rate of 280 mm per minute. Approximately 5 mm is trimmed from the edges of the laminates to remove epoxy ridges and provide uniform, straight edges. The convention used for coupon identification is illustrated in Figure 3.6. Because all laminates have the same layup, the coupons are identified not only by location in the laminate but by layup technician and laminate number per layup technician. This identification process allows a check for variability between layup technicians and between the first and nth laminates laid up by each individual.

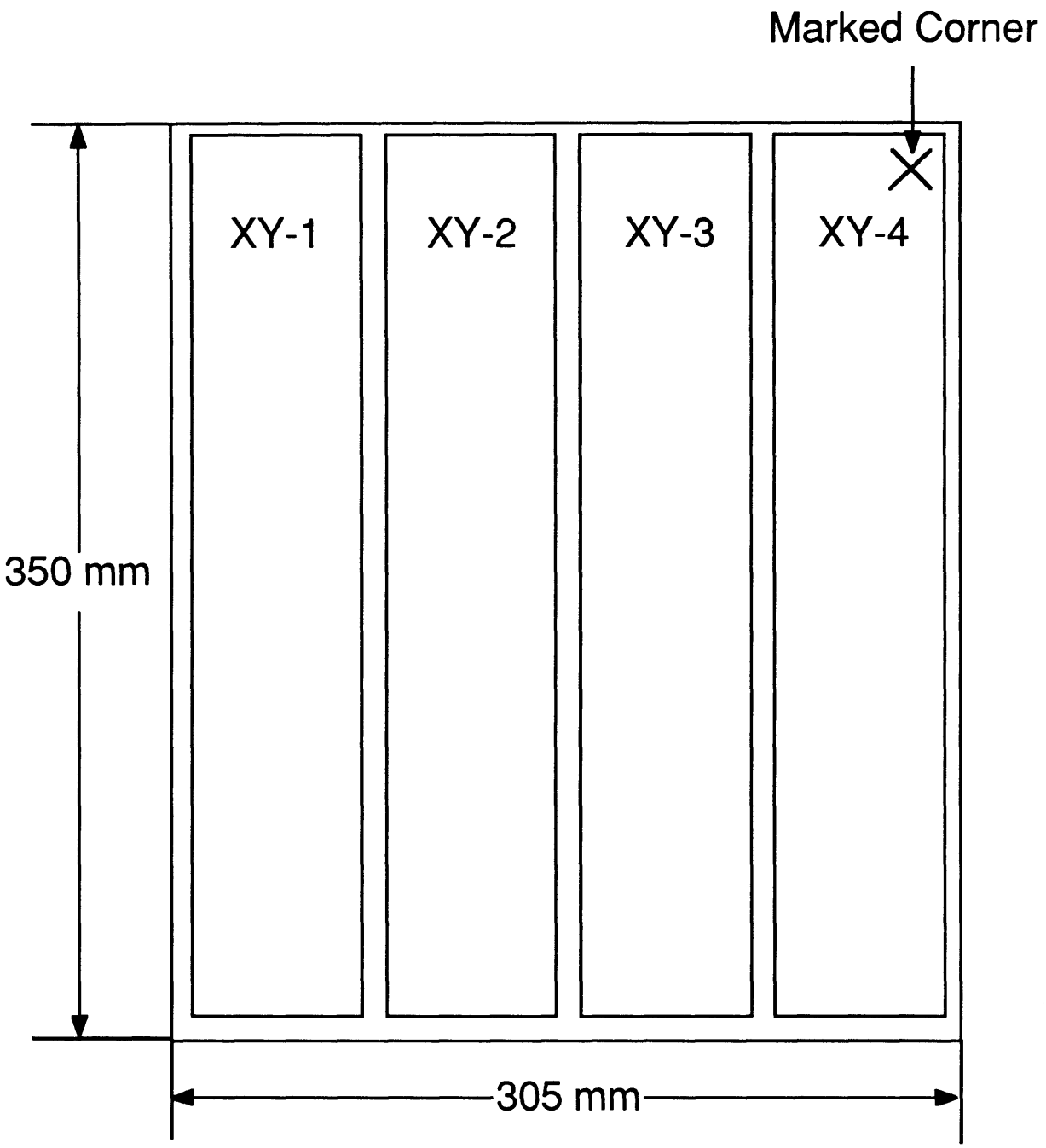

Figure 3.6 Illustration of Coupon Identification Convention.

To check for uniformity, the coupons are measured in three locations for width and nine locations for thickness. Locations of these measurement points are illustrated in Figure 3.7. The center mark used for coupon thickness measurement is also the intended center of impact or open hole location. The average ply thickness for all the specimens is 0.136 mm compared to the nominal ply thickness of 0.134 mm. The measured average thickness and average width for each coupon is used for stress calculations and is listed in Appendix A.

The coupons are now ready to be damaged (impact testing is discussed in Section 3.5.1). Holes are drilled in coupons on a press with diamond grit bits. The 12.7 mm hole is drilled using a set of bits. The first bit is a slightly undersized solid drill bit with a rougher grit (80 - 100 grit). This drill bit is used to go through the specimen. The second bit is a reamer that is the exact hole size and has a much finer grit (220 grit). The reamer is used to give the desired diameter and a smooth finish. The 19.1 mm and 25.4 mm holes are drilled with a single bit that is similar to the reamer used for the 12.7 mm hole. The coupon is centered under the drill bit using the middle thickness location mark and anchored with C-clamps on either end. Scrap fiberglass is located in a slot underneath the drilling location to provide support and prevent backside splitting or delamination. A drop of water is placed at the drill contact location on the coupon. The drill is lowered and contact pressure is cycled until the fiberglass is reached. Drops of water are added during this procedure as necessary.

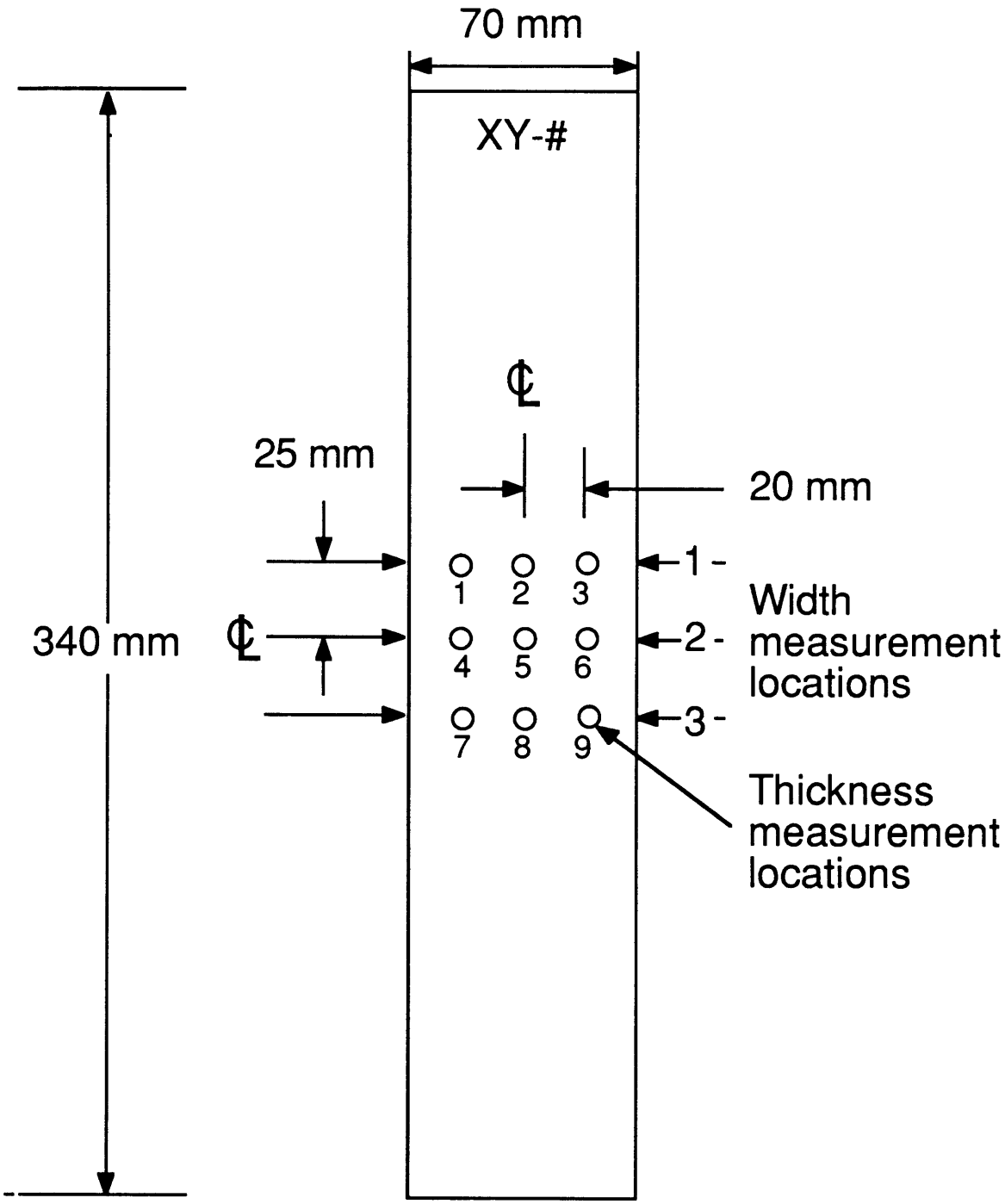

Figure 3.7 Location of Coupon Width and Thickness Measurements.

3.4.2 Compressive Residual Strength Specimen

The honeycomb core used for the compressive residual strength sandwich test specimen is 25.4 mm thick and manufactured by American Cyanamid. Two high density (352 kg/m^3) aluminum honeycomb pieces are cut to 90 mm in length by 305 mm in width on a bandsaw. One low density (72 kg/m^3) aluminum honeycomb piece is then cut to 160 mm in length by 305 mm in width. The ribbon direction is perpendicular to the width for both the high density and low density honeycomb cores. The low density honeycomb core is bonded at either end to the high density honeycomb core using a 0151 Clear Epoxi-Patch Kit manufactured by Dexter Hysol keeping the ribbon direction consistently perpendicular to the width. These pieces are compressed in a jig for at least two hours at room temperature until the epoxy sets to create an aluminum honeycomb core panel 305 mm wide by 340 mm long. The honeycomb core panel is then cut into four 70 mm wide by 340 mm long specimens on a bandsaw.

In preparation for bonding to the graphite/epoxy coupons, the honeycomb core is cleaned. The surface of the honeycomb core is first cleaned with brisk strokes from a wire brush. Then each surface of the honeycomb core is soaked in methylethylketone (MEK) for five minutes. The honeycomb core is now clean and is to be handled only with gloves.

Preparation of fiberglass tabs for secondary bonding begins with the selection of the correct thickness of $[0/90]_S$ precured Scotchply 1002 fiberglass laminates manufactured by 3M. For the $[\pm 45/0]_{2S}$ graphite/epoxy laminate, a 380 mm by 610 mm fiberglass laminate with thickness of 3.7 mm is used (at least twice the thickness of the graphite/epoxy laminate). The fiberglass laminate is cut into 70 mm by 75 mm tabs using the same

procedure and equipment as for the graphite/epoxy laminates described previously. One 70 mm side of the tab is beveled to 30° on a belt sander. The fiberglass tabs are then cleaned with alcohol and ready for bonding.

Two separate but similar bond cures are done to combine the graphite/epoxy coupon facesheets, the aluminum honeycomb core specimens, and the fiberglass end tabs. The first cure combines the facesheets to the core to create a sandwich. The second cure combines the resulting sandwich and the fiberglass tabs to form the compressive residual strength test specimen. FM-123-2 film adhesive manufactured by American Cyanamid is used for both bond cures. FM-123-2 is a modified nitrile epoxy supported film on a non-woven synthetic fabric carrier. It must be stored in a freezer at -18°C or colder. Each roll has identification information including roll number, batch number, and date of manufacture. This information is recorded for traceability of material consistency from specimen to specimen. The adhesive is taken out of the freezer and allowed no warm-up time.

For the first bond cure, the graphite/epoxy coupons are cleaned with cheesecloth and placed on the adhesive. The adhesive is cut slightly oversize with a sharp Stanley utility knife. The backing paper is removed and the coupon is centered on a clean honeycomb specimen. The convention used was a -1 coupon bonded with a -3 coupon and a -2 coupon bonded with a -4 coupon. For the second bond cure, clean fiberglass tabs are placed on the adhesive. Again, the adhesive is cut slightly oversize with a sharp Stanley utility knife. The backing paper is removed and tabs are placed on the end of each facesheet.

The materials used in the bond cure assembly are illustrated in Figure 3.8. To prepare for the bond cure of the facesheets to the core, the

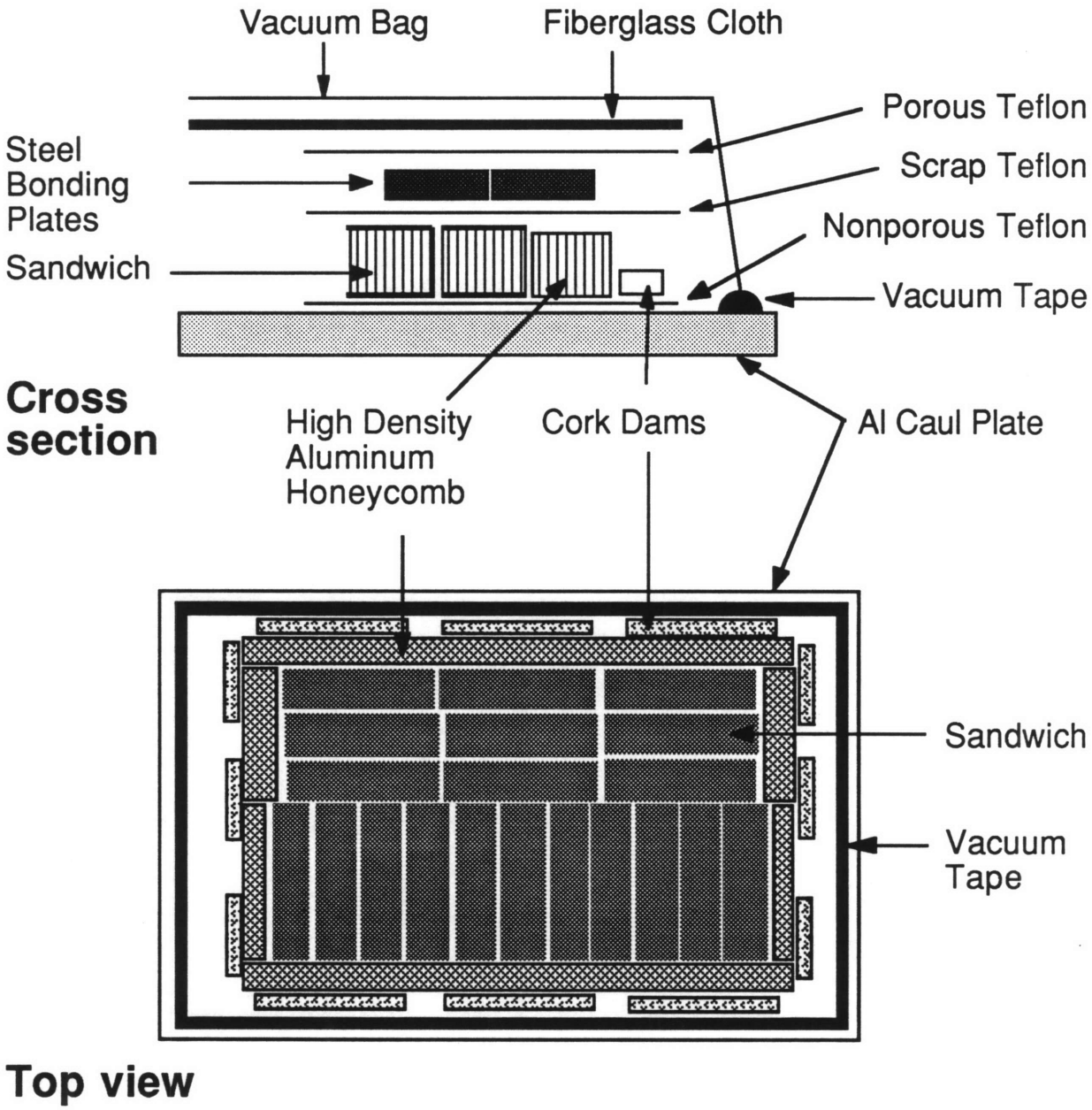

Figure 3.8 Illustration of Cure Assembly for Bonding Facesheets to Core.

aluminum caul plate is covered by Mold Wiz® mold release and nonporous teflon. The sandwich specimens are placed in the center of the aluminum caul plate in a rectangular array, as in Figure 3.8, and covered with scrap teflon. Steel bonding plates (57 mm by 368 mm) are placed over the teflon in a tight configuration to prevent slippage. The overhanging ends of the steel plates are supported with scrap high density aluminum honeycomb core to prevent crushing of the core. Cork dams are placed around the scrap honeycomb to minimize slippage during cure. As many as twenty specimens can be bonded at a time on one caul plate. The entire assembly is covered with sheets of porous teflon and a heavy fiberglass cloth serving as an air breather, and sealed with a high-temperature nylon bagging material and vacuum tape. For the bond cure assembly of fiberglass tabs to sandwich specimens, fiberglass tabs at both ends of each facesheet would be added. Also, scrap fiberglass pieces are used as shims in the middle of each facesheet to provide uniform support for the steel top plates.

Once the bond cure plate is ready, the assembly is rolled into the autoclave and the vacuum is set to exhaust. No vacuum is pulled during bond cures of sandwich specimens to prevent core crushing. Pressure is applied up to 0.28 MPa and held. The heater is then turned on to raise autoclave temperature at a rate of 1–3°C per minute to 107°C. The temperature is held at 107°C for two hours. The temperature is then lowered at a rate of 1–3°C per minute to 66°C and pressure is released. The autoclave door is opened to vent the cure assembly to room temperature. This bond cure cycle is illustrated in Figure 3.9.

When both bond cures have been completed, the compressive residual strength test specimens are measured for thickness in four locations (1, 3,

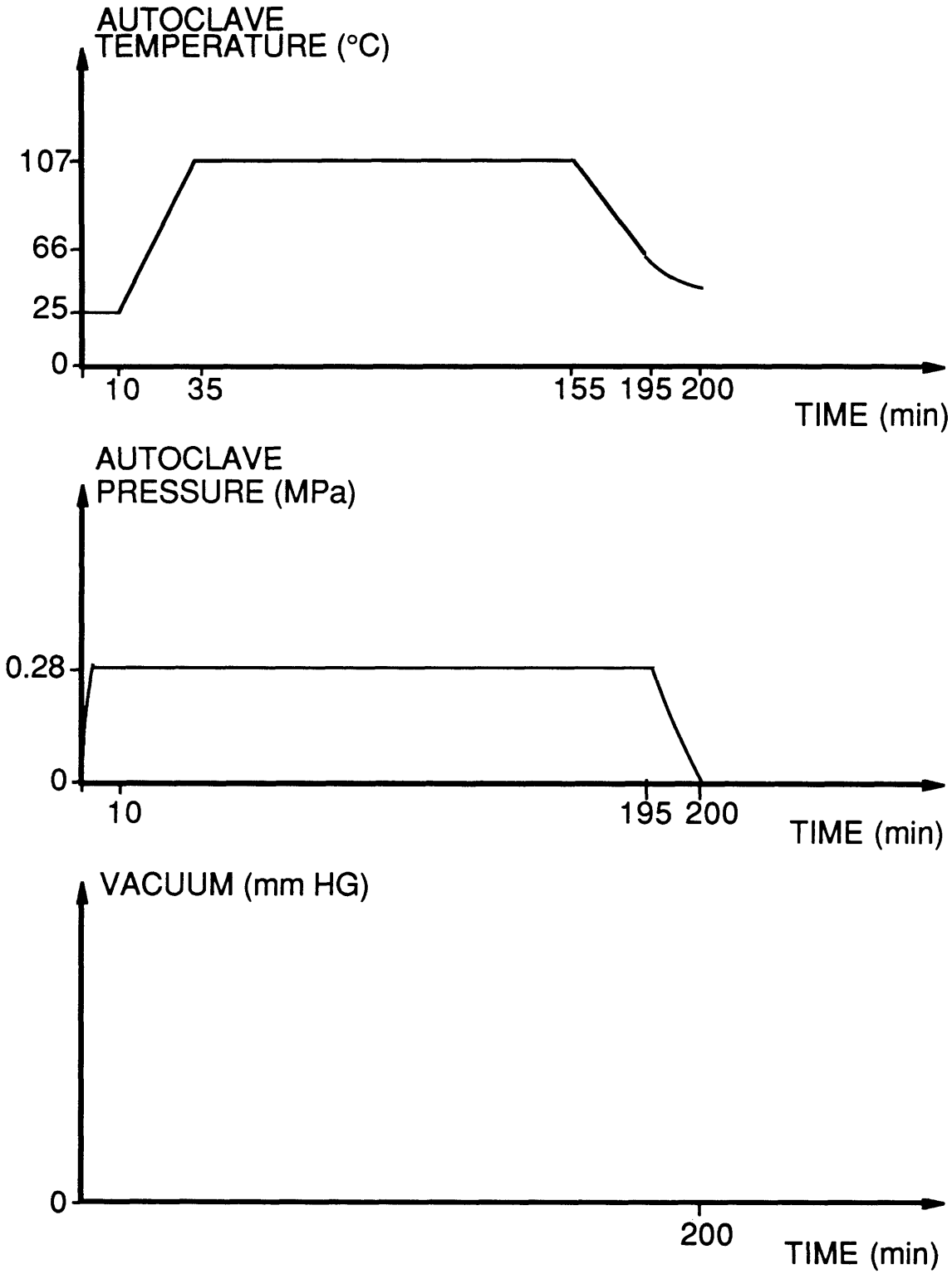

Figure 3.9 Bond Cure Cycle.

7, and 9 in Figure 3.7). The average beam thickness for all the specimens is 28.6 mm compared to the nominal thickness of 28.8 mm.

3.4.3 Instrumentation

The only instrumentation used in this investigation are EA-06-125AD-120 (120 ohm) strain gages manufactured by Micro Measurements. Strain gage manufacturing information is recorded for quality control and correct calibration during data acquisition. Each compressive residual strength test specimen has at least one strain gage. The location of this gage is on the vertical centerline of the damaged facesheet 25.4 mm below the edge of the "top" fiberglass tab, position A in Figure 3.10. The "top" was determined by the location in the upper grip of the MTS test fixture. This location provides far-field strain data at failure. This data is also used as a specimen quality check through laminate stiffness calculation.

On the open hole coupons there is a second strain gage located on the horizontal centerline of the coupon 9.6 mm to the right of the hole, position B in Figure 3.10. This location provides data on the open hole stress concentration at a consistent distance from the hole edge independent of hole size. On the compressive residual strength test specimens with a 19.1 mm open hole there is a third strain gage at position A on the undamaged coupon. This third gage was used to successfully verify equal compressive load distribution between the damaged and undamaged coupons.

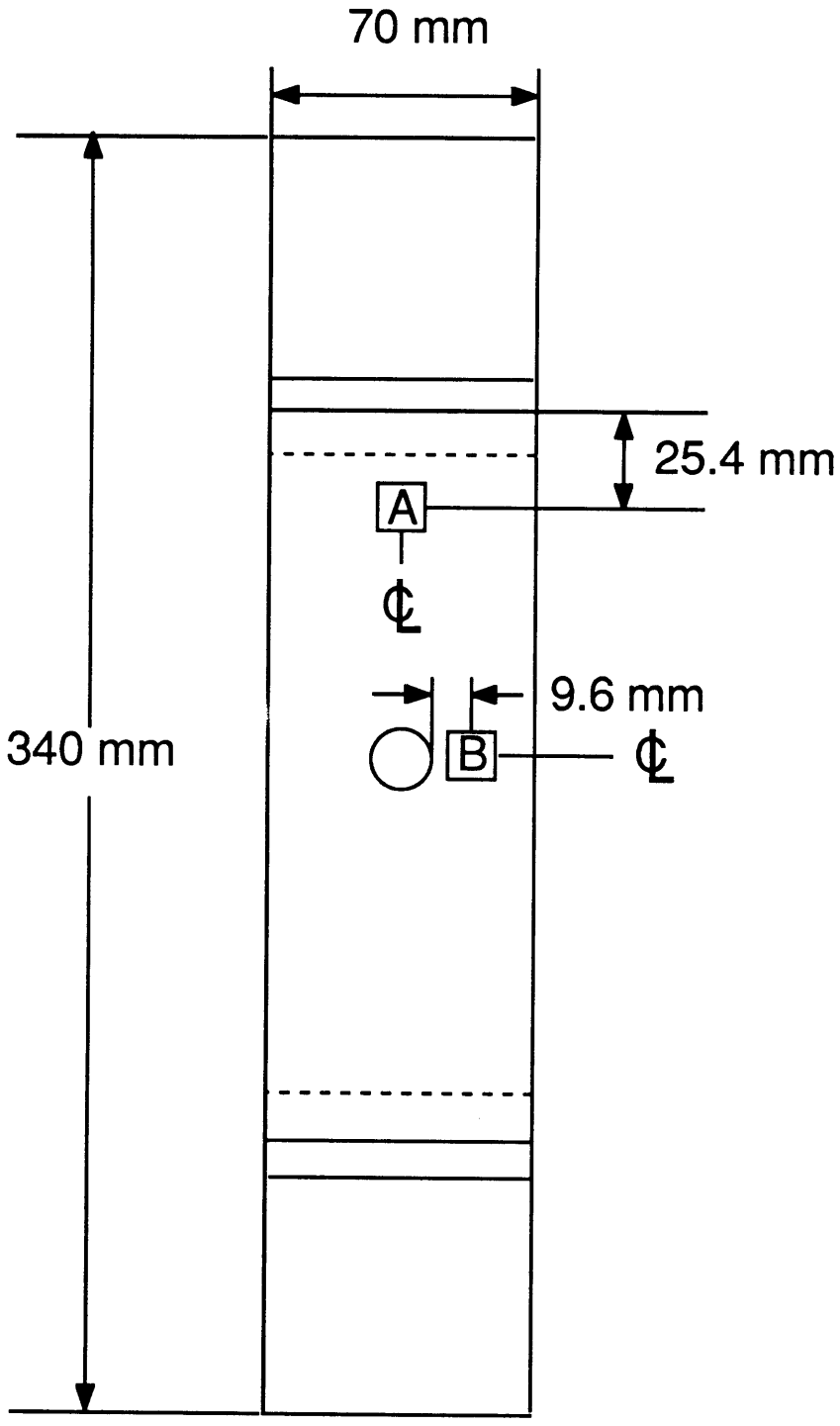

Figure 3.10 Strain Gage Locations.

3.5 Test Procedures

The test program has three separate phases: impact testing, damage detection, and compressive residual strength testing. Two distinct impact methods are used in the first phase of the test program. The purpose of the second phase of the test program is to determine the damage caused by the impact of the first phase. Damage is detected by NonDestructive Evaluation (NDE) methods as well as destructive methods. In the third phase of the test program, static tests are conducted to determine compressive residual strength of undamaged, open hole, and impact-damaged specimens. Details of the three separate phases of the test program are given in this section.

3.5.1 Impact

Even though two different impact test methods are used in this research, the test coupons are identical and use a common holding jig illustrated in Figure 3.11. The holding jig includes a large aluminum plate with a rectangular opening; aluminum bars (in this case, square bars to simulate clamped boundary conditions); and threaded rods with hex nuts used to apply consistent torque at each nut for each test. The contact surfaces of the square aluminum bars are covered with Carborundum Flexbac Metal Cloth (60M grit) to prevent slippage of the coupon in the grips. Each of the eight hex nuts is tightened, using a torque wrench, to 11.3 Nm for every impact test in an attempt to achieve consistent clamped boundary conditions.

Impact of each coupon is on the last ply laid up as shown in Figure 3.12. Thus, the impact surface corresponds to ply 12 in the laminate and

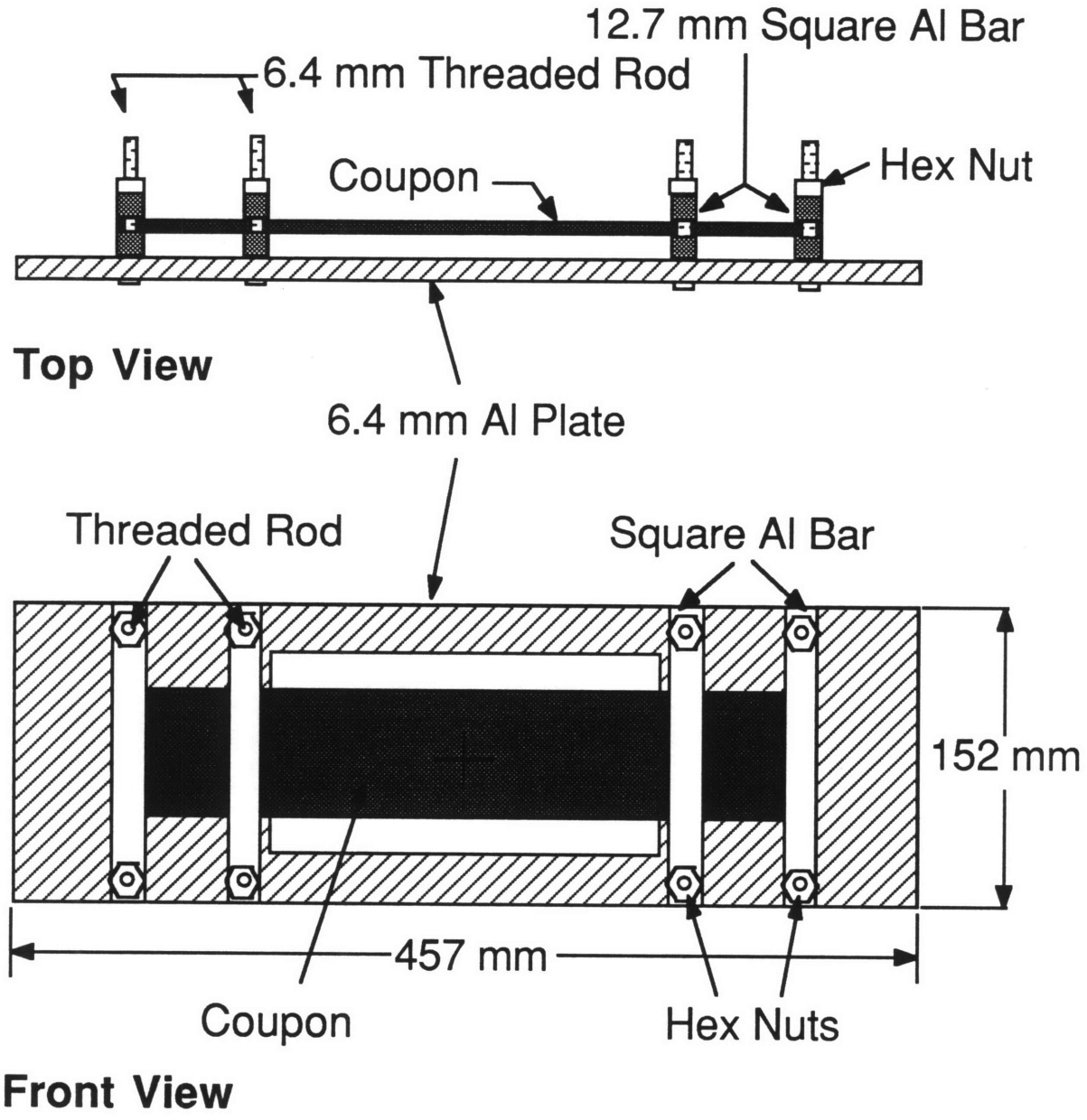

Figure 3.11 Illustration of Coupon Holding Jig for Impact Tests.

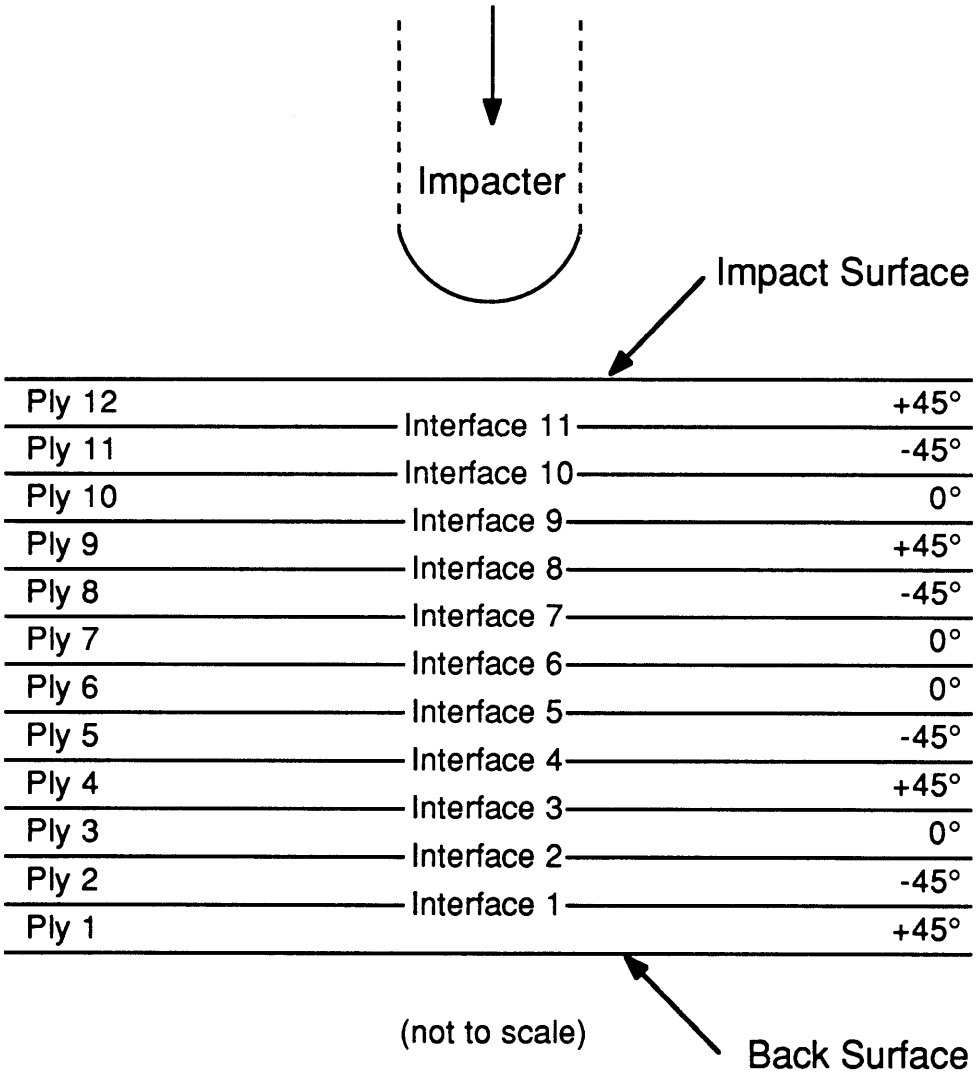

Figure 3.12 Illustration of Ply/Interface Identification Convention.

the back surface corresponds to ply 1. Unfortunately, in the early stages of impact testing, this convention was not always followed (evidenced by discussion of damage orientation in X-ray photographs and photographs of fractured impact-damaged specimens in Chapter 4.)

The two impact test methods available in TELAC correspond roughly to a "high mass/low velocity" system normally used in industry and a "low mass/high velocity" system used by NASA [32]. The "high mass/low velocity" system is the Free Rolling Energy Device (FRED). The "low mass/high velocity" system is the Air Gun. Each system is designed to represent a specific group of potential impact threats to aircraft/aerospace structures.

The FRED test apparatus was developed at TELAC [87] to simulate low velocity impact events such as tool drops. The overall test system consists of the striker unit and the impacter unit (Figure 3.13), the coupon holding jig (Figure 3.11), and the data acquisition equipment. In the striker unit, two 6700 N capacity electromagnets are energized to connect both ends of the unit. The hand winch is used to compress the main spring to a measured distance. Calibration runs are conducted to link distance to velocity. A ruler mounted on the apparatus near the electromagnets is used to measure spring compression. The impact event is initiated when the magnets are turned off and the main spring recoils. The striker rod then contacts the impacter rod.

The impacter unit consists of a tup (a 12.7 mm diameter steel tup was used in this work) connected to a rod (a steel rod of mass 1505 or 1523 g, and an aluminum rod of mass 578 g were used in this work). The small variation (approximately 1%) in impacter assembly mass with the steel rod

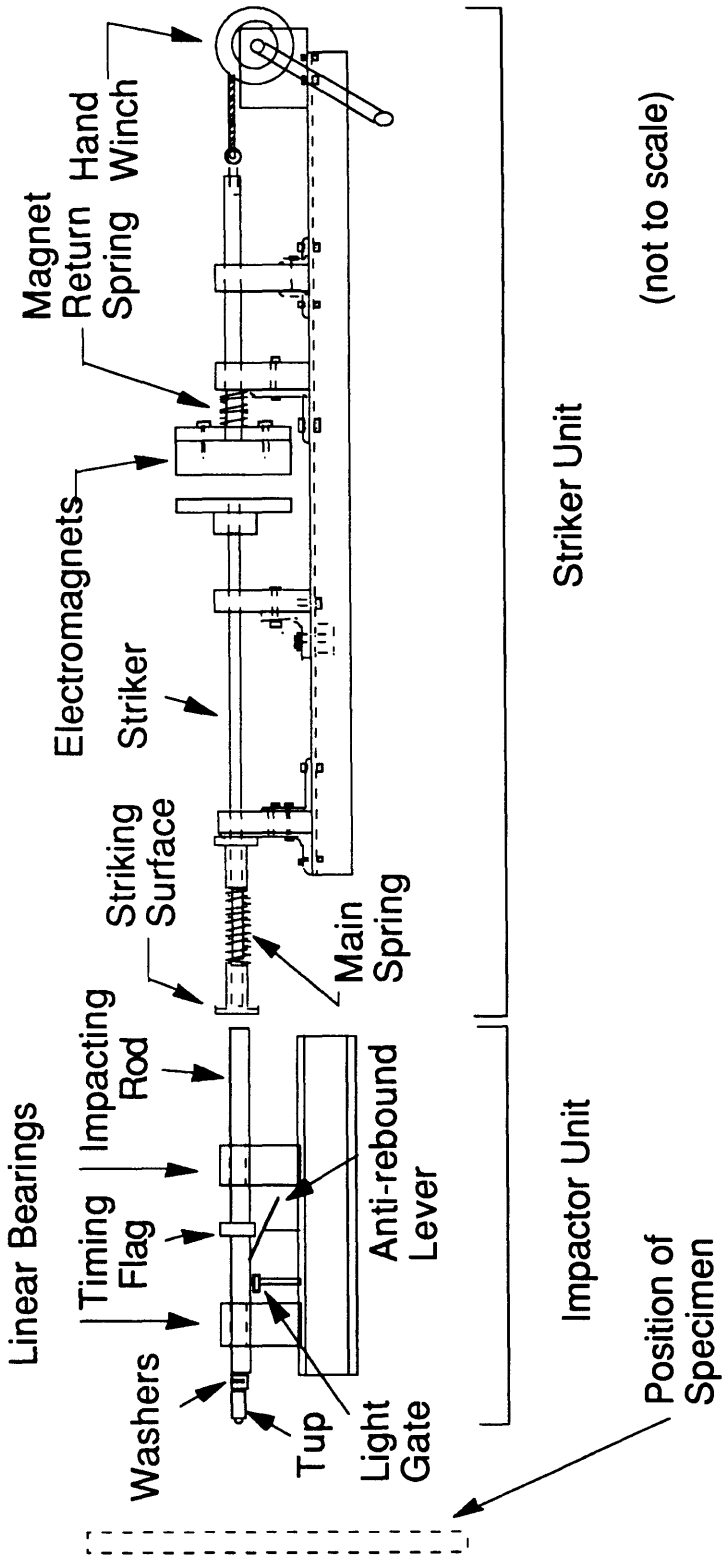

Figure 3.13 Illustration of Free Rolling Energy Device (FRED) Impact Test Apparatus and Setup.

is due to replacement of a short brass screw with a longer steel screw and the addition of washers to ensure a tight fit. The brass screw was too soft to withstand repeated impact at the energy levels that are of interest. The timing flag attached to the impacter rod is a 13 mm thick plastic doughnut. When the timing flag passes through the light gate it breaks a light beam. The time that the light beam is interrupted is measured by a CENCO Model 31707 timing system. Velocity of the rod is not simply determined by the thickness of the timing flag divided by the recorded time due to the finite width of the light beam. The correct "thickness" to use, 12.00 ± 0.01 mm, was measured by activating and deactivating the timing system by the 13 mm doughnut using a dial gage [29]. The timing flag has a secondary function of preventing multiple impacts with the aid of the anti-rebound lever.

Calibration runs are performed until the desired impacter velocity is repeatable to approximately ±0.5 m/s. However, measurements of spring compression are subject to human error. Also, friction in the four linear bearings (two for the striker rod, two for the impacter rod) is not constant. The combination of these variables often results in impacter velocities that vary from the desired velocities as mentioned in Section 3.2.

The Air Gun test apparatus design was developed and used extensively at NASA Langley Research Center [9, 15, 20, 30, 32, 49] to simulate impact damage from runway debris [15]. This test apparatus consists of a variable pressure source, a low pressure reservoir, a solenoid trigger, a gun barrel, and spherical projectiles (steel is used in this work) as illustrated in Figure 3.14. Along with the coupon holding jig (Figure 3.11), the impact container, and the data acquisition equipment, this

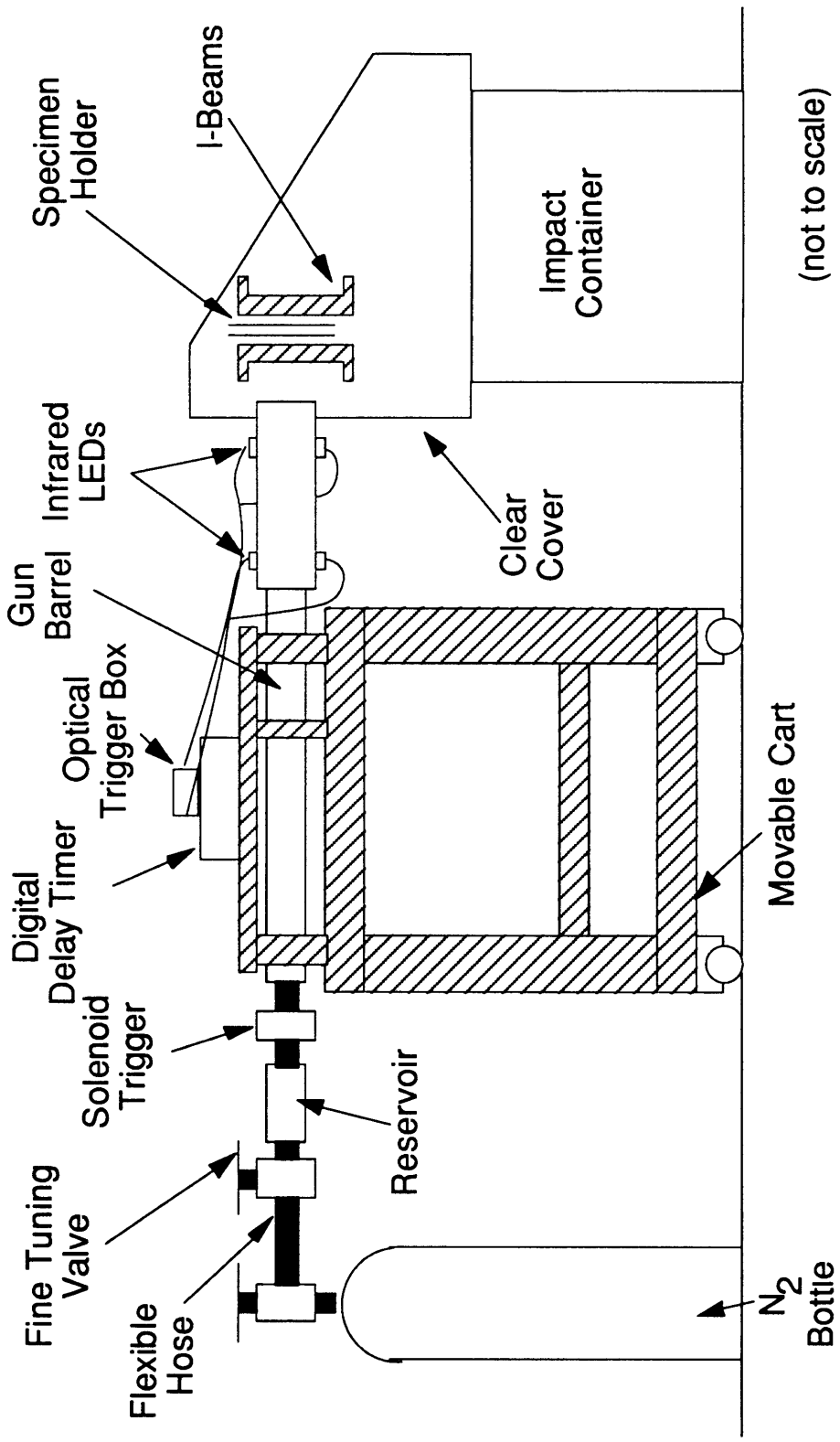

Figure 3.14 Illustration of Air Gun Impact Test Apparatus and Setup.

constitutes the entire Air Gun test system. The gun barrel, pressure reservoir, solenoid trigger, and data acquisition equipment are mounted on a movable cart.

After the coupon is loaded into the holding jig in the impact container, the impact cart is rolled into place. The gun barrel extends a short distance through the Lexan polycarbonate cover of the impact container. The data acquisition system is reset and a 12.7 mm diameter projectile (the steel projectile used in this work has a mass of 8.4 g) is loaded into the gun barrel through a side port that is closed by a screw-in bolt. Nitrogen is fed into the reservoir by adjusting the fine tuning valve until the desired pressure is reached. Then the valve between the reservoir and the bottle is closed. If too much gas is let into the reservoir, the excess can be released through a dump valve. Different orifice sizes are available for placement between the reservoir and the gun barrel to adjust gas velocity. An orifice size of 7.6 mm is used for this program. The desired pressure is determined by several calibrations until the desired impacter velocity is repeatable to ±0.4 m/s. The solenoid trigger is activated to release the nitrogen into the barrel to shoot the projectile forward. The projectile passes an infrared LED that sends a signal to the optical trigger box that triggers the timing mechanism on the Systron Donner Model 6250 Counter-Timer. The projectile passes a second infrared LED, located 200 mm further along the gun barrel, which sends a signal to the optical trigger box to stop the timing mechanism. The impacter velocity is calculated using the LED separation distance of 200 mm divided by the recorded time. Impact velocities were consistent as expected.

3.5.2 Damage Detection

The need for accurate damage assessment to understand the effect of impact damage on compressive residual strength is well-documented [16, 37, 49, 84, 88]. Proponents of destructive evaluation methods [37, 88] argue that nondestructive methods are severely limited in defining delamination at ply interfaces and only destructive methods can accurately determine the internal damage state. However, destructive methods are not an option for evaluation of composite structure in a production article nor are they useful when residual strength tests are to be subsequently conducted. Thus, nondestructive methods are being upgraded to accurately determine the through-the-thickness damage state. To that end, both destructive and nondestructive damage evaluation techniques were used in this study to characterize damage in some of the coupons subject to impact. All impact coupons are inspected by at least one NDE technique. The NDE techniques used are visual inspection, X-ray and ultrasonic scanning. Coupon sectioning and the deply technique are the destructive methods of damage evaluation. The different damage evaluation techniques are applied to compare accuracy and adequacy of information provided by the various methods.

All the impact coupons are evaluated using X-ray, as well as visual inspection. A small 0.8 mm hole is drilled in the impact surface at the center of the impact location. The hole is drilled, using a small hand drill, until approximately ten out of the twelve plies are penetrated. The coupons penetrated by the impacter do not need holes drilled. A syringe is used to inject 1,4-Diiodobutane (DiB) in the damage region until a small bubble forms on the surface of the graphite/epoxy coupon. DiB is a low viscosity

liquid that will penetrate into any exposed cracks through capillary action. The coupon sits for at least an hour before it is placed on Polaroid Type 52 PolaPan Instant Sheet Film in the Scanray Torrex 150D X-Ray Inspection System. The system is operated at 50 kV and nominally exposed to 160 mR using the "TIMERAD" control. The DiB blocks the X-rays. Thus, dark images on the film are damage areas. A schematic of the damage regions defined by X-ray evaluation is illustrated in Figure 3.15. The major and minor axes of damage are recorded as well as the dimensions of the central region or "core" damage. A typical X-ray photograph of impact damage is presented in Figure 3.16.

Damage characterization by ultrasonic scanning was performed by Hercules, Inc. with a Metro Tek C403 ultrasonic scanning system. Pulse-echo ultrasonic scanning is performed at 10 MHz by a transducer sending a signal into a water-immersed coupon perpendicular to the surface. The signal reflects at the front and back surfaces and also at discontinuities. The peak-to-peak amplitude of the signal from the backwall reflection occurs at a specified time interval or "gate". This time gate effectively corresponds to the thickness of the laminate divided by the velocity of the signal. The ultrasonic scanning system is capable of damage evaluation in one-dimension, two-dimensions, or three-dimensions. In one-dimensional scanning, also known as B-Scan, the transducer moves along a line. Two-dimensional scanning (C-Scan) is composed of several B-Scans. Three-dimensional scanning (time-of-flight C-Scan) is a series of C-Scans gated to different time intervals or depths in the specimen. Damage reduces the signal transmission and thus reduces the signal eventually returning to the transducer at the gated point.

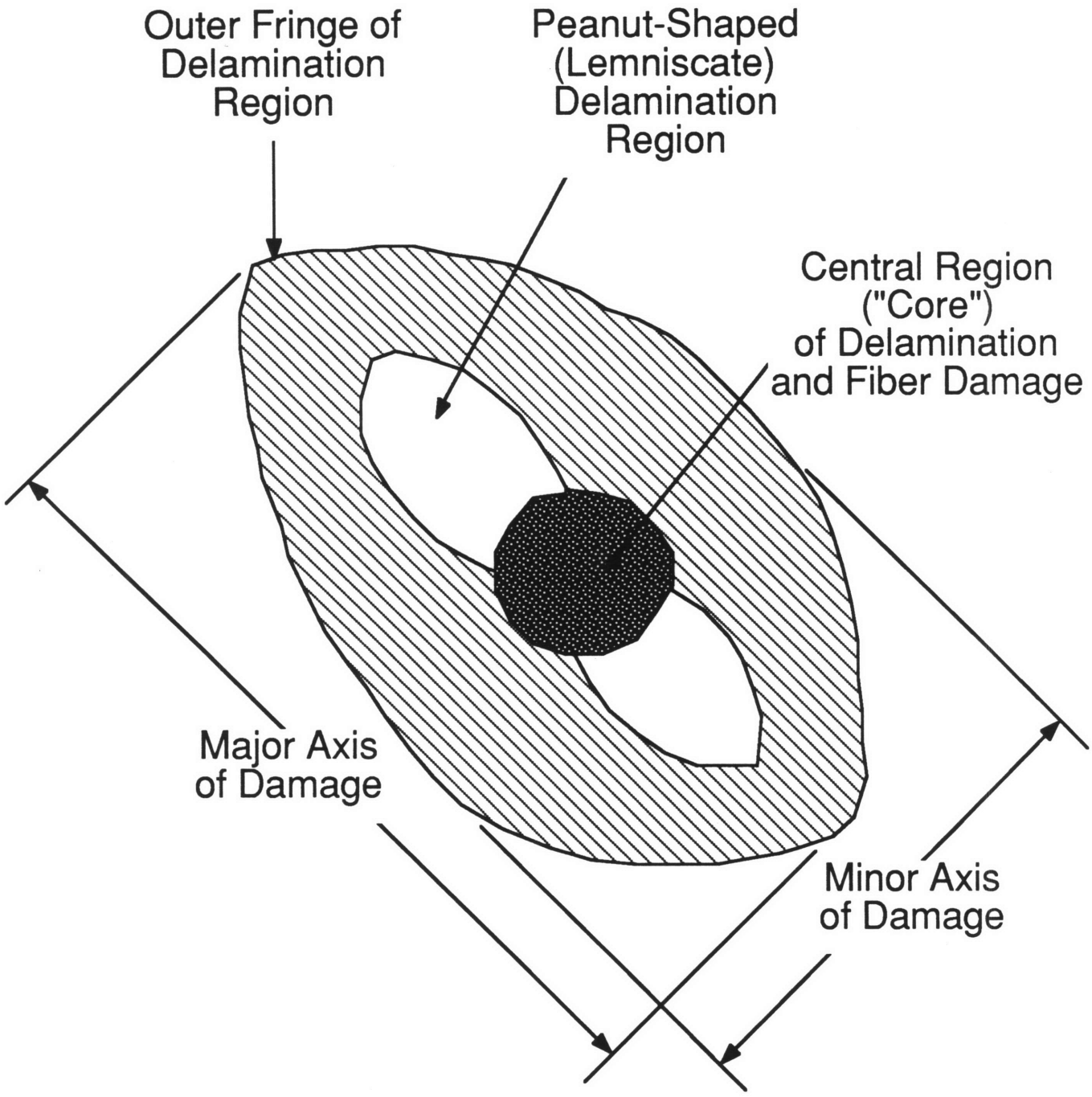

Figure 3.15 Schematic of Typical Damage Regions Illustrated by X-ray.

(X-ray is to scale)

Figure 3.16 Typical X-ray Photograph of Impact Damage (J9-2).

A typical ultrasonic C-Scan gives a map of the damage "smeared" through-the-thickness such that the through-the-thickness location(s) of the damage(s) is not indicated. An example is shown in Figure 3.17. A dark scan is the result of a low peak-to-peak amplitude of the backwall reflection, while a light scan results from a high peak-to-peak amplitude. There are sixty-four gray scales on these ultrasonic C-Scans provided by Hercules, Inc. The scale is set by equating a white pixel to the location of maximum amplitude reflection as gated. The gray scales represent lower amplitudes corresponding to increments equal to the maximum amplitude divided by sixty-four. A zero peak-to-peak amplitude of the backwall signal results in the black pixels on the scan. Black pixels thus indicate damage. White pixels nominally do not indicate damage except for those specimens with tape covering significant back surface splitting. The back surface delamination/split sealed with tape results in an air backwall instead of the water backwall. Thus, this area would appear white. Gray pixels indicate possible damage with darker gray indicating a greater possibility of damage.

The three-dimensional ultrasonic scan data is provided on a ply-by-ply basis. Because all plies are not of uniform thickness and the "time" thickness measurement of the laminate is divided by 12 to evaluate each ply, exact location within a ply is not known. The location is known to be within a ply, however, and is unlikely to coincide with a ply interface. Ply 12 is just below the laminate surface and ply 1 is just above the back surface (as determined from the backwall reflection in the two-dimensional C-Scan) keeping the convention shown in Figure 3.12. The same sixty-four gray scales apply to the three-dimensional ultrasonic C-Scan that apply to the two-dimensional ultrasonic C-Scan for that particular coupon. Thus, while

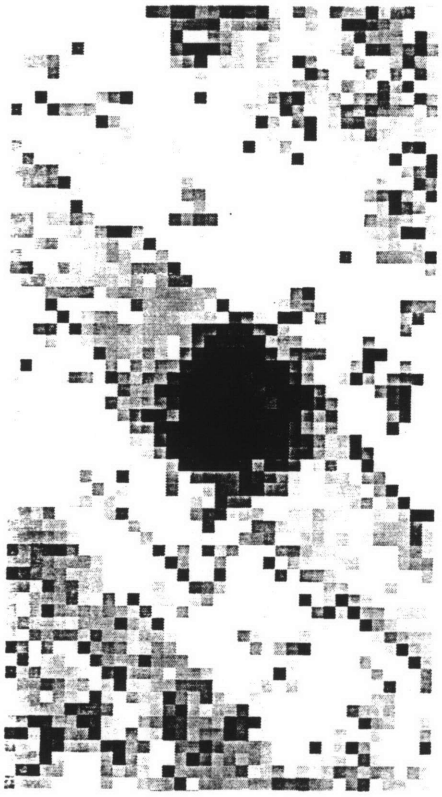

(C-Scan is to scale)

Figure 3.17 Example of Ultrasonic C-Scan of Impact Damage (J9-2).

comparison of gray scales from one coupon to another is not appropriate, two- and three-dimensional ultrasonic C-Scan data of the same coupon is comparable.

There is a reversal in damage interpretation by color scheme from the two-dimensional scans to the time-of-flight scans. Black represents damage in the two-dimensional case whereas white represents damage in the three-dimensional case. In the time-of-flight scans, only reflections at the ply of interest are "gated" and thus cause a signal to be received. These reflections occur at damage in the laminate. If there is no damage at the ply, no signal is received within the "gate" and a black pixel results (indicating no damage). However, if the signal is reflected before the ply, indicative of damage above that location, the area beneath the reflection will be "shadowed" in that little signal will be transmitted. Thus, even if damage at that ply exists, the reflected signal amplitude will be small and will result in darker pixels.

Therefore, when looking at these plots on a ply-by-ply basis, the white areas represent signal reflection by damage while the black areas indicate that no reflection occurred at the ply (no damage) conditional upon the possible shadow effect of a previous ply. Also, in the very central region of impact, results from impact damage due to perforation will be smeared because of immediate loss of the backwall signal. However, delamination should be discernible on a ply-by-ply basis away from the central region of damage.

For the time-of-flight ultrasonic C-Scan presented in Figure 3.18, the light pixels indicate the significant delamination that occurred between ply 1 and 2. The central region of dark pixels is the area of severe fiber and matrix damage due to the penetration of the tup into the coupon. C-Scans of

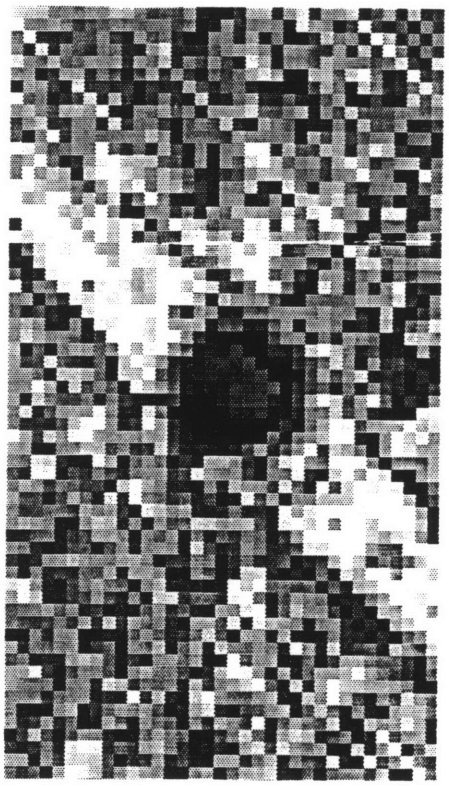

(C-Scan is to scale)

Figure 3.18 Example of Time-of-Flight Ultrasonic C-Scan of Impact Damage (J9-2/Ply 2).

the plies near the impact surface had light pixels in this region. Thus, for ply 2, the dark pixels in the central region represent a "shadow" cast by the previous plies and do not imply that no damage exists at this ply in this location.

After X-ray and ultrasonic scanning evaluation, several of the impact coupons are sectioned using the same milling procedure as described in Section 3.4.1 for the impact/open hole coupon. Due to the thickness of the blade, approximately 1.5 mm of the coupon is lost and correction is made for the actual position of the new surfaces. The thinnest sliced strip width consistently achievable is approximately 7 mm. The cut lines relative to damage orientation are illustrated in Figure 3.19. At least five cuts are made per coupon, the first of which is through the center of impact. The location of the center of impact is done by visual inspection upon placement of the coupon in the milling machine. From the center of impact towards the marked edge or "top" (discussed in Section 3.4.1) the strips are designated T1, T2, etc. The strips away from the marked edge are designated B1, B2, etc. The -1 and -2 designations refer to surface on the strip (-1 is always located closest to the impact center). Both sides of each cut are investigated under microscope using two spotlights to compare information from each surface. Delaminations and fiber breaks are measured by examination under a microscope at thirty times magnification. A superposition of two photographs of a typical edge through the center of impact is shown in Figure 3.20. The strip is identified by the aforementioned coupon identification system as well as transverse distance from the coupon edge.

The measurements from all surfaces exhibiting damage are transcribed to schematics of damage on a ply-by-ply basis. Cross-section

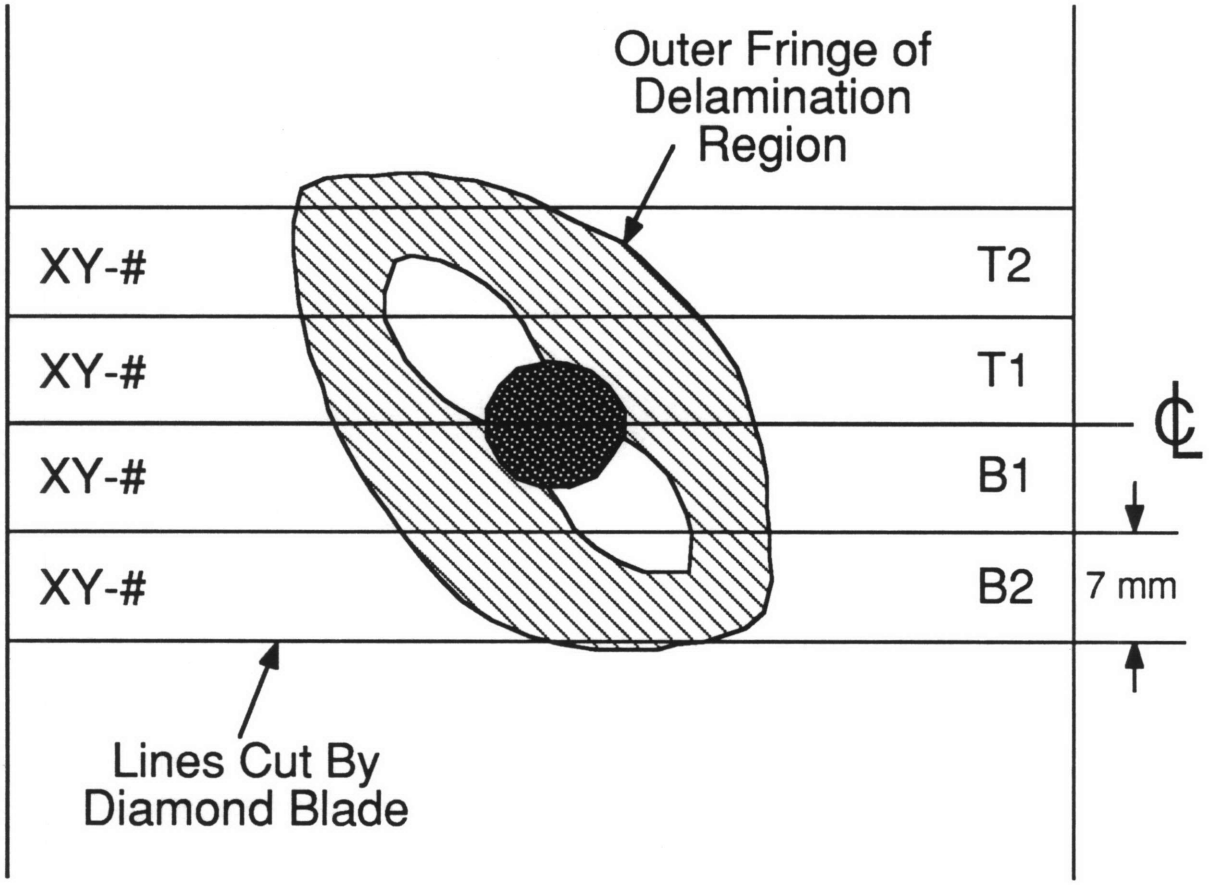

Figure 3.19 Schematic of Section Lines for Microscopic Evaluation.

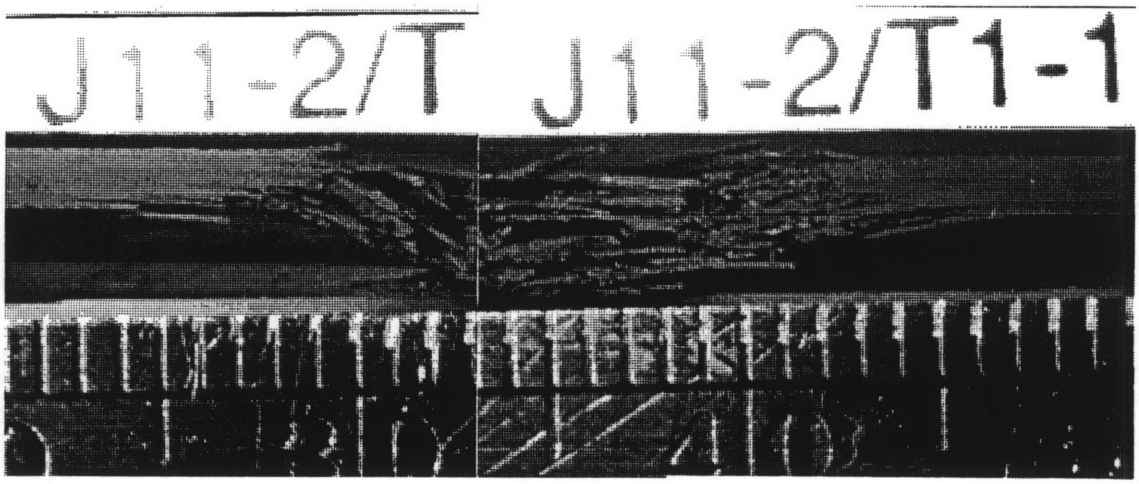

(Scale in picture is in mm)

Figure 3.20 Typical Photograph of Coupon Cross-Section through the Center of Impact (J11-2/T1-1).

schematics refer to the ply of interest and the interface between it and the next ply closer to the impact surface. Thus, ply 1 and interface 1 are on the same schematic. (Ply 1 is the back surface ply as shown in Figure 3.12.) Edges of delamination at ply interfaces are represented by open boxes. A single transverse crack representing a split in a ply is represented by a single X. A series of transverse cracks in a ply is represented by two X's connected by a dashed line. No information on crack density is supplied in the schematics. A typical schematic of ply 1/interface 1 is shown in Figure 3.21.

Another destructive damage evaluation method, the deply technique [88], was used on a number of coupons. The coupons are first trimmed to a rectangle containing only the damaged region. This reduces the amount of graphite/epoxy subject to pyrolysis and noxious fumes that must be properly vented to a chemical hood.

To apply the deply technique, it is necessary to use an enhancing agent such as gold chloride in diethyl ether. Results from a comparative study [49] showed that gold chloride in a carrier of isopropyl alcohol was just as successful as the ether carrier [88] but with less safety risk. The gold chloride purchased from Sigma Chemical Company was an anhydrous compound that was insoluble in ether. Thus, the enhancing agent used in this work was a solution composed of 10 g of gold chloride in 100 ml of isopropyl alcohol. A syringe is used to inject the solution into the damage region on the surface away from impact. Infiltration of the solution into all possible damage regions is considered probable within thirty minutes. The coupons are then placed in an oven at 66°C for thirty minutes to drive off the excess carrier.

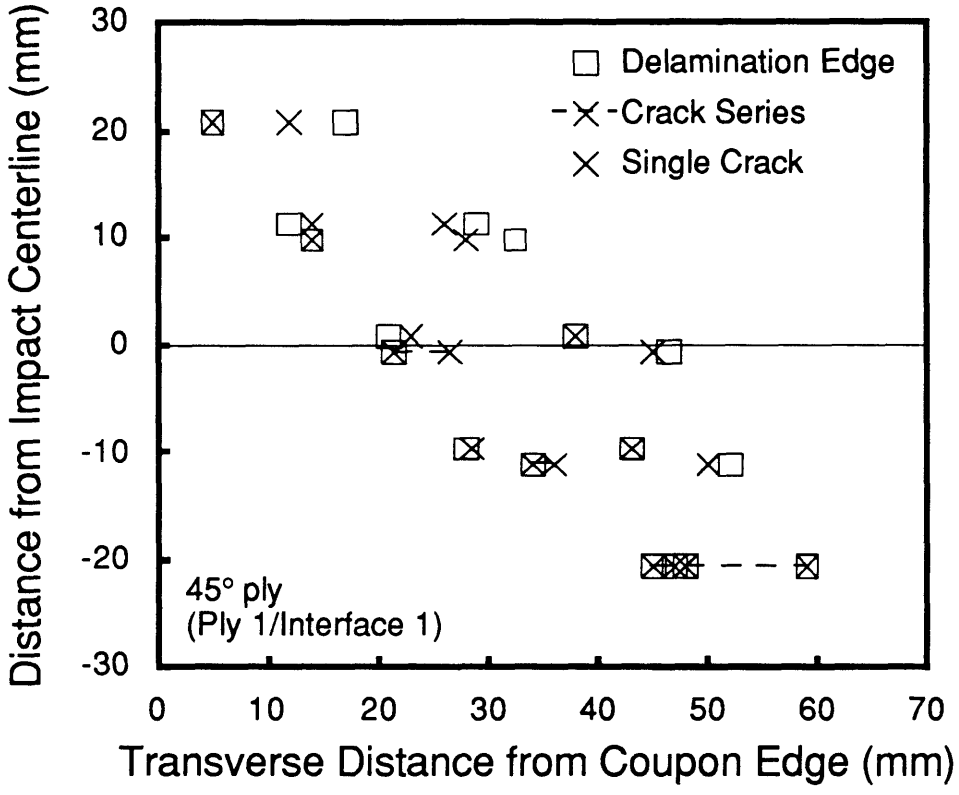

Figure 3.21 Typical Schematic from Cross-Sectioning of Coupon (J6-2/Ply 1).

The trimmed coupons are placed on a stainless steel wire mesh into a preheated (415–420°C) Lindbergh Furnace Type 51442. A positive pressure of nitrogen gas at approximately 0.02 MPa is fed into the furnace with the vent to an exhaust hood. This positive pressure of nitrogen removes the possibility of the harmful effects of oxygen. Partial pyrolysis of the coupons occurs after forty-five minutes (thirty minutes for eight plies [49, 88]).

For the "unstacking" of the laminate, a wide strip of transparent tape is placed over the top ply (beginning with the impact surface ply which is ply 12 in the $[\pm 45/0]_{2S}$ layup). The ply is gently worked free from the specimen and the tape is cut to ply dimensions. The newly exposed surface is interface 11. The above steps are repeated until all plies are separated (plies 6 and 7 are both 0° and impossible to separate). An attempt was made to "unstack" from ply 1. However, since significant back surface damage occurred for most of the deply specimens, a good grip with the transparent tape on the uneven surface was not possible. The view of damage in the specimens evaluated by the deply technique is from the back surface towards the impact surface which is opposite of the time-of-flight ultrasonic C-Scans and cross-section schematics. Thus, the ply angles are reflected about the vertical axis. The coupon identification, ply, and interface numbers are noted on the tape side of the specimen. Evaluation of the damage types (i.e., delamination and fiber damage) and sizes is done by visual inspection with a bright light shined on the ply to reflect the gold chloride. Photographs are then taken to provide a record of damage.

A typical photograph of ply 2 and interface 1 is shown in Figure 3.22. This specimen was impacted at 6.3 m/sec with an impacter mass of 1523 g (previously noted to cause complete penetration). There is obvious fiber

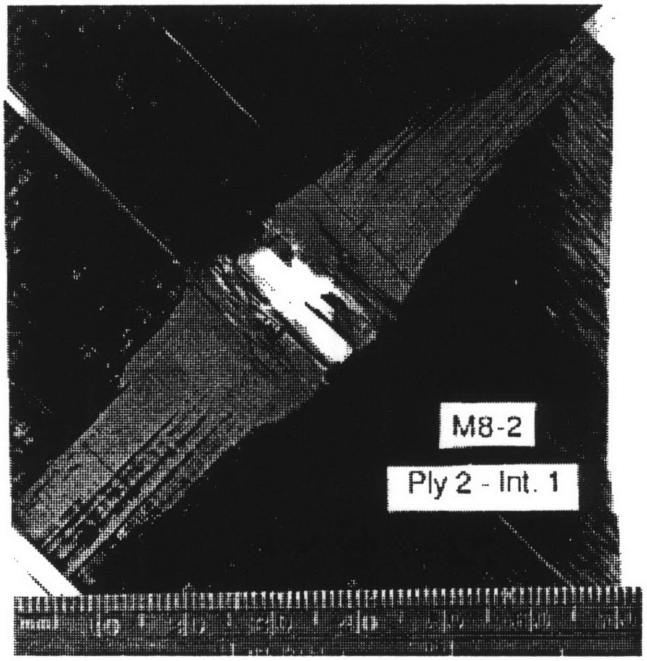

[45/<u>/-45</u>/0/45/-45/0/0/-45/45/0/-45/45] Impact Surface

(Scale in picture is in mm)

Figure 3.22 Typical Photograph of Ply 2/Interface 1 Damage by Deply Technique (M8-2).

damage in this ply where the tup passed through the coupon as evidenced by the white background showing in the photograph. The gold chloride, providing evidence of delamination where ply 1 (back surface from impact) separated from ply 2, typically appears gray compared to the white of the background and the black of the graphite/epoxy. As a matter of fact, on all the specimens evaluated by the deply technique, the gold chloride marks on ply 2 provide the necessary information for ply 1 as well. This delamination typically coincided with the ply splits in the back surface ply. Thus, when evaluating damage by the deply technique, ply 1 was not photographed.

After the impact coupons are evaluated by the prescribed destructive and nondestructive methods, details of the damage identified are compared. The C-Scan damage definition is directly comparable to X-ray results. The time-of-flight C-Scan damage definition is comparable to the schematics generated by cross-sectioning and the photographs from the deply evaluation.

3.5.3 Compressive Residual Strength

After nondestructive damage evaluation and specimen instrumentation, residual strength tests are conducted on an MTS 810 Material Testing System. Tests are conducted in stroke control at a rate of 1.1 mm/min. This results in an approximate strain rate of 5000 microstrain/min in the test section.

Before testing begins, a steel bar of similar dimensions to the compressive residual strength test specimen is used to verify hydraulic grip alignment in the test machine. Hydraulic grip pressure is held at 1.38 MPa for all pre-test set-up procedures to avoid spikes that could cause crushing

of the specimen (as a result of the first tests with the undamaged specimens).

A standard procedure is used for test specimen set-up. The test specimen is centered in the upper hydraulic grip placing the flat surface of the fiberglass tab completely within the grip. A right angle is placed against the edge of the specimen and the horizontal surface of the grip to verify correct longitudinal alignment. The top grip is then closed. The crosshead is unlocked to lower the specimen into the bottom hydraulic grip. The crosshead is then locked and the bottom grip is raised so the flat surface of the fiberglass tab is completely within the grip. This free hanging position (upper grip closed only) is designated the zero-load, zero-strain position.

The strain gage wires are attached to a connection box in parallel with a Decade Resistance Box Type 602-N. A shunt calibration program is run on the computer to calibrate the gage. Data calibration and acquisition are controlled by the Digital PDP 11/34 connected to the MTS processor interface.

When strain gage calibration is complete, the bottom grip is closed and the hydraulic grip pressure is raised to 3.45 MPa. The memory on the MTS 810 Series Automated Control Machine is reset, the data acquisition program is started, and the start button on the test machine is pushed. Data is taken every 0.5 second on every channel. Noises from the specimen are heard during loading and "marked" on the data file by a special keyboard entry. Each specimen is loaded until both facesheets fail. Failure of each facesheet is easily identified. The damaged facesheet fails first and is identified by a significant drop in load and a loud noise. The failure of the undamaged facesheet is identified by the second significant load drop and

loud noise. The recorded data is transferred into Microsoft Excel 2.2 files for easy manipulation and data evaluation.

Chapter 4

EXPERIMENTAL RESULTS

4.1 Overview

As mentioned in Chapter 3, the focus of the experimental work was to answer three questions raised by the previous research results [83] shown in Figure 4.1. One, what is the three-dimensional damage state that governs minimum compressive residual strength behavior? Two, is this minimum compressive residual strength value dependent upon impact method. And three, how is this minimum compressive residual strength value related to impacter mass and velocity?

The second and third questions were the easiest to address. Thus, the early focus of the experimental program was on generating compressive residual strength curves for two additional masses using a different impact apparatus. Compressive residual strength data for all three masses and the two impact methods are presented in Section 4.2. (Compressive residual strength results for the three impacter masses are compared in Chapter 5 in order to answer questions two and three.) Once the minima for the three impact masses were determined as a function of impacter velocity, question one could be addressed. Additional coupons, impacted at these velocities for the three masses, underwent extensive damage evaluation. The nondestructive and destructive damage evaluation data are presented in Sections 4.3 and 4.4, respectively. A comparison of the damage state definition by X-ray, ultrasonic C-Scan, cross-sectioning, and the deply technique at the respective MCRS-velocities for each of the impacter masses used in this work is made in Section 4.5

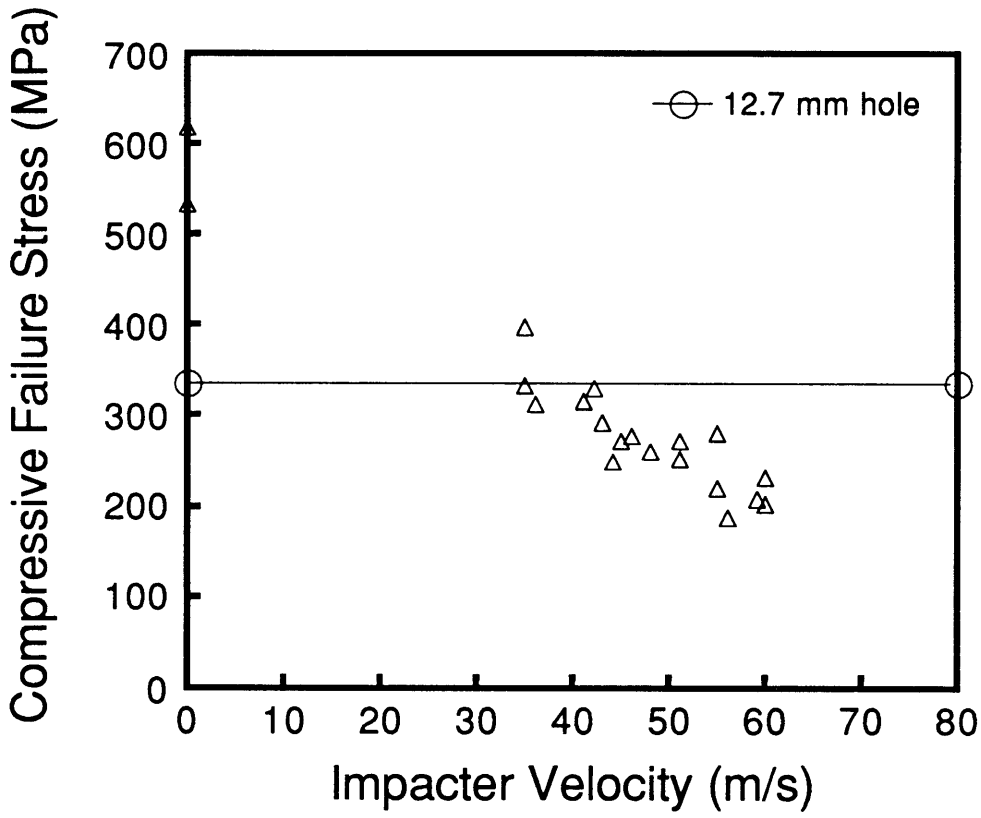

Figure 4.1 Compressive Residual Strength versus Impacter Velocity from Previous Project [83] (Impacter Mass = 8.4 g).

4.2 Compressive Residual Strength

To illustrate damage tolerance, residual strength data is often plotted as a function of measured damage from two-dimensional nondestructive evaluation data [8, 16, 25, 27, 30, 45, 49, 81–83]. More often however, data is presented as a function of impacter velocity or energy [10, 25, 30–34, 39, 43–45, 47, 74, 83]. This presentation method complicates interpretation of results for different laminates or material systems as the issues of damage resistance and damage tolerance are not separately addressed. Thus, to address damage resistance, damage size as a function of impacter energy or velocity should also be provided (as it is often done [25, 32, 35, 74, 83]). In this work, presentation of residual strength as a function of impacter velocity was used to determine the minimum compressive residual strength. Impacter velocity was the parameter then used in an attempt to repeat the damage state causing minimum compressive residual strength for intensive destructive damage evaluation.

Compressive residual strength data is presented as the failure stress of the impacted or open hole facesheet. Failure stress is calculated by dividing the failure load of the damaged facesheet by the measured area (average thickness and width). The failure load of the damaged facesheet is half the total column load at failure (approach discussed in Reference 85 and verified with the 19.1 mm open hole compressive residual strength tests). Strain data at failure is not included in this report as the results were not always representative of far-field strain. When the damage size was extensive, the strain gage readings were affected by the presence of the damage.

The damage size used for correlation to compressive residual strength is determined from the X-ray photographs of each impact coupon. The information provided by an X-ray photograph is an integrated through-the-thickness summary of damage in each coupon. These measurements represent the extent of this integrated damage as seen in the plane of the photograph. It is, thus, almost impossible to determine depth of damage from an X-ray photograph unless it is obvious from visual inspection that damage is at the impact or back surface. As seen previously in Figure 3.15, these measurements include the major and minor axes of the outer fringe of delamination as well as the diameter of the "core" area. The measurement of the major axis of damage does not include the spalling of fibers off of the back surface to the coupon edge as this is a surface phenomenon. The "core" area, which includes broken fibers and matrix damage, is the very dark central region on the X-ray photographs. This area is generally centered at the impacter point of contact.

The impact metrics, corresponding damage measurements and compressive residual strength test results for this work are summarized for each specimen in Appendix B.

4.2.1 Undamaged and Open Hole Specimens

Both undamaged and open hole specimens were tested for compressive strength to provide "control" data of known damage states. Failure of the undamaged specimens was characterized by virtually simultaneous front and back facesheet fracture. Typical facesheet fractures are detailed in the photograph of two fractured facesheets of the undamaged specimens shown in Figure 4.2. Fracture was apparently due

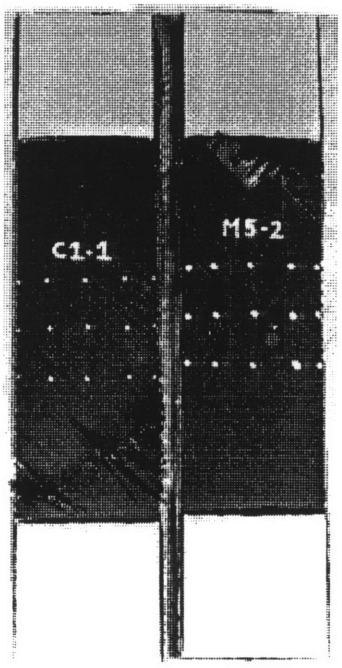

(Specimens - 70 x 340 mm)

Figure 4.2 Photograph of Undamaged Specimens After Fracture.

to in-plane mechanisms as catastrophic failure occurred completely through each facesheet with no indications of delamination. Failure was typically across the specimen width at a 45° or -45° angle and always occurred near a tab. If the failure initiation point was too close to the tab, the propagation across the width was arrested underneath the tab.

Three specimens per open hole diameter (12.7, 19.1, and 25.4 mm) were tested. Failure of the open hole specimens was characterized by fracture of the open hole facesheet first. Again, fracture was apparently due to in-plane mechanisms as catastrophic failure occurred completely through each facesheet with no indications of delamination. Fracture of the 12.7 mm diameter open hole facesheets normally occurred from the hole edge, at 90° from the load direction, straight out to the edge as shown in Figure 4.3. However, at least one facesheet experienced fracture from the 90° and 270° locations out to the edge at a 45° angle (T6-2 in Figure 4.3). Fracture was consistent on the three 19.1 mm diameter open hole facesheets from the 270° location as shown in Figure 4.4. Failure occurred straight out to the edge. At the 90° location, failure occurred out to the edge at a -45° angle for T5-3, didn't occur for M19-2, and went straight out to the edge for C6-2 in Figure 4.4. The 25.4 mm diameter open hole facesheets typically experienced angled fracture paths as shown in Figure 4.5. Specimen C5-3 experienced 45° angle fracture paths from both the 90° and 270° location around the hole. Specimen M7-2 experienced fracture at a 45° angle from the 90° location and at a -45° angle from the 270° location. Specimen T2-2 experienced a combination of the two fracture paths from the 90° location. Fracture began at a 45° angle then dropped down to the 90°

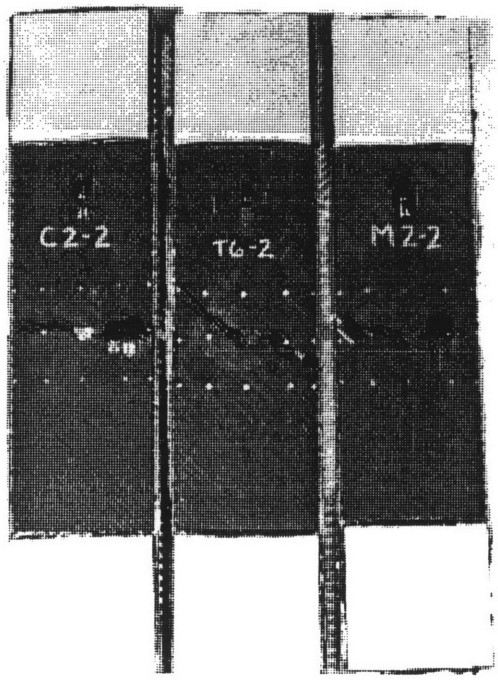

(Specimens - 70 x 340 mm)

Figure 4.3 Photograph of 12.7 mm Open Hole Specimens After Fracture.

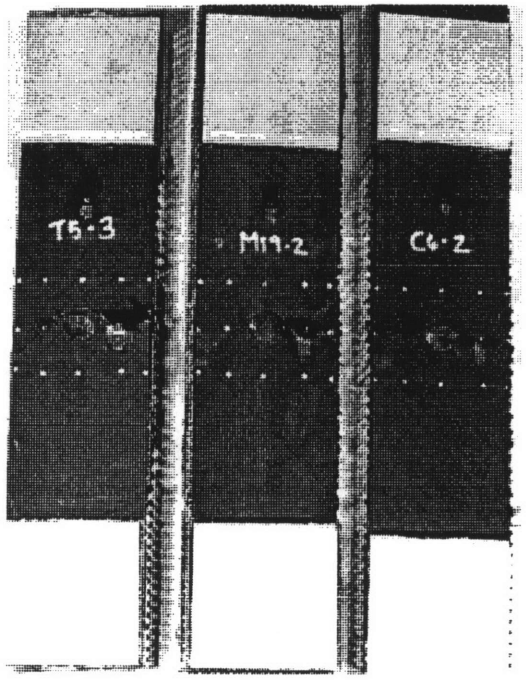

(Specimens - 70 x 340 mm)

Figure 4.4 Photograph of 19.1 mm Open Hole Specimens After Fracture.

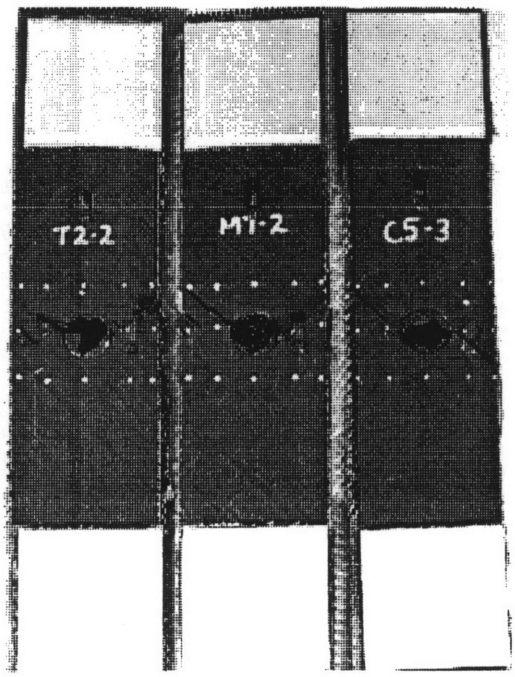

(Specimens - 70 x 340 mm)

Figure 4.5 Photograph of 25.4 mm Open Hole Specimens After Fracture.

position and continued straight out to the edge. At the 270° location of T2-2, fracture occurred at a -45° angle.

A summary of the compressive residual strength results of the undamaged and open hole specimens is presented in Table 4.1. There is very little scatter in the test data as evidenced by the relatively low coefficients of variation. The reductions in strength due to the presence of the 12.7, 19.1, and 25.4 mm open holes are 52, 44, and 42 %, respectively.

4.2.2 Impacter Mass of 1523 g

Plots of the major and minor axes of damage (as determined from X-ray photographs) versus impacter velocity due to an impacter mass of 1523 g are shown in Figure 4.6. The damage size levels off at a velocity of approximately 6.0 m/s. The maximum size of the major axis of damage is approximately 90 mm while the minor axis maximum size is approximately 30 mm. The core damage size, shown in Figure 4.7, levels off at a slightly lower velocity of approximately 5.7 m/s at a value of approximately 25 mm. Both of these velocities are within the penetration range. (The start of the penetration range is defined in this work by the existence of damage in every ply of the coupon — if light shines through the impact location when the coupon is held up to a light source. The range extends to complete penetration of the coupon by the impacter as defined in Chapter 3 in the case of the tup and breakthrough of the coupon by the spherical impacter.)

The plot of compressive residual strength versus major axis of damage is shown in Figure 4.8. As the damage size increases, the

Table 4.1 Undamaged and Open Hole Compressive Residual Strength Tests

Hole Diameter (mm)	Number of Specimens	Mean Compressive Strength (MPa)	Coefficient of Variation
0.0	2	645	2.3 %
12.7	3	332	3.1 %
19.1	3	285	4.2 %
25.4	3	268	10.1 %

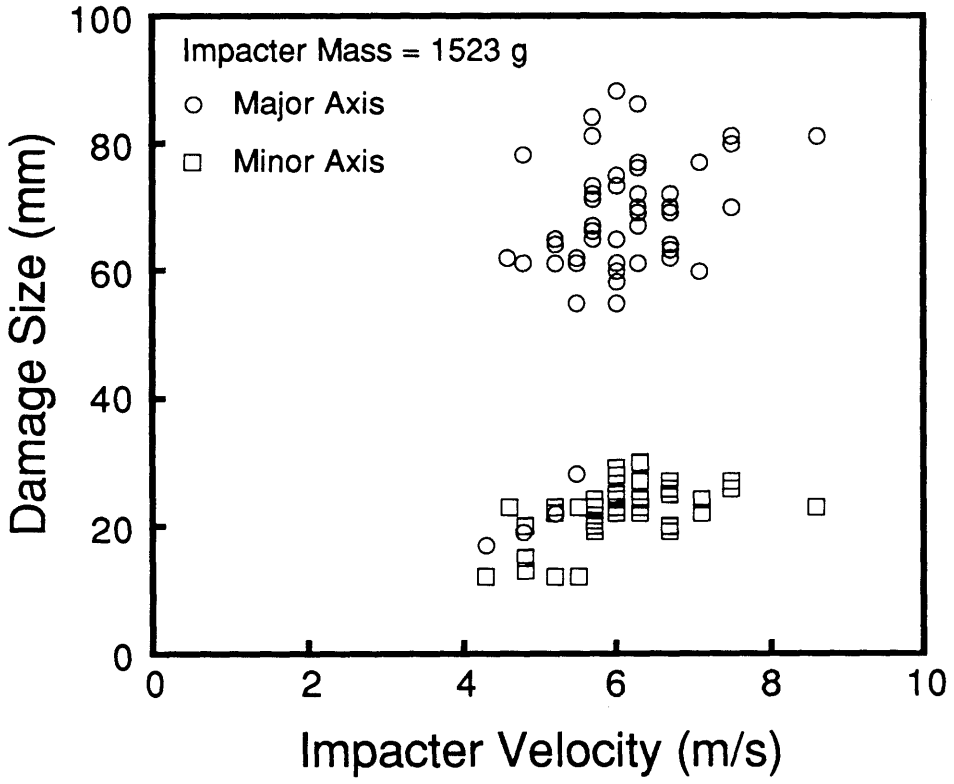

Figure 4.6 Damage Size versus Impacter Velocity (Impacter Mass = 1523 g).

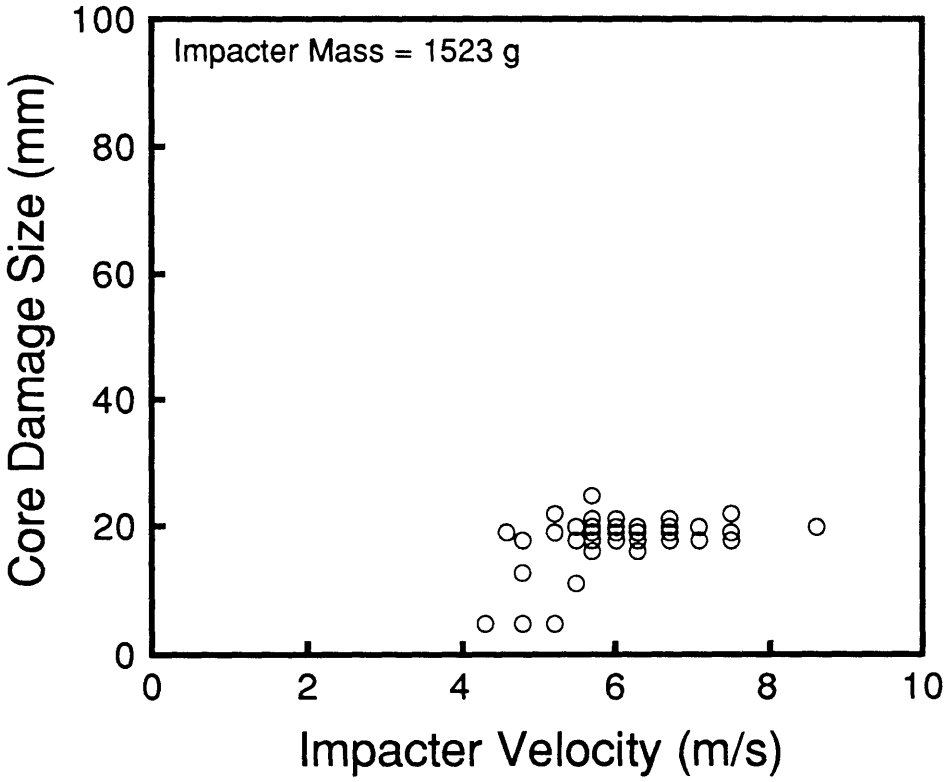

Figure 4.7 Core Damage Size versus Impacter Velocity (Impacter Mass = 1523 g).

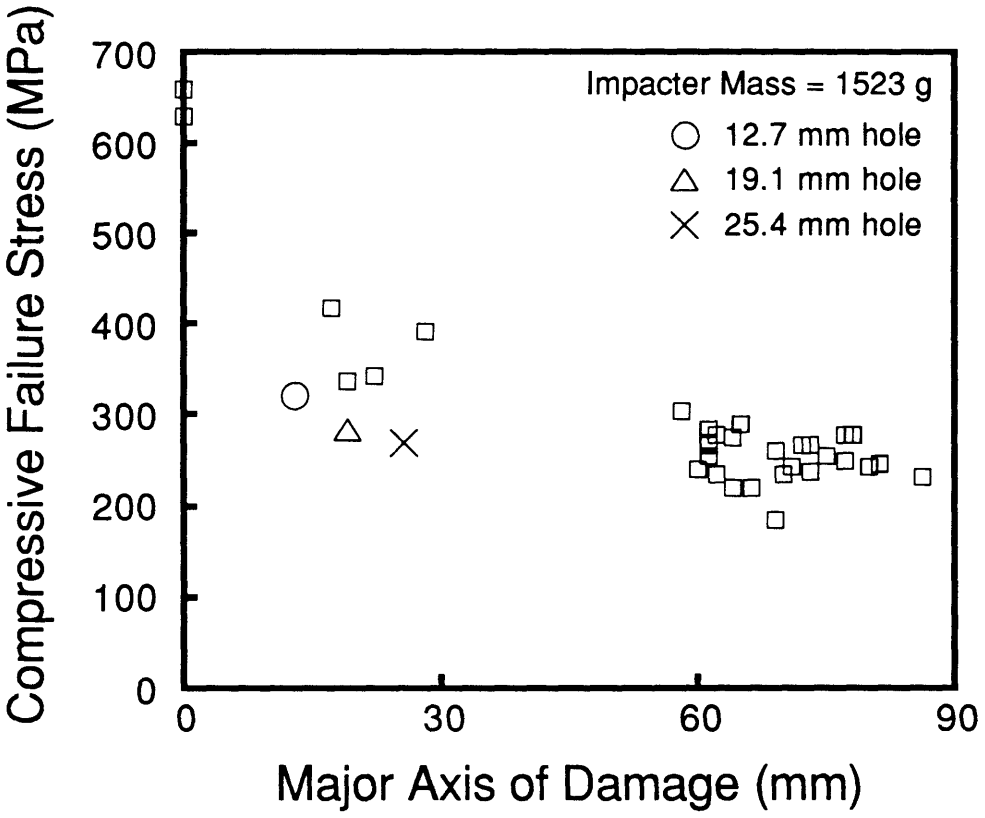

Figure 4.8 Compressive Residual Strength versus Major Axis of Damage (Impacter Mass = 1523 g).

compressive residual strength reaches an asymptote of approximately 200 MPa. This asymptotic behavior is consistent with what has commonly been reported in previous work [8, 27, 30, 82]. The open hole diameter (12.7, 19.1, and 25.4 mm) mean compressive residual strength results are also plotted in Figure 4.8. Compressive residual strengths of specimens with impact damage are greater than the compressive residual strengths of specimens with open holes of diameter equivalent to the major axis of damage of the impacted specimens.

As the minor axis of damage increases, the compressive residual strength also reaches an asymptote of approximately 200 MPa as shown in Figure 4.9. However, in this case, compressive residual strengths for open holes of diameter equivalent to the minor axis of damage are within the scatter band. The same conclusions apply to the compressive residual strength versus core damage size shown in Figure 4.10.

The compressive residual strength as a function of impacter velocity for the 1523 g impacter mass is presented in Figure 4.11. A minimum compressive residual strength of 184 MPa occurred due to damage imparted at a velocity of 6.3 m/s (which is hereto referred to as the "MCRS-velocity" for impacter mass of 1523 g). At velocities greater than the MCRS-velocity, the compressive residual strength increases towards the open hole value.

Photographs of the fractured specimens impacted near the lowest velocity, at the MCRS-velocity, and at the highest velocity with the 1523 g mass in this work are presented in Figures 4.12 through 4.14. The in-plane failure modes experienced by the impact-damaged specimens were similar to what is shown in Figures 4.3 through 4.5 for the open hole specimens.

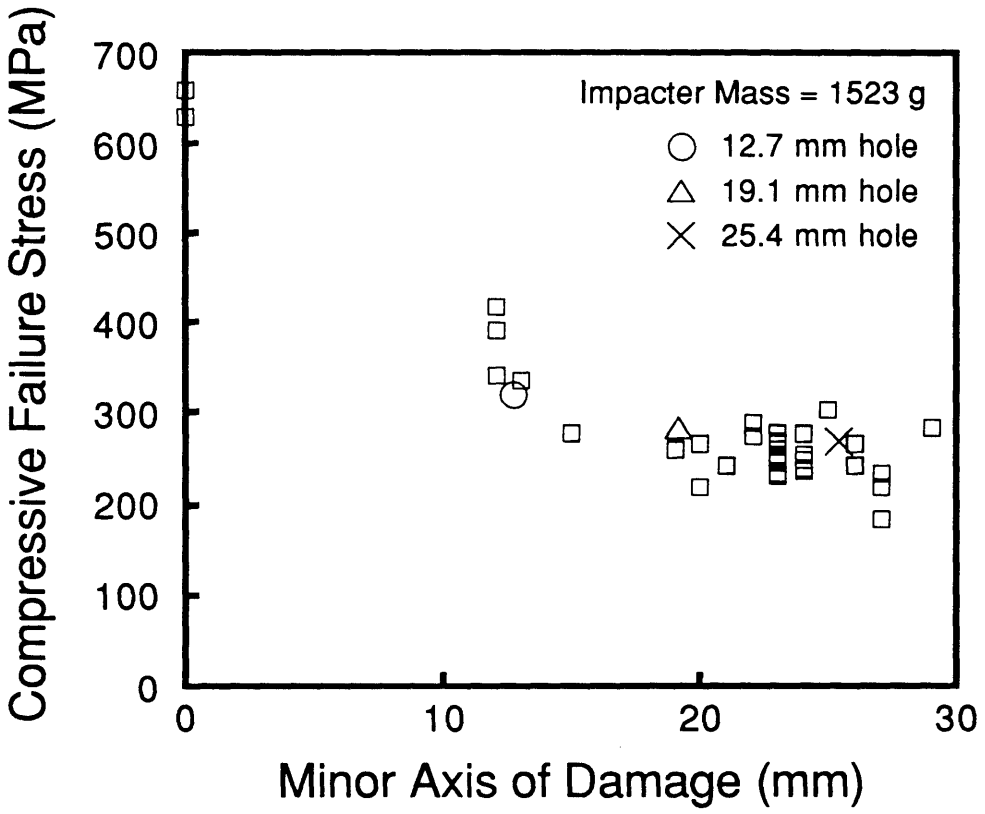

Figure 4.9 Compressive Residual Strength versus Minor Axis of Damage (Impacter Mass = 1523 g).

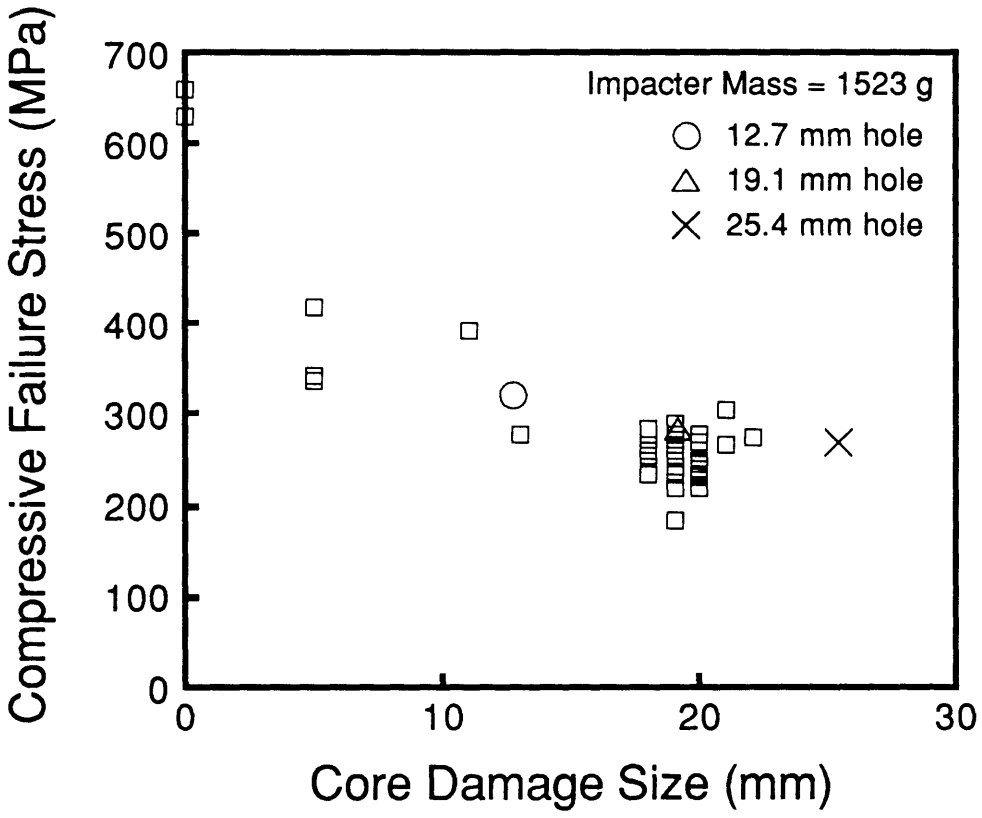

Figure 4.10 Compressive Residual Strength versus Core Damage Size (Impacter Mass = 1523 g).

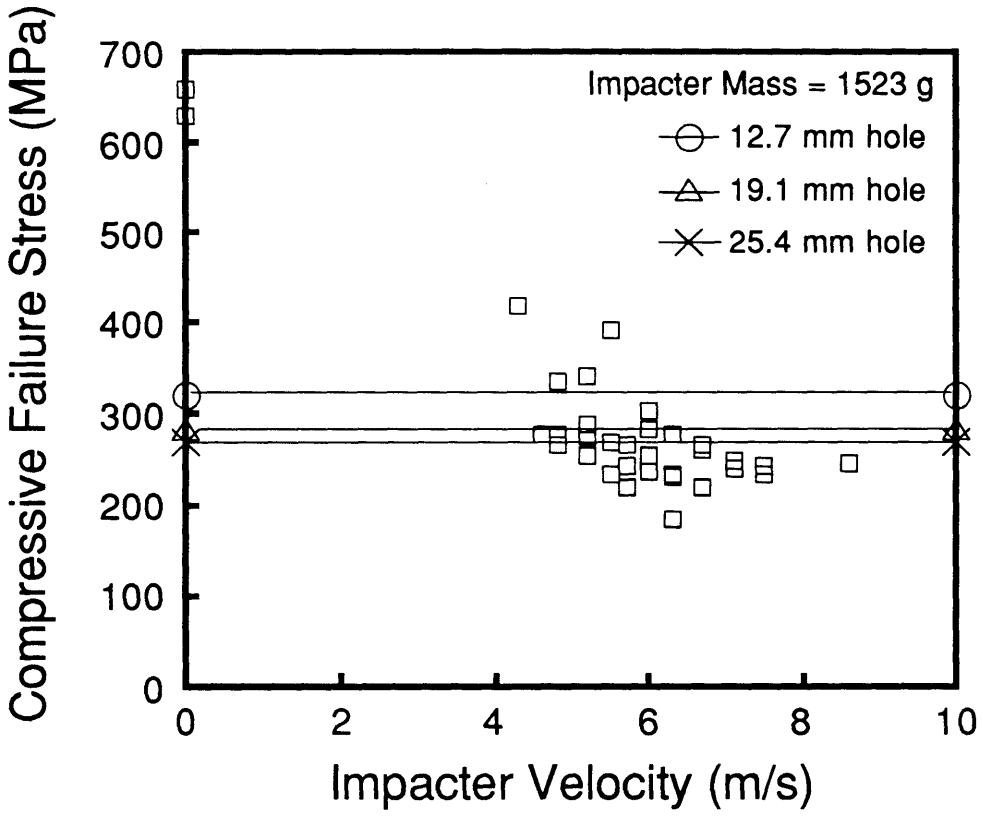

Figure 4.11 Compressive Residual Strength versus Impacter Velocity (Impacter Mass = 1523 g).

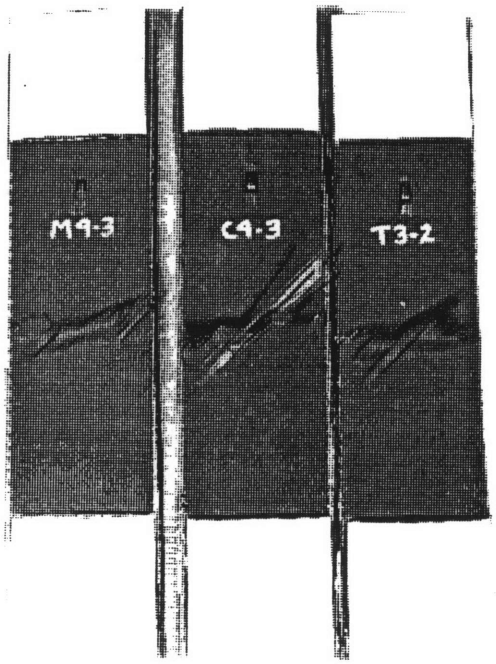

(Specimens - 70 x 340 mm)

Figure 4.12 Photograph of Impact-Damaged Specimens After Fracture (Impacter Mass = 1523 g, Velocity = 4.8 m/s).

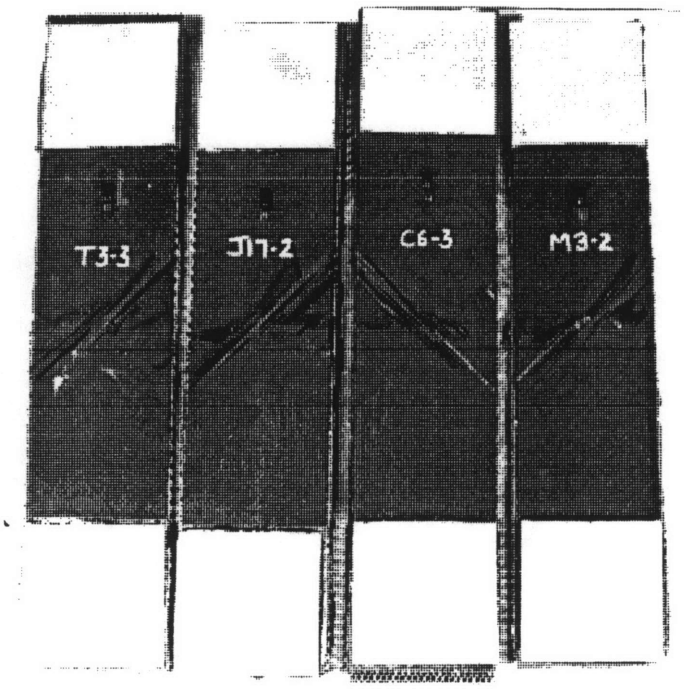

(Specimens - 70 x 340 mm)

Figure 4.13 Photograph of Impact-Damaged Specimens After Fracture (Impacter Mass = 1523 g, Velocity = 6.3 m/s).

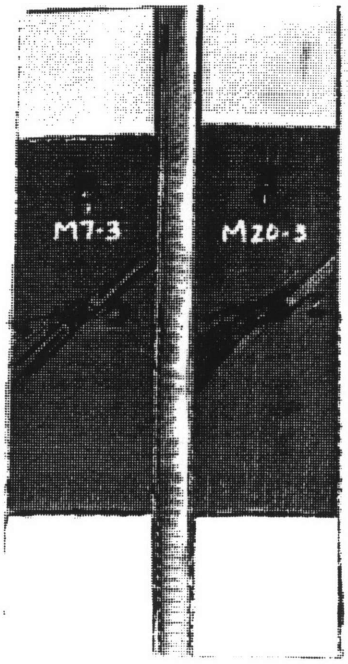

(Specimens - 70 x 340 mm)

Figure 4.14 Photograph of Impact-Damaged Specimens After Fracture (Impacter Mass = 1523 g, Velocity = 7.1 m/s).

The photograph of specimens impacted at 4.8 m/s, in Figure 4.12, clearly show sublaminate buckling in the impacted region for two out of the three specimens (sublaminate remains buckled even after the specimen is unloaded). Upon postmortem inspection of several specimens with obvious delamination, the sublaminate was consistently found to include only ply 1 (45°). Observation of the remaining plies showed fiber failure across the width. At this point, it is not possible to say whether delamination or fiber fracture is the primary mode of failure. The apparent across the width -45° damage on Specimen C4-3 in Figure 4.12 is the spalling of the back surface ply due to impact and not a result of the compressive residual strength test. The visual evidence of extensive back surface damage indicated by the spalling may be related to compressive residual strength. Specimen M4-3, which experienced both delamination and fiber failure, resulted in the highest compressive residual strength of the three specimens (337 MPa). Specimen C4-3, with back surface spalling, fiber failure, and no visual evidence of delamination, resulted in the lowest compressive residual strength of the three specimens (266 MPa). Specimen T3-2 , which failed at a compressive residual strength between the other two specimens (279 MPa), experienced both delamination and fiber failure. However, there is also evidence of damage in ply 1 of Specimen T3-2 similar in nature to the back surface spalling seen in Specimen C4-3, but not quite as extensive.

The photograph of specimens impacted at 6.3 m/s, in Figure 4.13, show sublaminate buckling of ply 1 and/or in-plane failure mechanisms. In those specimens exhibiting both failure modes, it is not obvious from visual examination which failure mode was primary and which was secondary. Typically, fracture occurred straight across the specimen. On the right side of C6-3 however, there is a change in failure path at the

impact location to a -45° angle. Again, the apparent across the width angle damage (-45° for Specimens T3-3, J17-2, and M3-2 and 45° for Specimen C6-3) in Figure 4.13 is the spalling of the back surface ply due to impact and not a result of the compressive residual strength tests. Specimen C6-3 failed at 278 MPa with evidence of extensive fiber failure and little evidence of delamination. Specimens T3-3 and J17-2 failed at virtually identical loads of 232 and 234 MPa, respectively, with evidence of delamination as well as fiber failure. Specimen M3-2, which also exhibits combined failure modes, failed at 184 MPa. Though all four specimens exhibit extensive damage with the back surface spalling, specimens also exhibiting delamination did not result in the higher failure loads as did the specimens impacted at 4.8 m/s. (The variation in damage orientation of Specimen C6-3 was due to impact on ply 1 instead of ply 12 as illustrated in Figure 3.12.)

The photograph of specimens impacted at 7.1 m/s, in Figure 4.14, show fracture to be dominated by fiber failure with little evidence of delamination. Typically, there was catastrophic fracture in every ply from the impact region straight out towards the specimen edge. On the right side of M7-3 however, there is a change in failure path at the impact location to a 45° angle. Again, the indication of across the width -45° damage in Figure 4.14 is the spalling of the back surface ply due to impact and not a result of the compressive residual strength tests. M20-3 and M7-3 failed at similar loads of 240 and 250 MPa, respectively.

4.2.3 Impacter Mass of 578 g

Plots of the major and minor axes of damage (as determined from X-ray photographs) versus impacter velocity due to an impacter mass of 578 g

are shown in Figure 4.15. These results show that damage levels off at a velocity of approximately 9.2 m/s. The maximum size of the major axis of damage is approximately 85 mm while the minor axis maximum size is approximately 30 mm. (These sizes are similar to those of 90 and 30 mm observed in Figure 4.6 for the case of the 1523 g impacter.) There is a bit more scatter in the major axis of damage as a function of impacter velocity in the 578 g case than that seen previously in the 1523 g case. Core damage size, shown in Figure 4.16, again levels off at a slightly lower velocity of approximately 8.6 m/s at a value of approximately 25 mm which is identical to that found for the case of the 1523 g impacter. And, as with the impacter mass of 1523 g, both of these velocities are within the penetration range.

The plot of compressive residual strength versus major axis of damage is shown in Figure 4.17. As the damage size increases, the compressive residual strength reaches an asymptote of approximately 200 MPa, similar to that shown in Figure 4.8. Compressive residual strengths of specimens with impact damage are again greater than the compressive residual strengths of specimens with open holes of diameter equivalent to the major axis of damage of the impacted specimens.

As the minor axis of damage increases, the compressive residual strength also reaches an asymptote of 200 MPa as shown in Figure 4.18. And compressive residual strengths for open holes of diameter equivalent to the minor axis of damage are still within the scatter band. The compressive residual strength versus core damage size is shown in Figure 4.19 for the case of the 578 g impacter mass. This curve still exhibits a downward trend in compressive residual strength. The minimum compressive residual strength occurred at the maximum core damage size for this impacter mass. The maximum core damage size did not occur at

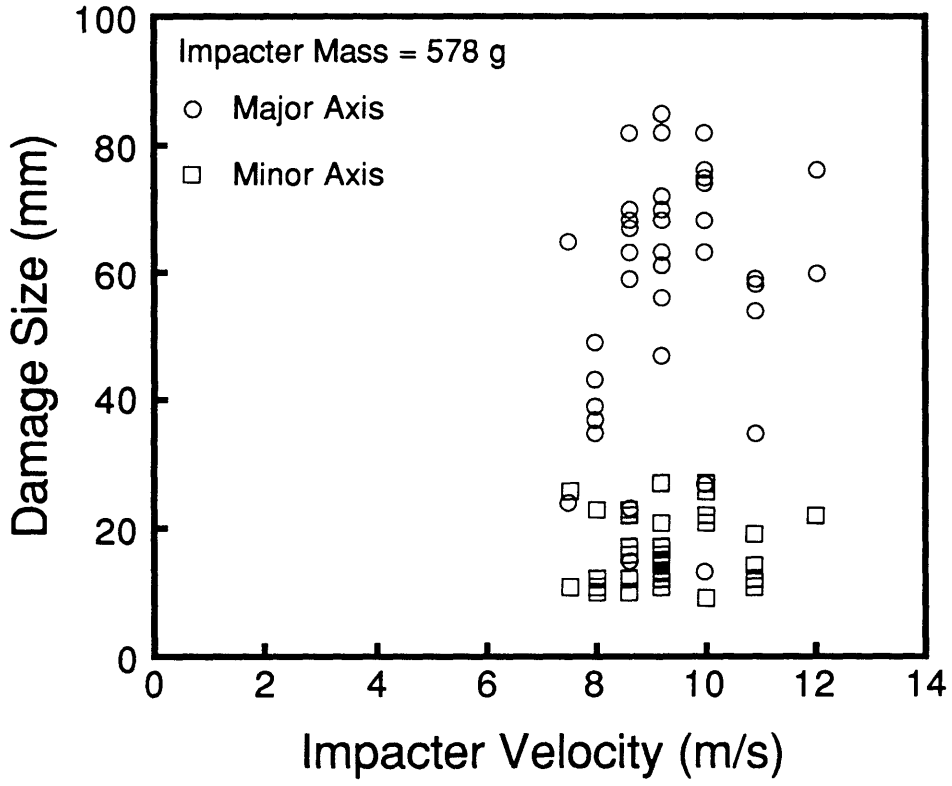

Figure 4.15 Damage Size versus Impacter Velocity (Impacter Mass = 578 g).

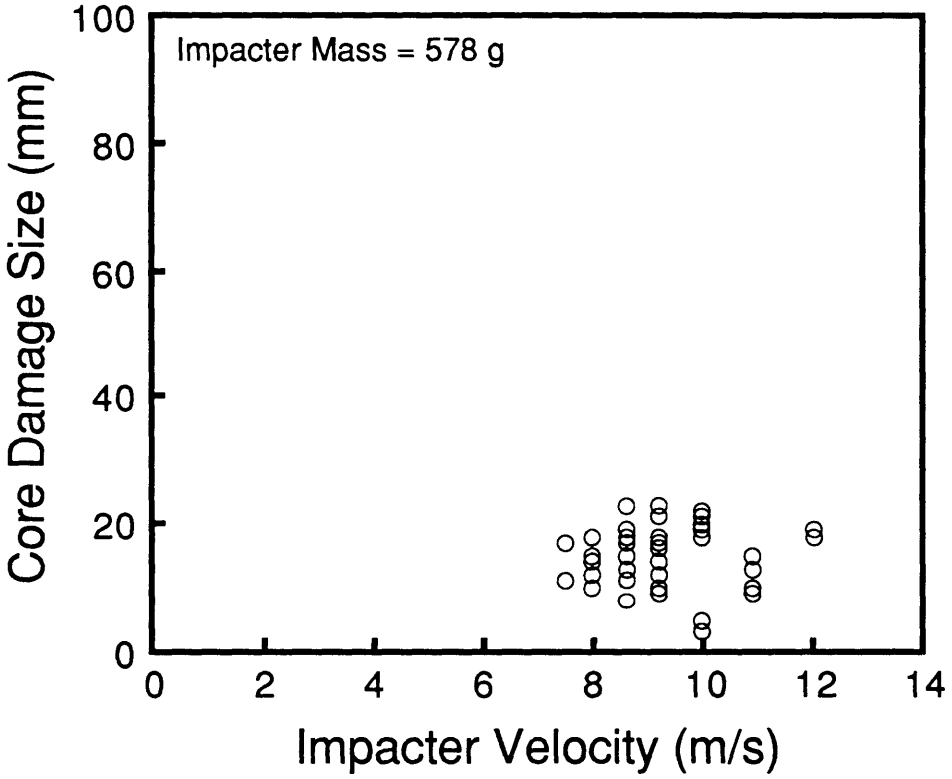

Figure 4.16 Core Damage Size versus Impacter Velocity (Impacter Mass = 578 g).

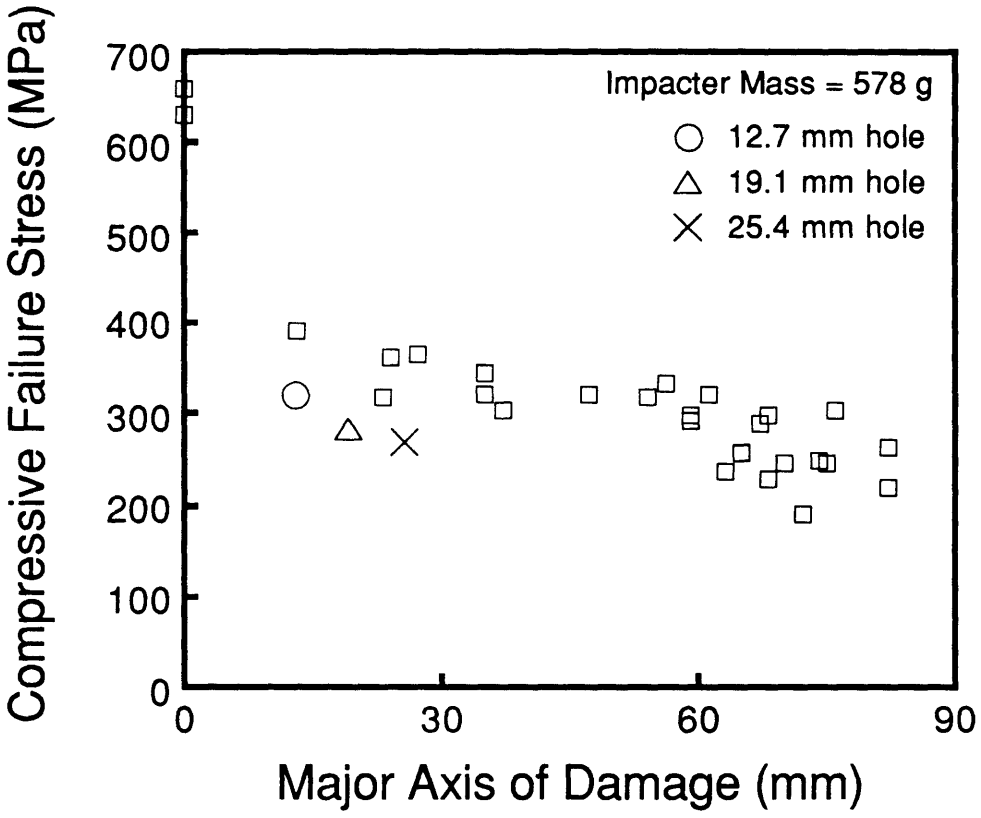

Figure 4.17 Compressive Residual Strength versus Major Axis of Damage (Impacter Mass = 578 g).

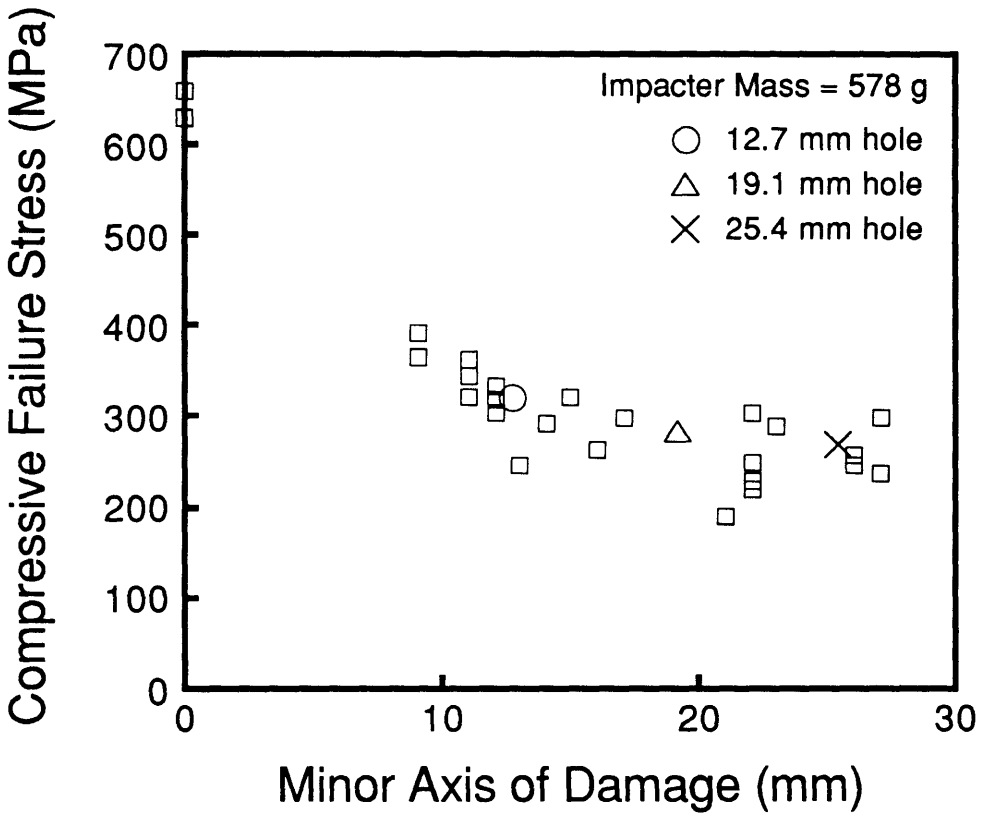

Figure 4.18 Compressive Residual Strength versus Minor Axis of Damage (Impacter Mass = 578 g).

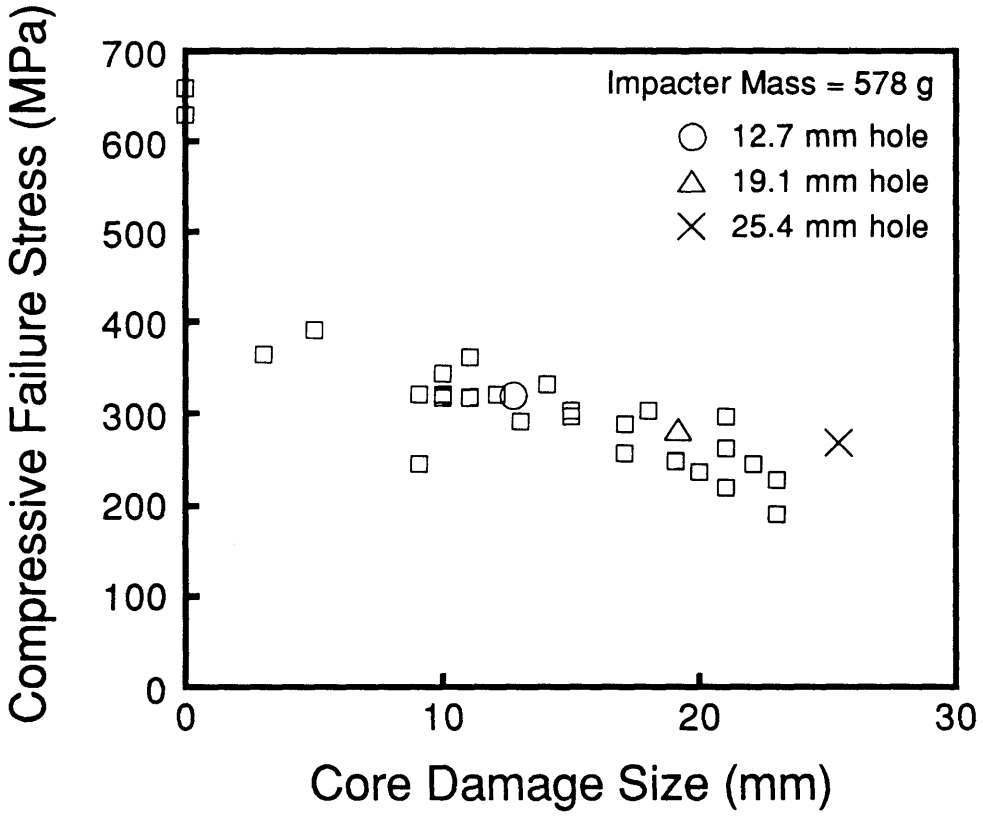

Figure 4.19 Compressive Residual Strength versus Core Damage Size (Impacter Mass = 578 g).

the highest impacter velocity tested. Thus, an increase in impacter velocity would not result in additional data on this curve to exhibit asymptotic behavior.

The compressive residual strength as a function of impacter velocity for the 578 g impacter mass is presented in Figure 4.20. The minimum compressive residual strength of 191 MPa occurred due to damage imparted at a velocity of 9.2 m/s (which is hereto referred to as the "MCRS-velocity" for impacter mass of 578 g). The large scatter at the 9.2 and 10.0 m/s velocities occurred due to scatter in the damage imparted at those velocities (discussed in Section 4.3.2). At velocities greater than the MCRS-velocity, the compressive residual strength increases towards the open hole value.

Photographs of the fractured specimens impacted at the lowest velocity, MCRS-velocity, and highest velocity with the 578 g mass in this work are presented in Figures 4.21 through 4.23. The photographs of specimens impacted at 7.5 m/s, in Figure 4.21, and at 9.2 m/s, in Figure 4.22, show evidence of sublaminate buckling. Again, upon postmortem inspection, the sublaminate was consistently found to include only ply 1 (45°) and the remaining plies showed fiber failure across the width. The specimens that exhibit delamination appear to fail straight across the coupon width as evidenced by Specimens J1-3 in Figure 4.21, and Specimens M20-4, J14-2 in Figure 4.22. Specimen J1-3 in Figure 4.21, which exhibits delamination, resulted in the highest compressive residual strength of the two specimens (364 MPa). Specimen J15-3, with back surface spalling, fiber failure, and no evidence of delamination, resulted in the lowest compressive residual strength of the two specimens (257 MPa). These correlations are similar to those seen in Figure 4.12 for specimens

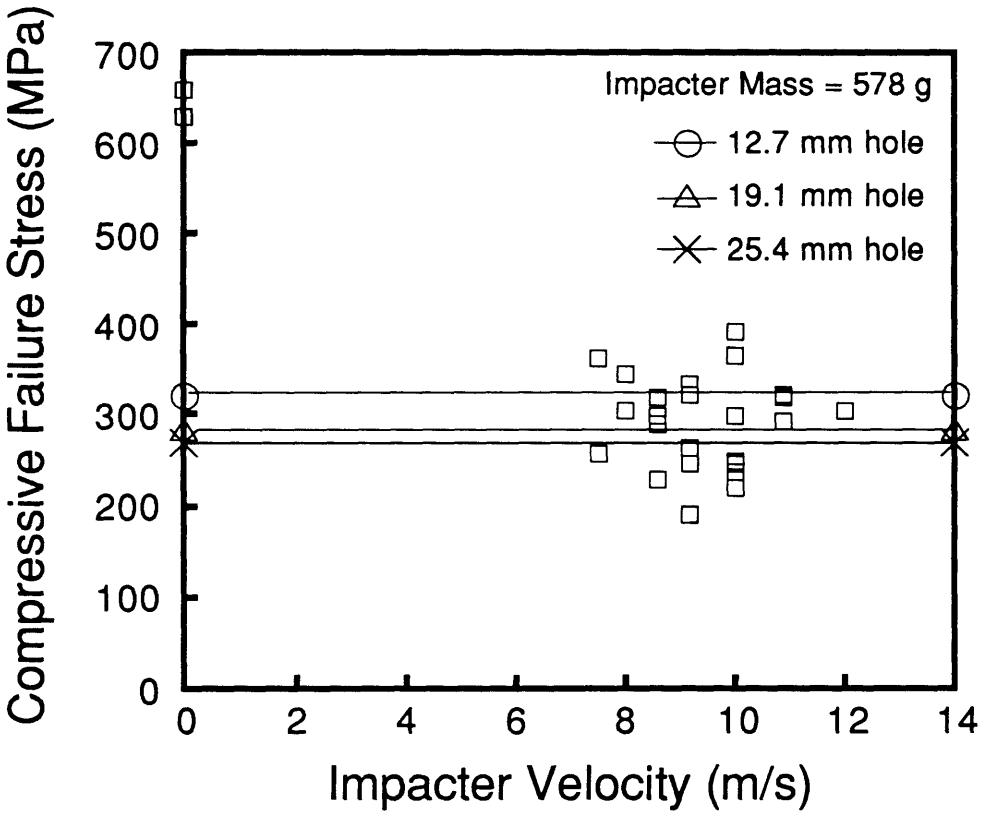

Figure 4.20 Compressive Residual Strength versus Impacter Velocity (Impacter Mass = 578 g).

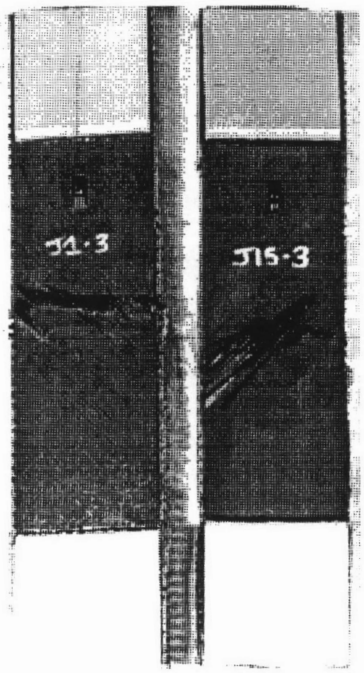

(Specimens - 70 x 340 mm)

Figure 4.21 Photograph of Impact-Damaged Specimens After Fracture (Impacter Mass = 578 g, Velocity = 7.5 m/s).

(Specimens - 70 x 340 mm)

Figure 4.22 Photograph of Impact-Damaged Specimens After Fracture (Impacter Mass = 578 g, Velocity = 9.2 m/s).

(Specimen - 70 x 340 mm)

Figure 4.23 Photograph of Impact-Damaged Specimen After Fracture (Impacter Mass = 578 g, Velocity = 12.0 m/s).

impacted with the 1523 g mass. When specimens exhibit both fiber failure and delamination, the failure path often changes to a 45° angle to the edge as evidenced by Specimens M26-3, M30-2, M24-3, and J1-2 in Figure 4.22. The indication of across the width -45° damage on Specimen J15-3 in Figure 4.21 and across the width 45° damage on Specimen J1-2 in Figure 4.22 is the spalling of the back surface ply due to impact and not a result of the compressive residual strength tests. The compressive residual strengths ranged from 245 to 335 MPa for all the specimens but J1-2. Failure for J1-2 occurred at 191 MPa. There was no obvious deviation from the failure paths or modes experienced in the other specimens to substantiate such a significant difference in compressive residual strength. (The variation in damage orientation of Specimens J1-3 and J1-2 is due to impact on ply 1 instead of ply 12 as illustrated in Figure 3.12.)

The photograph in Figure 4.23 is of the specimen impacted at 12.0 m/s. In this case, fracture is dominated by in-plane mechanisms as there was catastrophic failure in every ply from the impact region straight out towards the specimen edge and no evidence of delamination. Again, the indication of across the width -45° damage in Figure 4.23 is the spalling of the back surface ply due to impact and not a result of the compressive residual strength tests. Specimen M15-2 failed at 303 MPa.

4.2.4 Impacter Mass of 8.4 g

The data plotted in this section combines the results from the previous project [83] with the impact matrix presented in Table 3.7.

Plots of the major and minor axes of damage (as determined from X-ray photographs) versus impacter velocity due to an impacter mass of 8.4 g

are shown in Figure 4.24. These results show that the minor axis of damage levels off at a velocity of approximately 56 m/s at a value of approximately 30 mm. This is similar to the results of Cairns [25] of approximately 63 m/s for the same material system, laminate, impact apparatus, boundary conditions, and impacter. This value of 30 mm is also identical to that seen in Figures 4.6 and 4.15 for specimens impacted with the 1523 and 578 g masses, respectively. The major axis of damage however, does not level off. This is likely related to the fact that the spherical impacter did not physically pass through any of the coupons. The maximum value of the major axis of damage shown in Figure 4.24 is approximately 80 mm. Thus, while the curve does not level out, the maximum value reached is approaching those reported for the cases of the 1523 and 578 g impacter masses (90 and 85 mm, respectively). Core damage size levels off at the same approximate velocity as the minor axis of damage of 56 m/s at a value of approximately 20 mm as shown in Figure 4.25. This maximum core damage size of 20 mm for the impacter mass of 8.4 g is slightly smaller than the 25 mm size observed for specimens impacted by either the 1523 and 578 g mass.

The plot of compressive residual strength versus major axis of damage is shown in Figure 4.26. As the damage size increases, the compressive residual strength reaches an asymptote of approximately 200 MPa, similar to that shown in Figures 4.8 and 4.17. However, the compressive residual strength for open holes of diameter equivalent to the major axis of damage are within the scatter band. This is not the case for specimens impacted by the 1523 or 578 g mass. The major difference in these specimens as compared to the other two cases is the lack of extensive

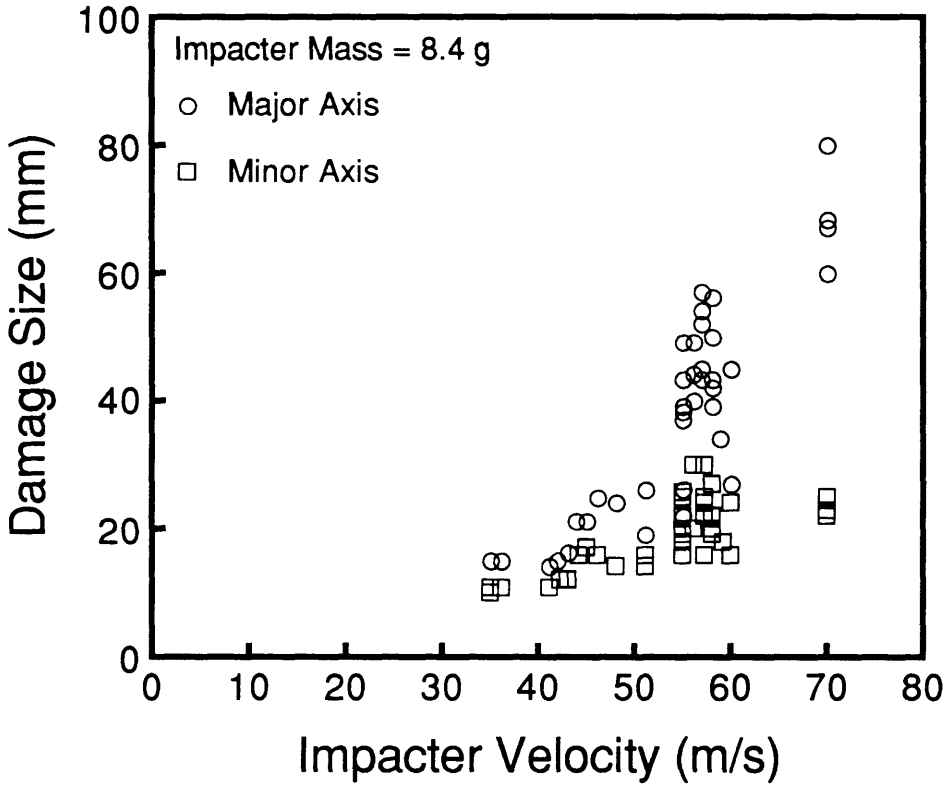

Figure 4.24 Damage Size versus Impacter Velocity (Impacter Mass = 8.4 g).

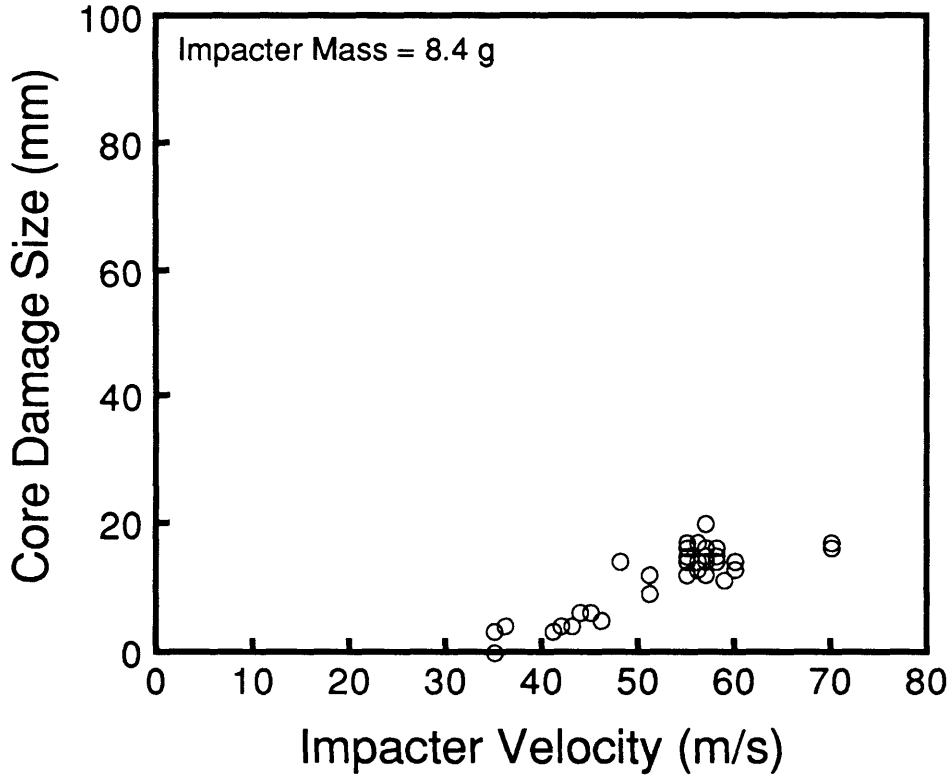

Figure 4.25 Core Damage Size versus Impacter Velocity (Impacter Mass = 8.4 g).

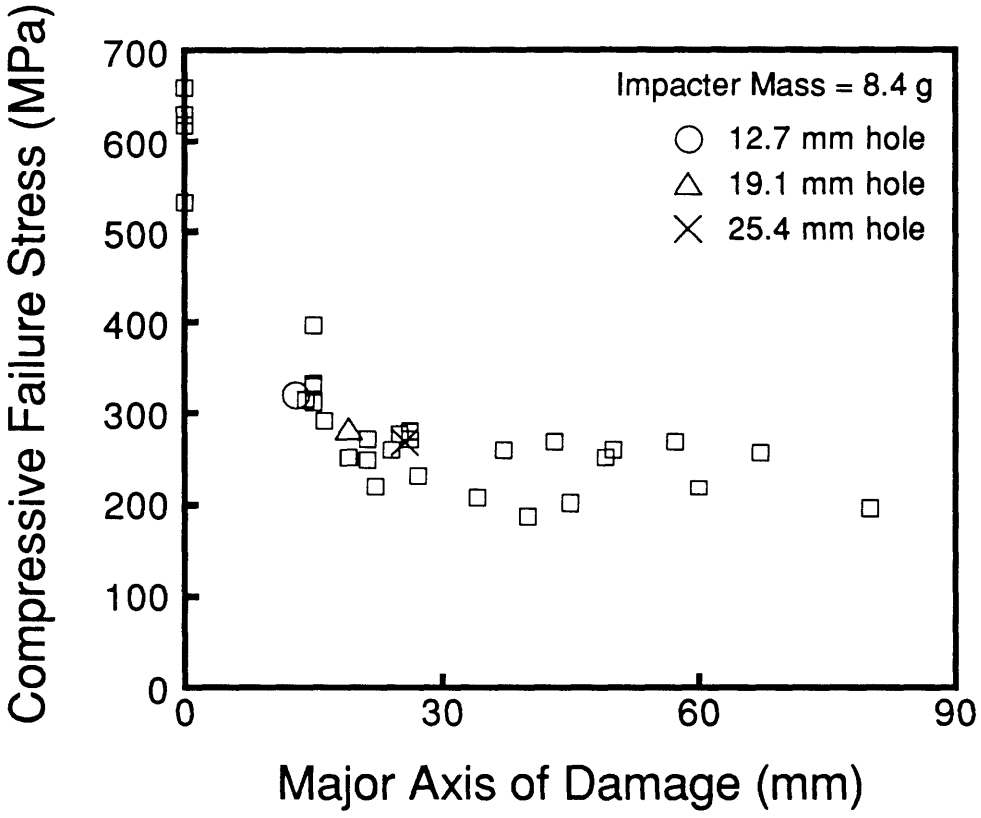

Figure 4.26 Compressive Residual Strength versus Major Axis of Damage (Impacter Mass = 8.4 g).

spalling of the back surface ply for specimens with similar compressive residual strengths to the open hole cases.

As the minor axis of damage increases, the compressive residual strength also reaches an asymptote of approximately 200 MPa as shown in Figure 4.27. And, compressive residual strength for open holes of diameter equivalent to the minor axis of damage are within the scatter band. The compressive residual strength versus core damage size also reaches an asymptote of approximately 200 MPa as shown in Figure 4.28. However, in this case, the open hole diameter (12.7, 19.1, and 25.4 mm) mean compressive residual strength results are apparently greater for diameters equivalent to the core damage size.

The compressive residual strength as a function of impacter velocity for the 8.4 g impacter mass is presented in Figure 4.29. The minimum compressive residual strength of 187 MPa occurred due to damage imparted at a velocity of approximately 57 m/s (which is hereto referred to as the "MCRS-velocity" for impacter mass of 8.4 g). At tested velocities greater than the MCRS-velocity, the compressive residual strength essentially maintained the MCRS value. The impacts at 70 m/s did result in significant fiber damage through the thickness. However, the impacter did not pass through the coupon. Thus, the impacter velocity penetration range was not completely defined. It is expected that once breakthrough occurs, the corresponding damage should be more representative of an open hole resulting in increased compressive residual strengths as previously demonstrated for the cases of the 1523 and 578 g mass impacters.

Photographs of the fractured specimens for the MCRS and highest impacter velocities used in this work with the 8.4 g mass are presented in Figures 4.30 and 4.31. The photographs of specimens impacted at 57 m/s in

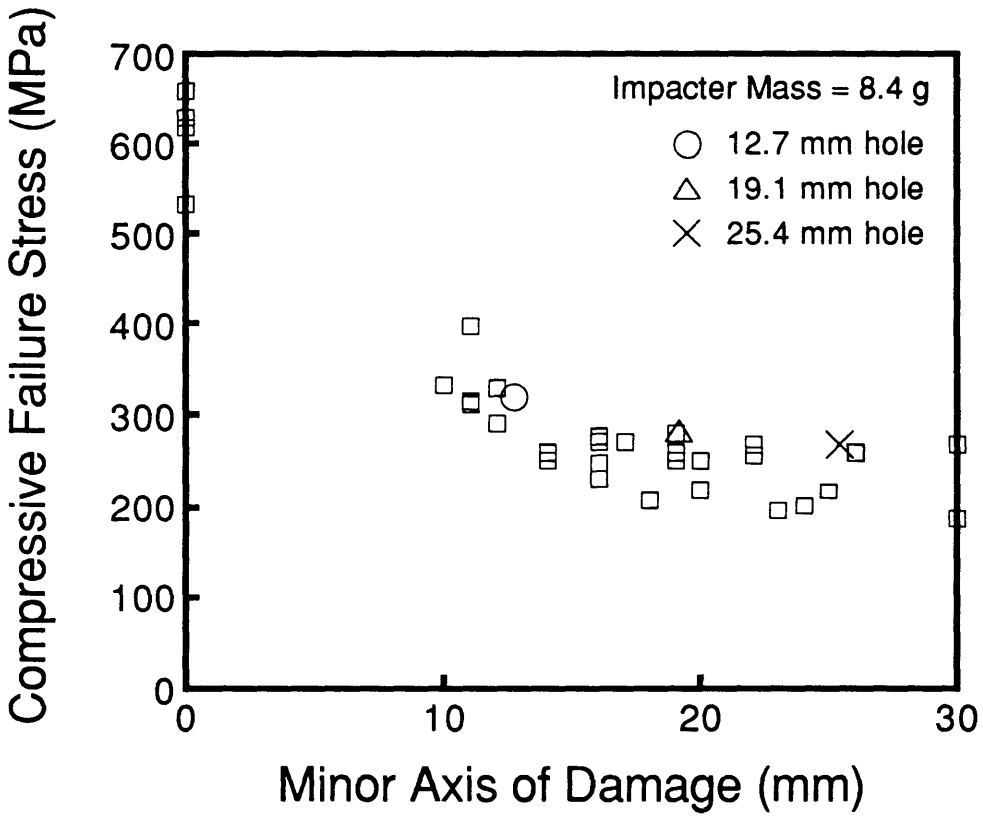

Figure 4.27 Compressive Residual Strength versus Minor Axis of Damage (Impacter Mass = 8.4 g).

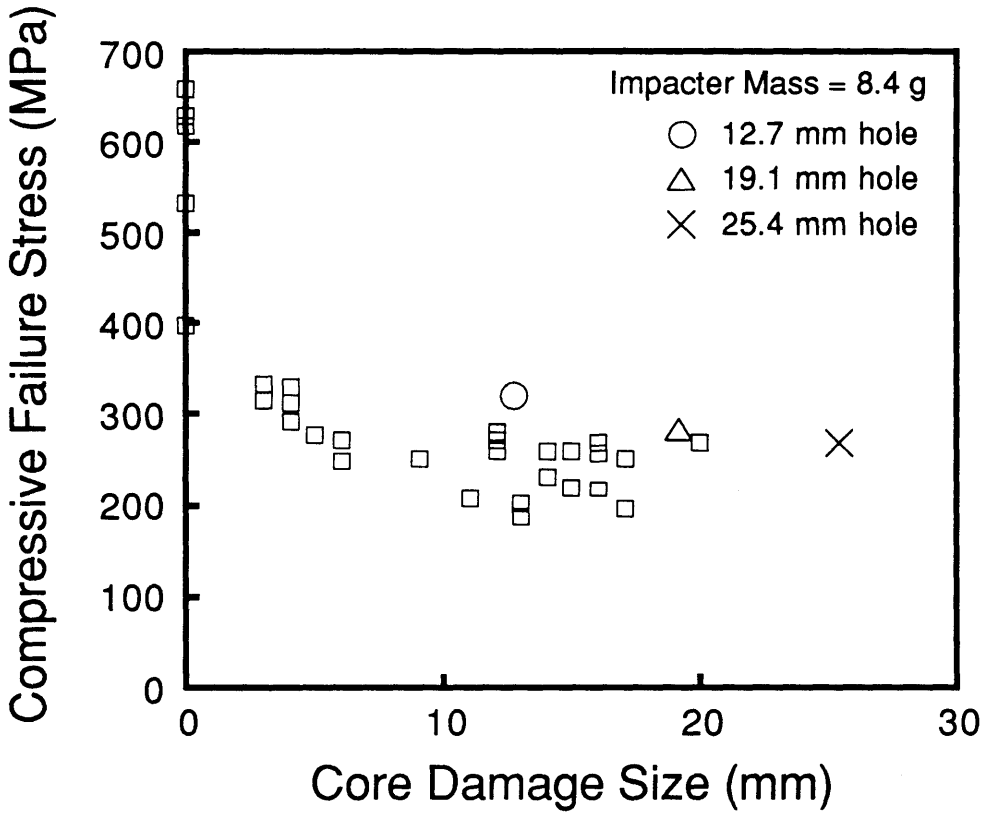

Figure 4.28 Compressive Residual Strength versus Core Damage Size (Impacter Mass = 8.4 g).

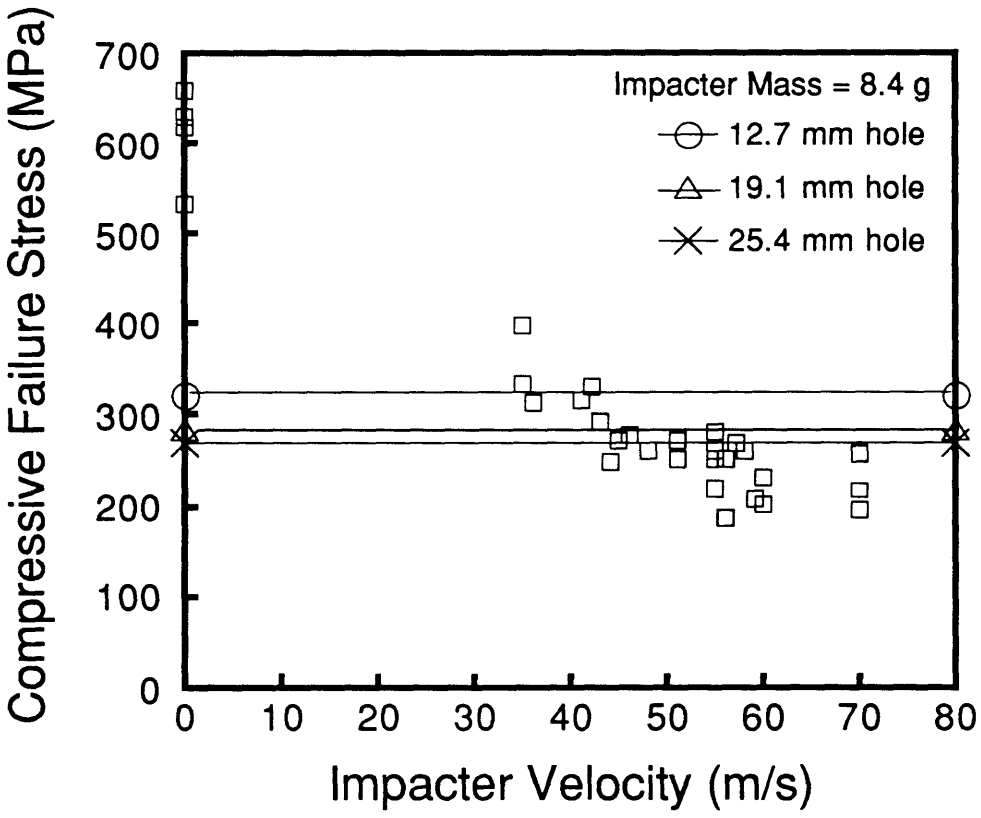

Figure 4.29 Compressive Residual Strength versus Impacter Velocity (Impacter Mass = 8.4 g).

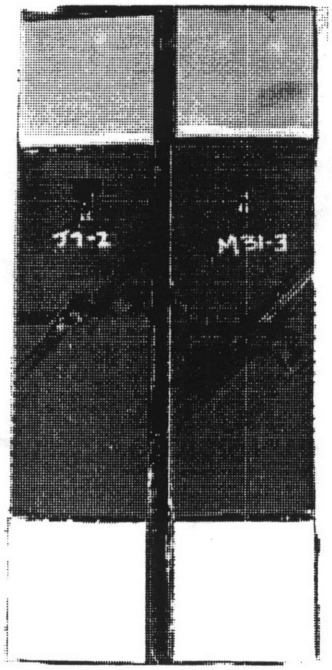

(Specimens - 70 x 340 mm)

Figure 4.30 Photograph of Impact-Damaged Specimens After Fracture (Impacter Mass = 8.4 g, Velocity = 57 m/s).

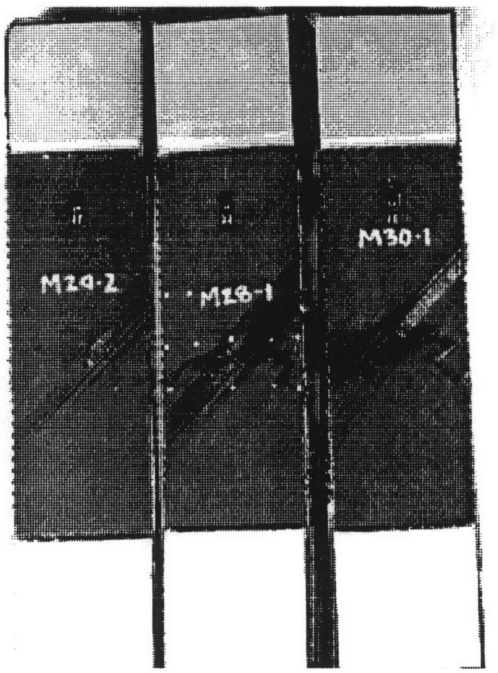

(Specimens - 70 x 340 mm)

Figure 4.31 Photograph of Impact-Damaged Specimens After Fracture (Impacter Mass = 8.4 g, Velocity = 70 m/s).

Figure 4.30 and at 70 m/s in Figure 4.31 show fracture by both delamination and fiber failure within the same specimens. The transition to fracture controlled by in-plane mechanisms only is expected to occur after impacter breakthrough when damage is more representative of an open hole. Again, the indication of across the width -45° damage in Figures 4.30 and 4.31 is the spalling of the back surface ply due to impact and not a result of the compressive residual strength tests. Both specimens impacted at 57 m/s and shown in Figure 4.30 failed at 270 MPa. Specimens M24-2, M28-1, and M30-1 impacted at 70 m/s and shown in Figure 4.31, failed at 218, 259, and 197 MPa, respectively. From observation of the failure modes, paths, and extent of damage, the explanation for this ranking or deviation in compressive residual strengths is not obvious.

4.3 Nondestructive Damage Evaluation

The nondestructive damage evaluation techniques employed in this work were visual inspection, X-ray, ultrasonic C-Scan, and time-of-flight ultrasonic C-Scan. Every impact coupon underwent nondestructive damage evaluation by visual inspection and X-ray using a dye penetrant. The measurement of damage size by X-ray is the standard available for all impacted coupons. Only those coupons listed in Tables 3.5 through 3.7 underwent nondestructive damage evaluation by ultrasonic C-Scan. Of the coupons ultrasonically C-Scanned, those designated for destructive evaluation by the deply technique and approximately one coupon from every impacter velocity group designated for cross-sectioning also had time-of-flight ultrasonic C-Scans. One compressive residual strength specimen from each impacter mass was also selected for evaluation by time-of-flight

ultrasonic C-Scanning. These specimens were selected in an attempt to compare three-dimensional damage states for specimens that actually exhibited similar compressive residual strengths (less than ten percent difference).

4.3.1 Visual

Both the front and back surfaces of each impacted specimen underwent visual inspection. For the impacter masses and corresponding velocities used in this work, nearly all the impacted specimens exhibited visual indications of damage. Complete penetration velocity was roughly characterized for two of the three masses used in this work (complete penetration is defined as the tip of the impacter progressing beyond the back surface of the laminate).

In the case of the 1523 g impacter mass, visual indications of damage occurred at velocities as low as 4.6 m/s. Only one specimen was impacted at a lower velocity of 4.3 m/s. For specimens impacted by the 1523 g mass, the lowest velocity where complete penetration occurred is also 4.6 m/s. However, several specimens impacted at higher velocities up to 5.2 m/s did not experience penetration or exhibit penetration threshold damage. Several of these coupons did not even have visual indications of damage. Accounting for scatter in damage at identical velocities, the penetration that occurred at 4.6 m/s is an extreme damage case representative of the maximum probable damage due to impact by a 1523 g mass at this velocity.

In the case of the 578 g impacter mass, visual indications of damage occurred at velocities as low as 7.5 m/s. This was the lowest velocity tested in the case of the 578 g impacter mass. For specimens impacted by the 578 g

mass, the lowest velocity where complete penetration occurred is also 7.5 m/s. However, several specimens impacted at higher velocities up to 10.0 m/s did not experience complete penetration. Accounting for scatter in damage at identical velocities, the penetration that occurred at 7.5 m/s is an extreme damage case representative of the maximum probable damage due to impact by a 578 g mass at this velocity.

In the case of the 8.4 g impacter mass, tested velocities in this work only ranged from 55 to 70 m/s. Visual indications of damage occurred at all these velocities. Complete penetration did not occur in the coupons impacted by the 8.4 g mass at the velocities selected for testing in this work. However, the specimens impacted at 70 m/s did experience extensive damage through the thickness (as evidenced by holding up a light source behind the impact location). Thus, the impacter velocity of 70 m/s is the start of the penetration range for the case of the 8.4 g impacter.

4.3.2 X-ray

The order of presentation of X-ray photographs for each impacter mass is intended to: first, provide an idea as to the range of damage exhibited from all the velocities tested; second, show the variation in damage at a single velocity and the corresponding compressive residual strengths; third, to show apparent maximum damage at each of three velocities tested (lowest, MCRS, and highest) and the corresponding compressive residual strengths; and fourth, compare damage of the extremes in compressive residual strength at the MCRS-velocity.

The extremes in damage as evidenced by X-ray occurred at impacter velocities of 4.8 and 6.3 m/s for the 1523 g impacter mass as shown in

Figure 4.32. The 4.8 m/s impacter velocity is near the lowest velocity used for the impact tests with the 1523 g mass. The 6.3 m/s impacter velocity was previously noted as the MCRS-velocity for this particular impacter mass. Specimen M3-2 is the specimen that resulted in the minimum compressive residual strength of 184 MPa, noted in Section 4.2.2.

There is significant scatter in X-ray measured damage imparted at a single velocity for the 1523 g impacter mass as shown in Figure 4.33. At an impacter velocity of 4.8 m/s, the major axis of damage ranges from 19 to 78 mm. The minor axis of damage ranges from 13 to 20 mm and core damage size ranges from 5 to 18 mm. The differences in compressive residual strengths may be attributed to the significant differences in damage size. (The variation in damage orientation of Specimen T3-2 is due to impact on ply 1 instead of ply 12 as illustrated in Figure 3.12.)

The maximum damage as evidenced by X-ray near the lowest velocity, at the MCRS-velocity, and at the highest velocity for the 1523 g impacter mass is not significantly different as shown in Figure 4.34. The variations in compressive residual strength for these three specimens cannot be explained by the damage sizes measured in the X-ray photographs.

Relating damage determined by X-ray to the extremes of compressive residual strength at the MCRS-velocity for the 1523 g impacter mass is also not successful. For similar damage illustrated by X-ray photographs shown in Figure 4.35, Specimen M3-2 failed at 66% of the failure load for Specimen C6-3. The X-ray photographs of these specimens provide no explanation for this phenomenon. (As previously mentioned, the variation in damage orientation of Specimen C6-3 is due to impact on ply 1 instead of ply 12.)

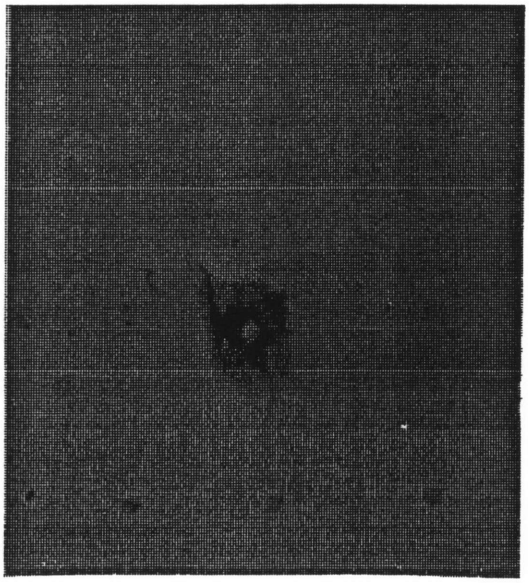

Velocity = 4.8 m/s (M4-3)

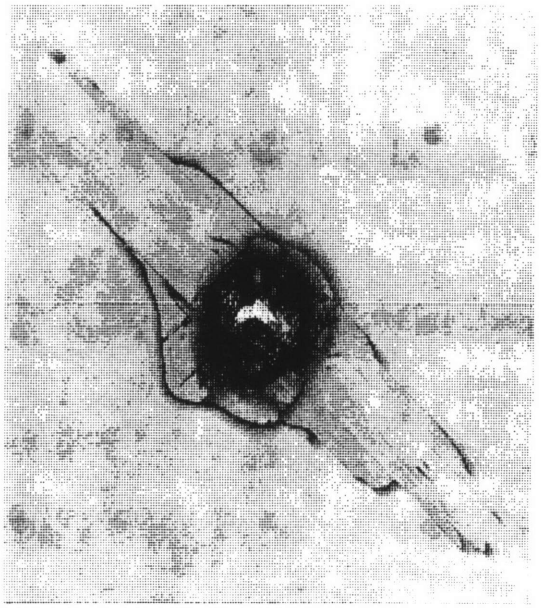

Velocity = 6.3 m/s (M3-2)

(X-rays are to scale)

Figure 4.32 X-ray Photographs Showing Extremes in Damage (Impacter Mass = 1523 g).

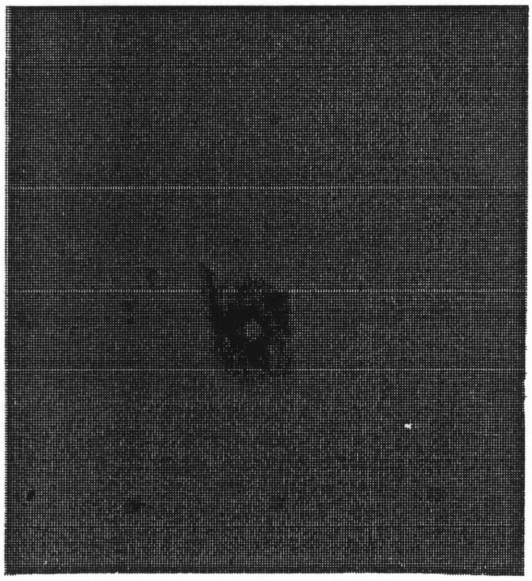

CRS = 337 MPa (M4-3)

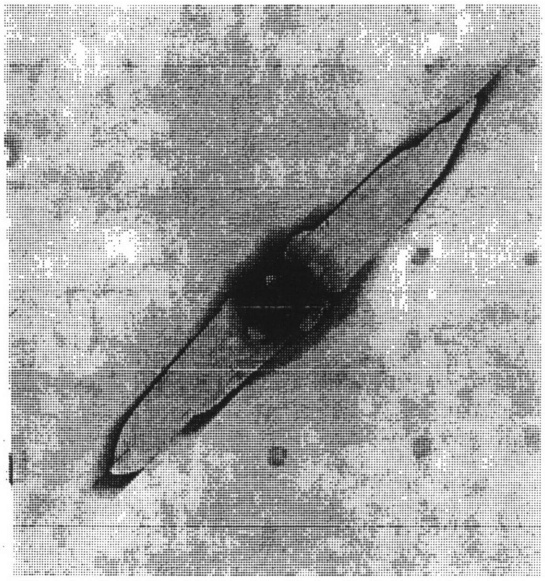

CRS = 279 MPa (T3-2)

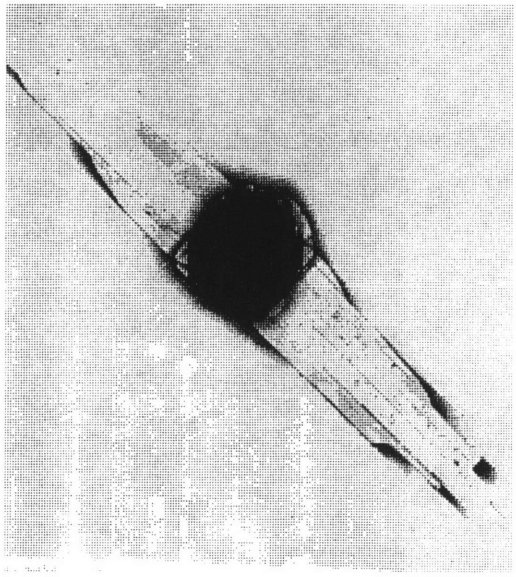

CRS = 266 MPa (C4-3)

(X-rays are to scale)

Figure 4.33 X-ray Photographs Showing Variation in Damage at a Single Impacter Velocity of 4.8 m/s (Impacter Mass = 1523 g).

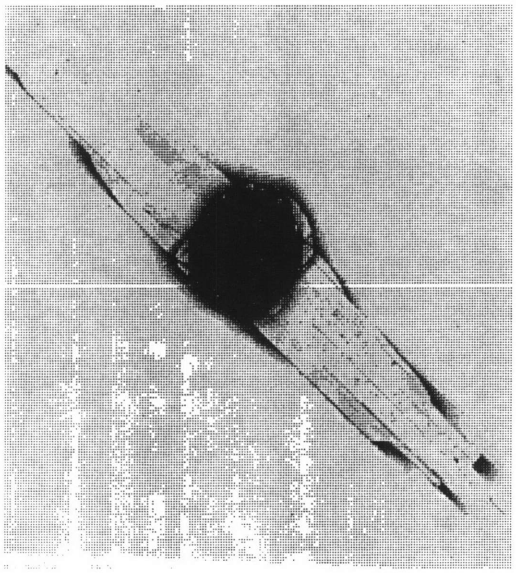

CRS = 266 MPa (C4-3)
Velocity = 4.8 m/s

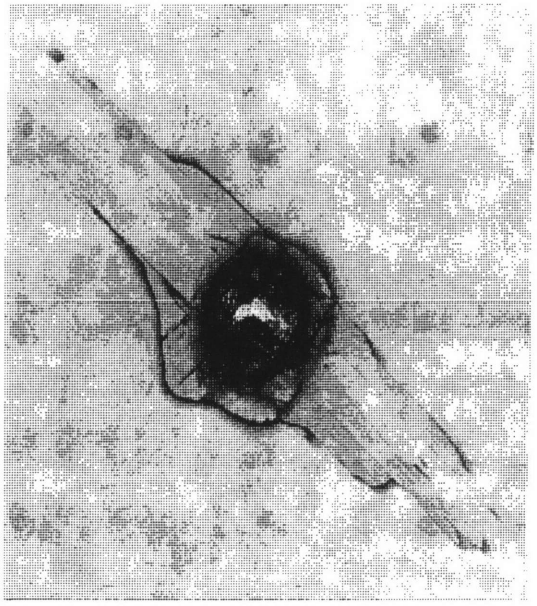

CRS = 184 MPa (M3-2)
Velocity = 6.3 m/s

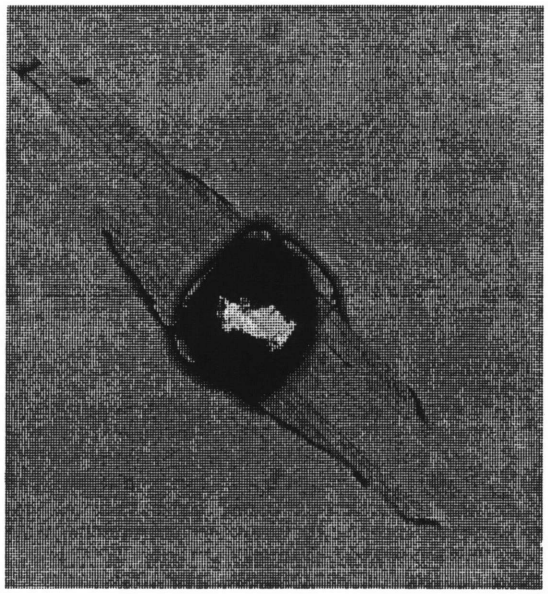

CRS = 247 MPa (C3-2)
Velocity = 8.6 m/s

(X-rays are to scale)

Figure 4.34 X-ray Photographs of Maximum Damage near Lowest, at MCRS and Highest Impacter Velocities (Impacter Mass = 1523 g).

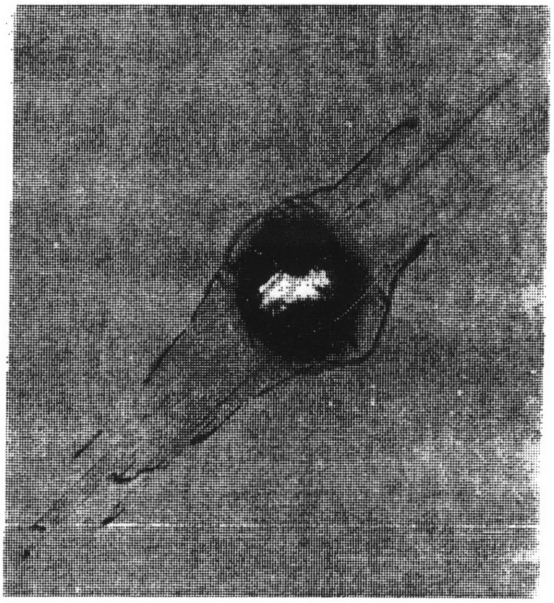

CRS = 278 MPa (C6-3)

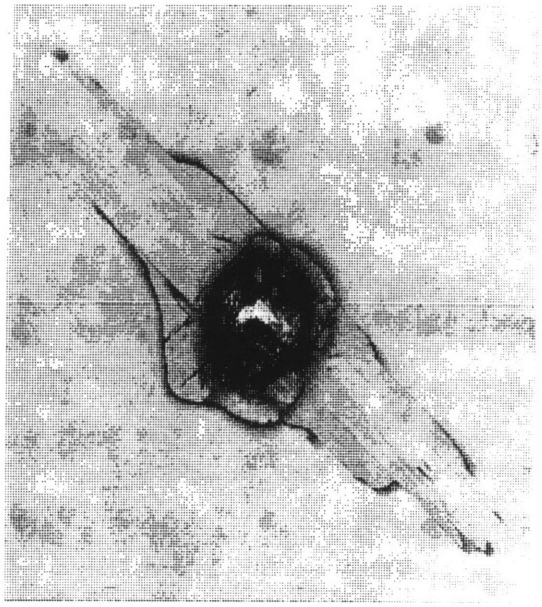

CRS = 184 MPa (M3-2)

(X-rays are to scale)

Figure 4.35 X-ray Photographs Showing Damage in Specimens at Extremes in Compressive Residual Strength at MCRS Impacter Velocity (Impacter Mass = 1523 g, Velocity = 6.3 m/s).

The extremes in damage as evidenced by X-ray occurred at impacter velocities of 7.5 and 9.2 m/s for the 578 g impacter mass as shown in Figure 4.36. The 7.5 m/s impacter velocity was previously noted to be the minimum test velocity for the 578 g impacter mass while the 9.2 m/s impacter velocity was previously noted to be the MCRS-velocity. (As previously mentioned, the variation in damage orientation of Specimen J1-3 is due to impact on ply 1 instead of ply 12.)

There is significant scatter in X-ray measured damage imparted at a single velocity for the 578 g impacter mass as shown in Figure 4.37. At an impacter velocity of 7.5 m/s, the major axis of damage ranges from 24 to 65 mm. The minor axis of damage ranges from 11 to 26 mm and core damage size ranges from 11 to 17 mm. The differences in compressive residual strengths may be attributed to the significant differences in damage size.

The maximum damage as evidenced by X-ray at the lowest, MCRS, and highest impacter velocities for the 578 g impacter mass is not significantly different as shown in Figure 4.38. Specimen J6-2 was designated for destructive damage evaluation. Thus, no compressive residual strength data is available. However, it is not obvious from the X-ray photographs why Specimen J15-3 failed at 85% of the failure load of Specimen M15-2.

Comparison of damage determined by X-ray to the extremes of compressive residual strength at the MCRS-velocity for the 578 g impacter mass is shown in Figure 4.39. The X-ray photographs of these specimens provide a possible explanation for the scatter in compressive residual strength at the MCRS-velocity of 9.2 m/s in that the damage is significantly different. (As previously mentioned, the variation in damage orientation of Specimen J1-2 is due to impact on ply 1 instead of ply 12.)

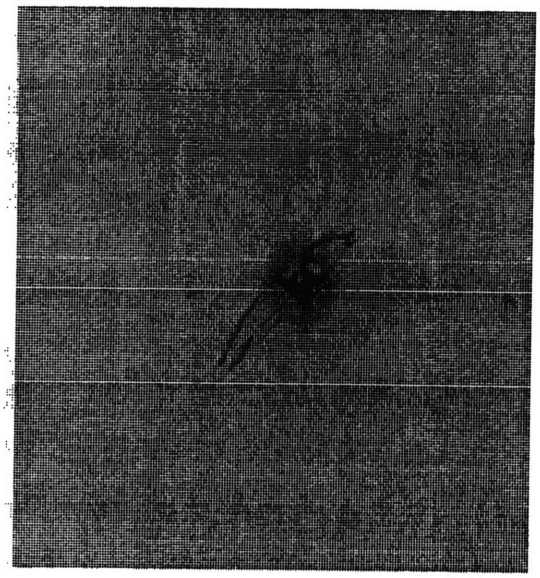

Velocity = 7.5 m/s (J1-3)

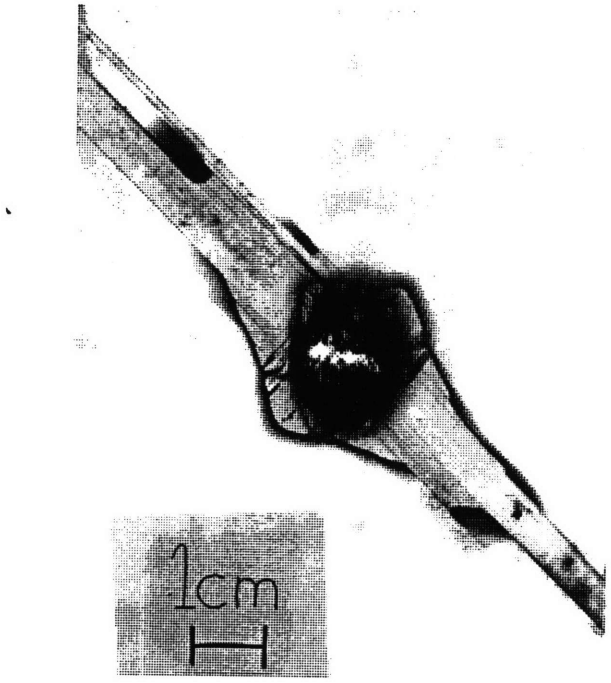

Velocity = 9.2 m/s (J6-2)

(X-rays are to scale)

Figure 4.36 X-ray Photographs Showing Extremes in Damage (Impacter Mass = 578 g).

CRS = 364 MPa (J1-3)

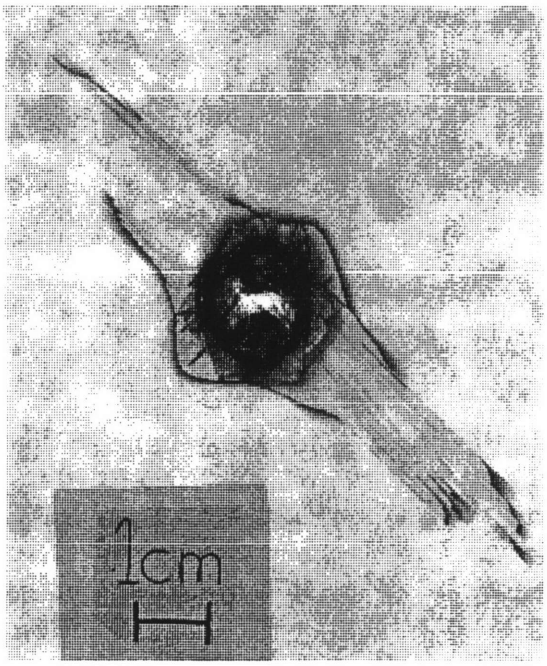

CRS = 257 MPa (J15-3)

(X-rays are to scale)

Figure 4.37 X-ray Photographs Showing Variation in Damage at a Single Impacter Velocity of 7.5 m/s (Impacter Mass = 578 g).

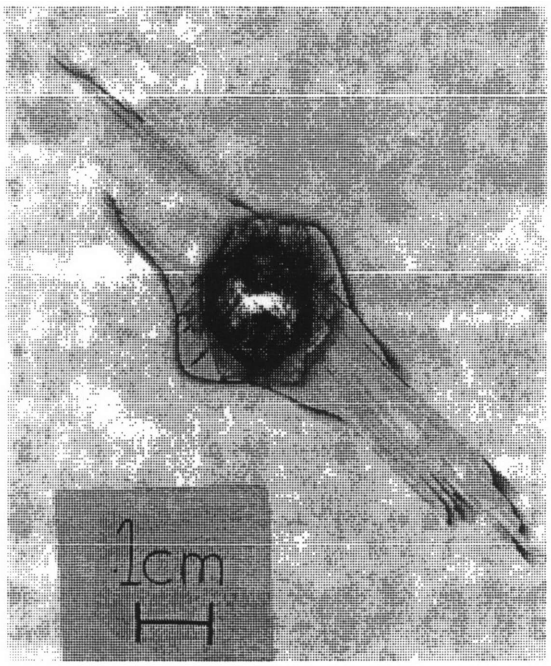

CRS = 257 MPa (J15-3)
Velocity = 7.5 m/s

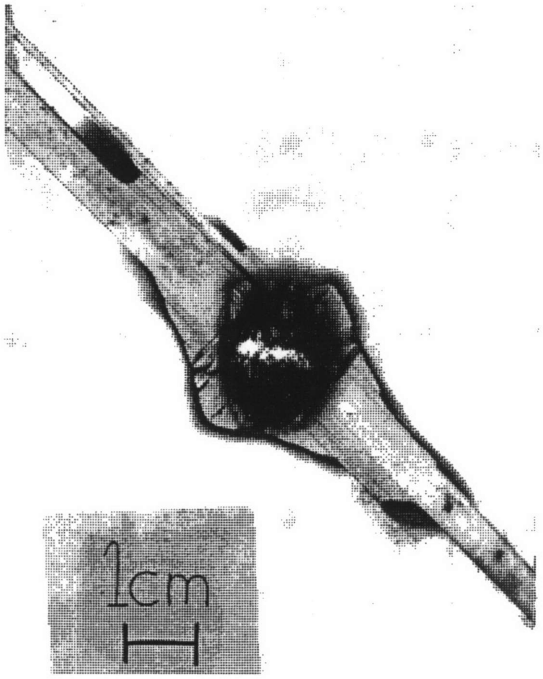

Cross-Section (J6-2)
Velocity = 9.2 m/s

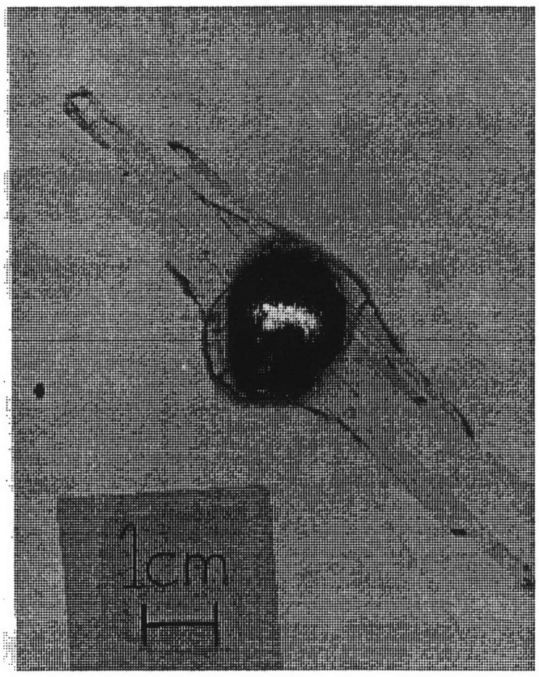

CRS = 303 MPa (M15-2)
Velocity = 12.0 m/s

(X-rays are to scale)

Figure 4.38 X-ray Photographs of Maximum Damage at Lowest, MCRS and Highest Impacter Velocities (Impacter Mass = 578 g).

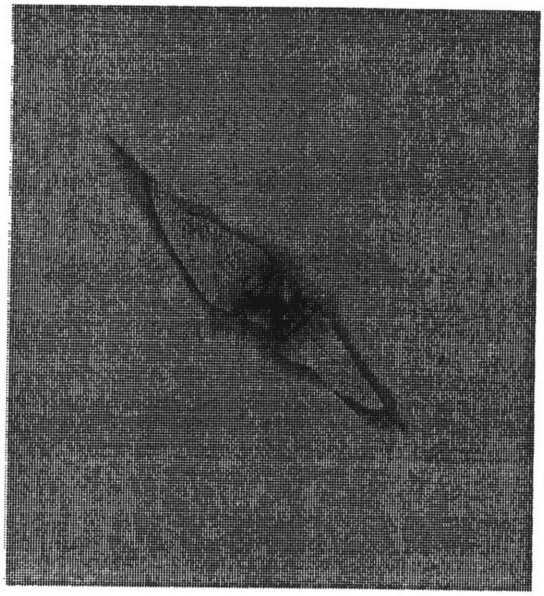

CRS = 335 MPa (M20-4)

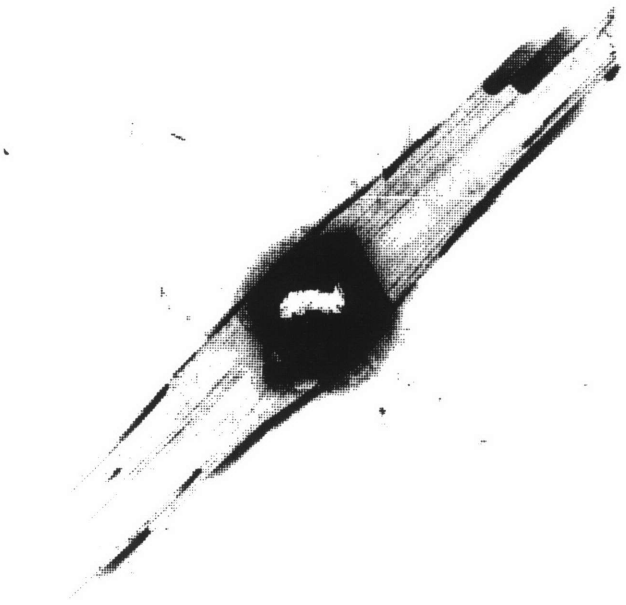

CRS = 191 MPa (J1-2)

(X-rays are to scale)

Figure 4.39 X-ray Photographs Showing Damage in Specimens at Extremes in Compressive Residual Strength at MCRS Impacter Velocity (Impacter Mass = 578 g, Velocity = 9.2 m/s).

The extremes in damage as evidenced by X-ray for the 55–70 m/s impacter velocities used in this work for the 8.4 g mass are presented in Figure 4.40. The maximum damage occurred at an impacter velocity of 70 m/s. Though 57 m/s was previously noted as the MCRS-velocity from data generated in Reference 83, damage imparted at 70 m/s in this work also resulted in near minimum compressive residual strength.

There was less scatter in X-ray measured damage imparted at a single velocity for the 8.4 g impacter mass than seen for the 1523 and 578 g impacter masses. As seen in Figure 4.41, at an impacter velocity of 57 m/s in this work, the major axis of damage ranges from 45 to 52 mm. The minor axis of damage ranges from 16 to 24 mm and core damage size ranges from 12 to 14 mm. Both of these specimens were designated for destructive damage evaluation. Thus, no compressive residual strength data is available.

The maximum delamination damage size as evidenced by X-ray at the lowest, MCRS, and highest impacter velocities for the 8.4 g impacter mass used in this work were not significantly different. This can be seen in the X-ray photographs of Figure 4.42. Specimen M29-2 (57 m/s) was designated for destructive damage evaluation. Thus, no compressive residual strength data is available. It is apparent that Specimen M24-2 (70 m/s) had more core damage than Specimen M12-1 (55 m/s), which could explain why M24-2 failed at a lower load than M12-1.

Relating damage determined by X-ray to the extremes of compressive residual strength at the highest impacter velocity (70 m/s) for the 8.4 g impacter mass was not successful. For similar damage illustrated by the X-ray photographs in Figure 4.43, Specimen M30-1 failed at 74% of the

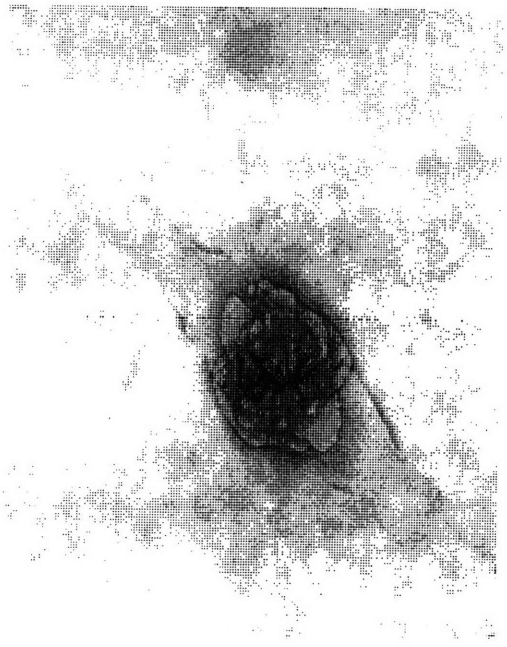

Velocity = 55 m/s (J16-4)

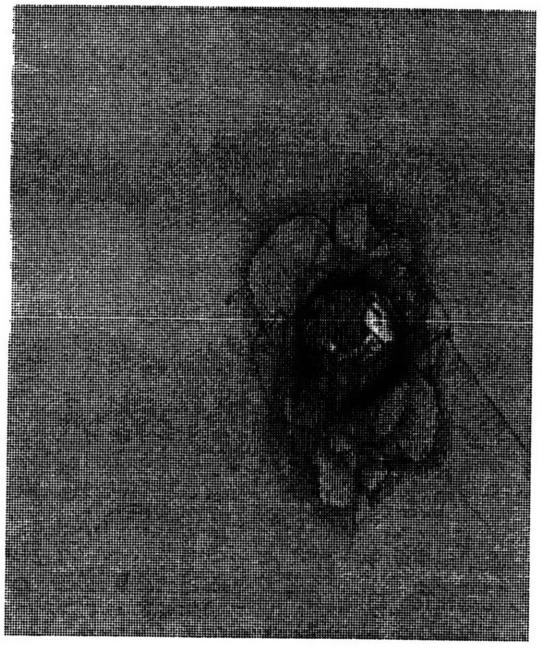

Velocity = 70 m/s (M24-2)

(X-rays are to scale)

Figure 4.40 X-ray Photographs Showing Extremes in Damage (Impacter Mass = 8.4 g).

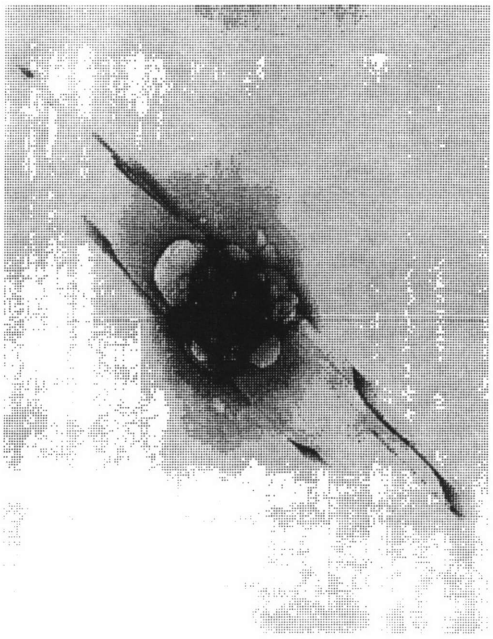

Cross-Section (M32-4)

Cross-Section (M29-2)

(X-rays are to scale)

Figure 4.41 X-ray Photographs Showing Variation in Damage at a Single Impacter Velocity of 57 m/s (Impacter Mass = 8.4 g).

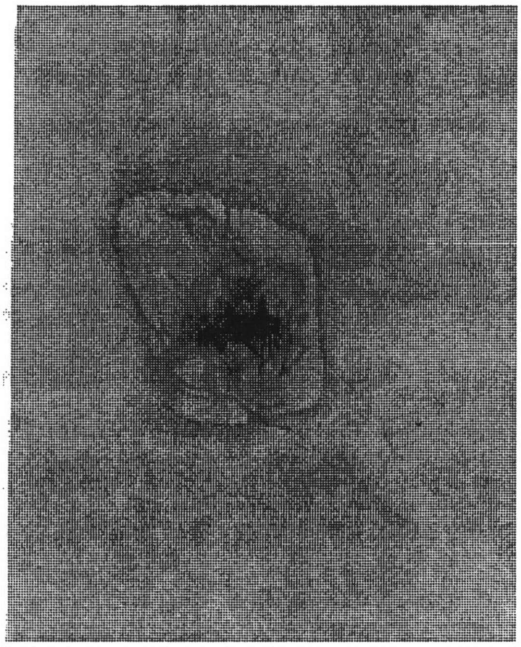

CRS = 261 MPa (M12-1)
Velocity = 55 m/s

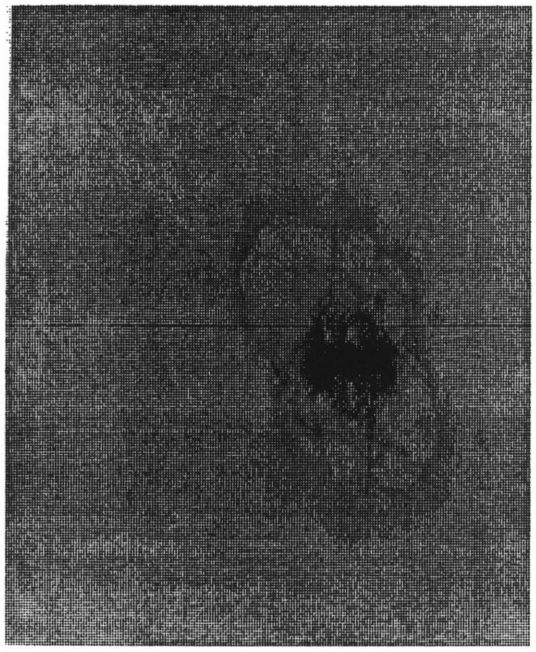

Cross-Section (M29-2)
Velocity = 57 m/s

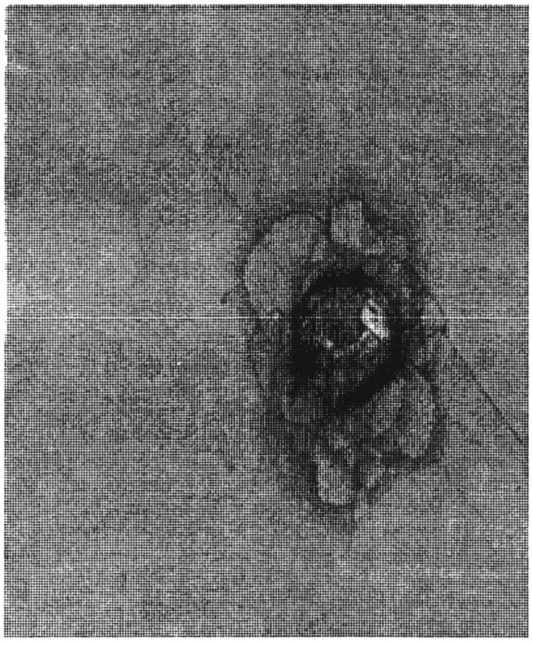

CRS = 218 MPa (M24-2)
Velocity = 70 m/s

(X-rays are to scale)

Figure 4.42 X-ray Photographs of Maximum Damage at Lowest, MCRS and Highest Impacter Velocities (Impacter Mass = 8.4 g).

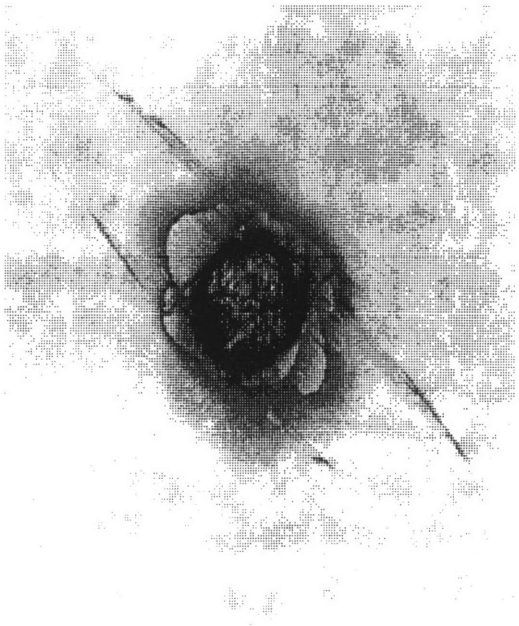

CRS = 259 MPa (M28-1)

CRS = 191 MPa (M30-1)

(X-rays are to scale)

Figure 4.43 X-ray Photographs Showing Damage in Specimens at Extremes in Compressive Residual Strength at Impacter Velocity of 70 m/s (Impacter Mass = 8.4 g).

failure load for Specimen M28-1. Though these two specimens represent the minimum and maximum compressive residual strengths for this impacter velocity, Specimen M24-2 (shown in Figure 4.42) apparently had greater delamination damage size than either of these specimens. And the compressive residual strength of this specimen was less than that of M28-1 and greater than that of M30-1. The X-ray photographs of these specimens do not provide an explanation for this phenomenon.

4.3.2 Ultrasonic C-Scan

Interpretation of the damage state from a two-dimensional ultrasonic C-Scan is difficult as fiber, matrix, and delamination damage is integrated through-the-thickness for a "summary" of the damage. The same held true for the X-ray photographs, but due to the wicking nature of the dye penetrant and the change in delamination shape from interface to interface, better insight into the possible three-dimensional damage state existed. Three-dimensional or time-of-flight ultrasonic C-Scan provides better detail on a ply-by-ply basis. However, both ultrasonic techniques are presently limited by the gray scale capability (64) of the printer used by Hercules, Inc.. The capability of the Hercules, Inc. computer screen provides much better resolution via 256 gray scales. Also, the 64 gray scales are not absolute. Each coupon has the 64 gray scales determined by the peak-to-peak amplitude of its backwall reflection. Thus, when comparing two or more coupons, levels of gray are not relevant. Only black and white pixels indicate similar damage information from coupon to coupon. Before presenting the ultrasonic C-Scan results, it should be noted that evaluation

of the results is not objective and is open to differences in individual interpretation.

The presentation of ultrasonic C-Scan results available for each impacter mass compares similar ultrasonic C-Scans for specimens with similar compressive residual strengths; compares dissimilar ultrasonic C-Scans for specimens with similar compressive residual strengths; and, for specimens impacted by the 8.4 g mass, compares similar damage at each of three velocities tested (lowest, MCRS, and highest) and the corresponding compressive residual strengths.

Comparison of damage determined by two-dimensional ultrasonic C-Scan to compressive residual strength was inconsistent for specimens impacted by the 1523 g mass. Figure 4.44 consists of two ultrasonic C-Scans of specimens that failed at virtually identical stresses (244, 243 MPa). In these two cases, the indicated damage was similar. However, in Figure 4.45, two ultrasonic C-Scans of specimens with identical failure stresses (234 MPa) showed dissimilar damage states. There was evidence of the back side splitting in the ultrasonic C-Scan of J17-2 that wasn't apparent in the ultrasonic C-Scan of M23-3. Comparing Figures 4.44 and 4.45 (failure stresses within 4%), only the damage in Specimen J17-2 appeared significantly different with evidence of extensive back side splitting due to impact. Visual inspection of all four coupons after impact resulted in observations of similar back surface damage. However, the ultrasonic C-Scans did not seem to provide evidence of such.

Comparison of damage indicated by the ultrasonic C-Scans to compressive residual strength was inconclusive for specimens impacted by the 578 g mass because of the limited number of ultrasonic C-Scans for

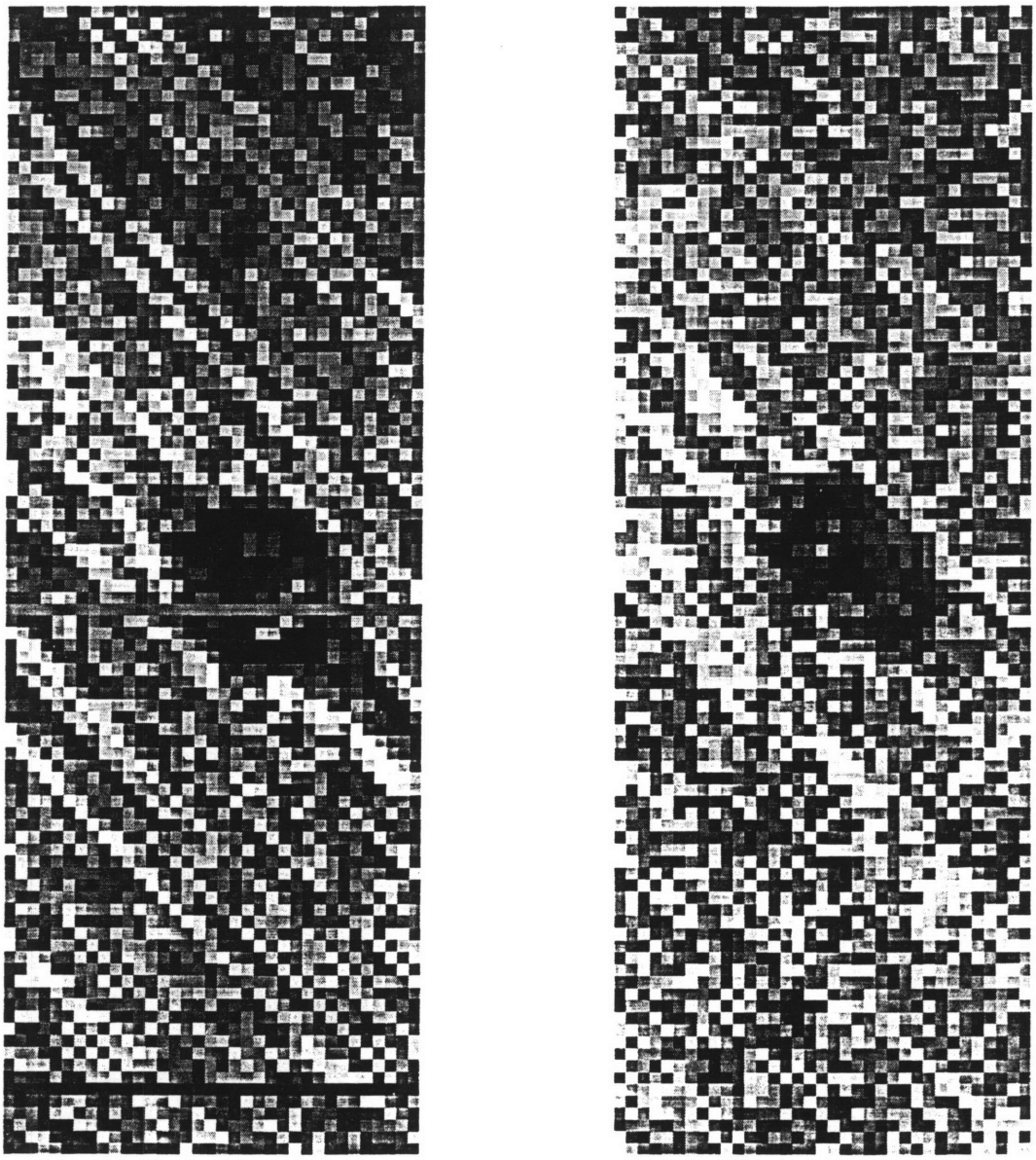

Velocity = 5.7 m/sec (M21-2)

Velocity = 7.5 m/sec (M14-3)

(C-Scans are to scale)

Figure 4.44 Ultrasonic C-Scans of Specimens with Identical Compressive Residual Strength - 244 MPa (Impacter Mass = 1523 g).

Velocity = 5.5 m/sec (M23-3)

Velocity = 6.3 m/sec (J17-2)

(C-Scans are to scale)

Figure 4.45 Ultrasonic C-Scans of Specimens with Identical Compressive Residual Strength - 234 MPa (Impacter Mass = 1523 g).

compressive residual strength test specimens. Figure 4.46 consists of two ultrasonic C-Scans for specimens that failed within 4% of the same failure stress. The central dark region indicating "core" damage appears slightly larger (by approximately 4 mm) for the specimen with the lower failure load.

Correlation of damage determined by two-dimensional ultrasonic C-Scan to compressive residual strength was also inconsistent for impacts with the 8.4 g mass. Figure 4.47 consists of two ultrasonic C-Scans of specimens that failed at the identical stress of 252 MPa with similar indication of core damage size, delamination, and back surface splitting. Figure 4.48 also consists of two ultrasonic C-Scans of specimens that failed at the identical failure stress of 270 MPa. However, the indications of delamination size were significantly different (major axes of 45 versus 22 mm). If only the impacter velocities (57 m/s) and the corresponding compressive residual strengths (270 MPa) were the reported values of interest, there would appear to be no scatter between these two specimens. However, if impacter velocity was unknown and only ultrasonic C-Scan evidence of the damage was available for evaluation, it is unlikely that the same compressive residual strength would be predicted. Another example of two specimens with dissimilar ultrasonic C-Scans that resulted in virtually identical residual stress (260, 261 MPa) is presented in Figure 4.49. Though evidence of back surface splitting was similar, the core sizes varied by approximately 7 mm and the delamination major axes varied by approximately 10 mm. The three ultrasonic C-Scans that indicate maximum delamination damage from specimens impacted at the lowest, MCRS, and highest velocities used in this work showed a significant

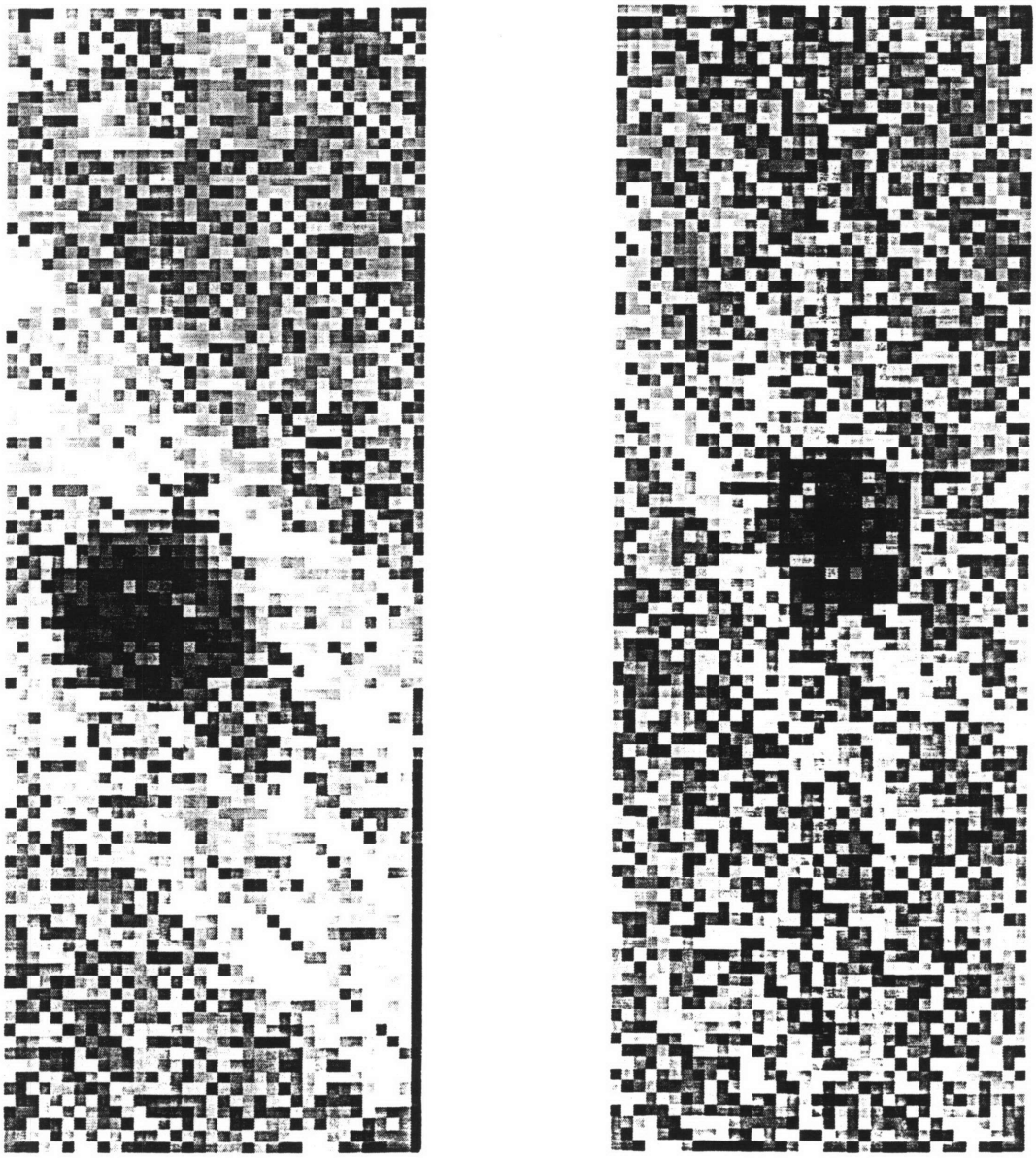

Velocity = 8.6 m/sec (M12-2)
CRS = 291 MPa

Velocity = 12.0 m/sec (M15-2)
CRS = 303 MPa

(C-Scans are to scale)

Figure 4.46 Ultrasonic C-Scans of Specimens with Similar Compressive Residual Strength (Impacter Mass = 578 g).

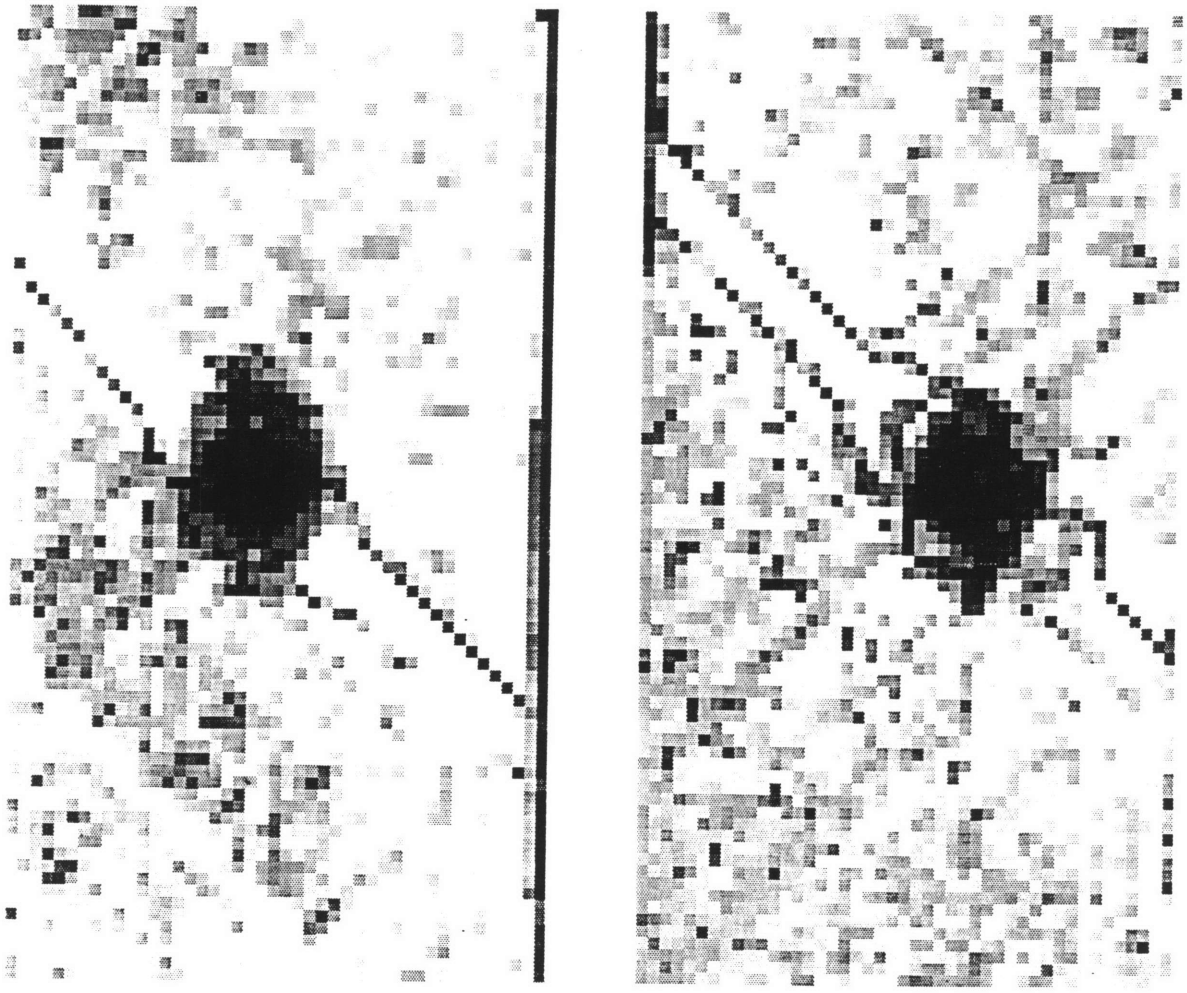

Velocity = 55 m/sec (J16-4)

Velocity = 56 m/sec (J9-4)

(C-Scans are to scale)

Figure 4.47 Ultrasonic C-Scans of Specimens with Identical Compressive Residual Strength - 252 MPa (Impacter Mass = 8.4 g).

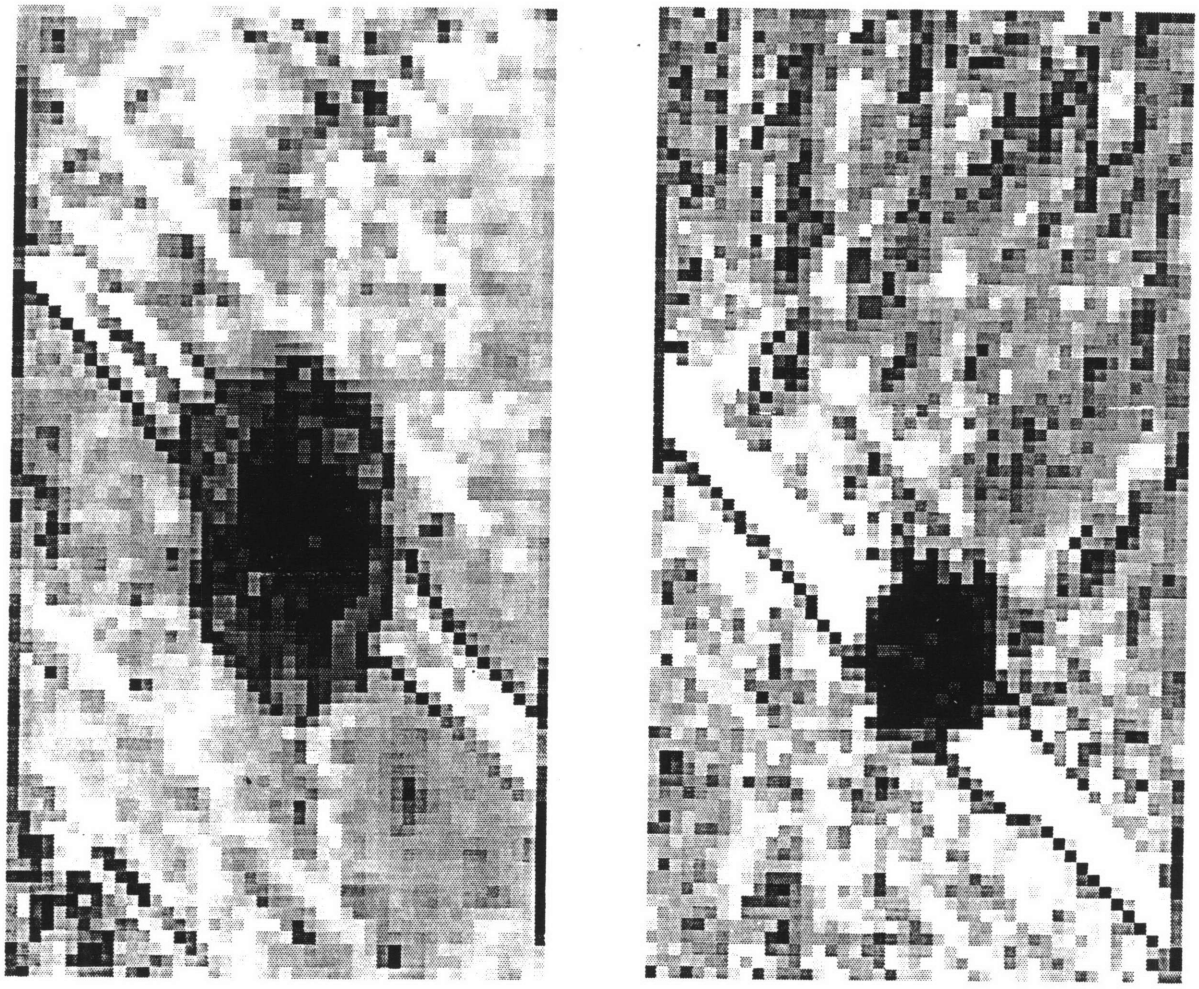

Velocity = 57 m/sec (M31-3)

Velocity = 57 m/sec (J7-2)

(C-Scans are to scale)

Figure 4.48 Ultrasonic C-Scans of Specimens with Identical Compressive Residual Strength - 270 MPa (Impacter Mass = 8.4 g).

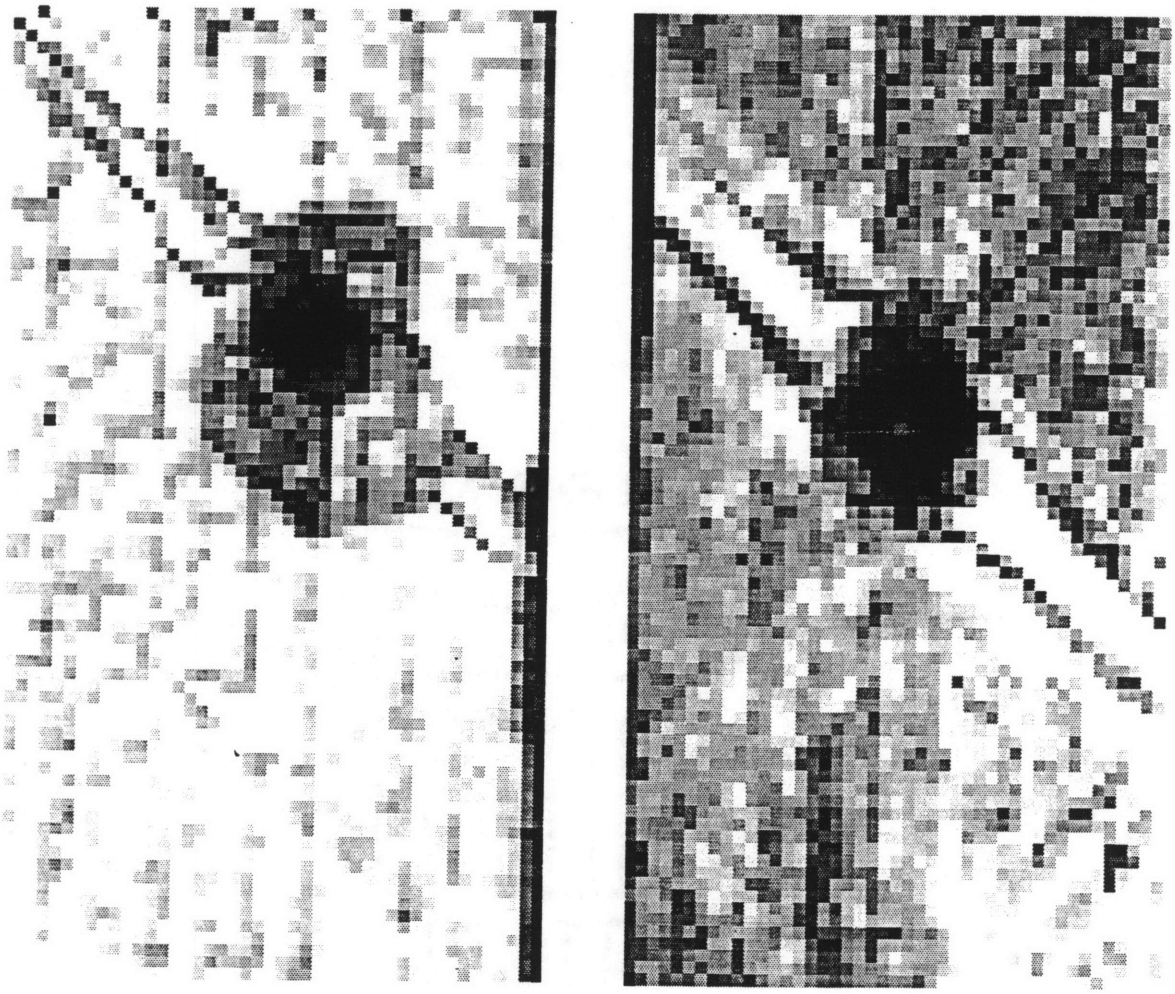

Velocity = 55 m/sec (M12-1)

Velocity = 58 m/sec (M22-2)

(C-Scans are to scale)

Figure 4.49 Ultrasonic C-Scans of Specimens with Identical Compressive Residual Strength - 261 MPa (Impacter Mass = 8.4 g).

difference in the resulting compressive residual strengths from apparently similar damage states as shown in Figure 4.50. The X-ray photographs of these three specimens, in Figure 4.51, indicate that the damage states were actually not as similar as they appeared in the ultrasonic C-Scans. It is apparent that Specimen M30-1, which failed at the lowest compressive residual strength of 197 MPa, had significantly greater core damage (approximately 18 mm in diameter) compared to the other two specimens (approximately 11 mm). The major and minor axes of delamination do not appear significantly different (discounting the spalling of the back surface ply).

The original intent of the time-of-flight ultrasonic C-Scan was for comparison of nondestructive and destructive three-dimensional damage evaluation capability. However, significant differences in compressive residual strength could not always be explained by X-ray photographs or two-dimensional ultrasonic C-Scans which often indicated similar damage states. Thus, additional time-of-flight data from Hercules, Inc. was provided. One specimen from each impacter mass that failed within ±4% of 268 MPa was selected. Specimen T2-3 was impacted with the 1523 g mass at 4.6 m/s which resulted in a compressive residual strength of 278 MPa. Specimen J15-3 was impacted with the 578 g mass at 7.5 m/s which resulted in a compressive residual strength of 257 MPa. And Specimen M31-3 was impacted with the 8.4 g mass at 57 m/s which resulted in a compressive residual strength of 270 MPa.

Ply identification relative to the impact surface is consistent with that defined for coupon layup and impact as illustrated in Figure 3.12. Ply 12 is the first ply to encounter the impacter, and ply 1 is the back surface ply.

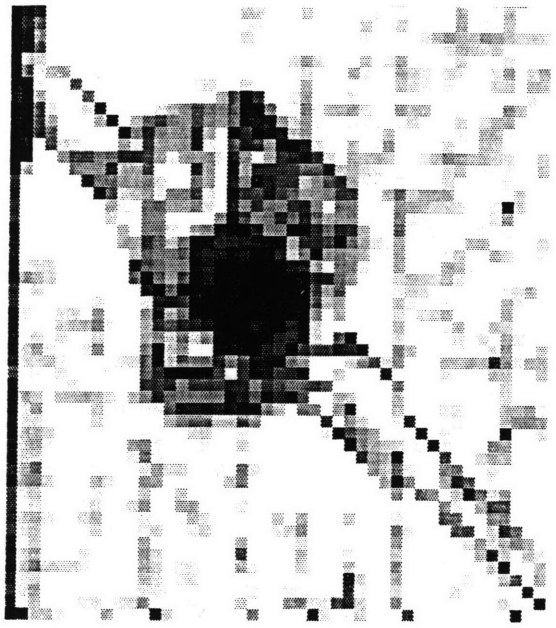

Velocity = 55 m/sec (M12-1)
CRS = 261 MPa

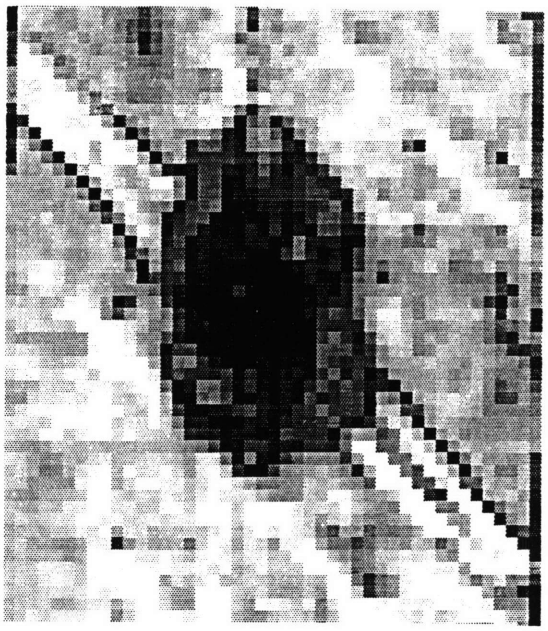

Velocity = 57 m/sec (M31-3)
CRS = 270 MPa

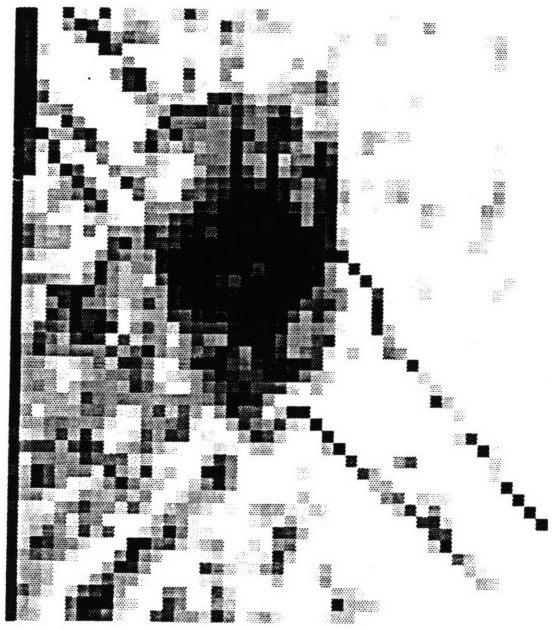

Velocity = 70 m/sec (M30-1)
CRS = 197 MPa

(C-Scans are to scale)

Figure 4.50 Ultrasonic C-Scans of Specimens Indicating Similar Damage at Lowest, MCRS, and Highest Impacter Velocities (Impacter Mass = 8.4 g).

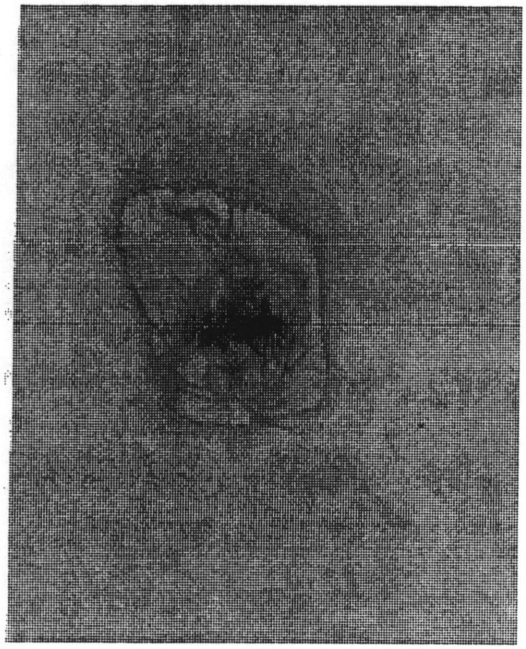

CRS = 261 MPa (M12-1)
Velocity = 55 m/s

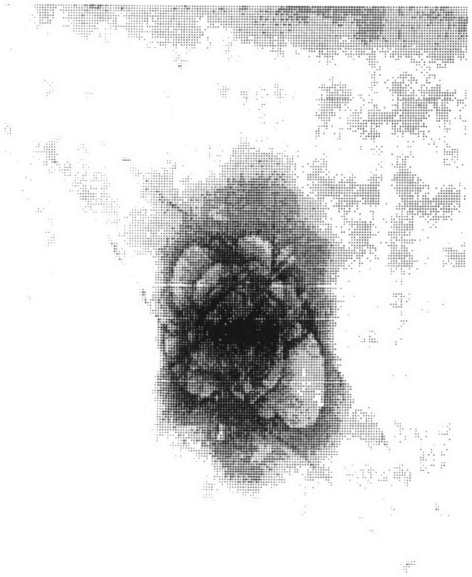

CRS = 270 MPa (M31-3)
Velocity = 57 m/s

CRS = 191 MPa (M30-1)
Velocity = 70 m/s

(X-rays are to scale)

Figure 4.51 X-ray Photographs Corresponding to Ultrasonic C-Scans of Specimens in Figure 4.50 (Impacter Mass = 8.4 g).

Evaluation of the damage state began with the impact surface and worked towards the back surface. Thus, the "shadowing" effect of the previous plies in time-of-flight ultrasonic C-Scanning must be kept in mind. Results of previous work [2, 48, 49] suggest that the orientation of the delamination between one ply and the next (away from the impact surface) should be in the orientation of the ply further away from the impact surface.

The time-of-flight ultrasonic C-Scans for all twelve plies of Specimen T2-3, impacted by the 1523 g mass at 4.6 m/s, are presented in Figures 4.52 through 4.54. There is little evidence of any damage in plies 12 through 10 in Figure 4.52 as each ply appeared to be varying shades of gray. The first indication of damage occurs in ply 9 as shown in Figure 4.52. However, the indication is minimal and only access to the back surface ply damage data provides the location to watch for the few white pixels that appear (vertically centered, horizontally to the right). A few additional light pixels appear in the impact area of ply 8 in Figure 4.53. However, ply 7, shown in Figure 4.53, exhibits minimal evidence of damage with the shadowing of the previous light pixels and the addition of only a few more. Ply 6 exhibits little evidence of damage but delamination between plies 6 and 7 is not expected as there is no change in angle of orientation [2–4, 15, 34, 35, 40, 48]. Locations of light pixels indicating damage in previous plies are now dark in ply 5 due to shadowing. The shadowing of damage from previous plies is more prominent in ply 4 as evidenced in Figure 4.54. There is apparently no damage in ply 4 that is not shadowed from the previous plies. The impact area is even darker in ply 3 than ply 4. The trend witnessed from ply 4 to ply 3 is repeated from ply 3 to ply 2. What was previously damaged became darker where no new damage occurred. The time-of-flight

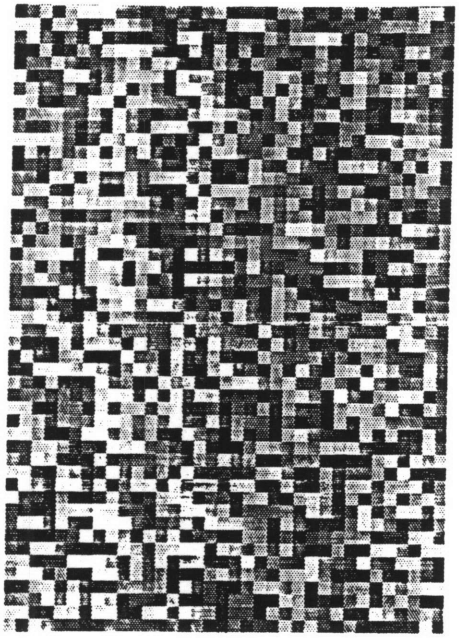

Ply 12 (+45°)

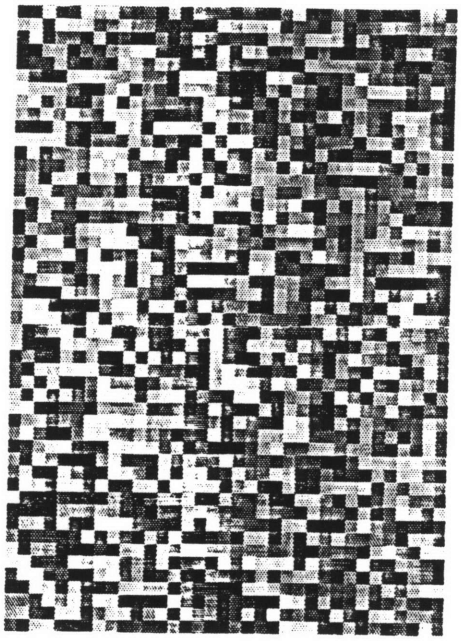

Ply 11 (-45°)

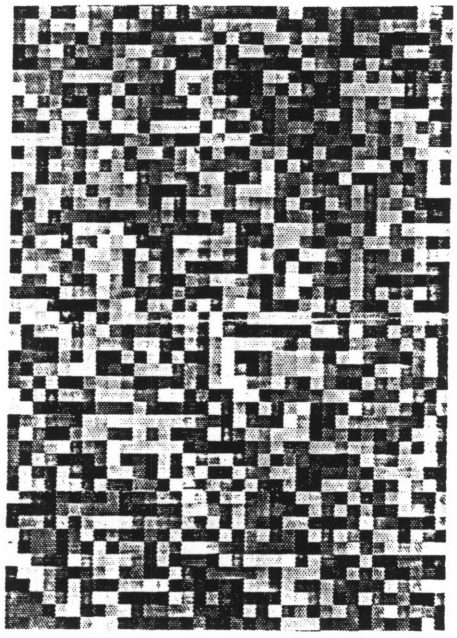

Ply 10 (0°)

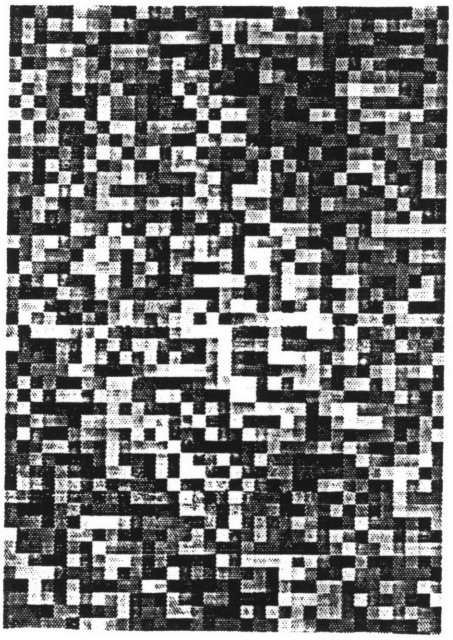

Ply 9 (+45°)

(C-Scans are to scale)

Figure 4.52 Time-of-Flight Ultrasonic C-Scans of Plies 12 through 9 of Specimen T2-3 — CRS = 278 MPa (Impacter Mass = 1523 g, Velocity = 4.6 m/s).

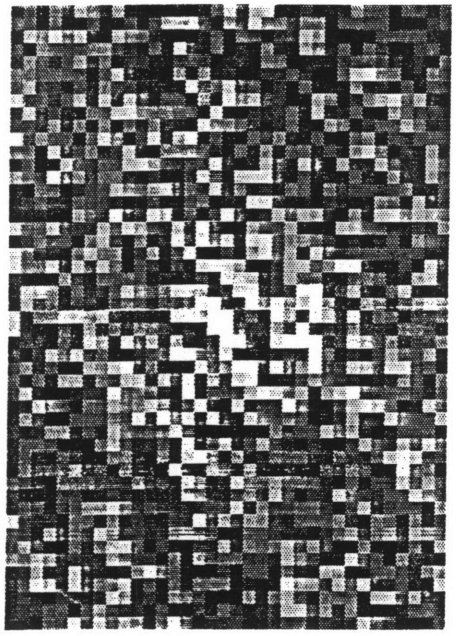

Ply 8 (-45°)

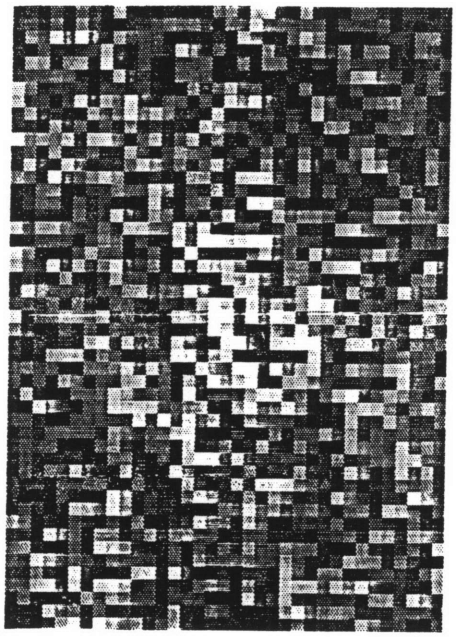

Ply 7 (0°)

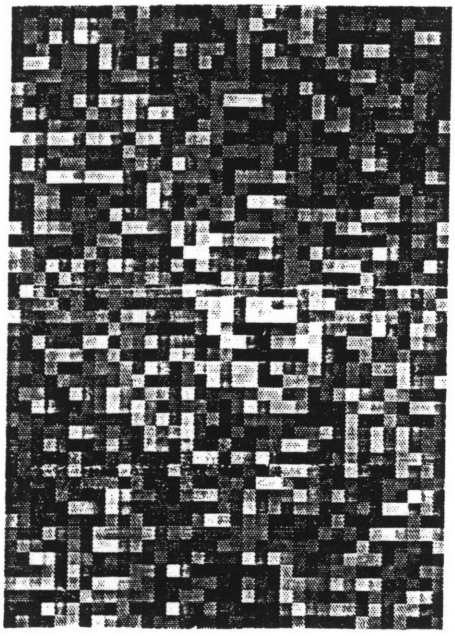

Ply 6 (0°)

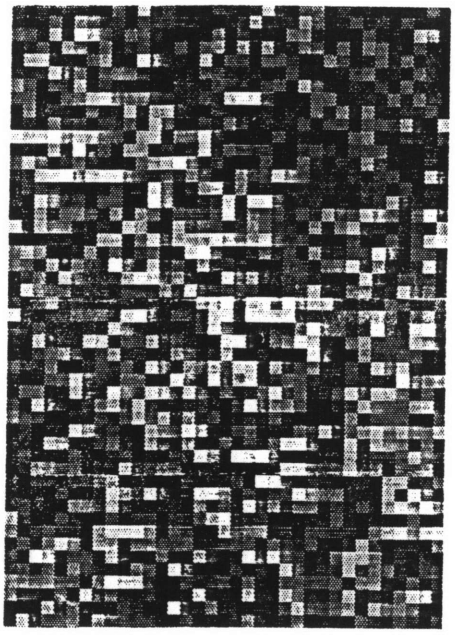

Ply 5 (-45°)

(C-Scans are to scale)

Figure 4.53 Time-of-Flight Ultrasonic C-Scans of Plies 8 through 5 of Specimen T2-3 — CRS = 278 MPa (Impacter Mass = 1523 g, Velocity = 4.6 m/s).

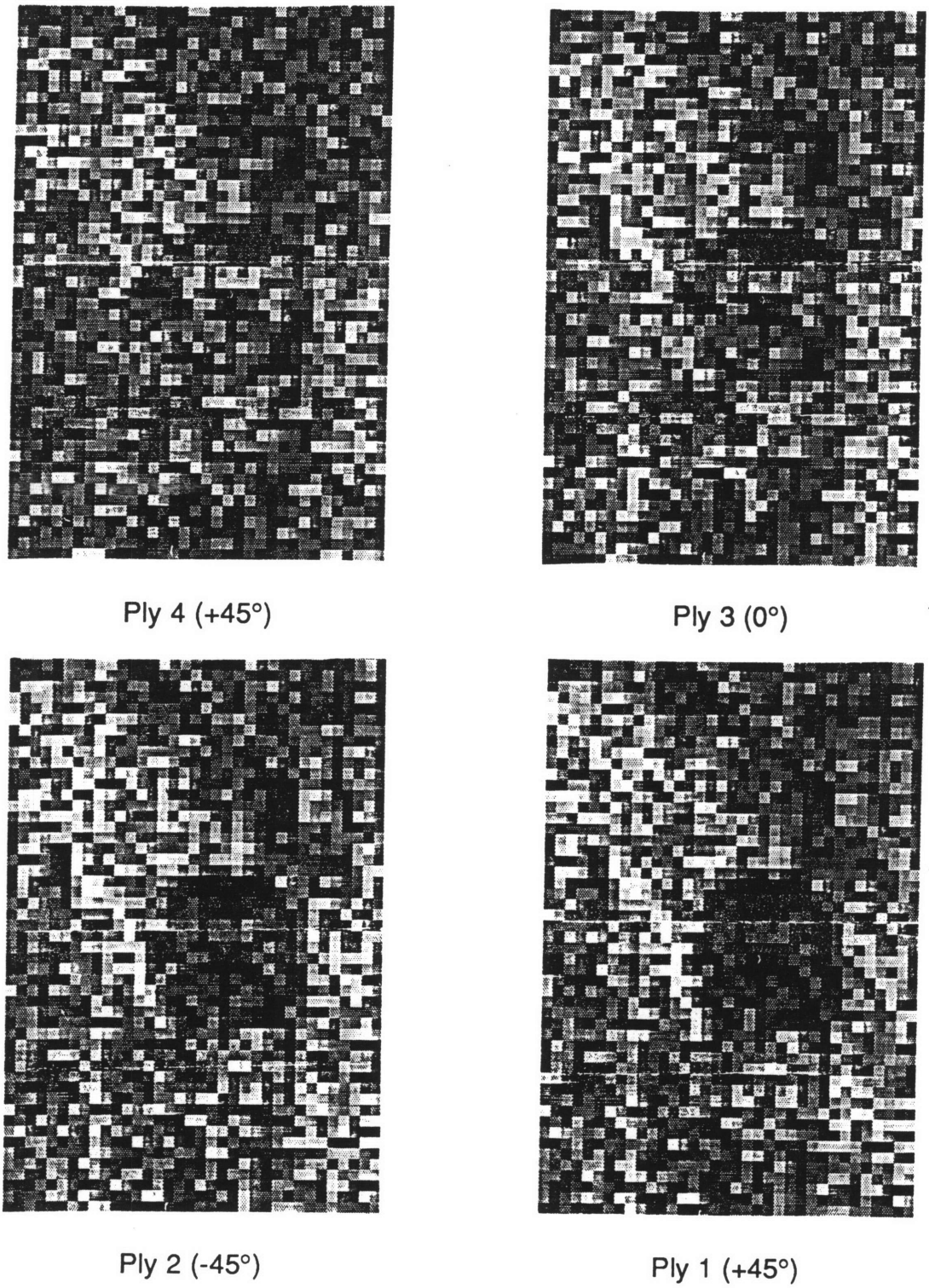

Figure 4.54 Time-of-Flight Ultrasonic C-Scans of Plies 4 through 1 of Specimen T2-3 — CRS = 278 MPa (Impacter Mass = 1523 g, Velocity = 4.6 m/s).

ultrasonic C-Scan of the back surface ply did not provide much additional data to the damage definition provided by the previous plies. In this case, the time-of-flight ultrasonic C-Scans provide very little useful data about the ply-by-ply damage state.

The time-of-flight ultrasonic C-Scans for all twelve plies of Specimen J15-3, impacted by the 578 g mass at 7.5 m/s, are presented in Figures 4.55 through 4.57. There are some obvious indications of damage in ply 12 near the impact location as shown in Figure 4.55. The pixels appear dark around the impact location from the possible loss of the backwall signal reflection due to the extent of core damage in this specimen (explained in Chapter 3). Damage near the impact location is thus indicated by the darker pixels, again, in ply 11. The evidence of damage around the impact location does not change much from ply 11 to ply 10. Groups of light pixels appear in ply 9 providing the first information on possible delamination between plies 9 and 10. No conclusions about delamination orientation can be made. The time-of-flight ultrasonic C-Scan of ply 8 in Figure 4.56 provides obvious evidence of damage with orientation in the -45° direction. The damage area in ply 7 appears circular in nature and is not as obvious as damage in the previous ply. Ply 6 exhibits little evidence of damage as shown in Figure 4.56. Again, delamination between plies 6 and 7 is not expected as there is no change of angle orientation. Light pixels indicating damage in previous plies are shadowed in ply 5. The shadowing of damage from previous plies is more prominent in ply 4 as evidenced in Figure 4.57. There is apparently no damage in ply 4 that is not shadowed by the previous plies. While the impact area in ply 3 is darker, a few light pixels appear indicating potential damage in the 45° direction. Ply 3 is of 0° orientation,

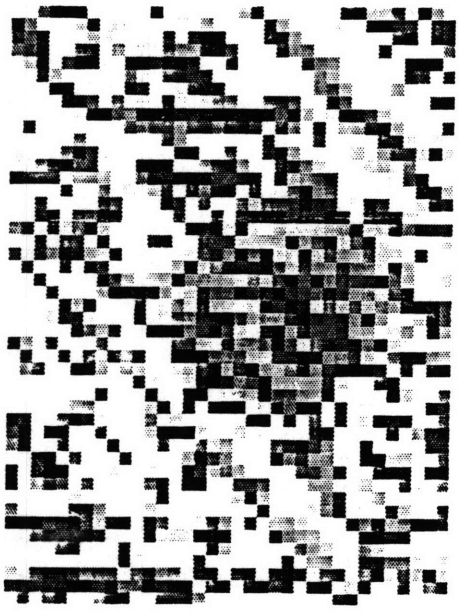

Ply 12 (+45°)

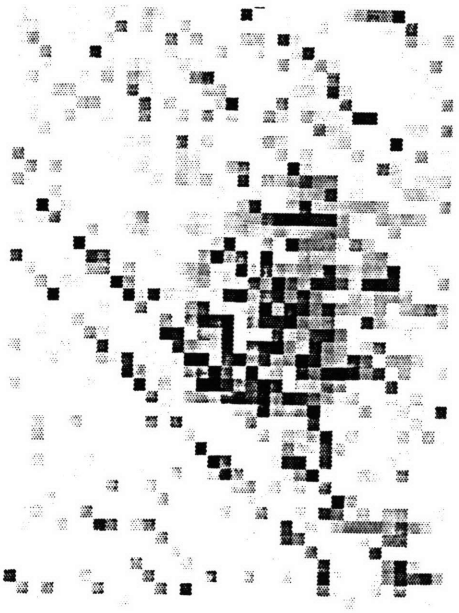

Ply 11 (-45°)

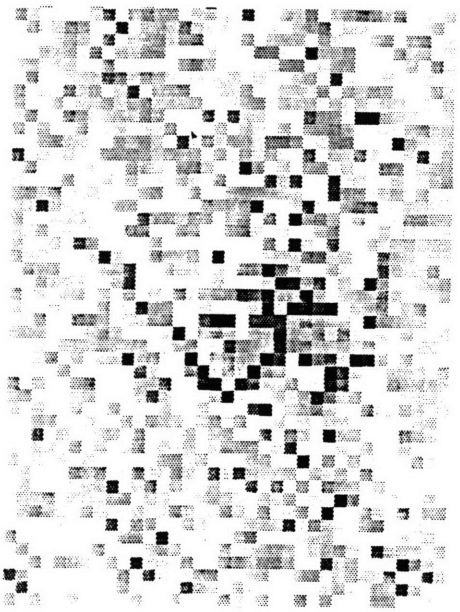

Ply 10 (0°)

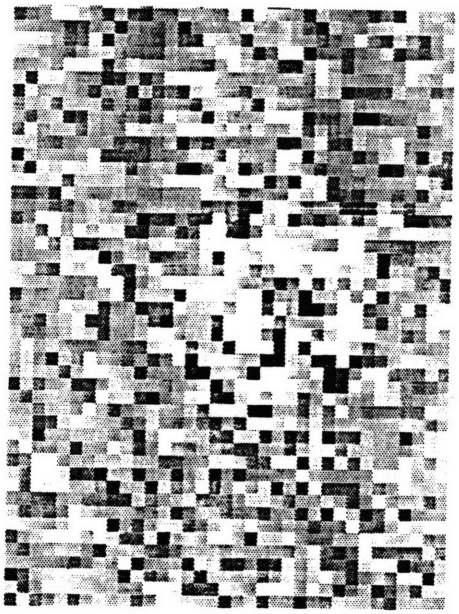

Ply 9 (+45°)

(C-Scans are to scale)

Figure 4.55 Time-of-Flight Ultrasonic C-Scans of Plies 12 through 9 of Specimen J15-3 — CRS = 257 MPa (Impacter Mass = 578 g, Velocity = 7.5 m/s).

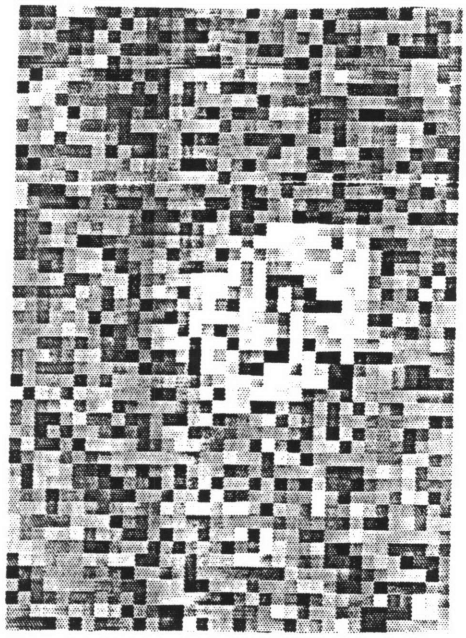

Ply 8 (-45°)

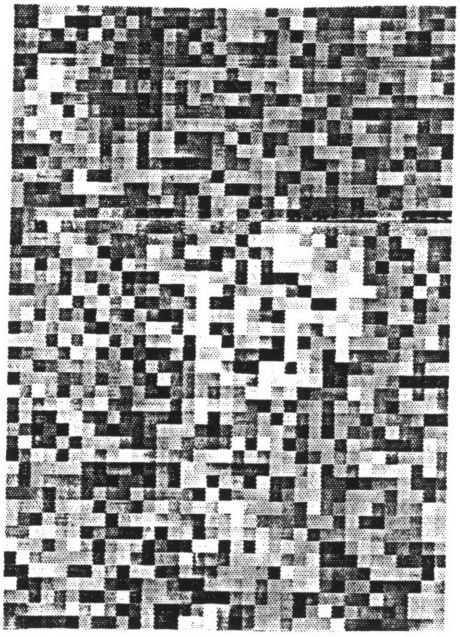

Ply 7 (0°)

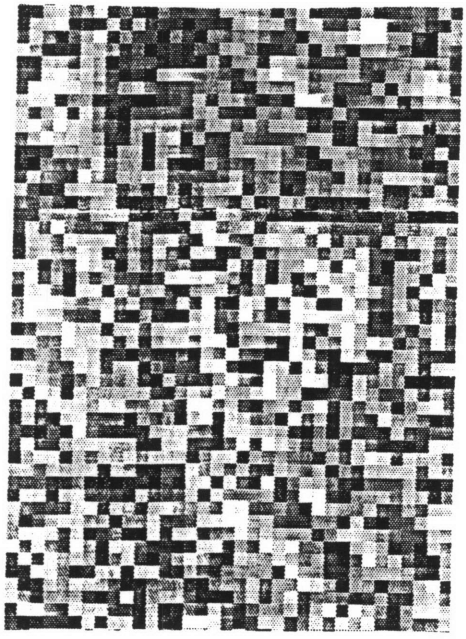

Ply 6 (0°)

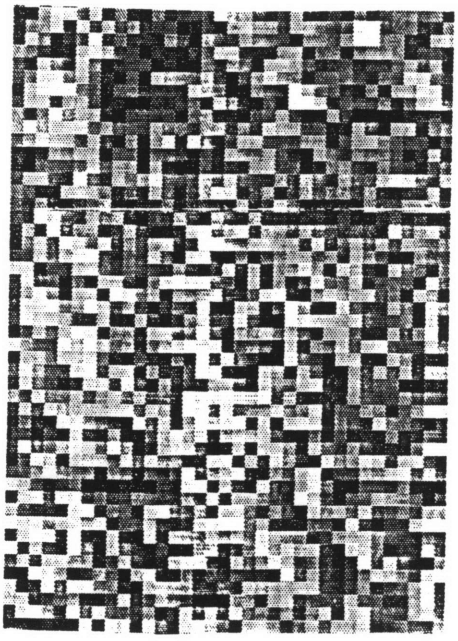

Ply 5 (-45°)

(C-Scans are to scale)

Figure 4.56 Time-of-Flight Ultrasonic C-Scans of Plies 8 through 5 of Specimen J15-3 — CRS = 257 MPa (Impacter Mass = 578 g, Velocity = 7.5 m/s).

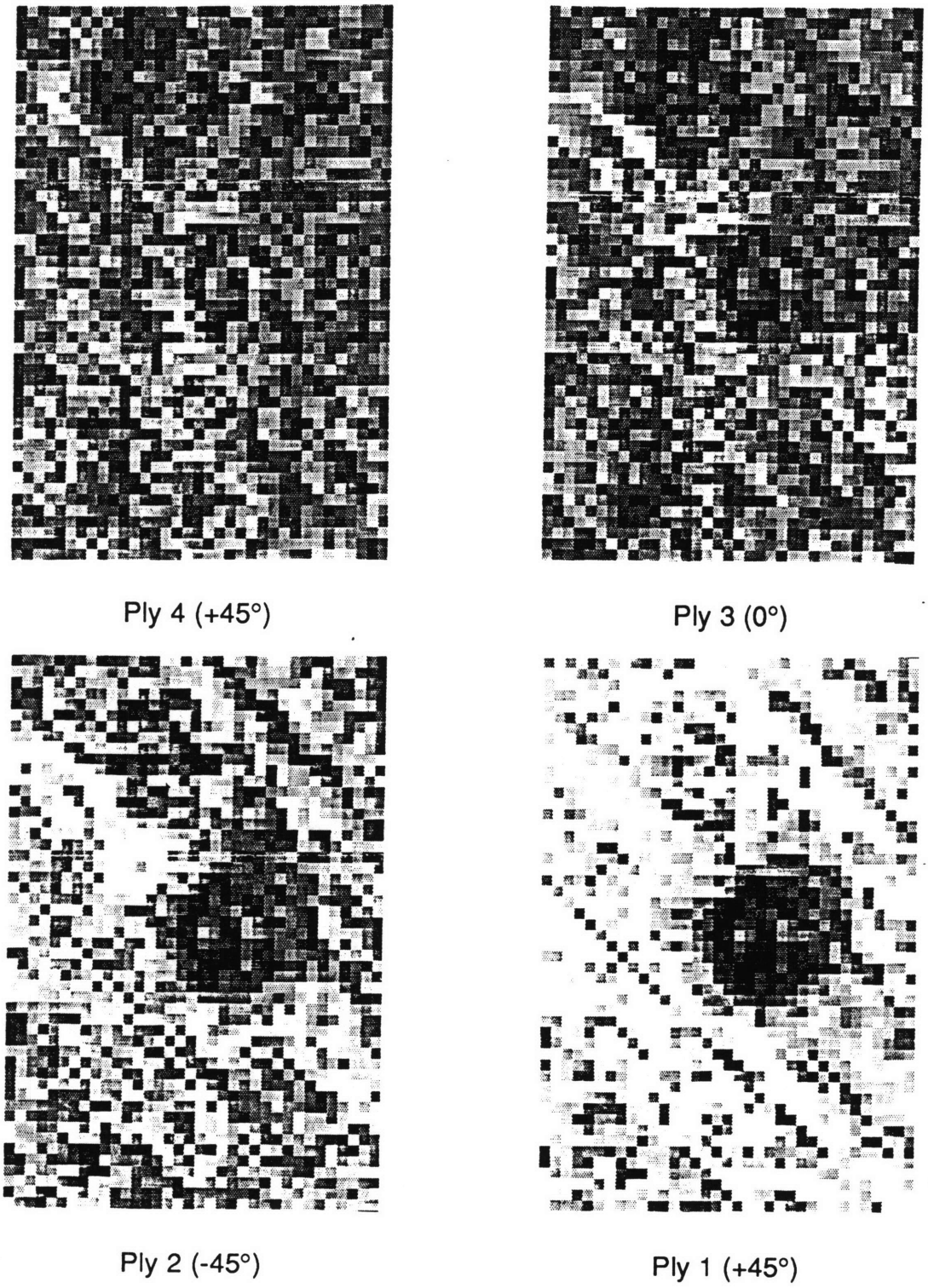

Figure 4.57 Time-of-Flight Ultrasonic C-Scans of Plies 4 through 1 of Specimen J15-3 — CRS = 257 MPa (Impacter Mass = 578 g, Velocity = 7.5 m/s).

followed by ply 2 of -45° orientation. Thus, an indication of damage oriented in a +45° direction in the time-of-flight ultrasonic C-Scan of ply 3 appears to provide a preview of the delamination damage that is known to exist between plies 1 and 2. The trend witnessed from ply 4 to ply 3 is repeated from ply 3 to ply 2. What was previously damaged became darker and more light pixels appeared in the region of delamination between plies 1 and 2. The time-of-flight ultrasonic C-Scan of the back surface ply provided a clearer outline of the ply split due to spalling of fibers. Though more detail appeared in the time-of-flight ultrasonic C-Scans for this specimen, the information provided still appears to contain too much integrated data from surrounding plies to be useful in defining the actual ply-by-ply damage state.

The time-of-flight ultrasonic C-Scans for all twelve plies of Specimen M31-3, impacted by the 8.4 g mass at 57 m/s, are presented in Figures 4.58 through 4.60. There are some obvious indications of damage in ply 12 near the impact location as shown in Figure 4.58. The pixels appeared dark around the impact location from the possible loss of the backwall signal reflection due to the extent of core damage in this specimen (explained in Chapter 3). There are also some light pixels around the impact location in ply 12. However, due to the light nature of the rest of the coupon, it is doubtful that these pixels indicate damage in this ply. Additional light pixels are around the impact location in ply 11, giving the first indication of minor delamination damage in the interface between plies 11 and 12. The change in damage indications from the time-of-flight ultrasonic C-Scans of ply 11 to ply 10 is quite significant. The whole coupon appears gray with the center of impact dark. The minor delaminations around the impact

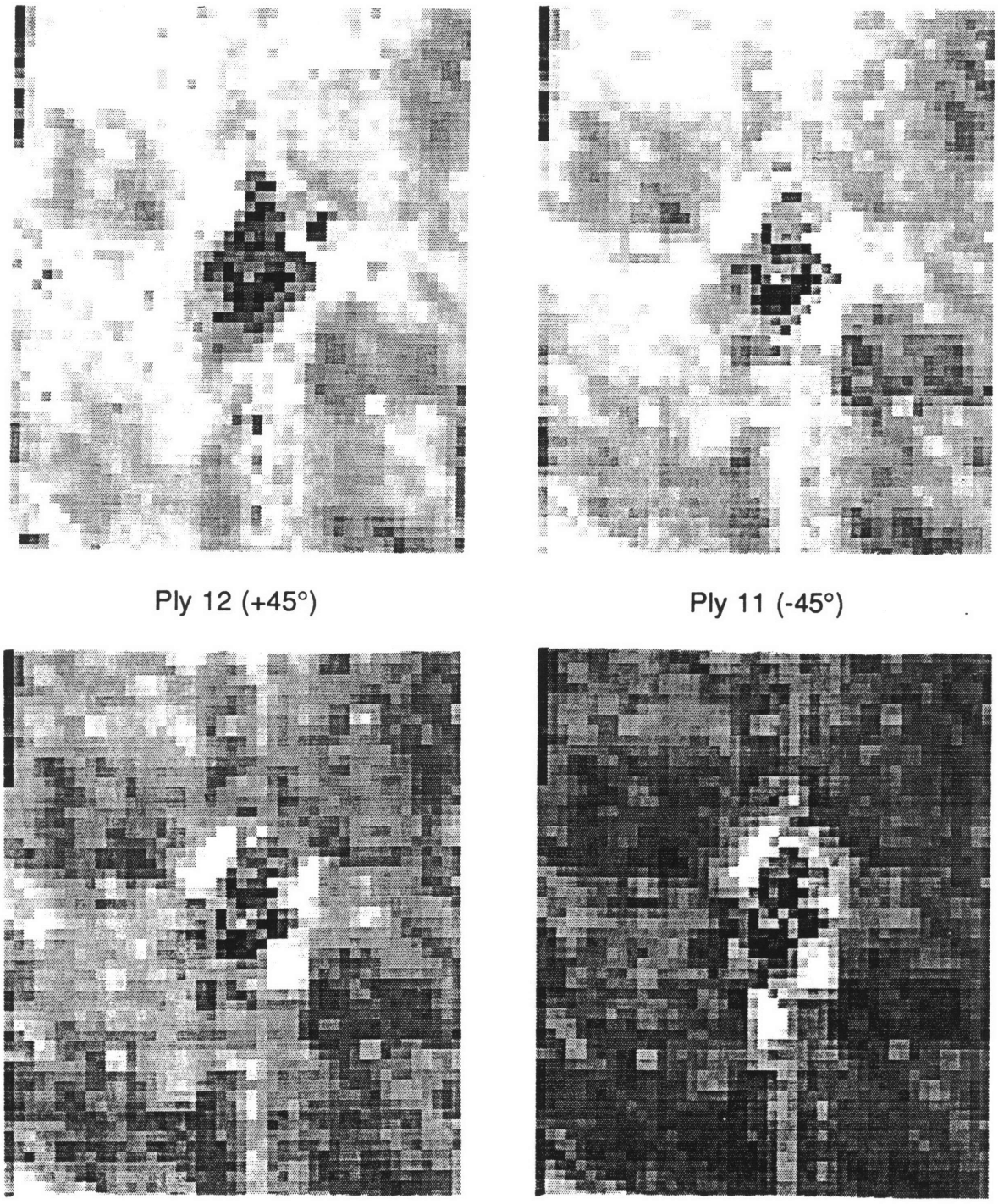

Figure 4.58 Time-of-Flight Ultrasonic C-Scans of Plies 12 through 9 of Specimen M31-3 — CRS = 270 MPa (Impacter Mass = 8.4 g, Velocity = 57 m/s).

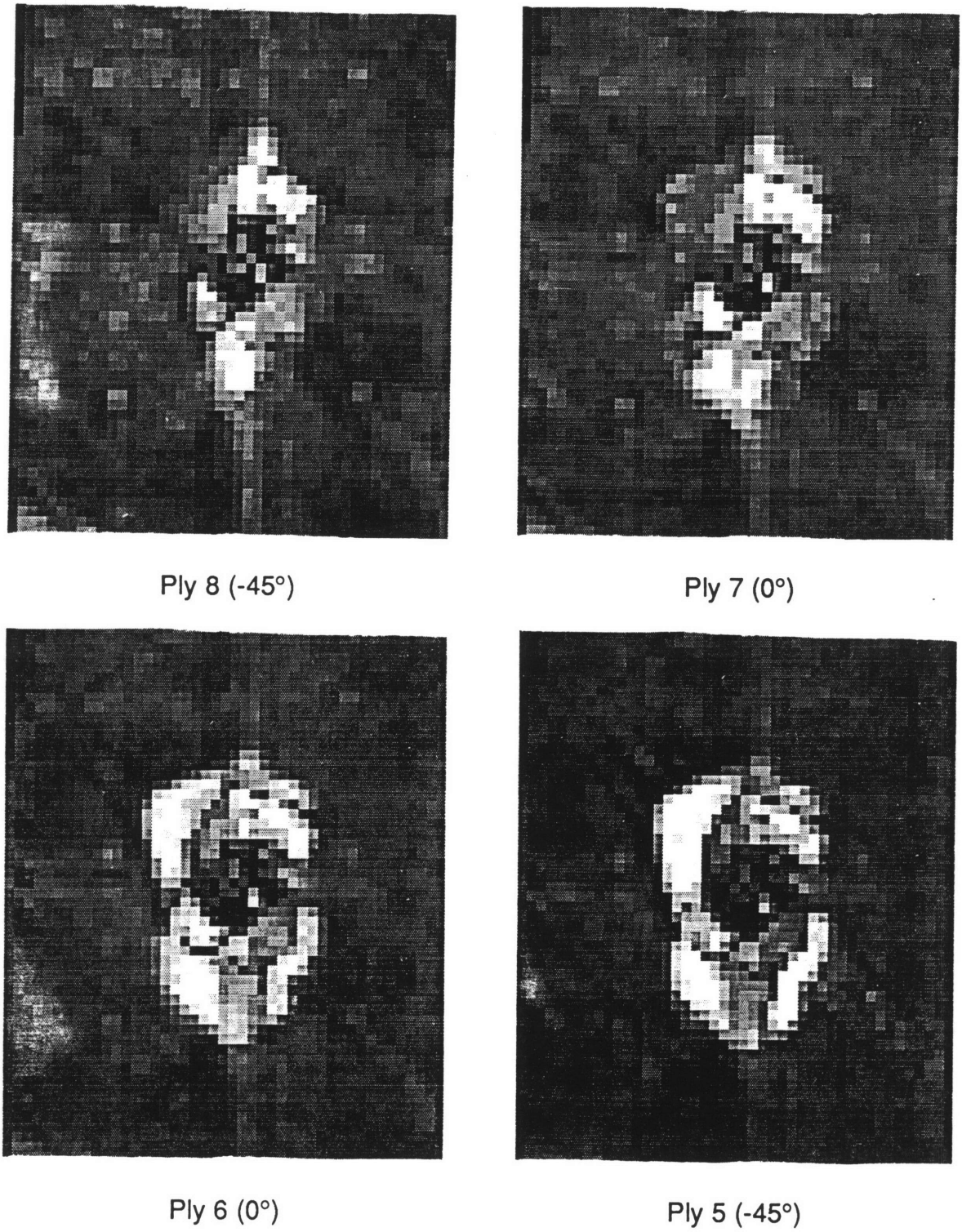

Figure 4.59 Time-of-Flight Ultrasonic C-Scans of Plies 8 through 5 of Specimen M31-3 — CRS = 270 MPa (Impacter Mass = 8.4 g, Velocity = 57 m/s).

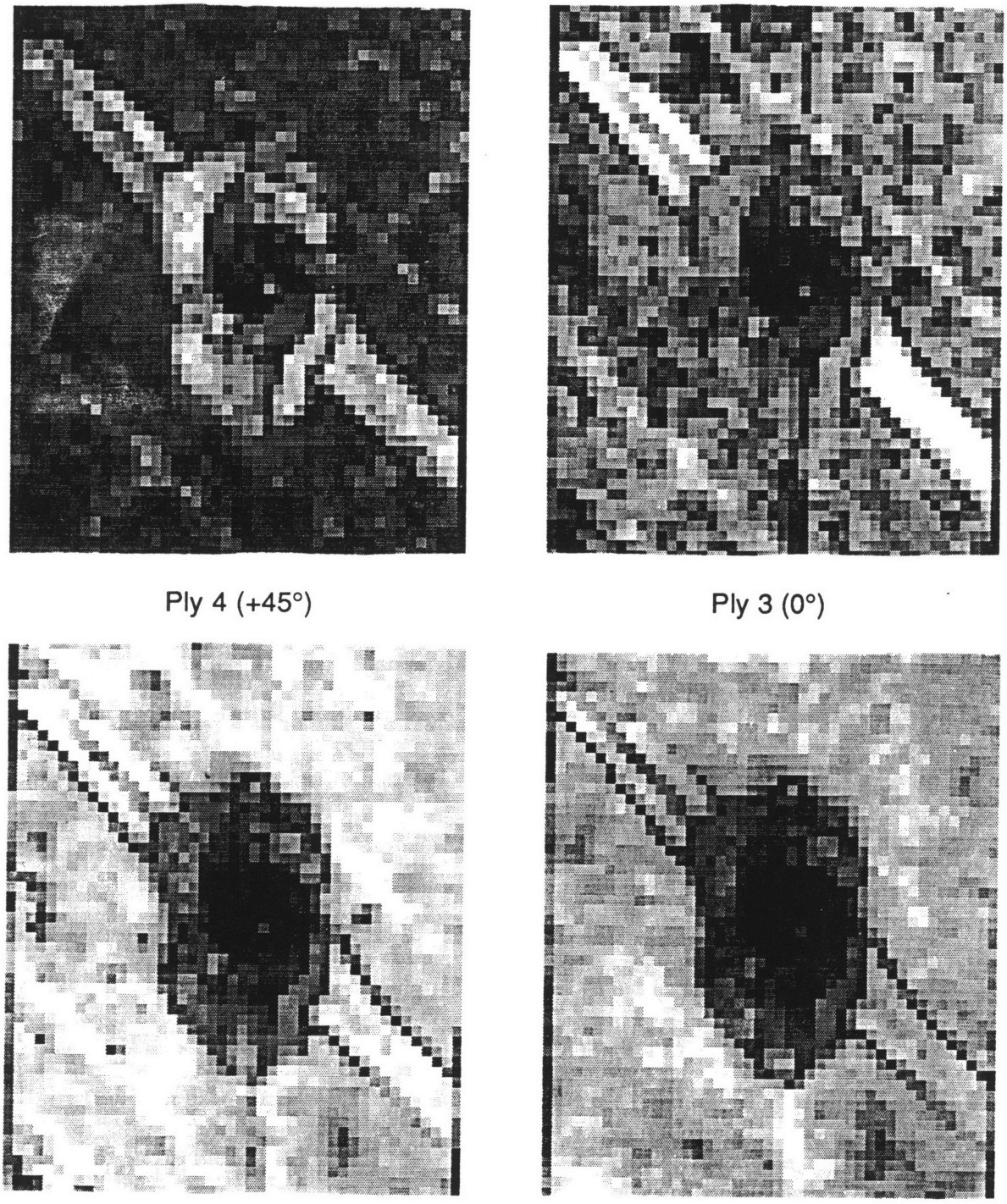

Figure 4.60 Time-of-Flight Ultrasonic C-Scans of Plies 4 through 1 of Specimen M31-3 — CRS = 270 MPa (Impacter Mass = 8.4 g, Velocity = 57 m/s).

location are definitely light enough to indicate damage in this ply. The orientation of the possible delamination is apparently not in the 0° direction of ply 10. Ply 9 has darker pixels in place of the previous ply's light pixels providing the shadow effect discussed in Chapter 3. There is additional delamination data with new light pixels. Again, delamination orientation is not obvious. Additional shadowing and extended delamination evidence is evident in Figure 4.59 for ply 8 with a slight bias in orientation to the -45° direction. There is clear evidence that damage dimensions increased between ply 8 and ply 7 (approximately 4 mm in both the major and minor axes of damage). Ply 6 has a few light pixels that, from the explanation provided in Chapter 3, should indicate potential delamination between plies 6 and 7. This does not appear likely as there is no change in angle orientation between these two plies. Additional damage evidence appears in ply 5. However, conclusions about orientation cannot be made. As depth increases, it becomes more difficult to keep track of the pixels that are "shadowed" from previous plies and thus appear dark but do not eliminate the possibility of damage in the ply of interest. A very prominent indication of potential damage occurs across the coupon width in the 45° direction of ply 4 shown in Figure 4.60. The 45° direction damage observed in ply 4 also appears in ply 3. The pixels in the time-of-flight ultrasonic C-Scan of ply 3 are lighter than those in ply 4 in this damage area, thus, indicating damage should be in ply 3. However, this damage area corresponds to the major back surface splitting of ply 1 and it is doubtful if delamination also existed in this orientation between plies 3 and 4. What was previously damaged became darker in ply 2 and there were still some light pixels in the area of back surface splitting. The time-of-flight ultrasonic C-Scan of ply 1 gives a clear indication of the ply split location.

Though the time-of-flight ultrasonic C-Scans provide more information about damage in a single ply than the two-dimensional ultrasonic C-Scans, there is still some evidence of integrated information. Damage due to the penetration of the impacter (damage in every ply) results in loss of the backwall signal in the impact region and dark pixels in every ply. Damage in previous plies could shadow the ply of interest. Thus, information on the damage state of that ply can be inconclusive. Time-of-flight ultrasonic scanning also appears to provide a "preview" capability. For those specimens with significant back surface damage (i.e., splitting and delamination between plies 1 and 2), evidence of this damage could be seen as many as four plies nearer to the impact surface.

4.4 Destructive Damage Evaluation

The two destructive damage evaluation techniques employed in this work were cross-sectioning and the deply technique. Cross-sectioning of impact coupons gave through-the-thickness damage information that was converted to schematics of damage on a ply-by-ply basis for comparison to the time-of-flight ultrasonic C-Scans. The deply technique provided damage definition in each ply and its interface directly. (Comparison of destructive and nondestructive damage evaluation results is discussed in Chapter 5.)

4.4.1 Cross-Sectioning

The cross-sectioning method of damage evaluation provides information on delamination and matrix cracking through-the-thickness at a selected location. The first cut was the visually identified center of

impact. The next cut(s) were intended to result in 7 mm wide strips. Unfortunately, for the specimens impacted by the 1523 g and 578 g masses, the scale used was English. Thus, the resulting strip width was 7/16 of an inch (9.5 mm). This problem was corrected for cross-sectioning of the specimens impacted with the 8.4 g mass.

Through-the-thickness damage measurements were transferred to schematics of damage on a ply-by-ply basis. Ply identification relative to the impact surface is consistent with that defined for coupon layup, impact, and time-of-flight ultrasonic C-Scan as illustrated in Figure 3.12. Ply 12 is the first ply to encounter the impacter, and ply 1 is the back surface ply. Evaluation of the damage state began with the impact surface and worked towards the back surface.

Schematics of ply-by-ply damage in a typical coupon impacted with the 1523 g mass at the MCRS-velocity (6.3 m/s) are presented in Figures 4.61 through 4.66. Five cuts were made on this coupon resulting in four strips of approximately 9.5 mm width (T1, T2, B1, and B2). Eight surfaces were examined under a microscope. If less than eight indications are present on the schematics relative to the distance from the impact centerline axis, then no damage was observed on those surfaces. Both ply 12 (45°) and ply 11 (-45°) experienced extensive matrix cracking, as shown in Figure 4.61, as the plies split to make way for tup penetration. The schematic of ply 11/interface 11 also provides evidence of delamination approximately 15 mm in width at the impact location between the two plies. Results from previous work [2, 48, 49] suggest that the orientation of the delamination between plies 11 and 12 should be the -45° orientation of ply 11. However, in Figure 4.61, the orientation of delamination between the two plies is not

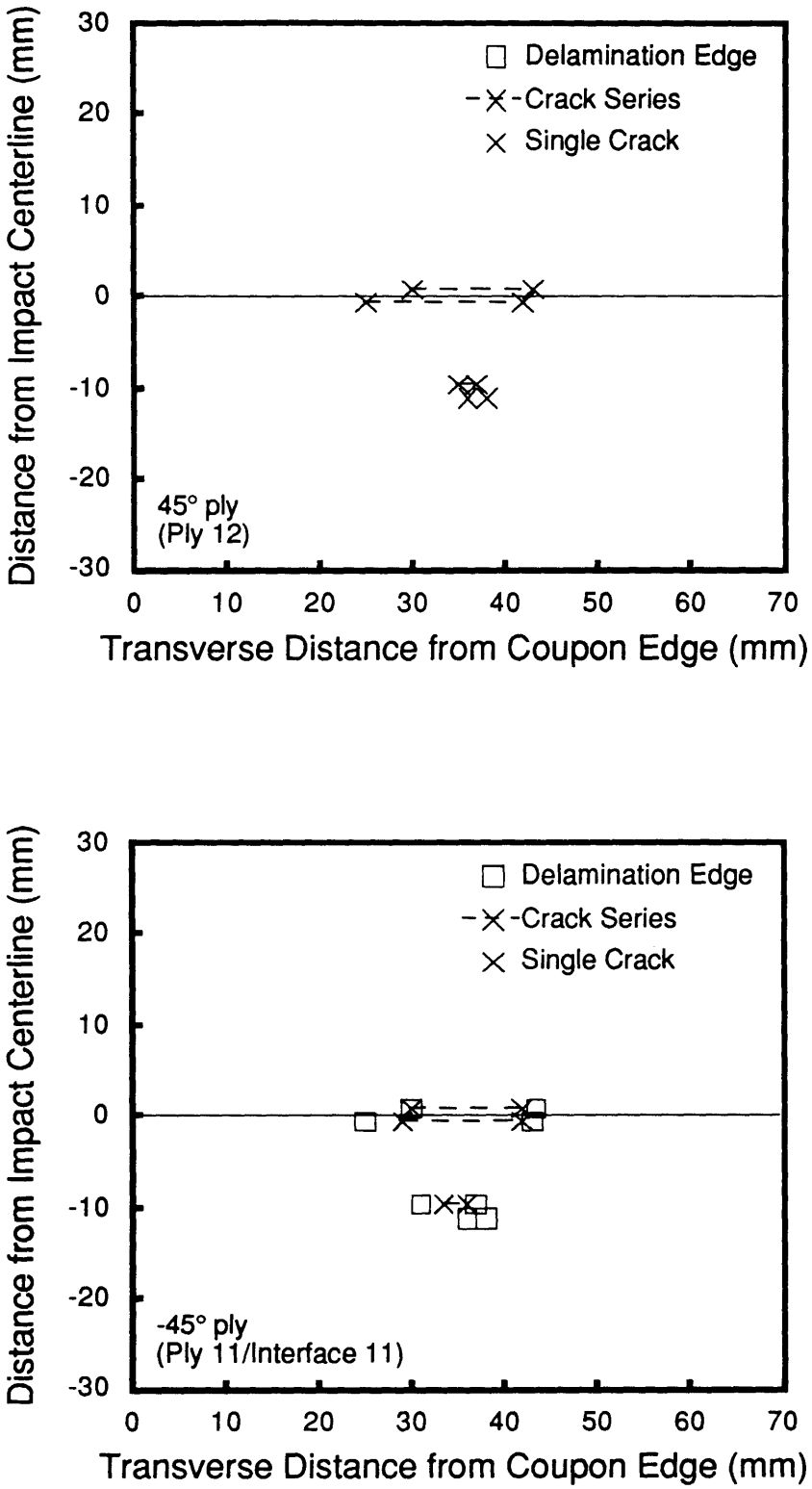

Figure 4.61 Cross-Section Schematics of Specimen T5-2 — Ply 12 and Ply 11 (Impacter Mass = 1523 g, Velocity = 6.3 m/s).

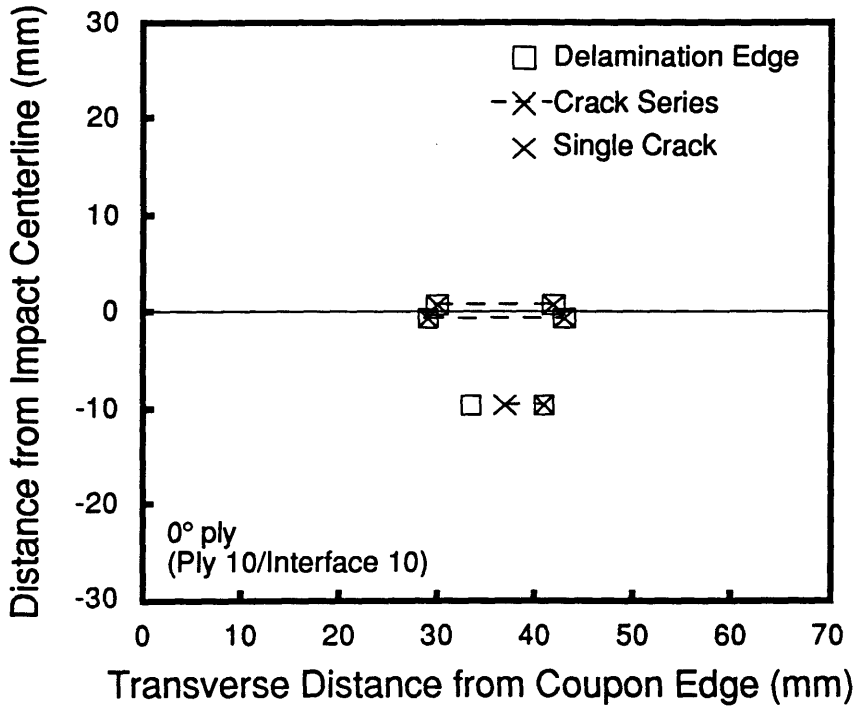

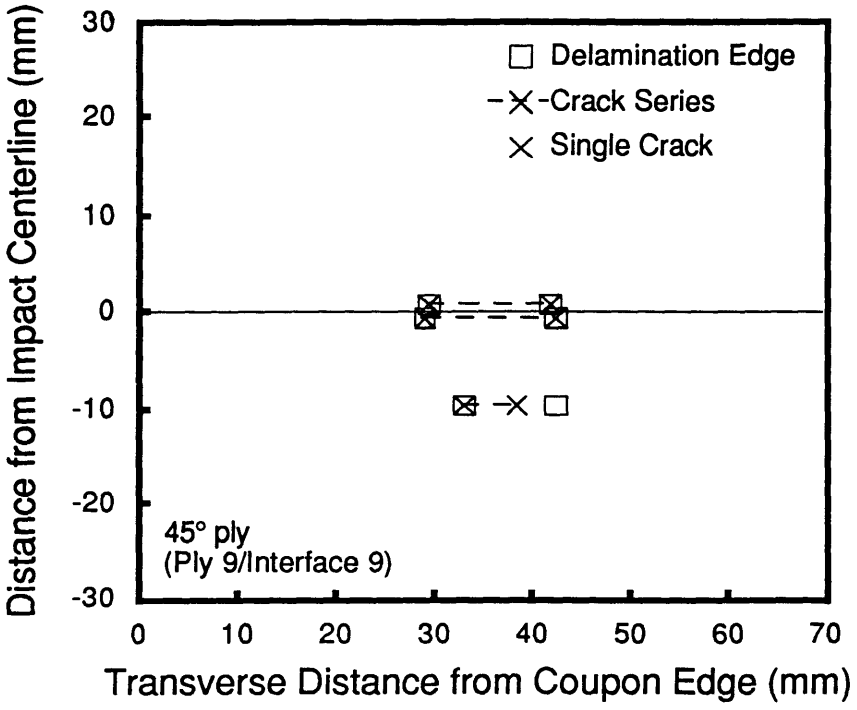

Figure 4.62 Cross-Section Schematics of Specimen T5-2 — Ply 10 and Ply 9 (Impacter Mass = 1523 g, Velocity = 6.3 m/s).

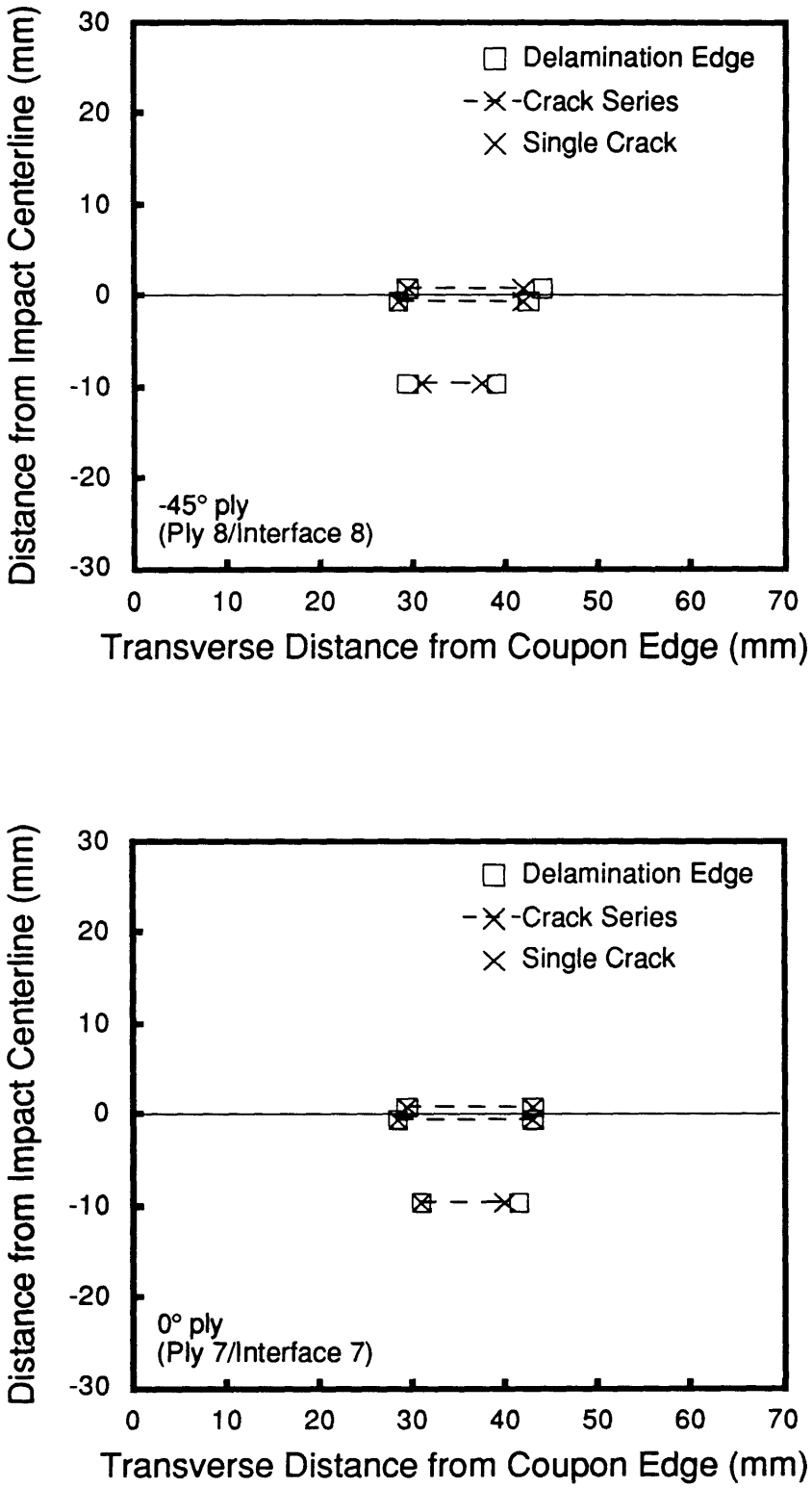

Figure 4.63 Cross-Section Schematics of Specimen T5-2 — Ply 8 and Ply 7 (Impacter Mass = 1523 g, Velocity = 6.3 m/s).

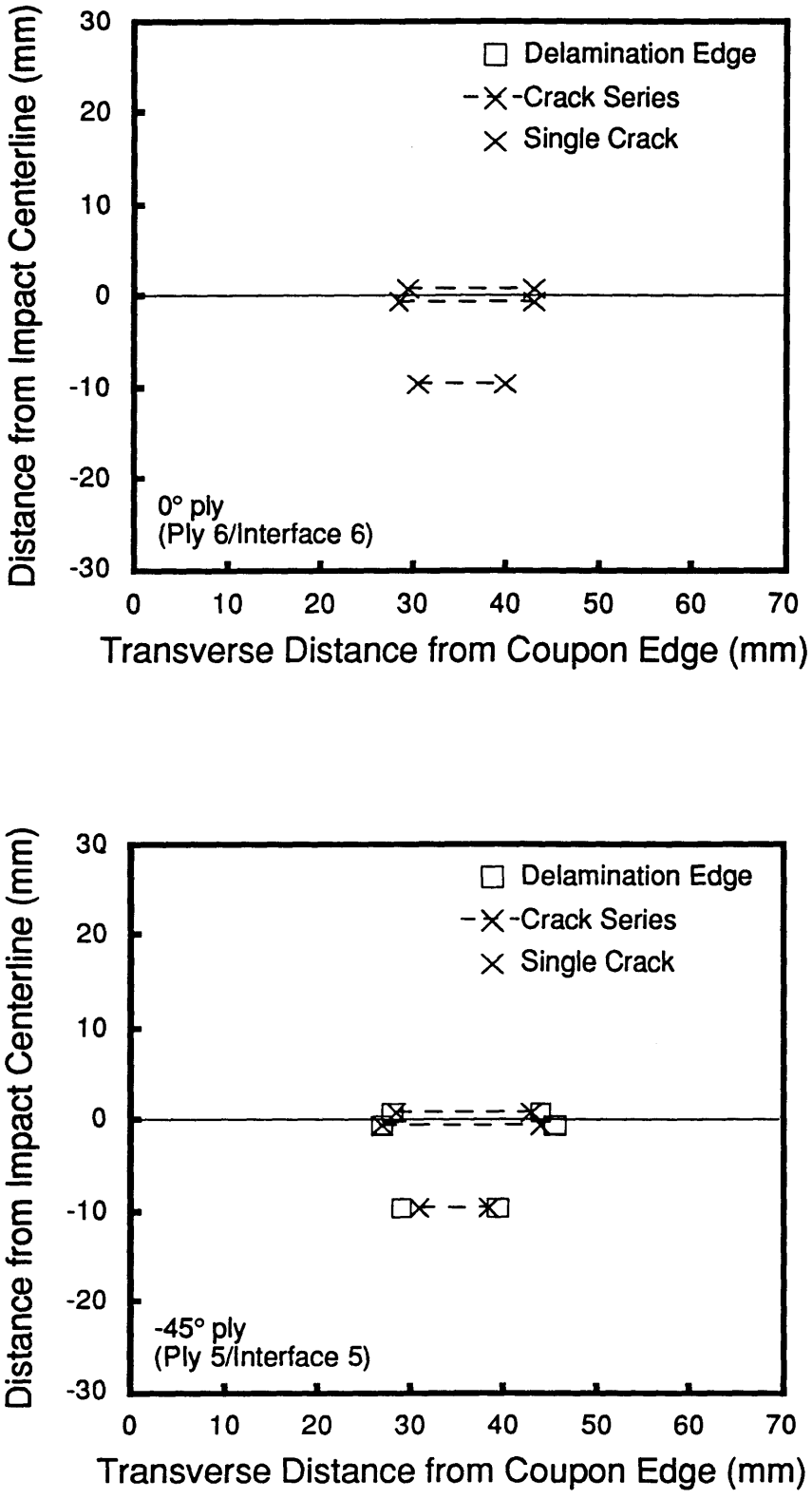

Figure 4.64 Cross-Section Schematics of Specimen T5-2 — Ply 6 and Ply 5 (Impacter Mass = 1523 g, Velocity = 6.3 m/s).

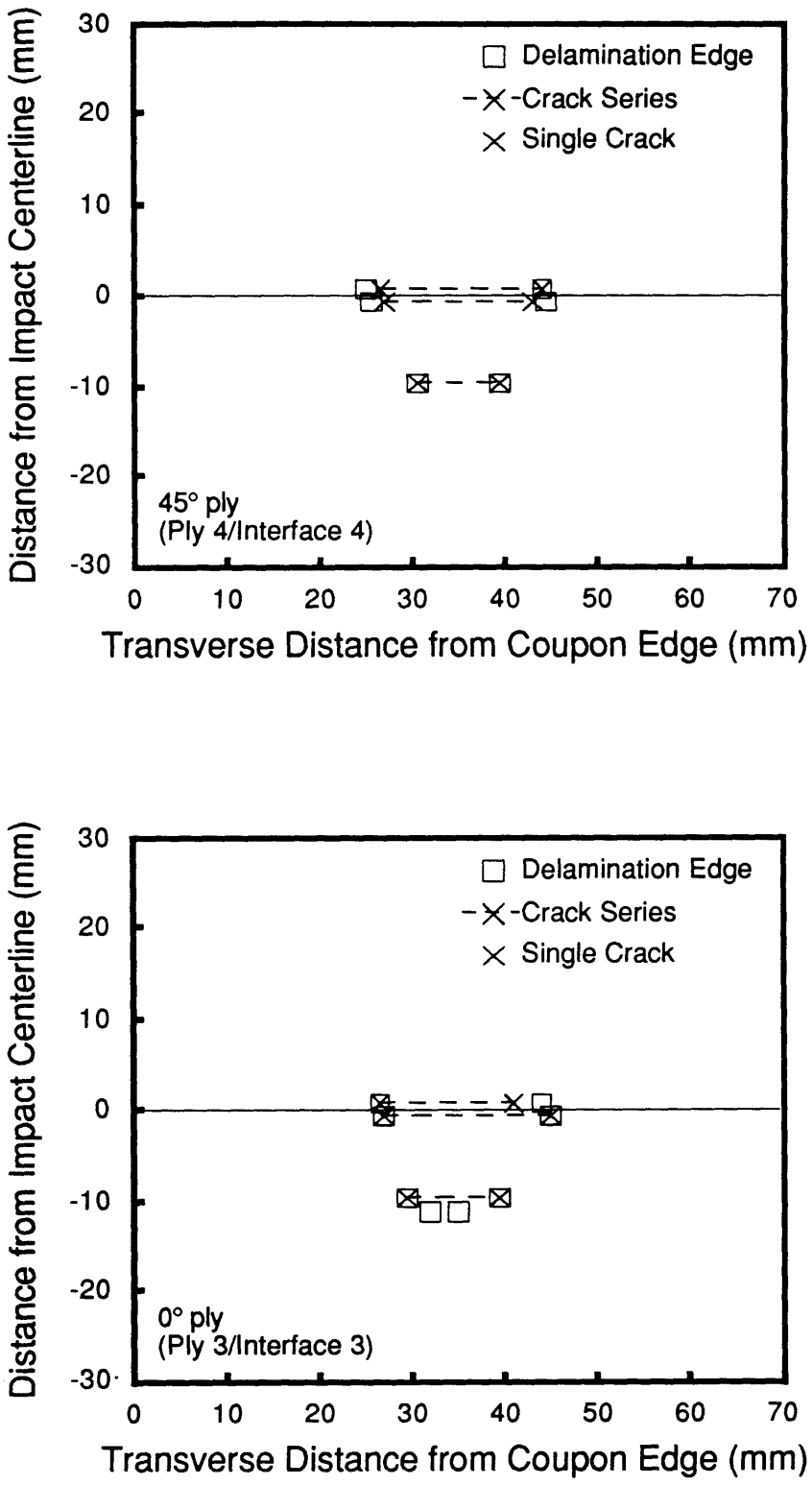

Figure 4.65 Cross-Section Schematics of Specimen T5-2 — Ply 4 and Ply 3 (Impacter Mass = 1523 g, Velocity = 6.3 m/s).

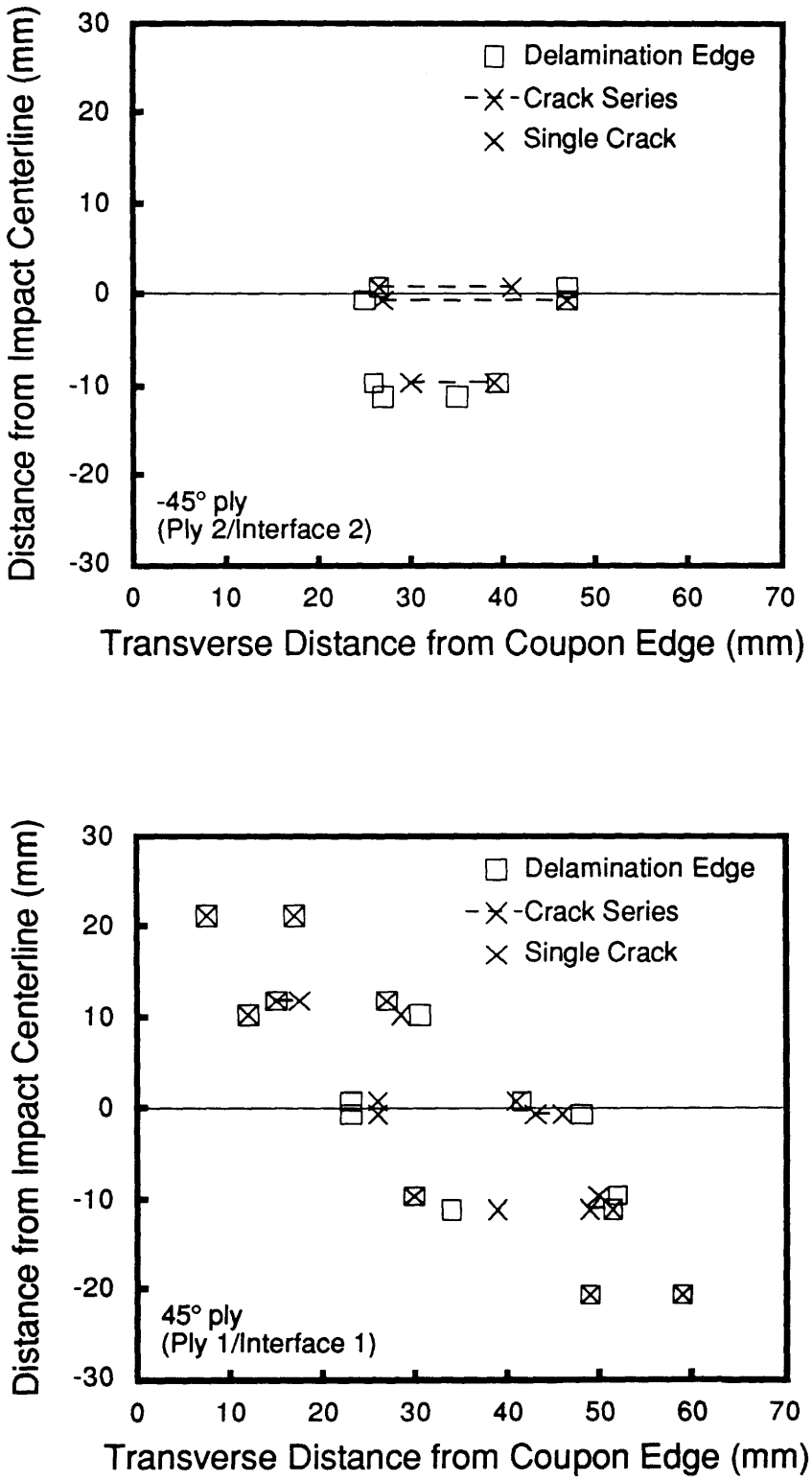

Figure 4.66 Cross-Section Schematics of Specimen T5-2 — Ply 2 and Ply 1 (Impacter Mass = 1523 g, Velocity = 6.3 m/s).

obvious. Plies 10 (0°) and 9 (45°), shown in Figure 4.62, also experienced matrix cracking as the plies split to make way for tup penetration. The delamination between plies 10 and 11 appears oriented in the 0° direction of ply 10 as does the delamination between plies 9 and 10. As the strip widths were wider than desired, information above the impact centerline was often missing. Thus, it is difficult to determine the orientation of the damage for most of the ±45° plies. Delamination size and the dimension of the series of transverse cracks through the impact location are consistent at approximately 15 mm. Both ply 8 (-45°) and ply 7 (0°), shown in Figure 4.63, exhibit delamination and transverse crack series with dimensions similar to the previous four plies. The delamination between plies 8 and 9 appears slightly biased in the -45° direction of ply 8. And the orientation between plies 7 and 8 is in the 0° direction of ply 7. Ply 6 (0°) and ply 5 (-45°), shown in Figure 4.64, exhibit similar matrix crack dimensions to those of the previous plies (approximately 15 mm). There is typically no delamination between plies 6 and 7 in the coupons under investigation. The delamination dimension between plies 5 and 6 at the impact location increases to approximately 20 mm but is not obviously oriented in the -45° direction of ply 5. While matrix cracking dimensions remain consistent with those previously seen (approximately 15 mm), delamination orientation between plies 4 and 5 and plies 3 and 4 are not obviously in the orientation of the plies further away from the impact surface as shown in Figure 4.65. The delaminations between plies 4 and 5 appears oriented in a 0° direction, but ply 4 is of 45° orientation. And the delamination between plies 3 and 4 appeared slightly biased to the -45° orientation, but ply 3 is of 0° orientation. The extent of matrix cracking and delamination is slightly larger (approximately 25 mm through the impact location) for the two plies near

the back surface as shown in Figure 4.66. Delamination orientations between plies 2 and 3 and plies 1 and 2 are definitely in the orientation of the next ply further away from the impact surface. The back surface split and the fibers peeled towards the edge of the coupon between plies 1 and 2. These fibers may have remained connected to the coupon, but once tape was removed from the cross-sectioned strip, so were the fibers.

Similar observations are made from the ply-by-ply damage evaluation data of a typical coupon impacted with the 578 g mass at the MCRS-velocity (9.2 m/s). These results are presented in Figures 4.67 through 4.72. Five cuts were made on this coupon resulting in four strips of approximately 9.5 mm width (T1, T2, B1, and B2). Eight surfaces were examined under a microscope. If less than eight indications are present on the schematics relative to the distance from the impact centerline axis, then no damage was observed on those surfaces. Matrix cracking measurements are approximately 15 mm at the center of impact for plies 12 through 5 with a gradual increase to approximately 25 mm in ply 1. The delamination sizes through the center of impact also are consistent at approximately 15 mm from interface 11 through interface 5 (except no delamination at interface 6 between two 0° plies) with a gradual increase to approximately 30 mm in ply 1 The orientation of most of the delaminations appear to be either at 0° or just slightly offset in the direction of the ply further away from the impact surface. Only the delamination orientation between plies 1 and 2 and plies 3 and 4, shown in Figure 4.72, are obviously in the direction of the ply further away from the impact surface. Thus, the information available on delamination orientation from this method does not appear to agree well

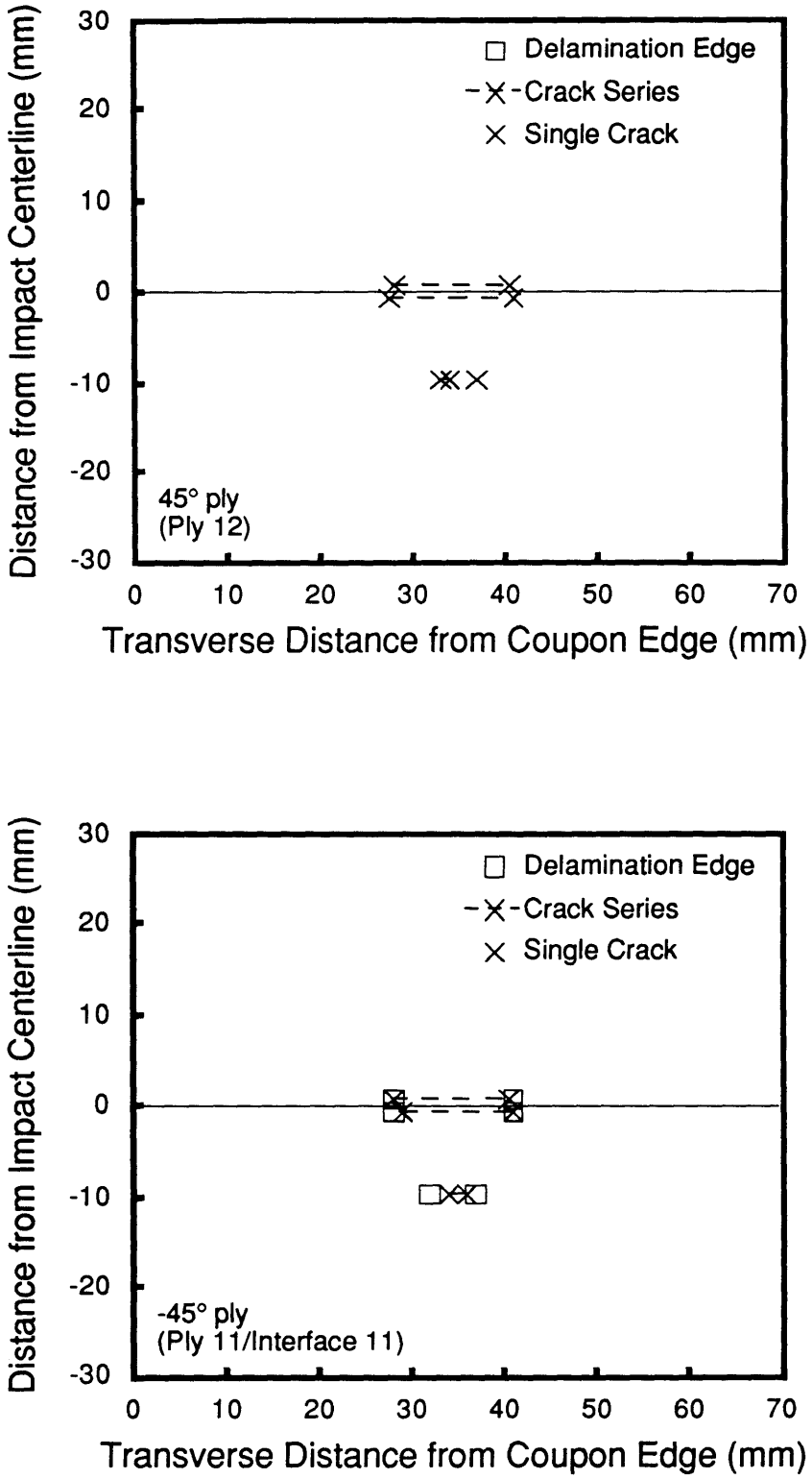

Figure 4.67 Cross-Section Schematics of Specimen J6-2 — Ply 12 and Ply 11 (Impacter Mass = 578 g, Velocity = 9.2 m/s).

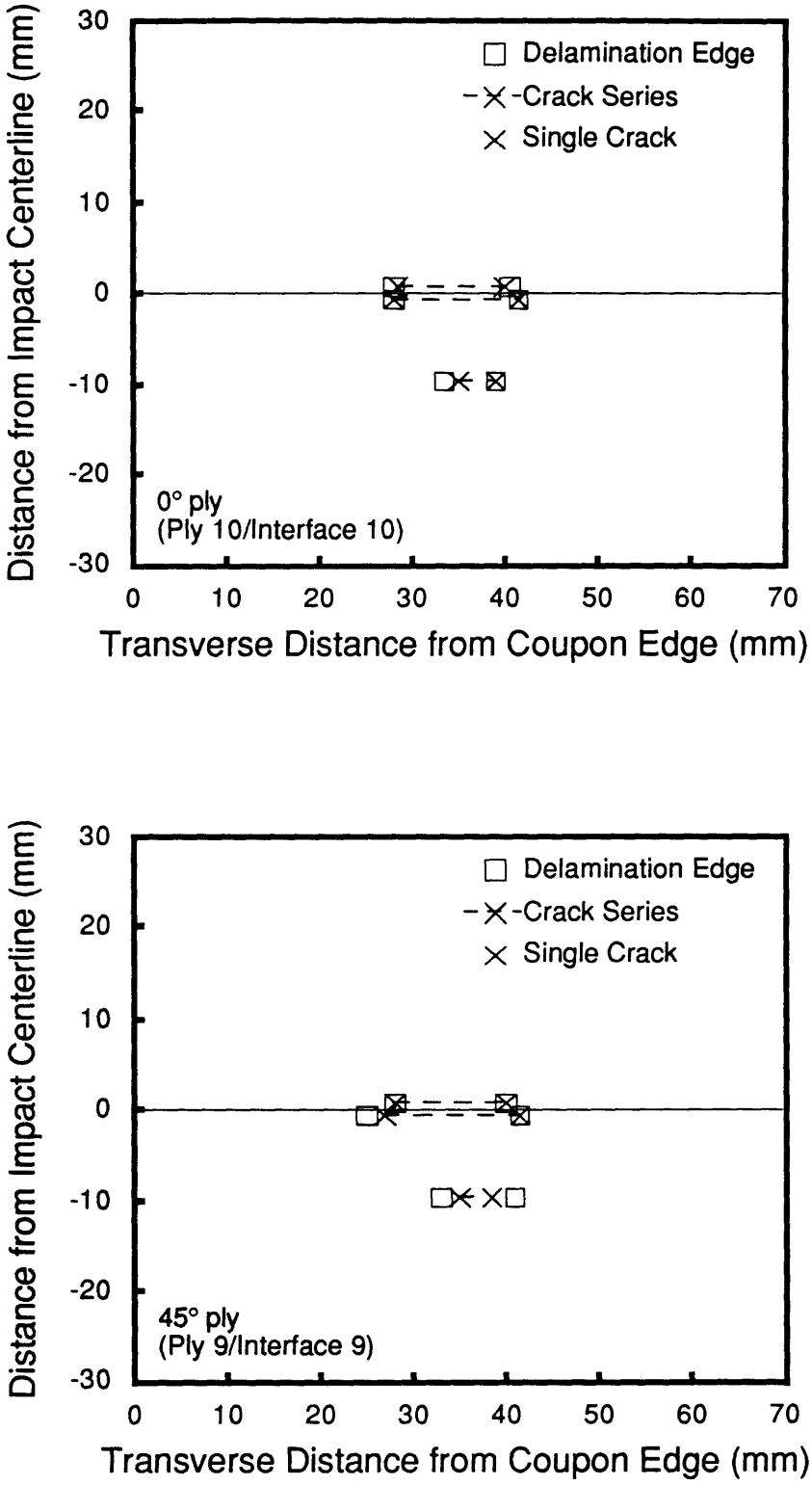

Figure 4.68 Cross-Section Schematics of Specimen J6-2 — Ply 10 and Ply 9 (Impacter Mass = 578 g, Velocity = 9.2 m/s).

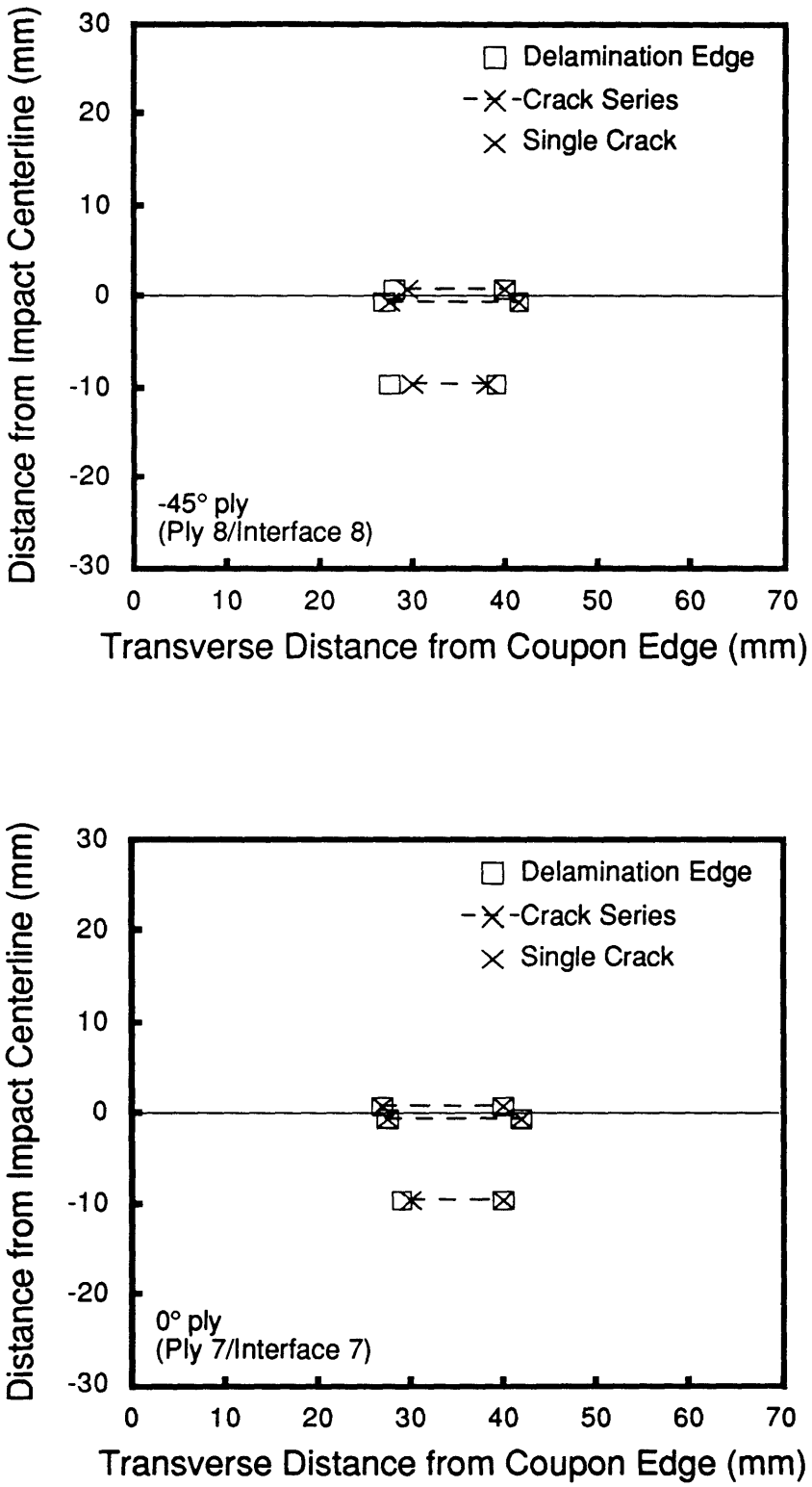

Figure 4.69 Cross-Section Schematics of Specimen J6-2 — Ply 8 and Ply 7 (Impacter Mass = 578 g, Velocity = 9.2 m/s).

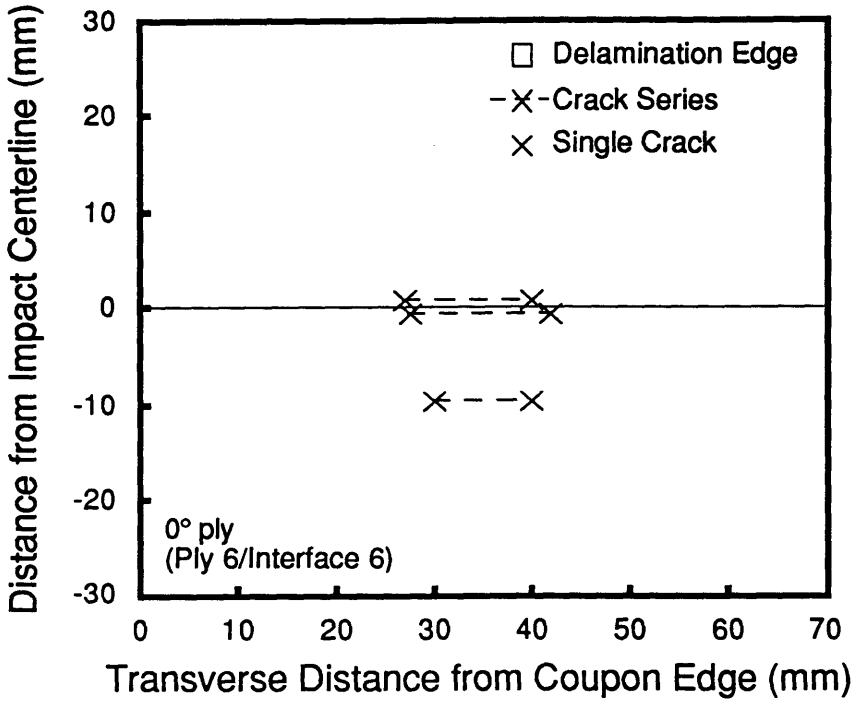

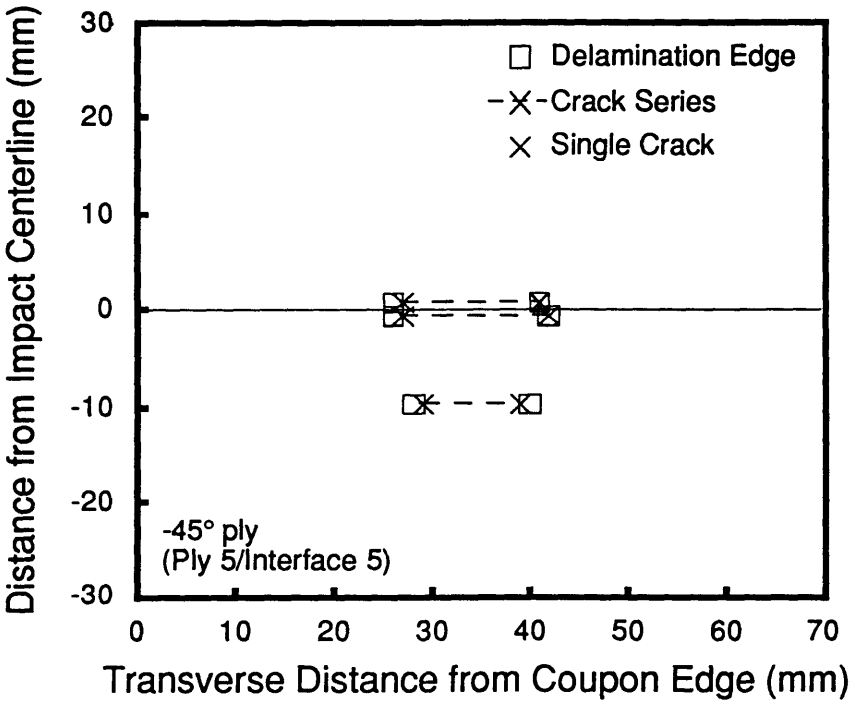

Figure 4.70 Cross-Section Schematics of Specimen J6-2 — Ply 6 and Ply 5 (Impacter Mass = 578 g, Velocity = 9.2 m/s).

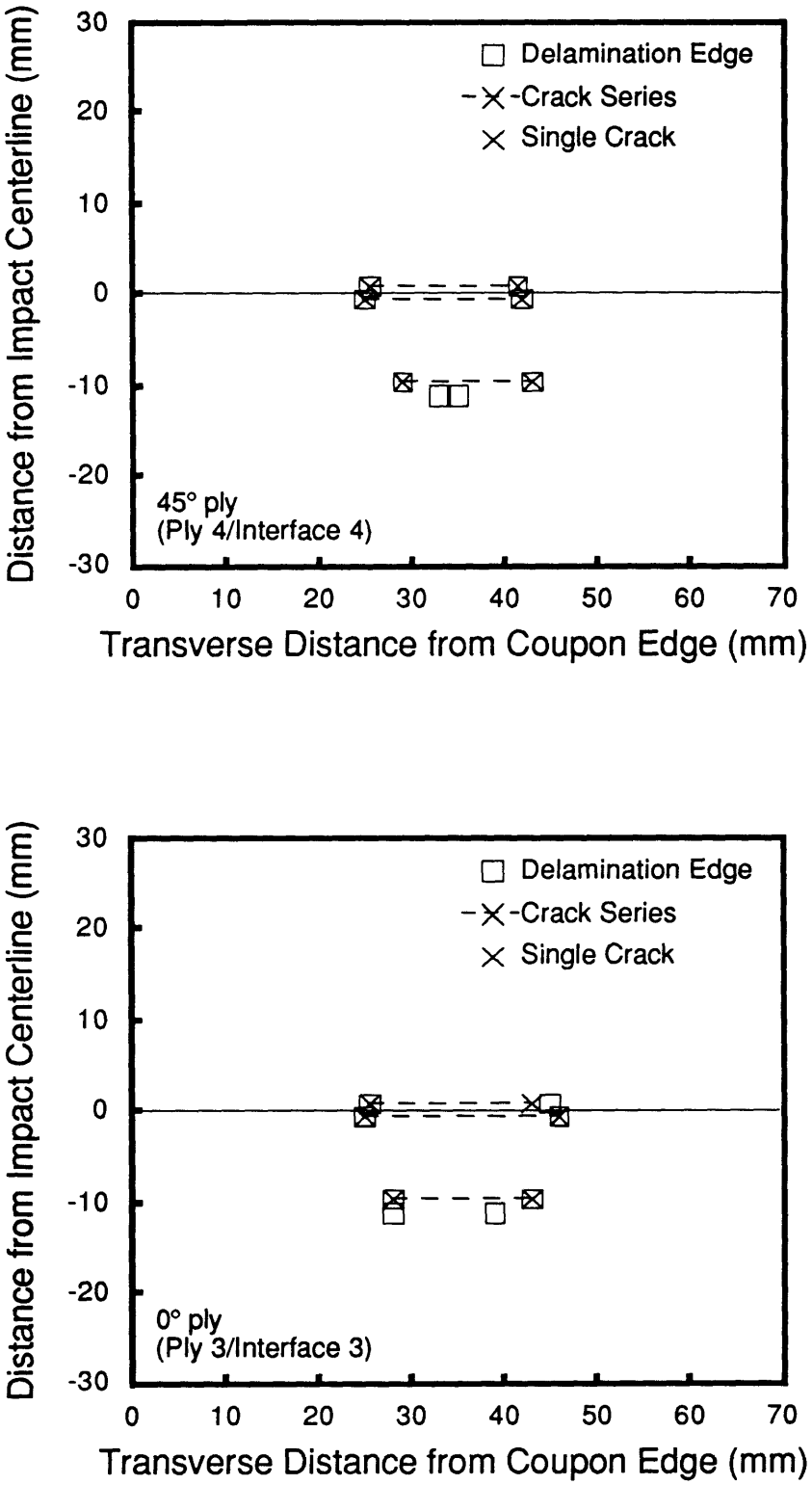

Figure 4.71 Cross-Section Schematics of Specimen J6-2 — Ply 4 and Ply 3 (Impacter Mass = 578 g, Velocity = 9.2 m/s).

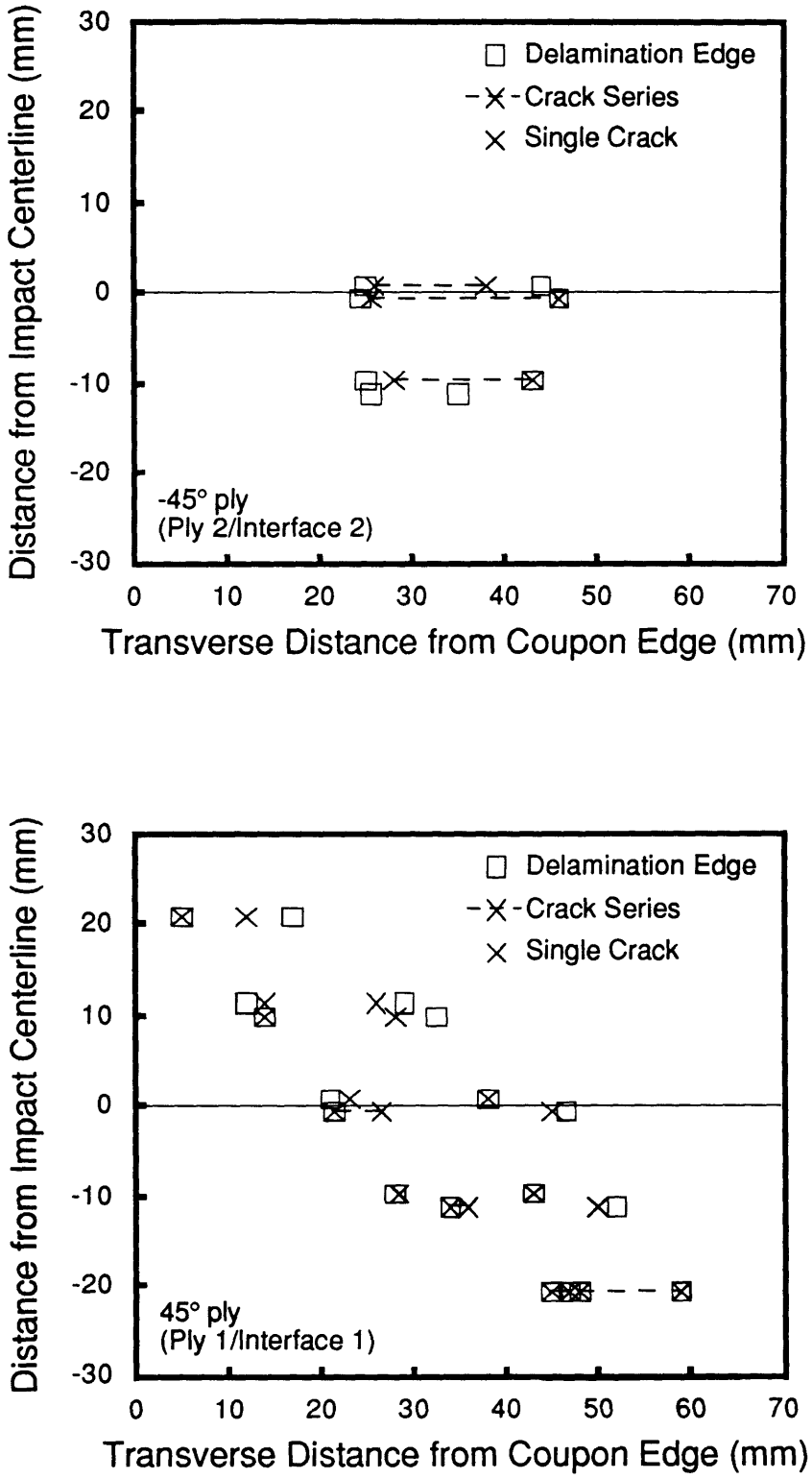

Figure 4.72 Cross-Section Schematics of Specimen J6-2 — Ply 2 and Ply 1 (Impacter Mass = 578 g, Velocity = 9.2 m/s).

with previously reported results [2, 48, 49]. If the strip widths were smaller, the additional information would provide more conclusive evidence on delamination orientation.

A better correlation of delamination orientation to previously reported results [2, 48, 49] is seen in the ply-by-ply damage evaluation data of a typical coupon impacted with the 8.4 g mass at the MCRS-velocity (57 m/s). These results are presented in Figures 4.73 through 4.78. Six cuts were made on this coupon resulting in four strips of approximately 6.5 mm width (T1, T2, T3, B1, and B2). Ten surfaces were examined under a microscope. If less than ten indications are present on the schematics relative to the distance from the impact centerline axis, then no damage was observed on those surfaces. Matrix cracking is not as extensive through-the-thickness as that seen for the specimens impacted by the 1523 and 578 g masses at their respective MCRS-velocities. This is likely related to the fact that as the spherical impacter did not break through the coupon. The series of matrix cracks in ply 12 through the center of impact in Figure 4.73 is only approximately 10 mm in width, whereas impact at the respective MCRS-velocities by the 1523 and the 578 g impacter masses resulted in approximately 15 mm of matrix cracks. Matrix cracking measurements are approximately 10 mm at the center of impact for plies 12 through 6 with a gradual increase to approximately 20 mm in ply 1. The delamination sizes through the center of impact are also consistent at approximately 10 mm from interface 11 through interface 7. There is no delamination at interface 6 between the two 0° plies. The delamination at interface 5 is approximately 15 mm with a gradual increase to approximately 20 mm in ply 1 The orientation of the delaminations are

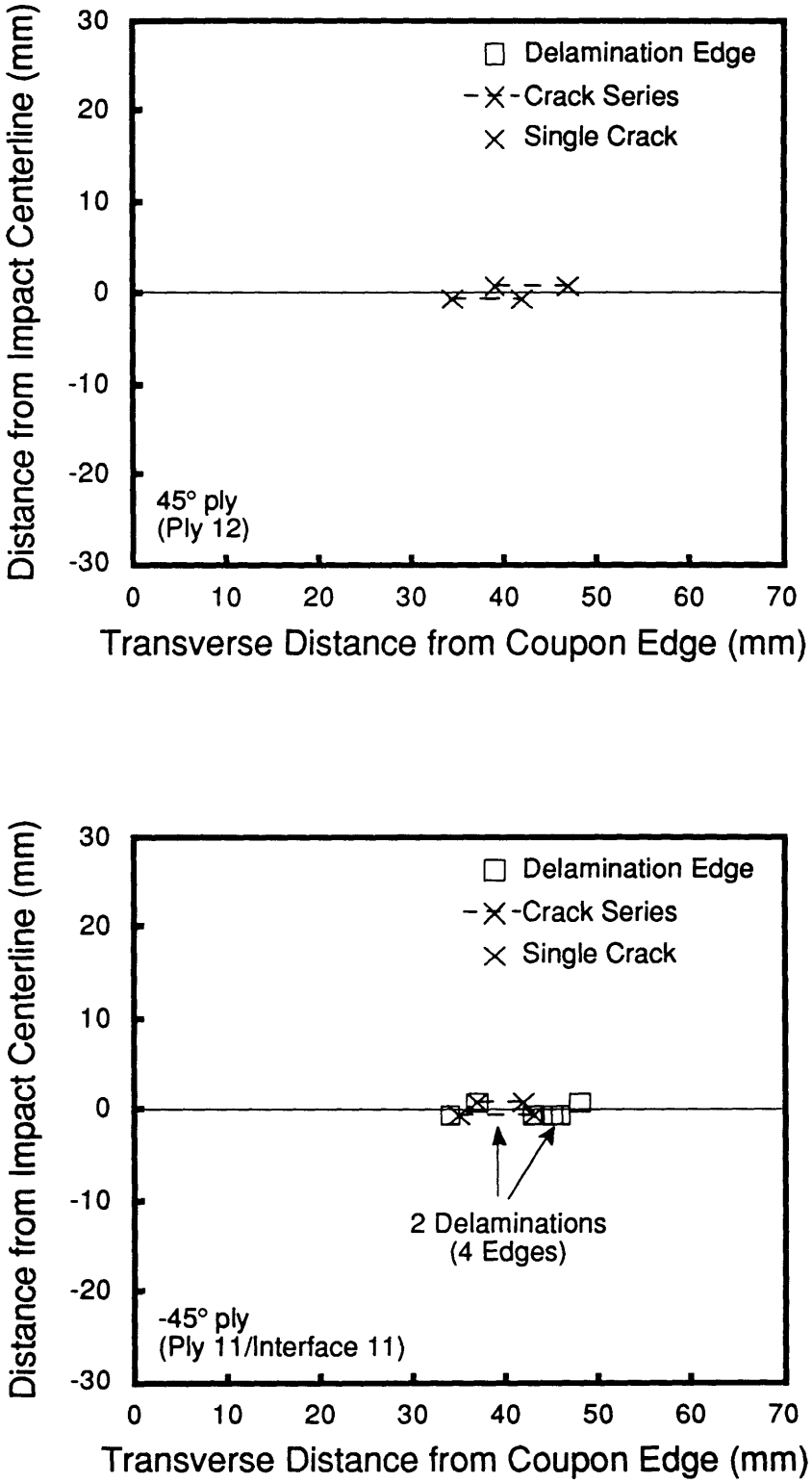

Figure 4.73 Cross-Section Schematics of Specimen M32-4 — Ply 12 and Ply 11 (Impacter Mass = 8.4 g, Velocity = 57 m/s).

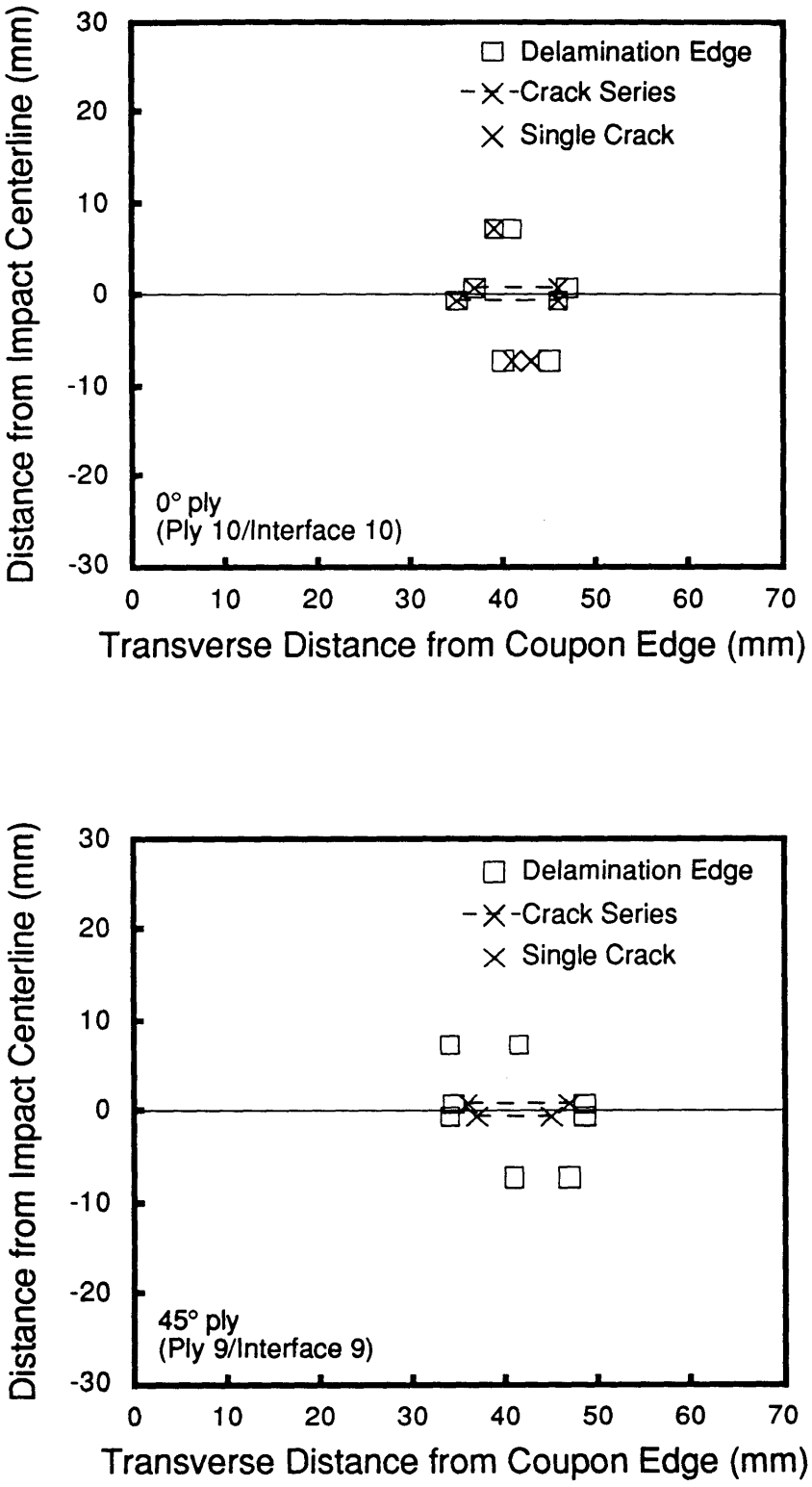

Figure 4.74 Cross-Section Schematics of Specimen M32-4 — Ply 10 and Ply 9 (Impacter Mass = 8.4 g, Velocity = 57 m/s).

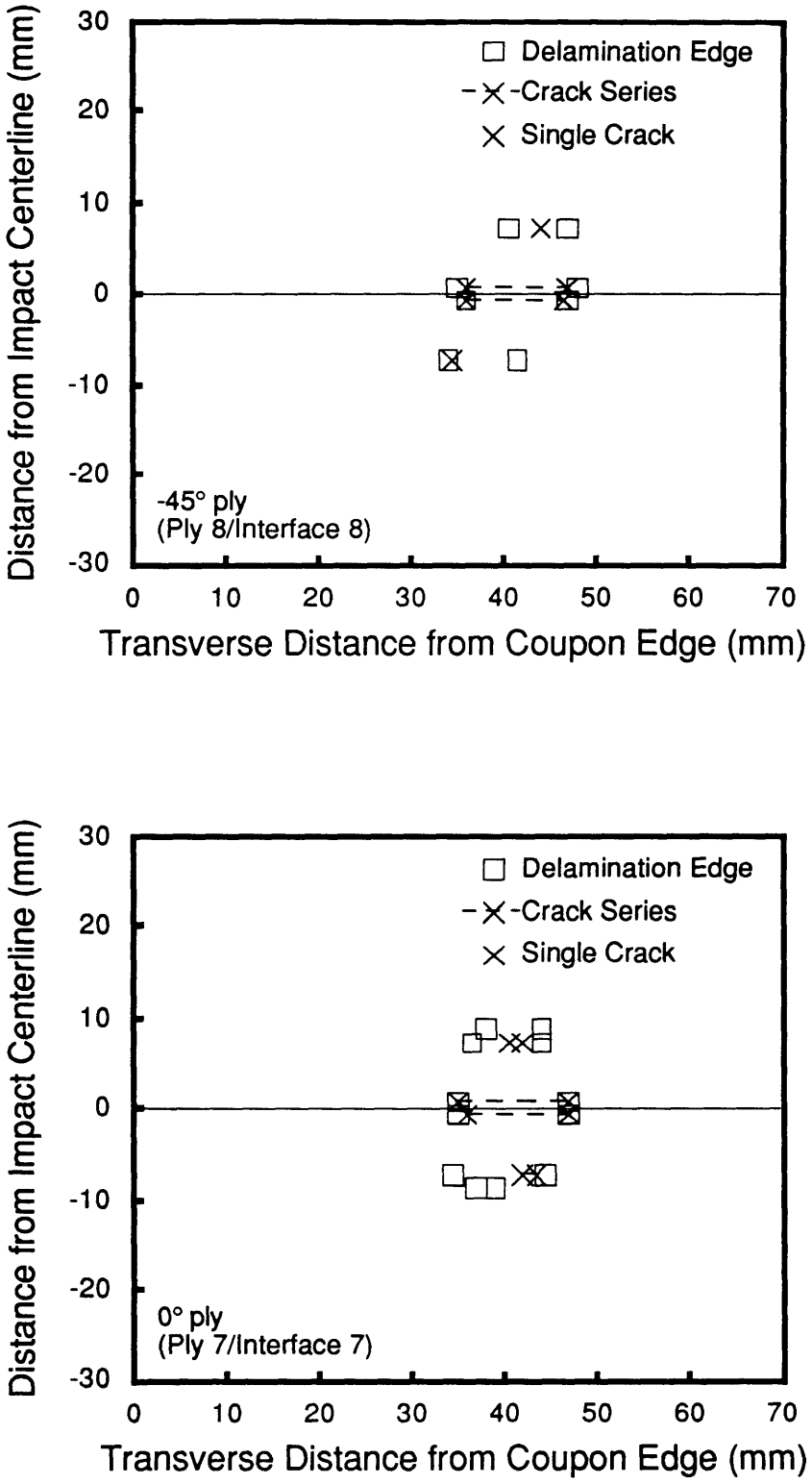

Figure 4.75 Cross-Section Schematics of Specimen M32-4 — Ply 8 and Ply 7 (Impacter Mass = 8.4 g, Velocity = 57 m/s).

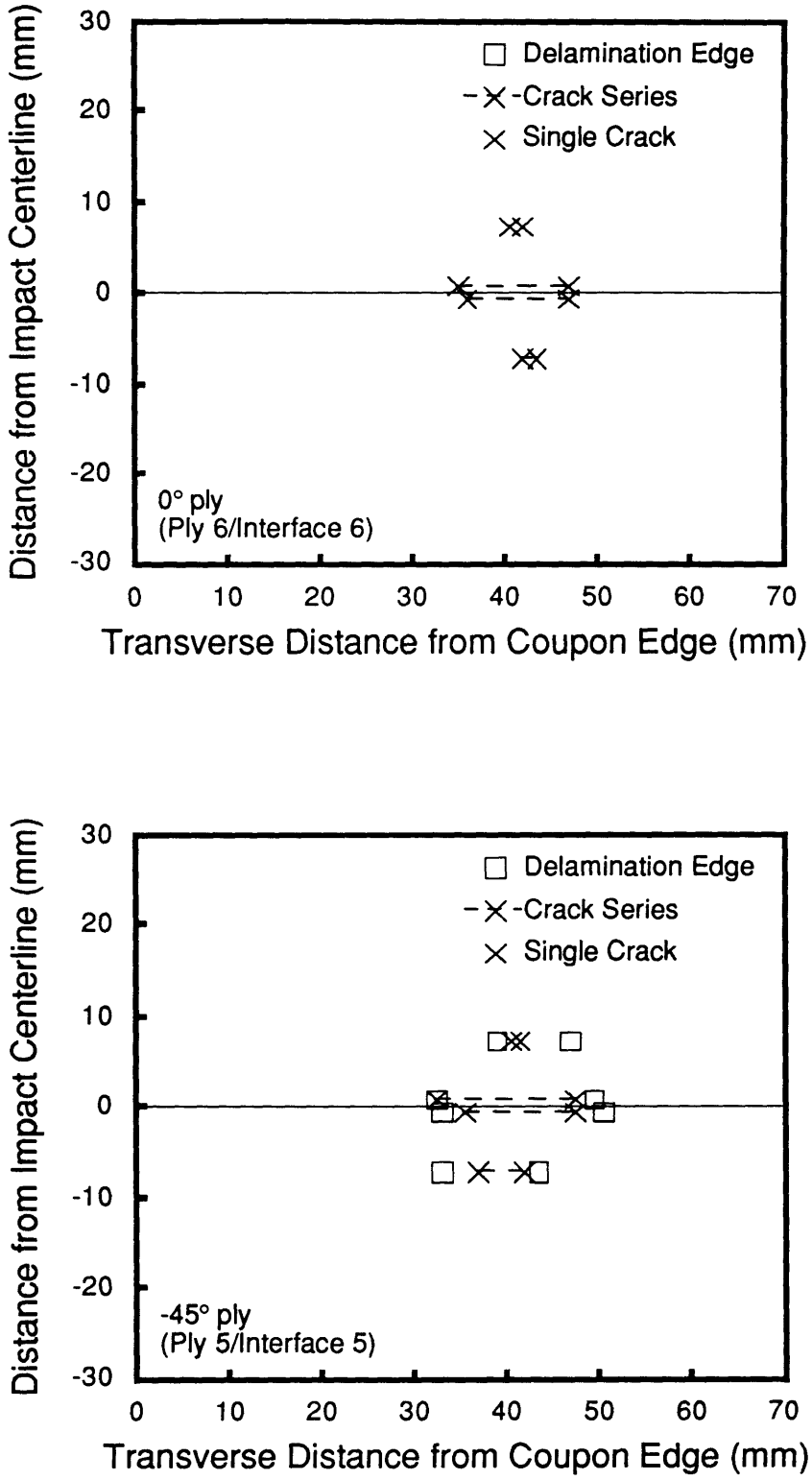

Figure 4.76 Cross-Section Schematics of Specimen M32-4 — Ply 6 and Ply 5 (Impacter Mass = 8.4 g, Velocity = 57 m/s).

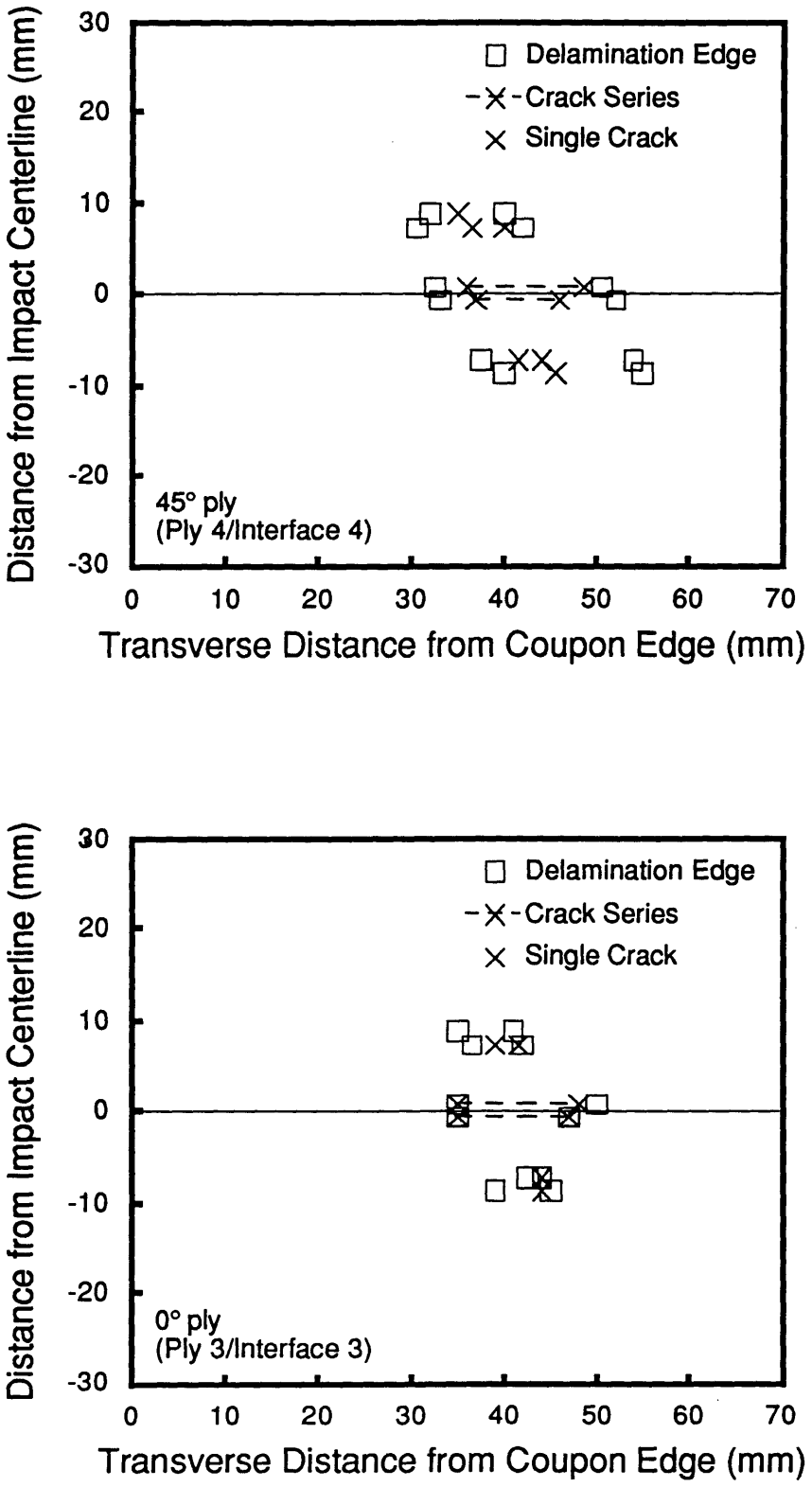

Figure 4.77 Cross-Section Schematics of Specimen M32-4 — Ply 4 and Ply 3 (Impacter Mass = 8.4 g, Velocity = 57 m/s).

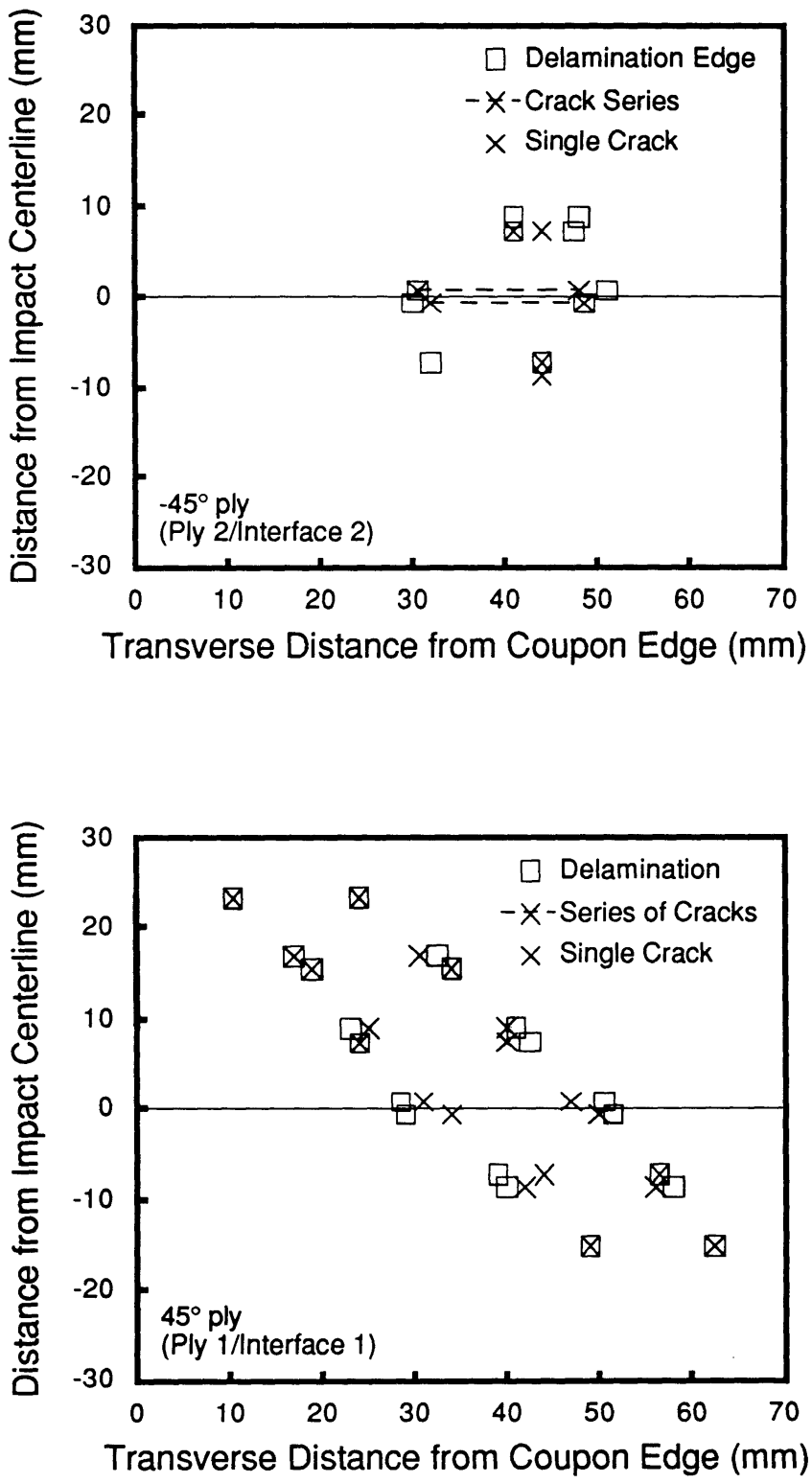

Figure 4.78 Cross-Section Schematics of Specimen M32-4 — Ply 2 and Ply 1 (Impacter Mass = 8.4 g, Velocity = 57 m/s).

obviously in the direction of the next ply further away from the impact surface. Even though the impacter did not break through the coupon, there is extensive damage in each ply. The back surface split and the fibers peeled towards the edge of the coupon between plies 1 and 2. These fibers may have remained connected to the coupon, but once tape was removed from the cross-sectioned strip, so were the fibers.

Cross-sectioning of the coupons, though a time-consuming task, provides valuable information on the three-dimensional damage state at the velocities investigated. A comparison of cross-section results at the respective MCRS-velocities for the three impacter masses used in this work is made in Section 4.5.

4.4.2 Deply

The deply technique directly provides damage information on a ply-by-ply basis. Delamination and fiber breaks are clearly evident during visual examination of a ply by light reflection off the gold chloride penetrant. However, magnification would be required to find evidence of matrix cracks. As delamination is usually accompanied by matrix cracks, no attempt was made to identify the matrix cracks by magnification of the deply specimens.

Ply identification relative to the impact surface is consistent with that defined for coupon layup, impact, time-of-flight ultrasonic C-Scan, and cross-sectioning as illustrated in Figure 3.12. Ply 12 is the first ply to encounter the impacter, and ply 1 is the back surface ply. Evaluation of the damage state began with the impact surface and worked towards the back surface. The difference between the cross-section evaluation and deply

evaluation is the interface associated with each ply. Because deply is done from the impact surface towards the back surface, the ply closest to the impact surface exhibits the delamination markings. Thus, ply 12 damage also includes the delamination data on interface 11 (between ply 11 and ply 12), ply 11 damage includes delamination data on interface 10 (between ply 10 and ply 11), etc. This results in viewing each ply from the back surface instead of the impact surface. That means the ±45° orientations are opposite of the cross-section and time-of-flight ultrasonic C-Scan results. There is no information available on ply 7/interface 6 from the deply method of damage evaluation as the two 0° plies could not be separated.

Interpretation of the damage data in the deply photographs is sometimes difficult due to the lighting conditions under which the photograph was taken. Gold chloride in a black and white photo appears as a lighter shade of gray compared to the black of the graphite/epoxy. However, under certain lighting conditions, the graphite/epoxy may also have a gray appearance. In a black and white photograph, it is difficult to distinguish the gray appearance of the gold chloride from the gray appearance of the graphite/epoxy. The white area in the central location of the deply photographs is the background showing through the ply where fibers no longer exist. Other "white" areas are due to light reflections off the graphite/epoxy. Though interpretation of the photographs may be difficult, the visual inspection of each ply under various lighting conditions results in positive identification of damage present.

Ply-by-ply photographs of damage in a typical coupon impacted with the 1523 g mass at the MCRS velocity (6.3 m/s) are presented in Figures 4.79 through 4.83. Both ply 12 (45°) and ply 11 (-45°) experienced extensive

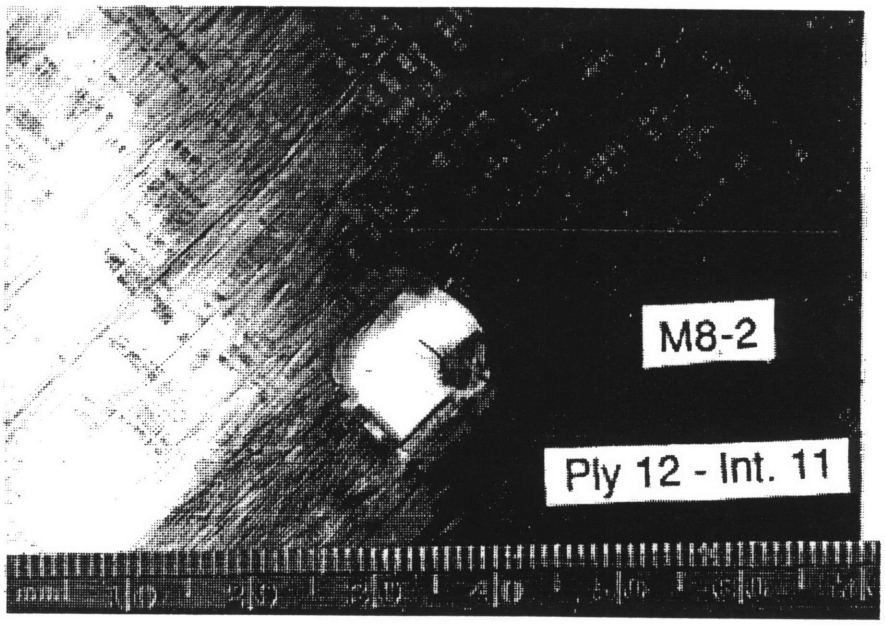

[45/-45/0/45/-45/0/0/-45/45/0/-45/**/45**] Impact Surface

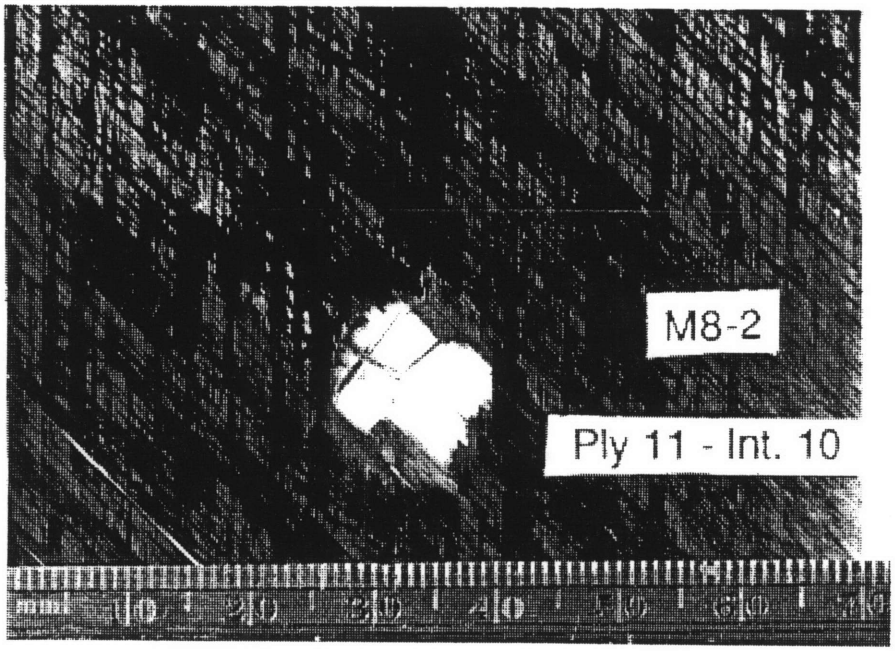

[45/-45/0/45/-45/0/0/-45/45/0/**/-45**/45] Impact Surface

Figure 4.79 Deply Photographs of Specimen M8-2 — Ply 12 and Ply 11 (Impacter Mass = 1523 g, Velocity = 6.3 m/s).

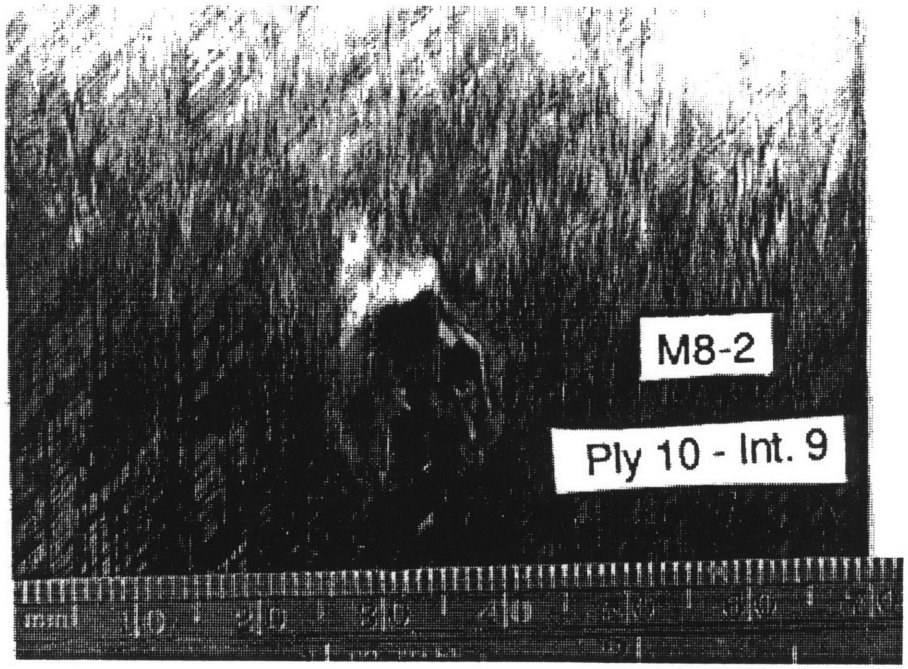

[45/-45/0/45/-45/0/0/-45/45/<u>/**0**</u>/-45/45] Impact Surface

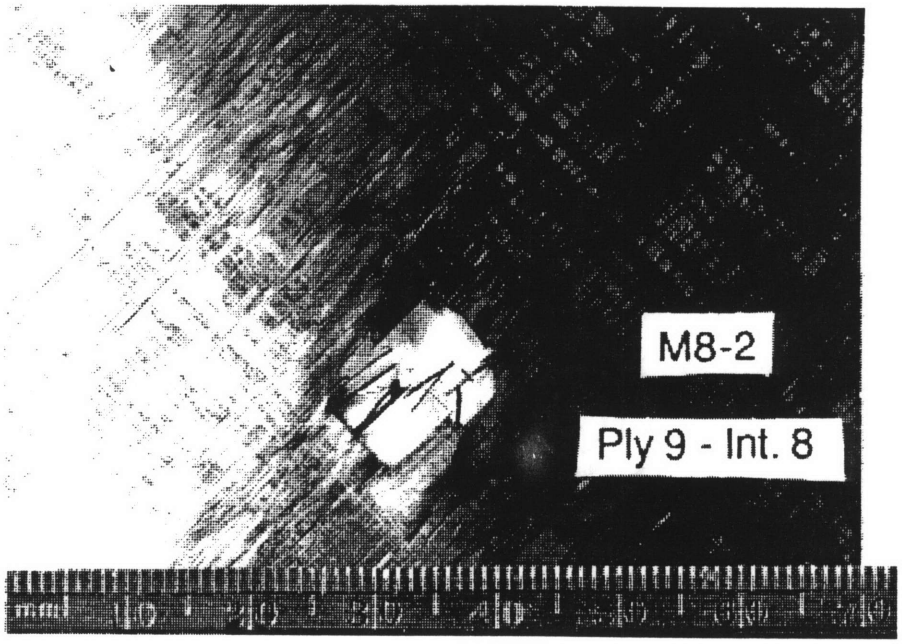

[45/-45/0/45/-45/0/0/-45/<u>/**45**</u>/0/-45/45] Impact Surface

Figure 4.80 Deply Photographs of Specimen M8-2 — Ply 10 and Ply 9 (Impacter Mass = 1523 g, Velocity = 6.3 m/s).

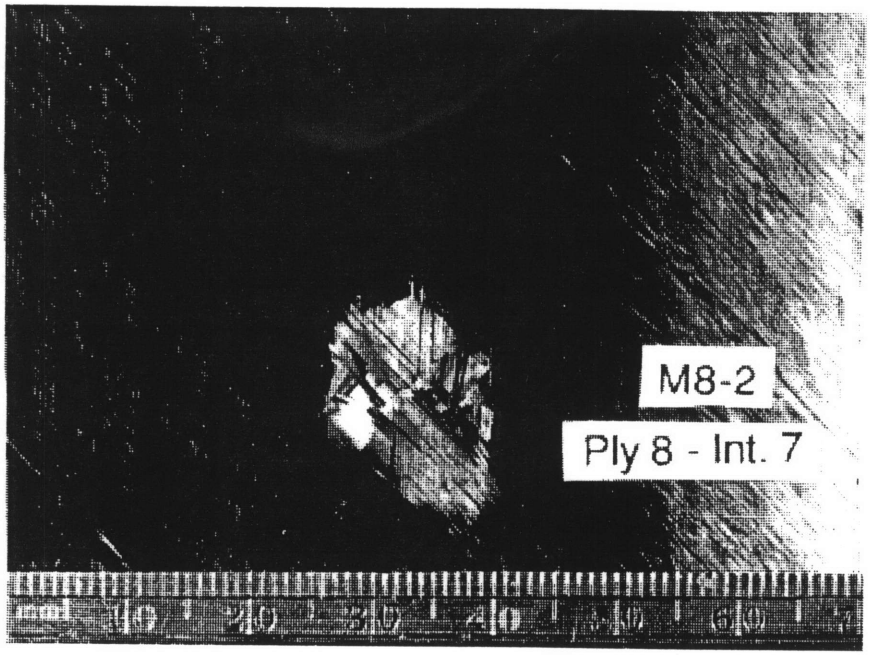

[45/-45/0/45/-45/0/0/**-45**/45/0/-45/45] Impact Surface

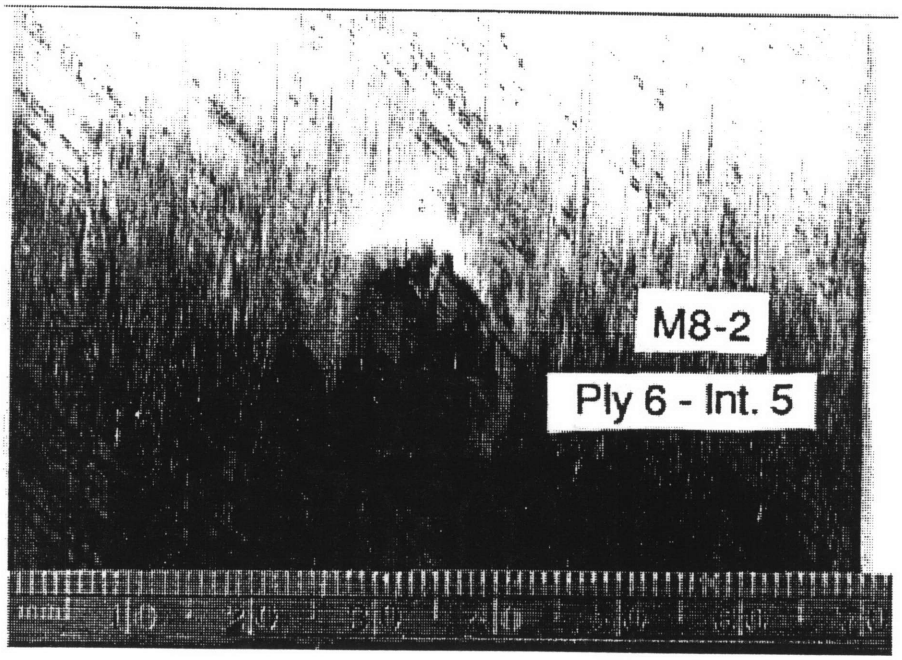

[45/-45/0/45/-45/**0**/0/-45/45/0/-45/45] Impact Surface

Figure 4.81 Deply Photographs of Specimen M8-2 — Ply 8 and Ply 6 (Impacter Mass = 1523 g, Velocity = 6.3 m/s).

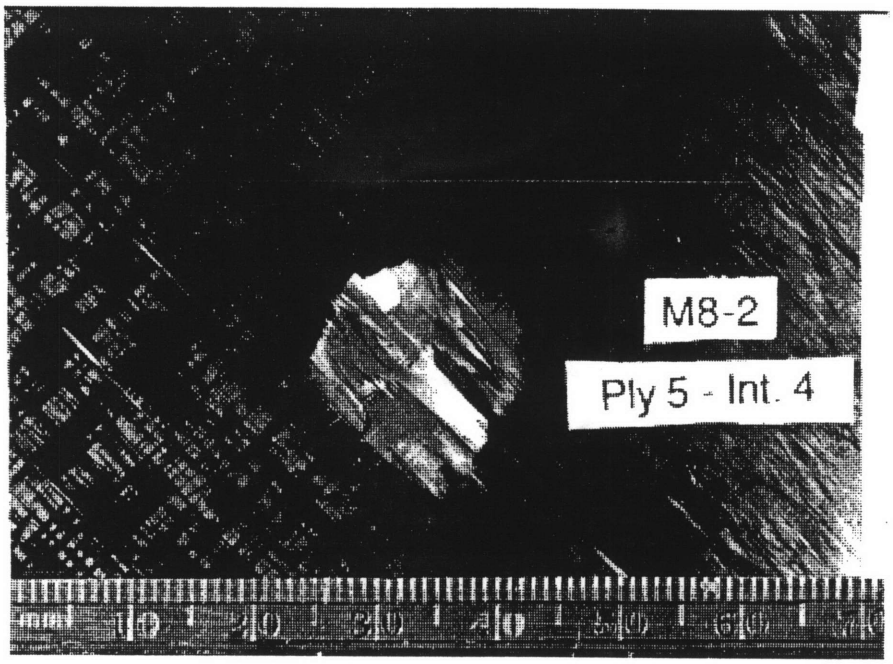

[45/-45/0/45/**/-45**/0/0/-45/45/0/-45/45] Impact Surface

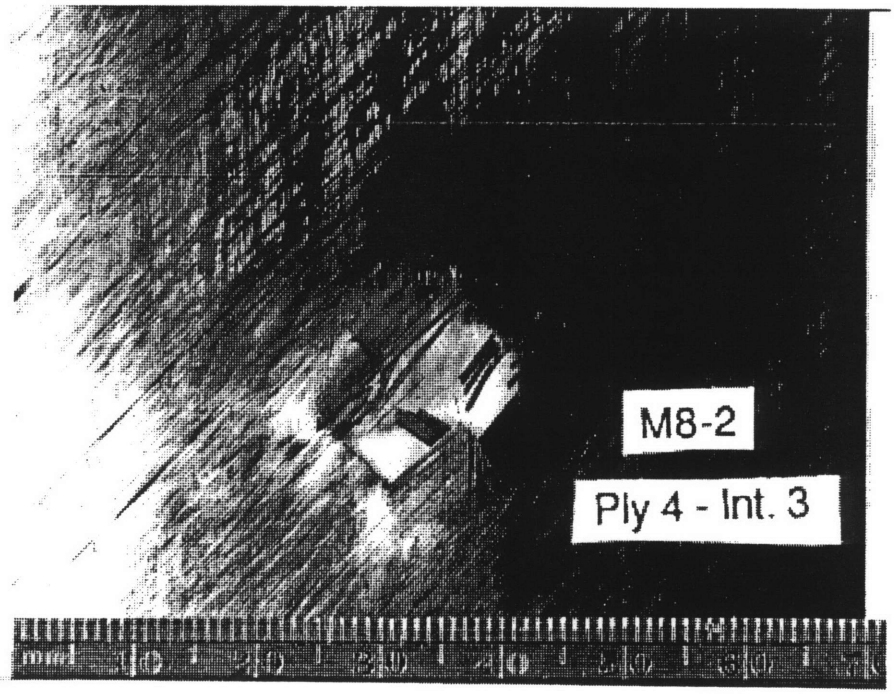

[45/-45/0/**/45**/-45/0/0/-45/45/0/-45/45] Impact Surface

Figure 4.82 Deply Photographs of Specimen M8-2 — Ply 5 and Ply 4 (Impacter Mass = 1523 g, Velocity = 6.3 m/s).

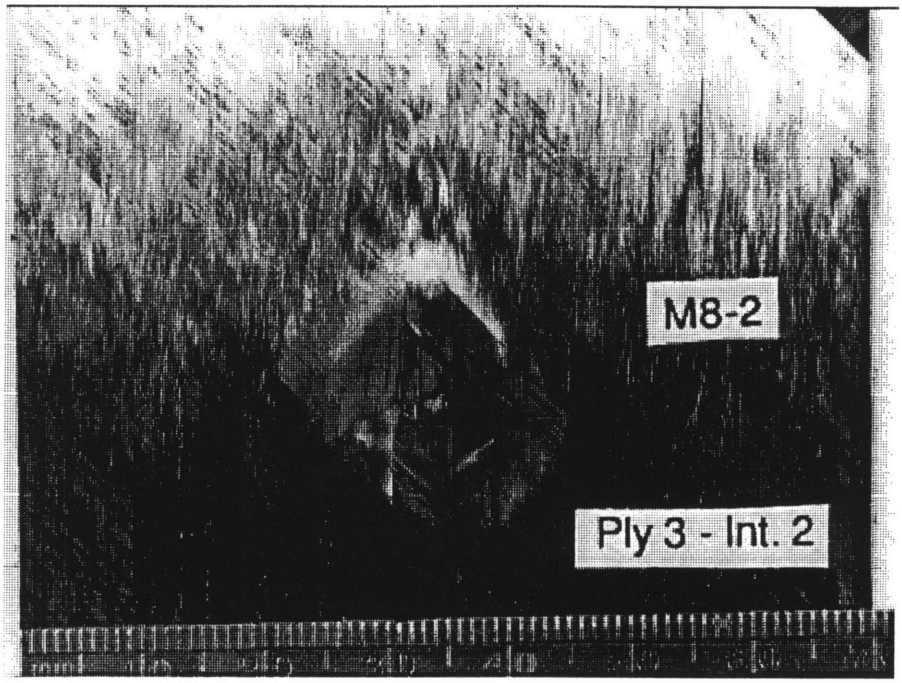

[45/-45/**0**/45/-45/0/0/-45/45/0/-45/45] Impact Surface

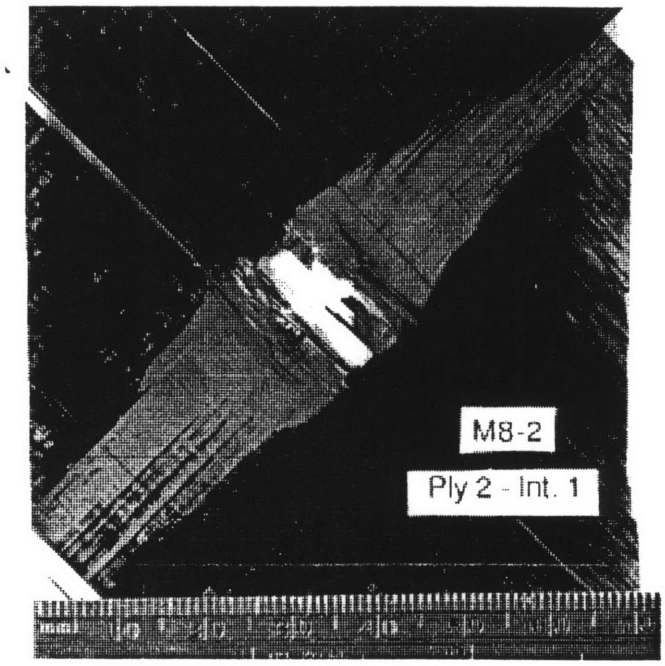

[45/**-45**/0/45/-45/0/0/-45/45/0/-45/45] Impact Surface

Figure 4.83 Deply Photographs of Specimen M8-2 — Ply 3 and Ply 2 (Impacter Mass = 1523 g, Velocity = 6.3 m/s).

matrix cracking and fiber damage as the plies split to make way for tup penetration as shown in Figure 4.79. There is very little evidence of delamination between plies 11 and 12 in the photograph, but visual inspection results in identification of the major axis of damage at approximately 15 mm and with orientation in the direction of ply 11 (-45°). What was left of ply 11 at the impact location exhibited delamination between plies 10 and 11 with a major axis dimension of approximately 16 mm and orientation in the 0° direction of ply 10. Plies 10 (0°) and 9 (45°) also experienced significant fiber damage as shown in Figure 4.80. Though the gold chloride marker doesn't show clearly in the photographs of plies 9 and 10, visual examination of each ply gave evidence of delamination right around the edges of tup penetration. The major axes of delamination damage measured approximately 18 mm for interface 9 and 20 mm for interface 8 with orientations of both in the direction of the next ply further away from the impact surface. In the photograph of ply 8 in Figure 4.81, the major axis of damage measured approximately 20 mm and visual inspection of the delamination indicated 0° orientation. The lighting used to photograph ply 6 (as with ply 10 also of 0° orientation), did not result in obvious delamination markings in the photographs. The major axis of damage for interface 5 measured approximately 19 mm and was oriented in the -45° direction of the next ply. Photographs of ply 5 (-45°) and ply 4 (45°) in Figure 4.82 exhibit similar fiber damage dimensions to those of the previous ±45° plies (19 mm). Visual inspection of the delamination orientation between plies 4 and 5 and plies 3 and 4 identifies the orientation to be in the direction of the next plies further away from the impact surface. Delamination orientation between plies 2 and 3 is in the orientation of ply 2, though it did not show up well in the photograph in Figure 4.83. The major

axis of delamination measures approximately 22 mm. The delamination between plies 1 and 2 is oriented in the direction of ply 1. The back surface split and the fibers peeled towards the edge of the coupon between plies 1 and 2 as evidenced by the gold chloride marker on ply 2. The gold chloride marker on ply 2 provides all the necessary information for ply 1.

Ply-by-ply photographs of damage in a typical coupon impacted with the 578 g mass at the MCRS velocity (9.2 m/s) are presented in Figures 4.84 through 4.88. All of these photographs clearly show evidence of extensive damage from the impact penetration point towards the top of the photograph. These damage indications were unique to the deply damage evaluation technique as X-ray, ultrasonic C-Scan, and time-of-flight ultrasonic C-Scan for this specimens did not pick up any indications of this sort. Thus, the nature of this damage was in question. However, if the gold chloride was able to wick into these porous locations, the dye penetrant used for X-ray should have done the same. Ply-by-ply photographs, in Figures 4.89 through 4.93, of a coupon impacted by the 578 g impacter mass at a slightly lower velocity (8.6 m/s) were evaluated to determine if the indications of additional damage was typical for impact with the 578 g impacter mass. It was not. These photographs consistently show delamination orientation in the direction of the next ply further away from the impact surface. Penetration of the tup occurred in this coupon as evidenced by the extensive fiber damage in each ply (obvious by white background in central area of photographs). The major axis of delamination increases from 15 to 22 mm in length for the first five interfaces near the impact surface (interfaces 11 through 7, Figures 4.89 and 4.91). As distance through-the-thickness increases, the major axis of

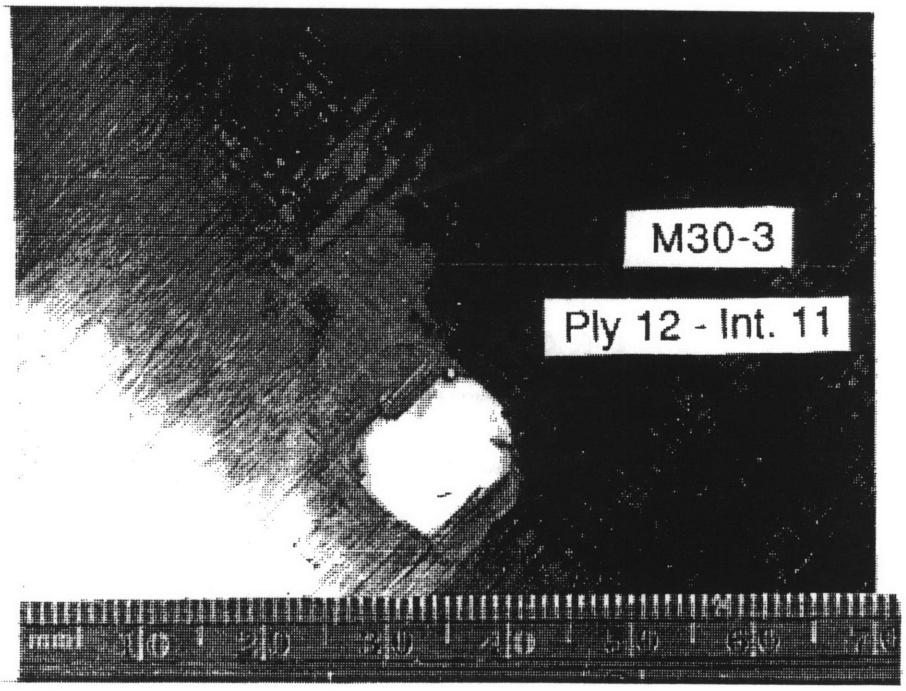

[45/-45/0/45/-45/0/0/-45/45/0/-45/**45**] Impact Surface

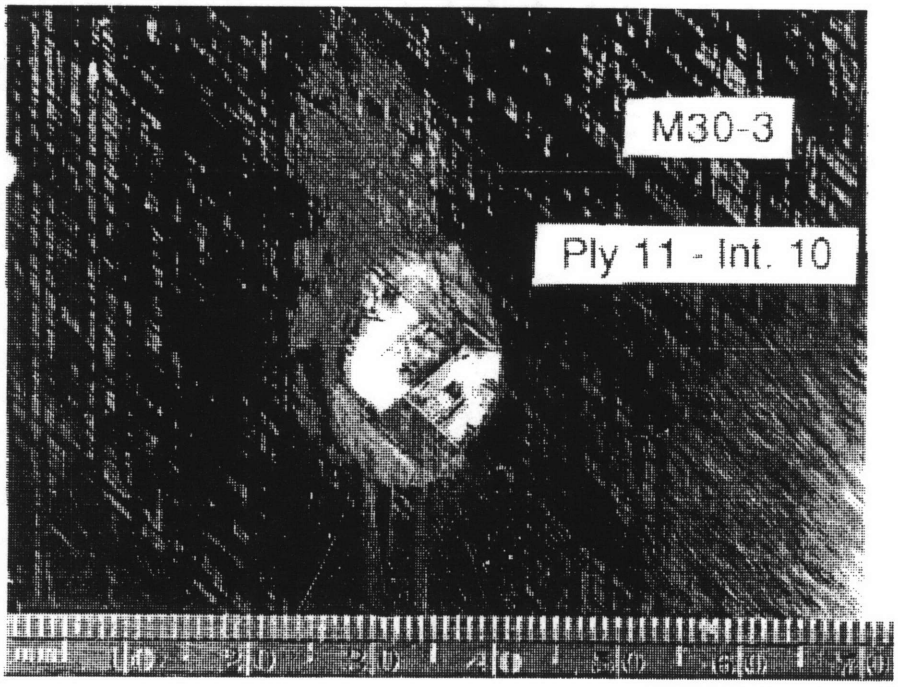

[45/-45/0/45/-45/0/0/-45/45/0/**-45**/45] Impact Surface

Figure 4.84 Deply Photographs of Specimen M30-3 — Ply 12 and Ply 11 (Impacter Mass = 578 g, Velocity = 9.2 m/s).

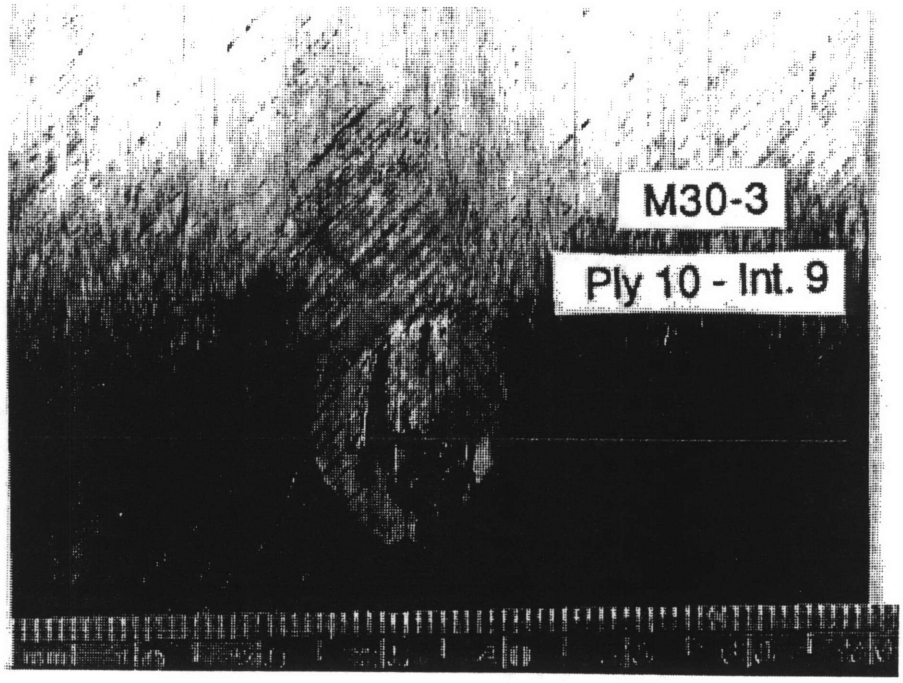

[45/-45/0/45/-45/0/0/-45/45/<u>/0</u>/-45/45] Impact Surface

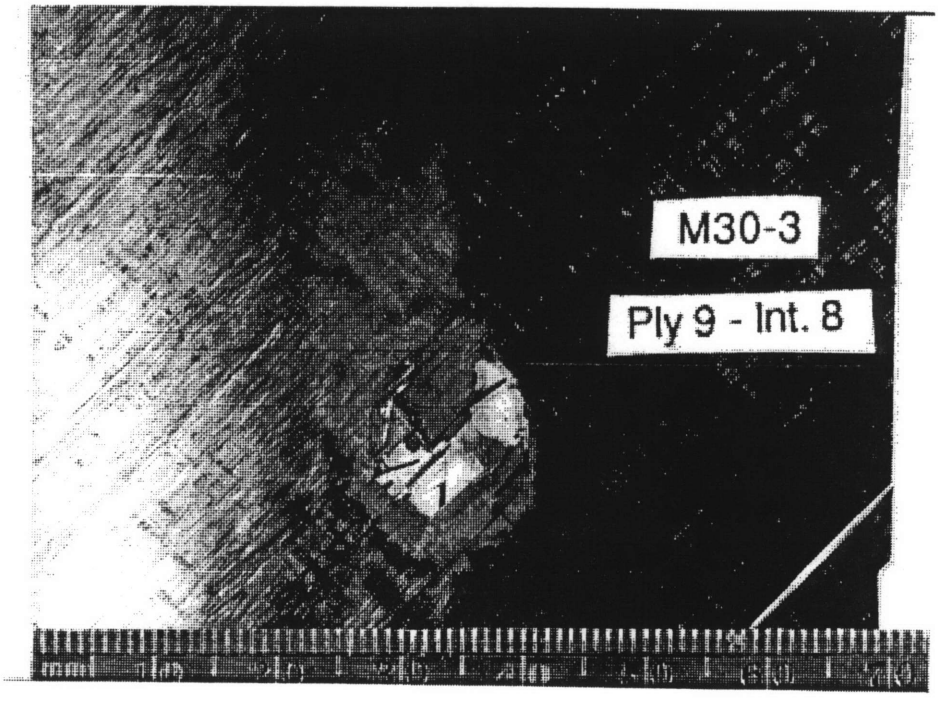

[45/-45/0/45/-45/0/0/-45/<u>/45</u>/0/-45/45] Impact Surface

Figure 4.85 Deply Photographs of Specimen M30-3 — Ply 10 and Ply 9 (Impacter Mass = 578 g, Velocity = 9.2 m/s).

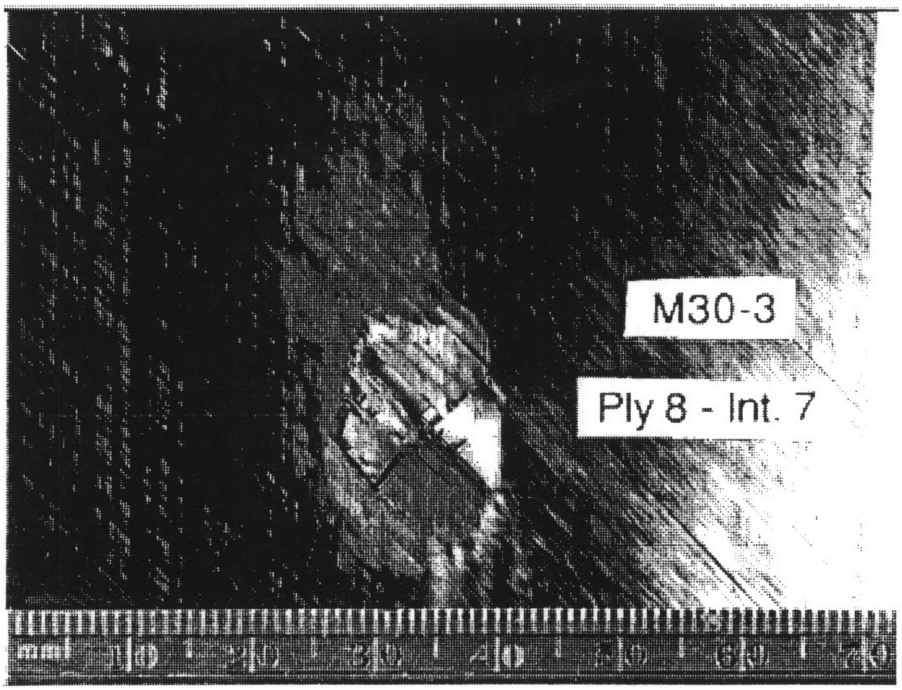

[45/-45/0/45/-45/0/0/**-45**/45/0/-45/45] Impact Surface

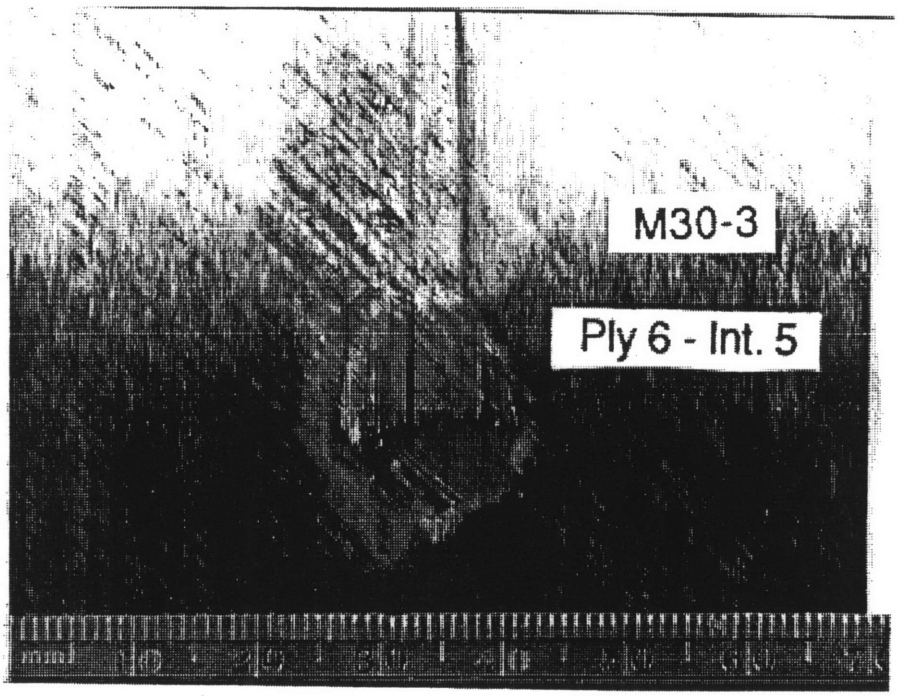

[45/-45/0/45/-45/**0**/0/-45/45/0/-45/45] Impact Surface

Figure 4.86 Deply Photographs of Specimen M30-3 — Ply 8 and Ply 6 (Impacter Mass = 578 g, Velocity = 9.2 m/s).

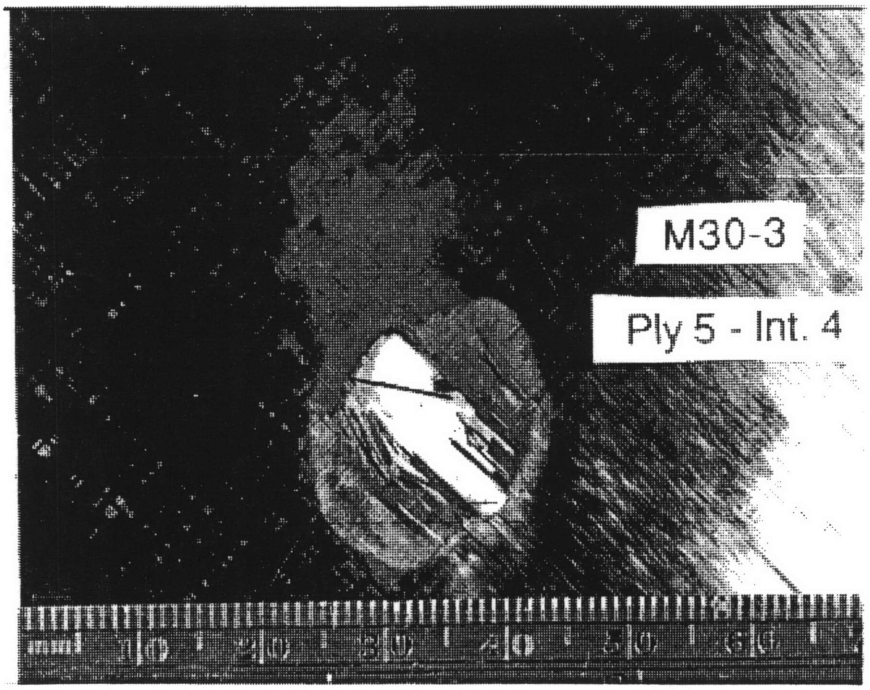

[45/-45/0/45/**/-45**/0/0/-45/45/0/-45/45] Impact Surface

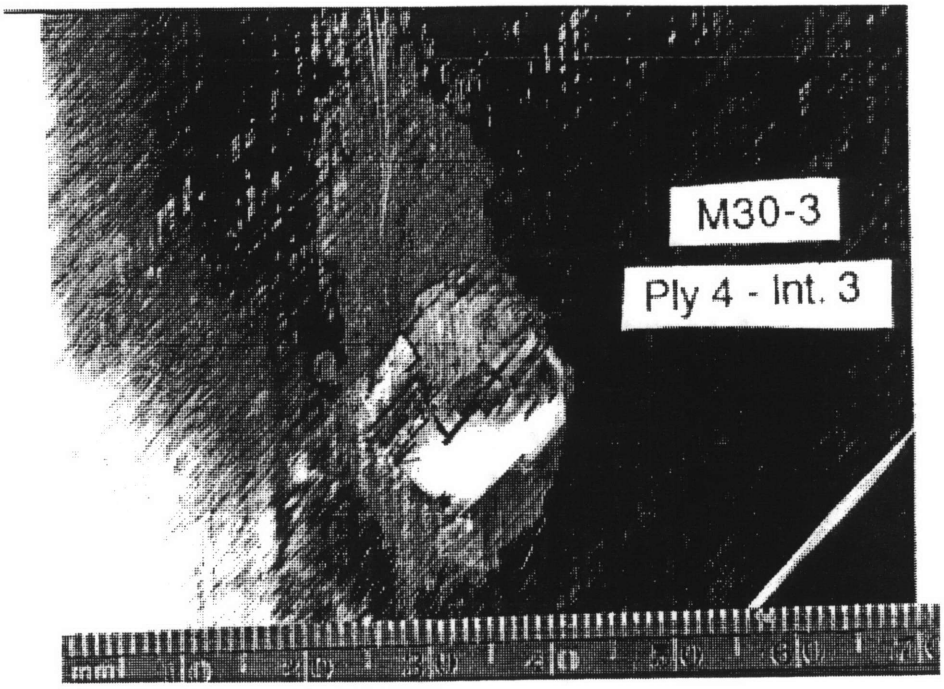

[45/-45/0/**/45**/-45/0/0/-45/45/0/-45/45] Impact Surface

Figure 4.87 Deply Photographs of Specimen M30-3 — Ply 5 and Ply 4 (Impacter Mass = 578 g, Velocity = 9.2 m/s).

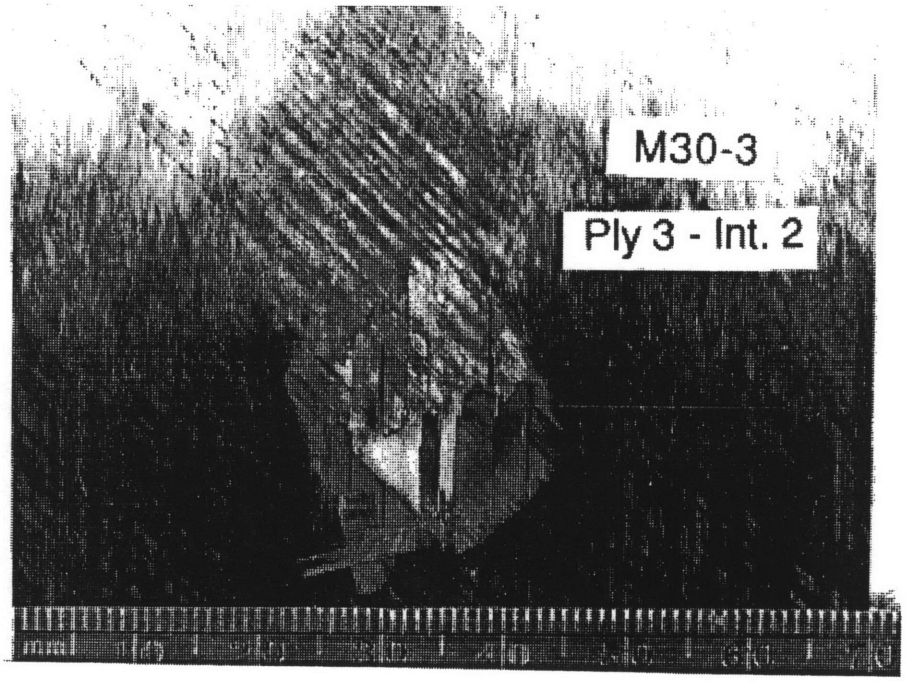

[45/-45/**/0**/45/-45/0/0/-45/45/0/-45/45] Impact Surface

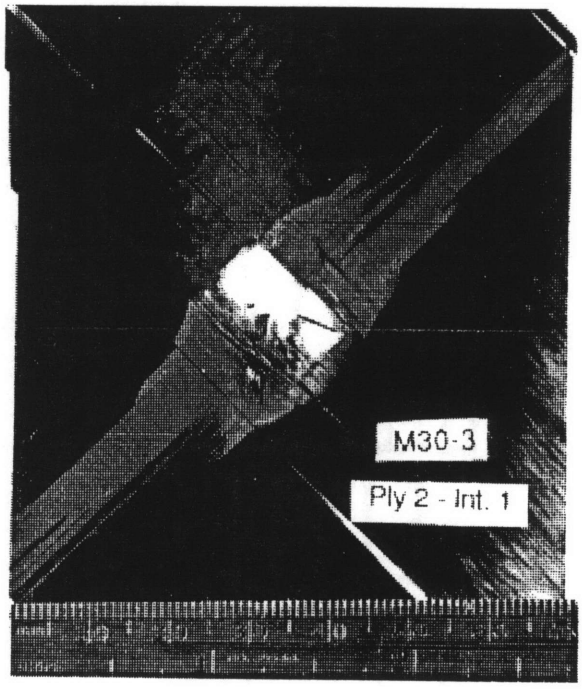

[45/**/-45**/0/45/-45/0/0/-45/45/0/-45/45] Impact Surface

Figure 4.88 Deply Photographs of Specimen M30-3 — Ply 3 and Ply 2 (Impacter Mass = 578 g, Velocity = 9.2 m/s).

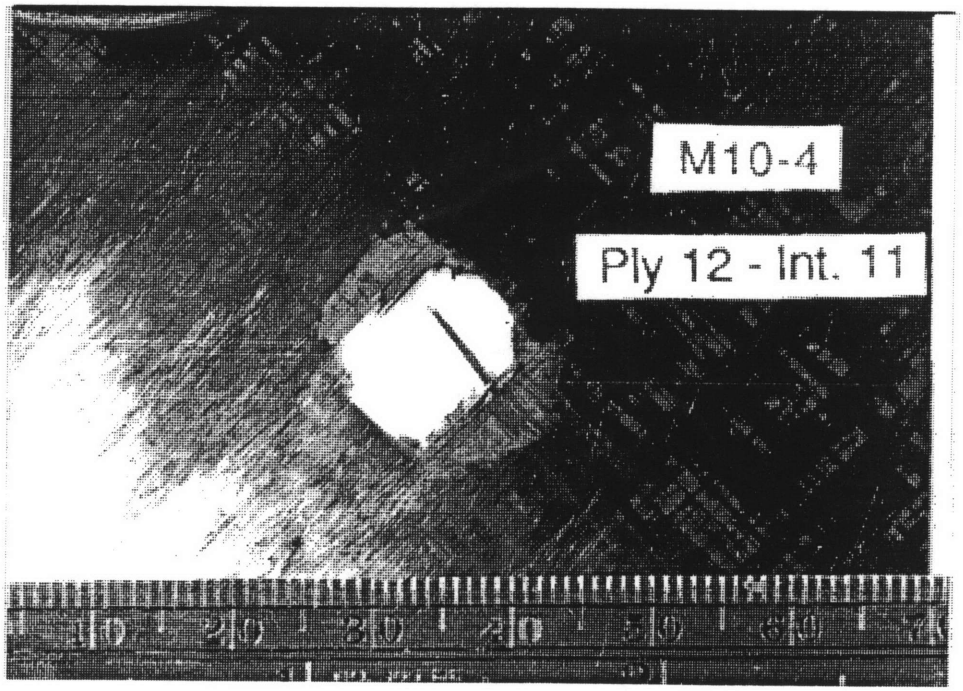

[45/-45/0/45/-45/0/0/-45/45/0/-45/**/45**] Impact Surface

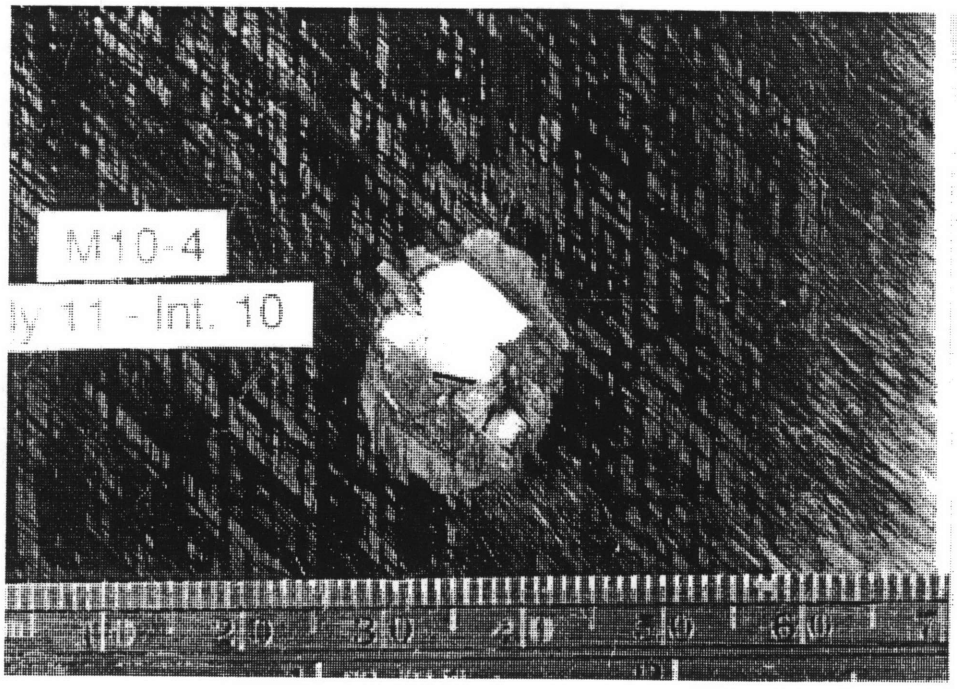

[45/-45/0/45/-45/0/0/-45/45/0/**/-45**/45] Impact Surface

Figure 4.89 Deply Photographs of Specimen M10-4 — Ply 12 and Ply 11 (Impacter Mass = 578 g, Velocity = 8.6 m/s).

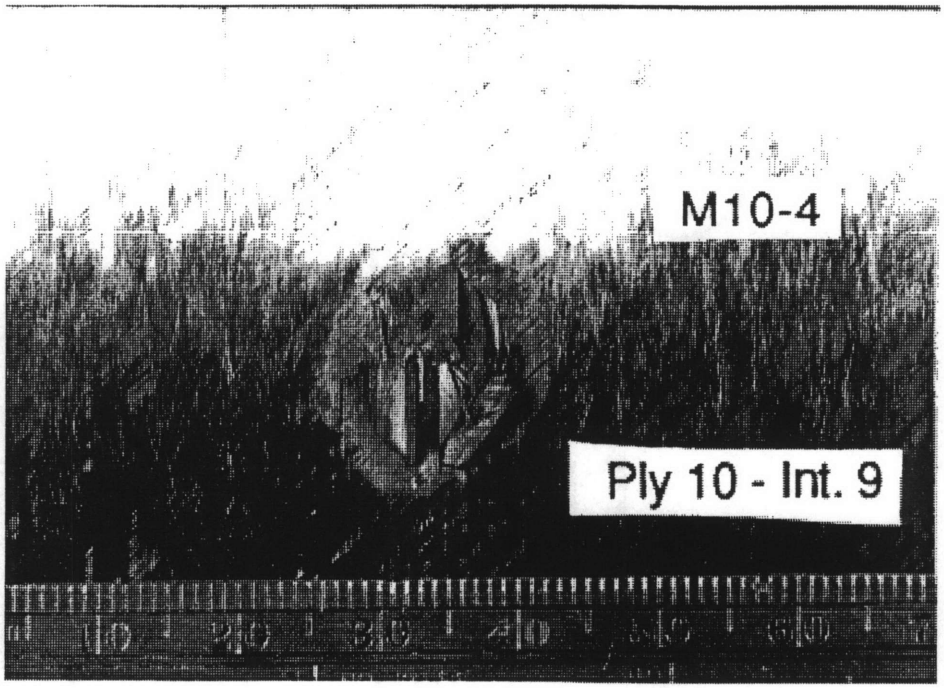

[45/-45/0/45/-45/0/0/-45/45/**/0**/-45/45] Impact Surface

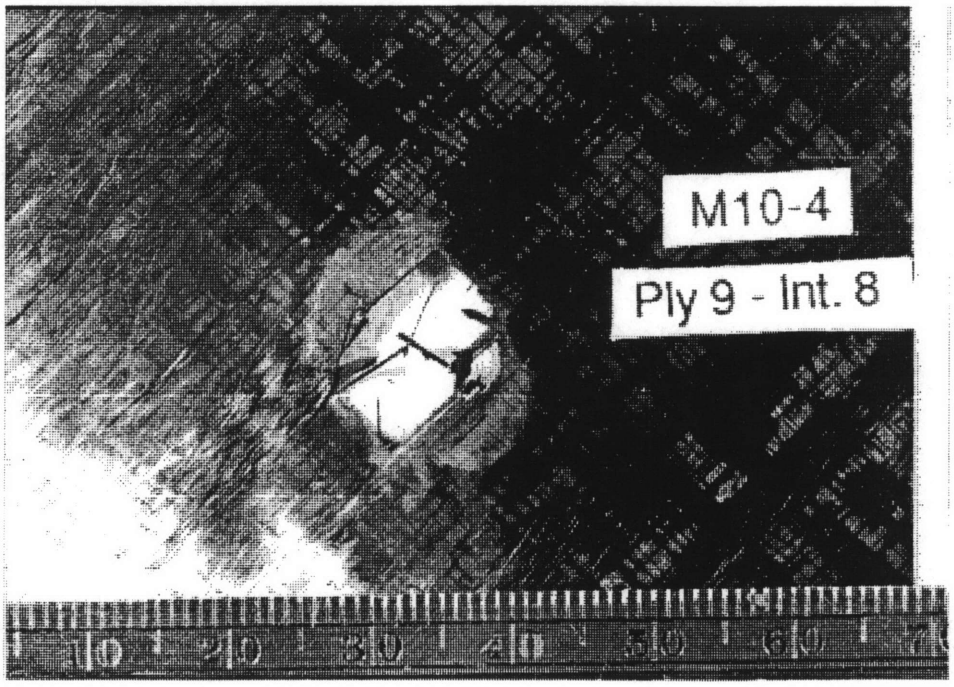

[45/-45/0/45/-45/0/0/-45/**/45**/0/-45/45] Impact Surface

Figure 4.90 Deply Photographs of Specimen M10-4 — Ply 10 and Ply 9 (Impacter Mass = 578 g, Velocity = 8.6 m/s).

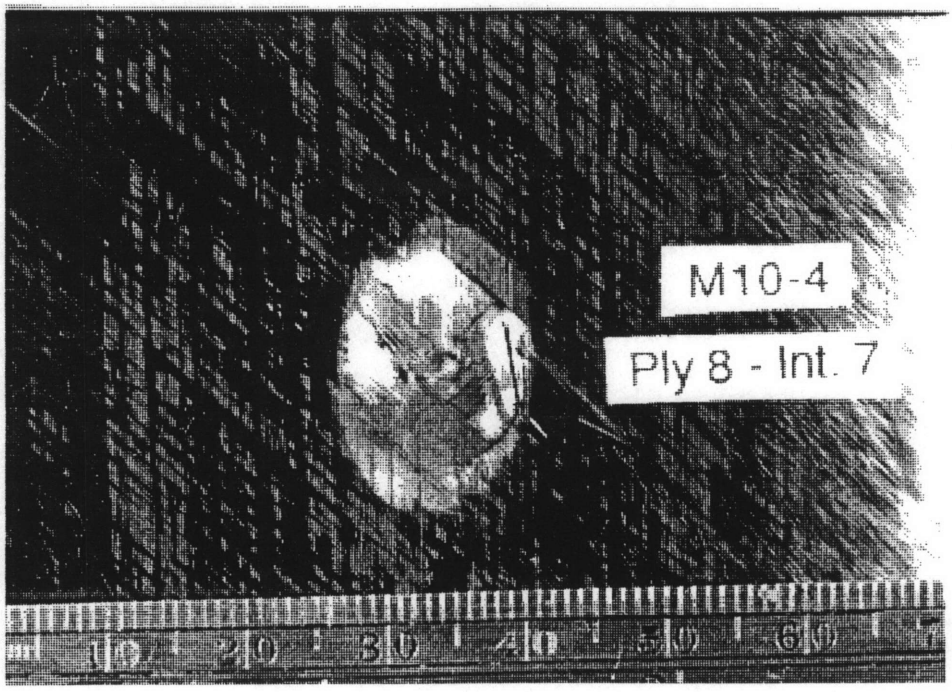

[45/-45/0/45/-45/0/0/**-45**/45/0/-45/45] Impact Surface

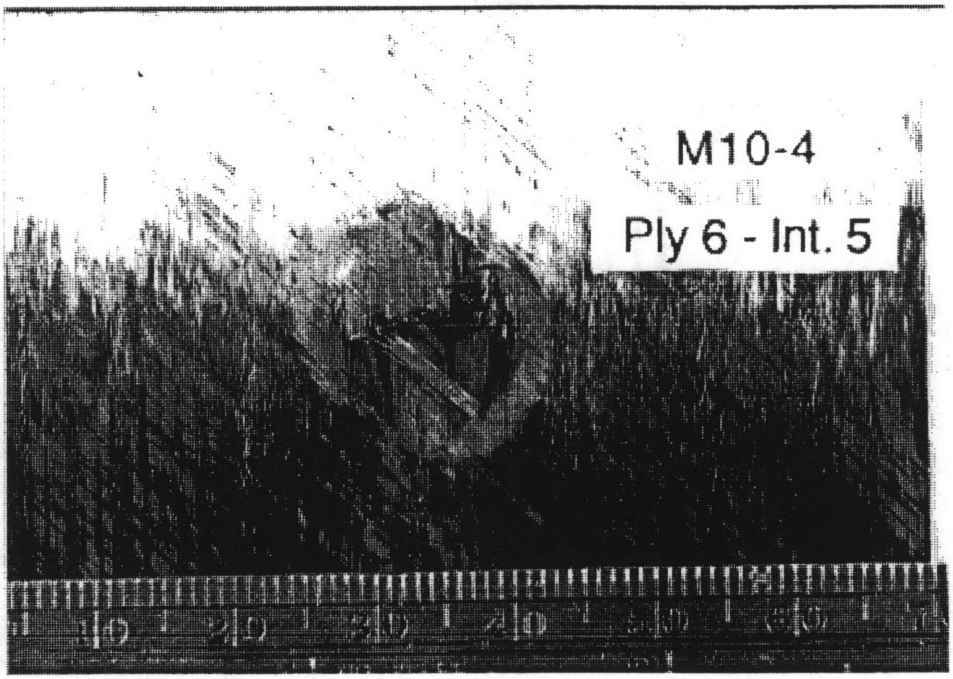

[45/-45/0/45/-45/**0**/0/-45/45/0/-45/45] Impact Surface

Figure 4.91 Deply Photographs of Specimen M10-4 — Ply 8 and Ply 6 (Impacter Mass = 578 g, Velocity = 8.6 m/s).

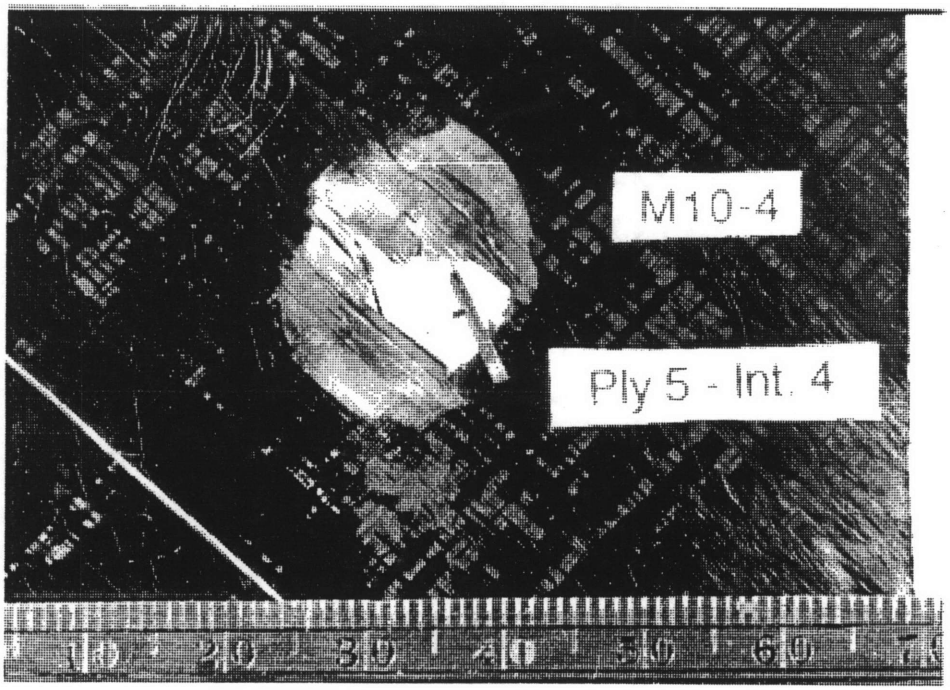

[45/-45/0/45/**/-45**/0/0/-45/45/0/-45/45] Impact Surface

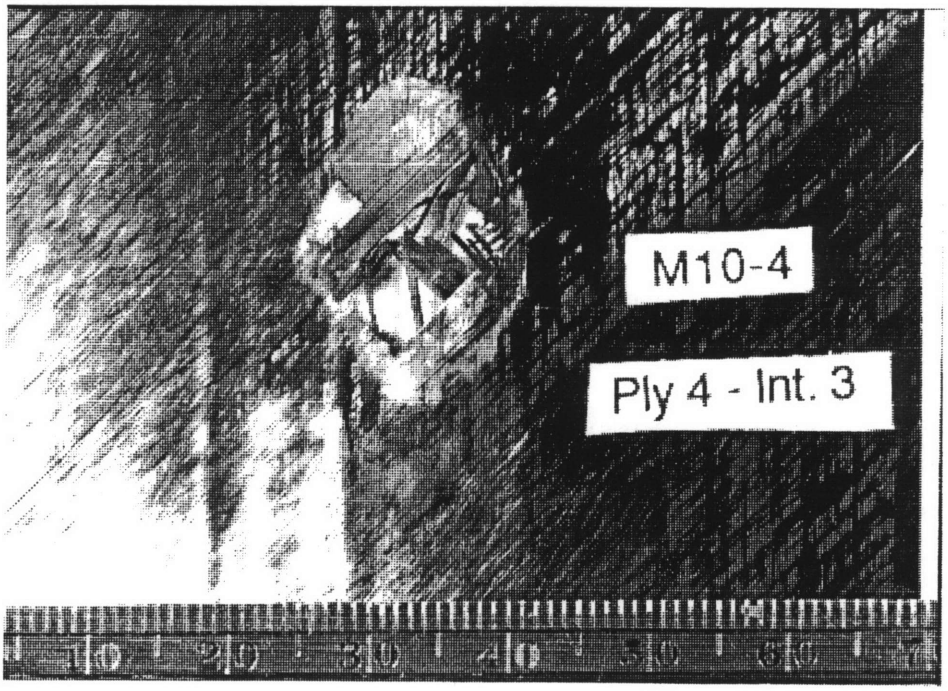

[45/-45/0/**/45**/-45/0/0/-45/45/0/-45/45] Impact Surface

Figure 4.92 Deply Photographs of Specimen M10-4 — Ply 5 and Ply 4 (Impacter Mass = 578 g, Velocity = 8.6 m/s).

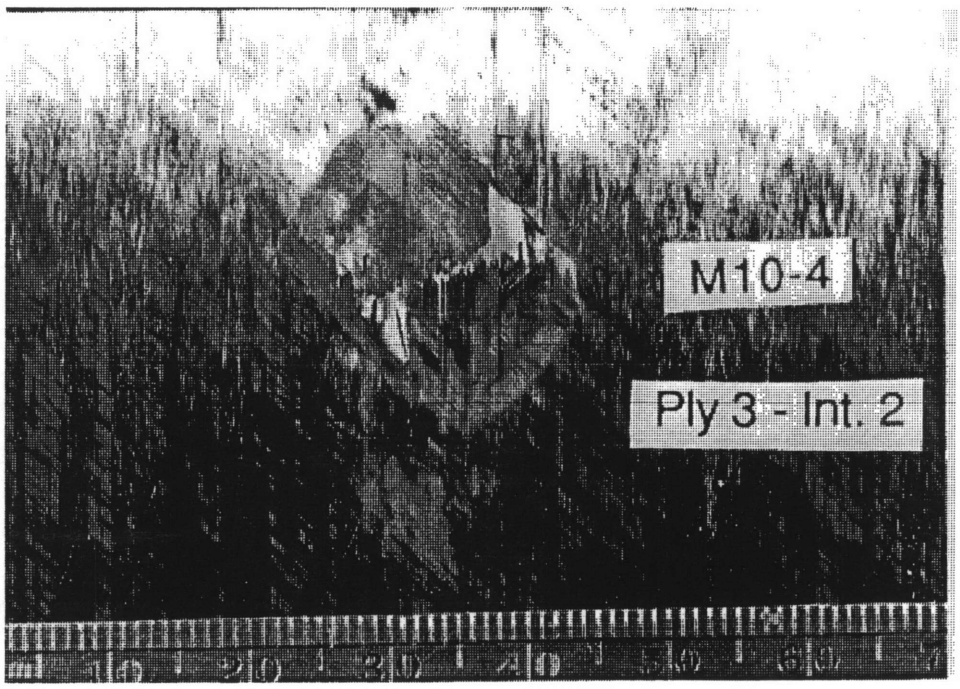

[45/-45/**0**/45/-45/0/0/-45/45/0/-45/45] Impact Surface

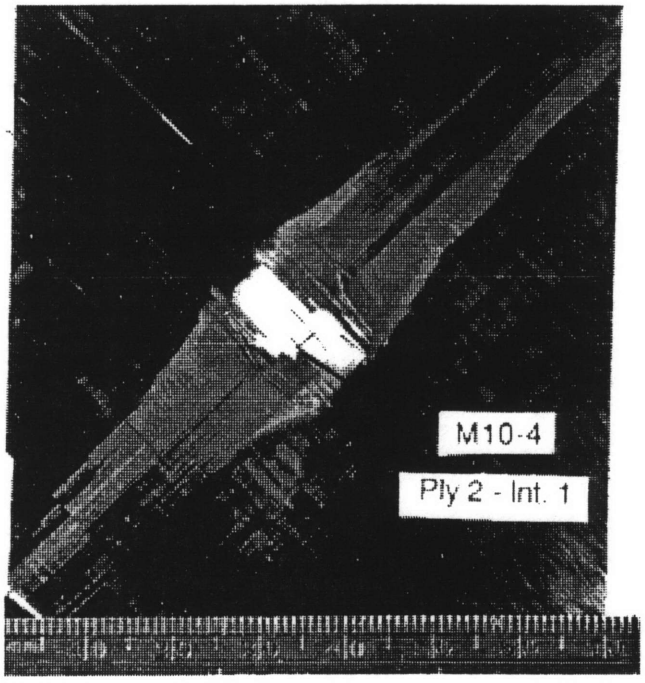

[45/**-45**/0/45/-45/0/0/-45/45/0/-45/45] Impact Surface

Figure 4.93 Deply Photographs of Specimen M10-4 — Ply 3 and Ply 2 (Impacter Mass = 578 g, Velocity = 8.6 m/s).

delamination size increases from approximately 19 mm at interface 5 to 70 mm at interface 1 as shown in Figures 4.91 through 4.93. As with the previously examined photographs in Figures 4.83 and 4.88 of coupons impacted at MCRS-velocities, the back surface split and the fibers peeled towards the edge of the coupon between plies 1 and 2.

Ply-by-ply photographs of damage in a typical coupon impacted with the 8.4 g mass at the MCRS velocity (57 m/s) are presented in Figures 4.94 through 4.98. The photograph of ply 12 in Figure 4.94 exhibits evidence of fiber damage as well as delamination between plies 11 and 12. The major axis of delamination is approximately 14 mm and oriented in the -45° direction of ply 11. Ply 11 exhibits little to no fiber damage and a major axis of delamination between plies 10 and 11 of approximately 13 mm oriented in the 0° direction of ply 10. Though the gold chloride marker did not show clearly in the photographs of plies 9 and 10 in Figure 4.95, visual examination of each ply gave evidence of delamination in the area of impact. The major axes of damage measured 14 and 19 mm respectively with orientations of these delaminations slightly off 0° in the direction of the next plies further away from the impact surface. In the photograph of ply 8 in Figure 4.96, the major axis of delamination measured approximately 31 mm and orientation of the delamination is in the 0° direction of ply 7. Evidence of ply splitting is exaggerated due to the unstacking of the ply. The photograph of ply 6 does not provide a good indication of delamination at the ply 5 interface, though visual inspection resulted in a major axis of delamination measurement of approximately 19 mm in the orientation of the next ply further away from the impact surface. The delamination orientation between plies 4 and 5 and plies 3 and 4 are also in the

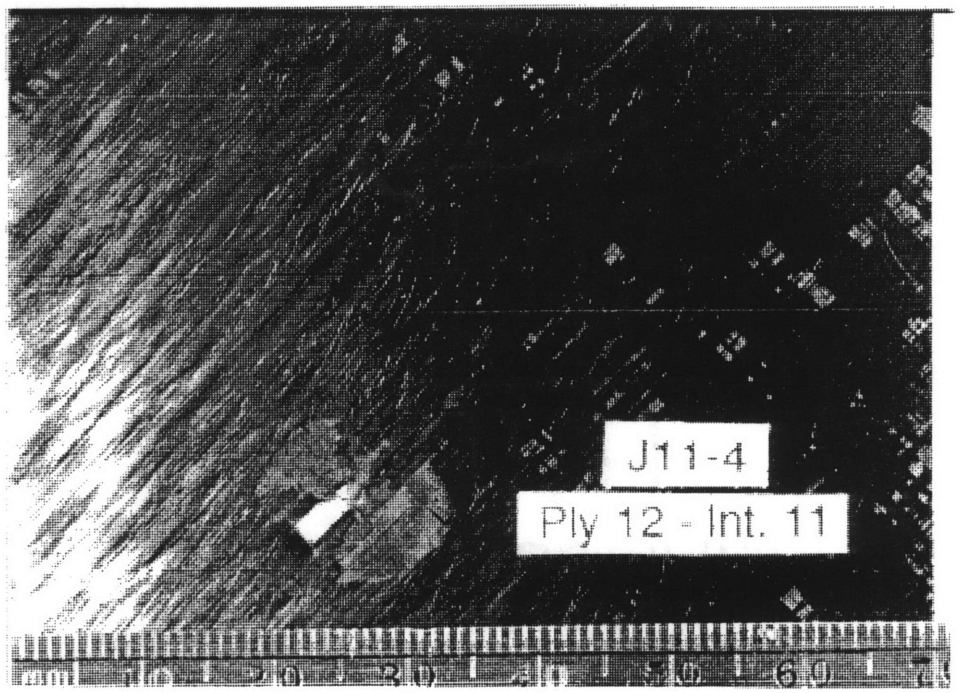

[45/-45/0/45/-45/0/0/-45/45/0/-45//**45**] Impact Surface

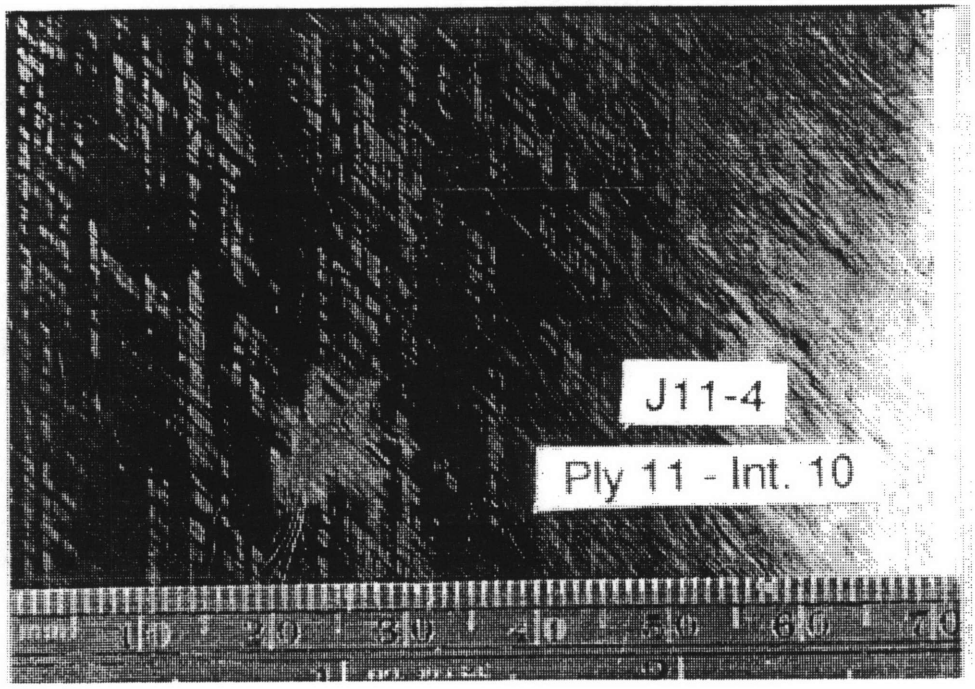

[45/-45/0/45/-45/0/0/-45/45/0/**/-45**/45] Impact Surface

Figure 4.94 Deply Photographs of Specimen J11-4 — Ply 12 and Ply 11 (Impacter Mass = 8.4 g, Velocity = 57 m/s).

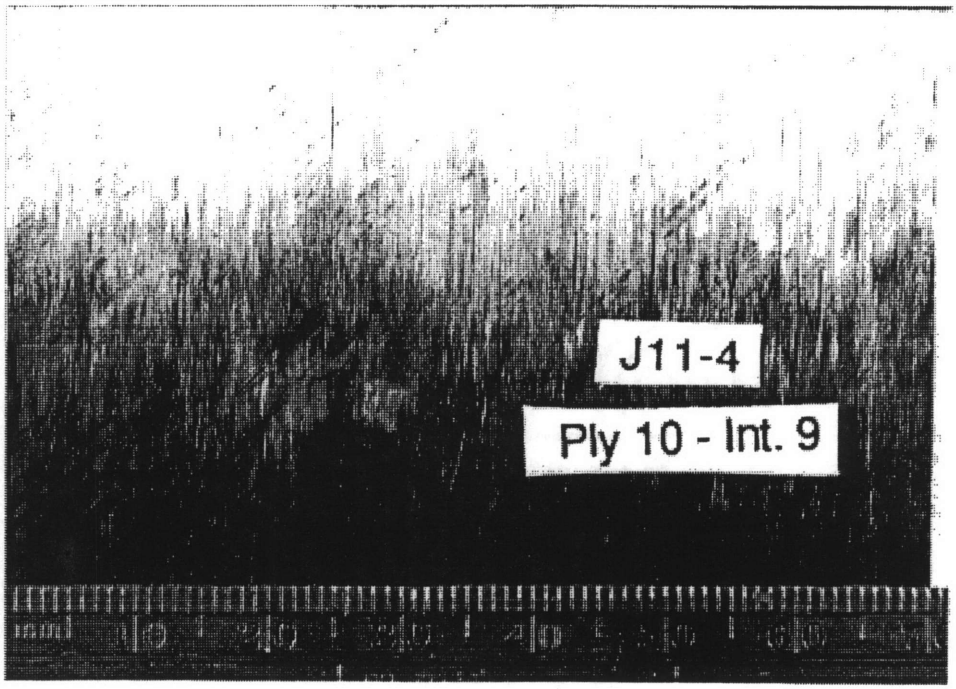

[45/-45/0/45/-45/0/0/-45/45/<u>/0</u>/-45/45] Impact Surface

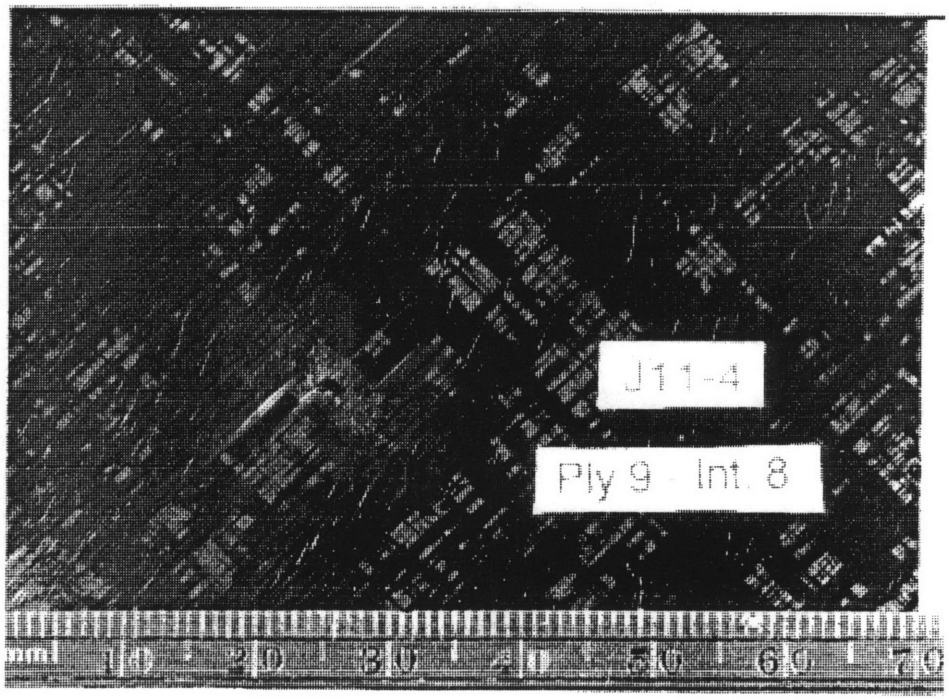

[45/-45/0/45/-45/0/0/-45/<u>/45</u>/0/-45/45] Impact Surface

Figure 4.95 Deply Photographs of Specimen J11-4 — Ply 10 and Ply 9 (Impacter Mass = 8.4 g, Velocity = 57 m/s).

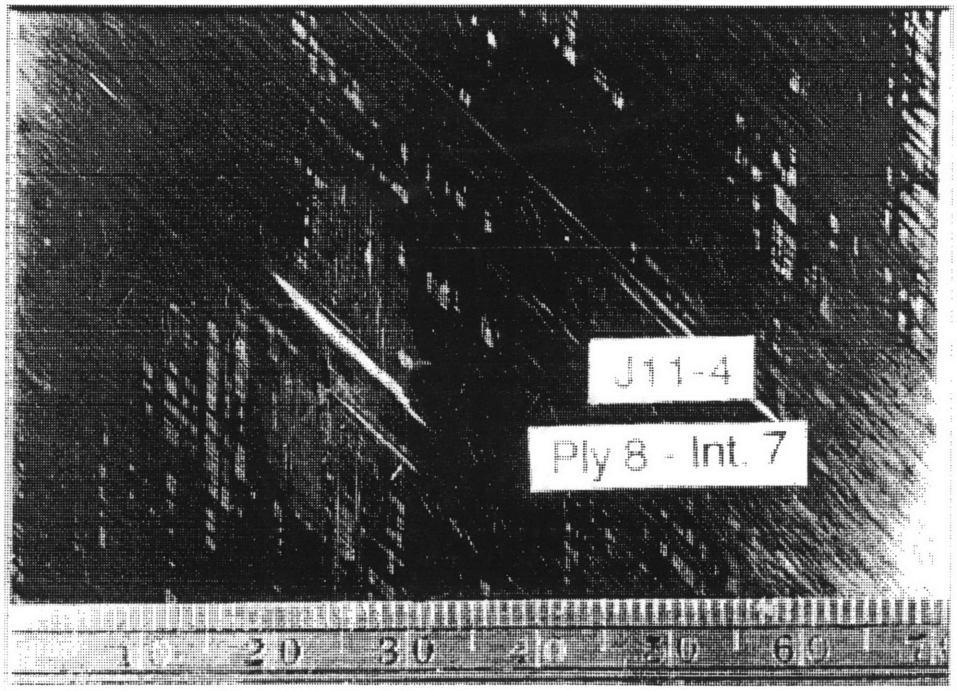

[45/-45/0/45/-45/0/0/**/-45**/45/0/-45/45] Impact Surface

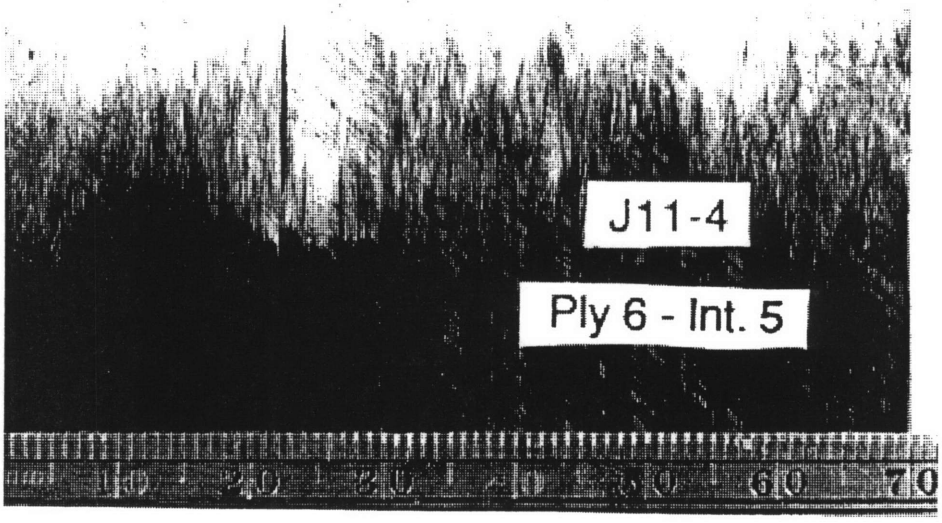

[45/-45/0/45/-45/**/0**/0/-45/45/0/-45/45] Impact Surface

Figure 4.96 Deply Photographs of Specimen J11-4 — Ply 8 and Ply 6 (Impacter Mass = 8.4 g, Velocity = 57 m/s).

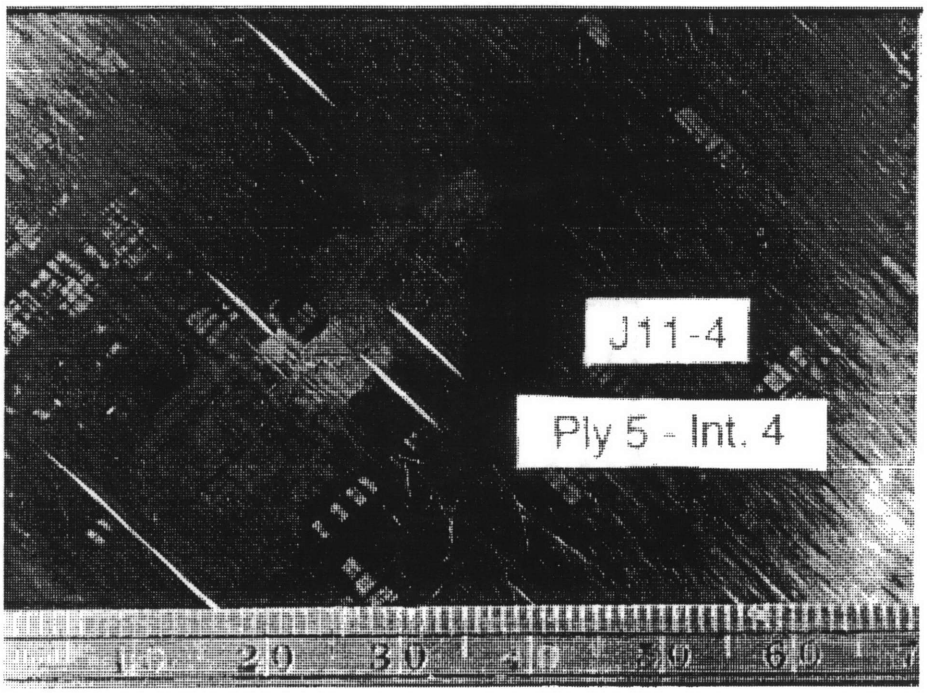

[45/-45/0/45/**/-45**/0/0/-45/45/0/-45/45] Impact Surface

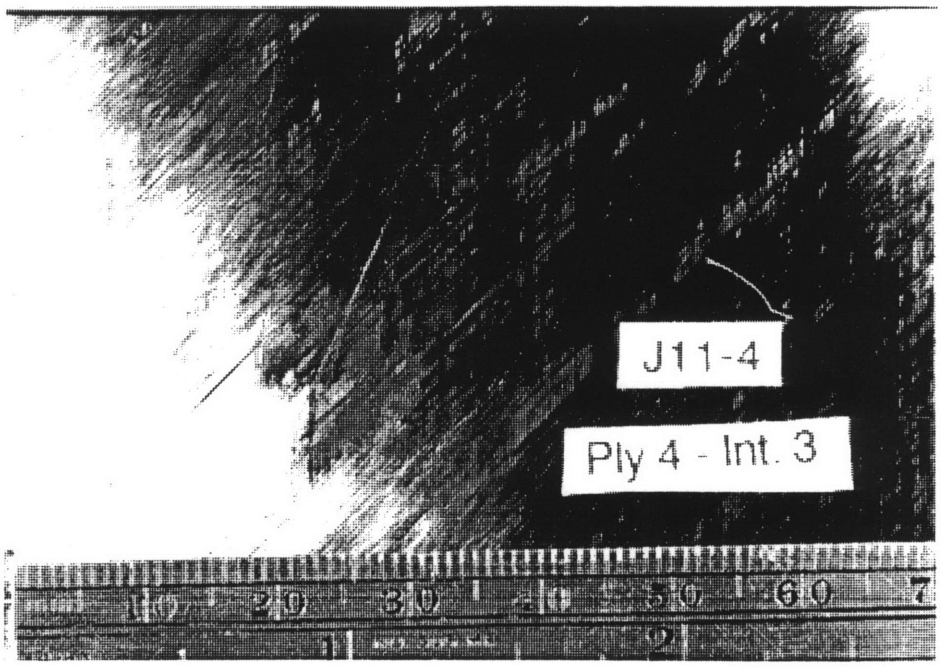

[45/-45/0/**/45**/-45/0/0/-45/45/0/-45/45] Impact Surface

Figure 4.97 Deply Photographs of Specimen J11-4 — Ply 5 and Ply 4 (Impacter Mass = 8.4 g, Velocity = 57 m/s).

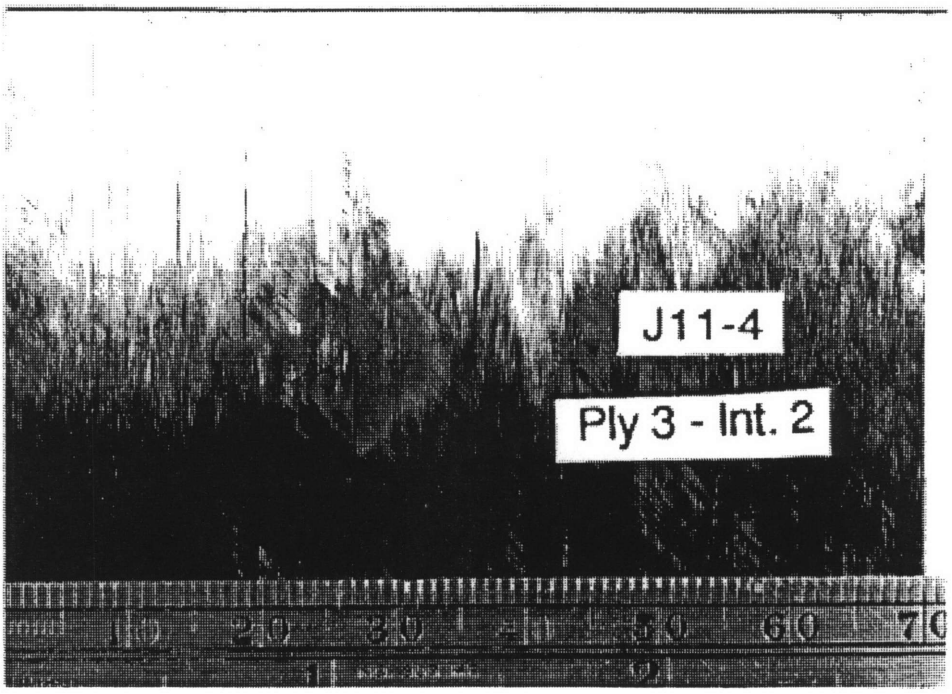

[45/-45/**0**/45/-45/0/0/-45/45/0/-45/45] Impact Surface

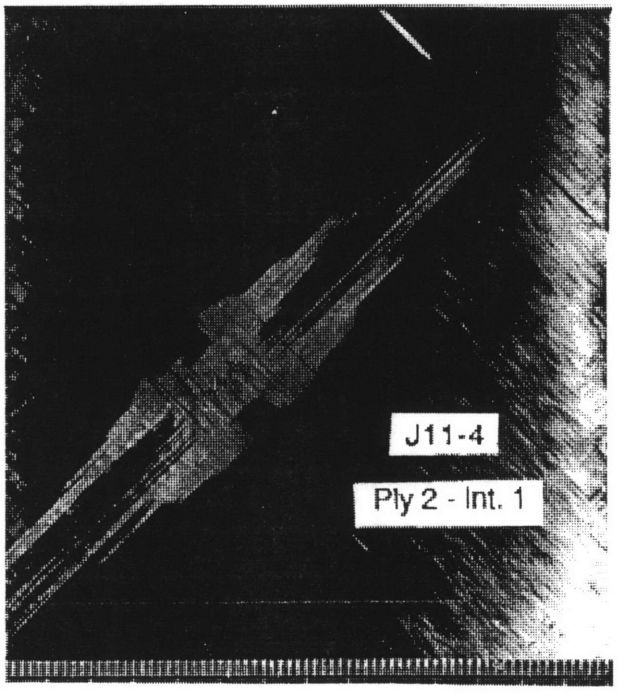

[45/**-45**/0/45/-45/0/0/-45/45/0/-45/45] Impact Surface

Figure 4.98 Deply Photographs of Specimen J11-4 — Ply 3 and Ply 2 (Impacter Mass = 8.4 g, Velocity = 57 m/s).

orientation of the next plies further away from the impact surface as shown in Figure 4.97. However, the major axis of delamination between plies 4 and 5 measures approximately 41 mm while the major axis between plies 3 and 4 is only 16 mm. Delamination orientation between plies 2 and 3 is in the -45° direction of ply 2 though it does not show up well in the photograph in Figure 4.98. The major axis of delamination measures approximately 16 mm. The delamination between plies 1 and 2 is oriented in the ply 1 direction and the major axis measures approximately 58 mm. The back surface split and the fibers peeled towards the edge of the coupon between plies 1 and 2 as evidenced by the gold chloride marker on ply 2.

Though 57 m/s was identified as the MCRS-velocity for impact with the 8.4 g mass, testing conducted in this work resulted in a similar compressive residual strength at 70 m/s. Thus, a coupon impacted by an 8.4 g mass at 70 m/s was also evaluated by the deply technique as shown in Figures 4.99 through 4.103. Though the spherical impacter did not break through the coupon at this velocity, through-the-thickness damage was similar to the coupons impacted with the 1523 and 578 g masses at their respective MCRS-velocities. Significant fiber damage occurred in each ply. Delamination orientation coincided with the orientation of the next ply further away from the impact surface and delamination size increased away from the impact surface. The major axis of delamination size increases from approximately 20 mm at interface 11 in Figure 4.98 to 70 mm at interface 1 in Figure 4.103. This differs from the photographs of the coupon impacted at the MCRS-velocity for the 8.4 g impacter mass in Figures 4.94 through 4.98 where delamination size does not consistently increase as distance from the impact surface increases. For the coupon

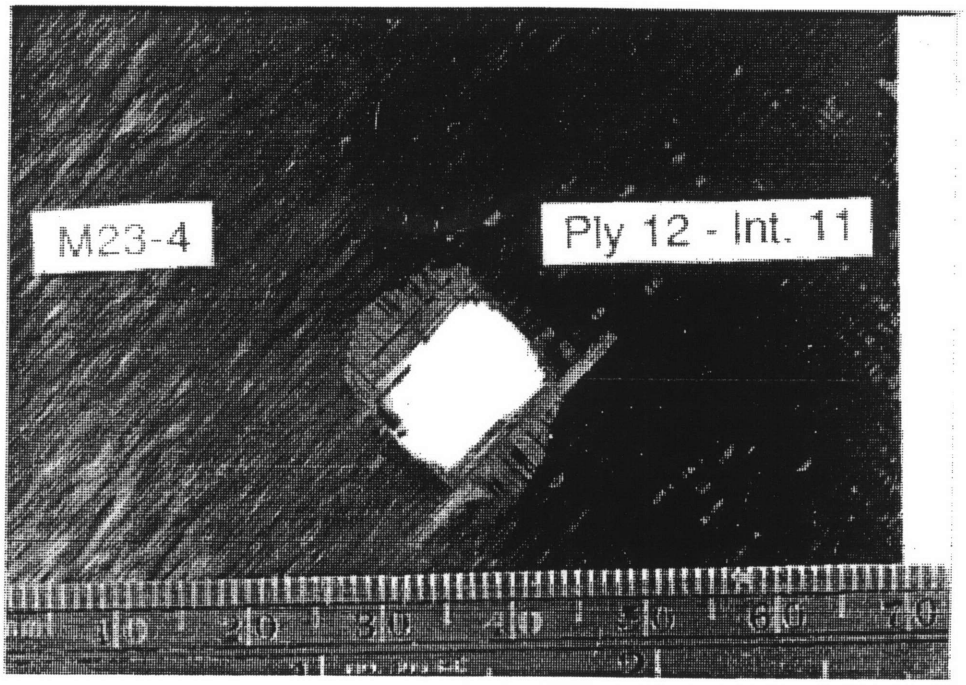

[45/-45/0/45/-45/0/0/-45/45/0/-45/**45**] Impact Surface

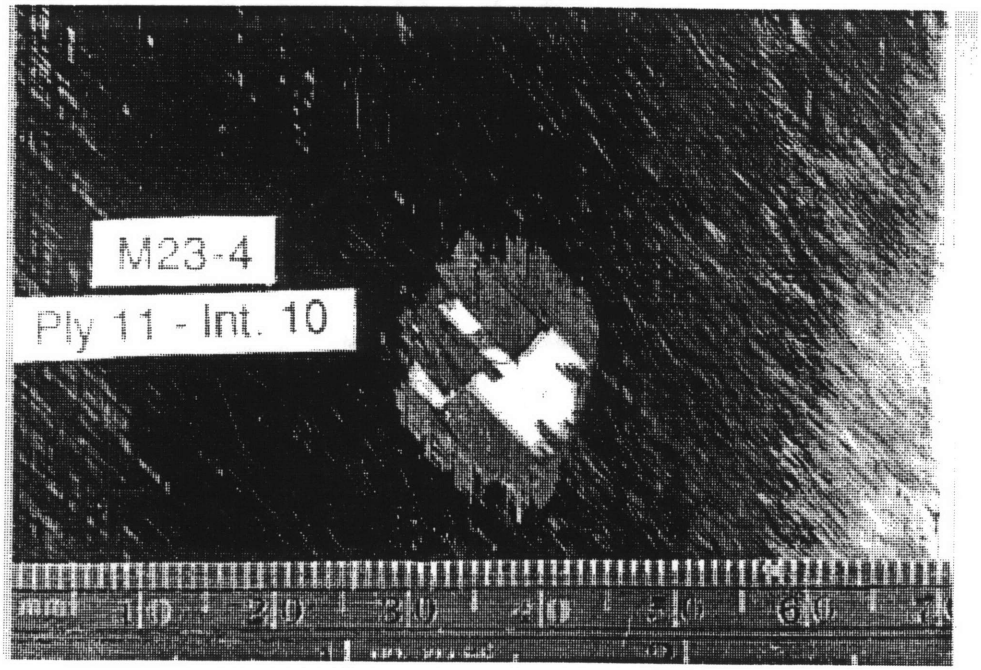

[45/-45/0/45/-45/0/0/-45/45/0/**-45**/45] Impact Surface

Figure 4.99 Deply Photographs of Specimen M23-4 — Ply 12 and Ply 11 (Impacter Mass = 8.4 g, Velocity = 70 m/s).

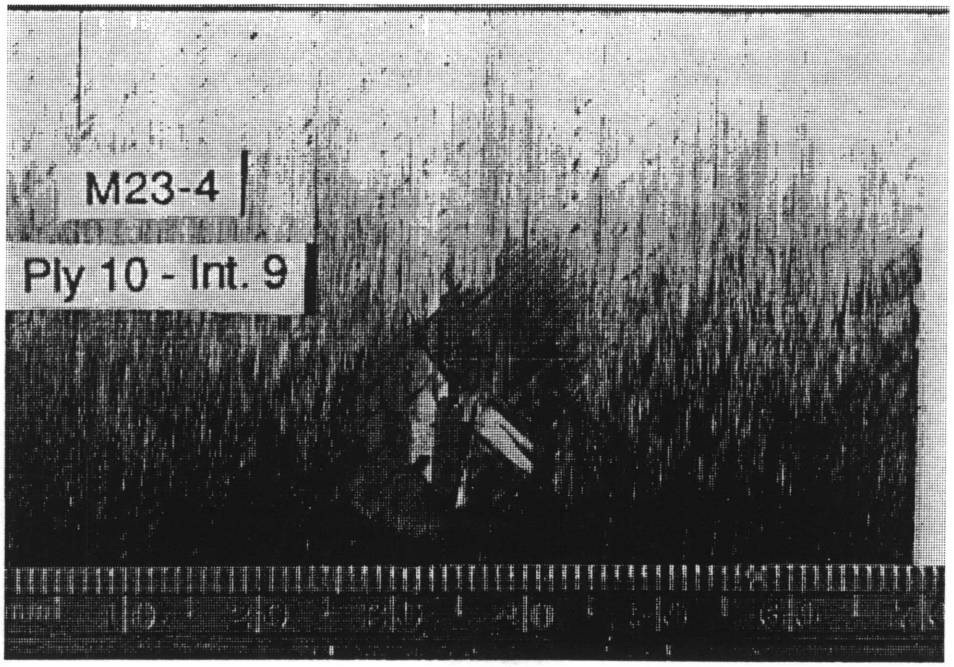

[45/-45/0/45/-45/0/0/-45/45/**/0**/-45/45] Impact Surface

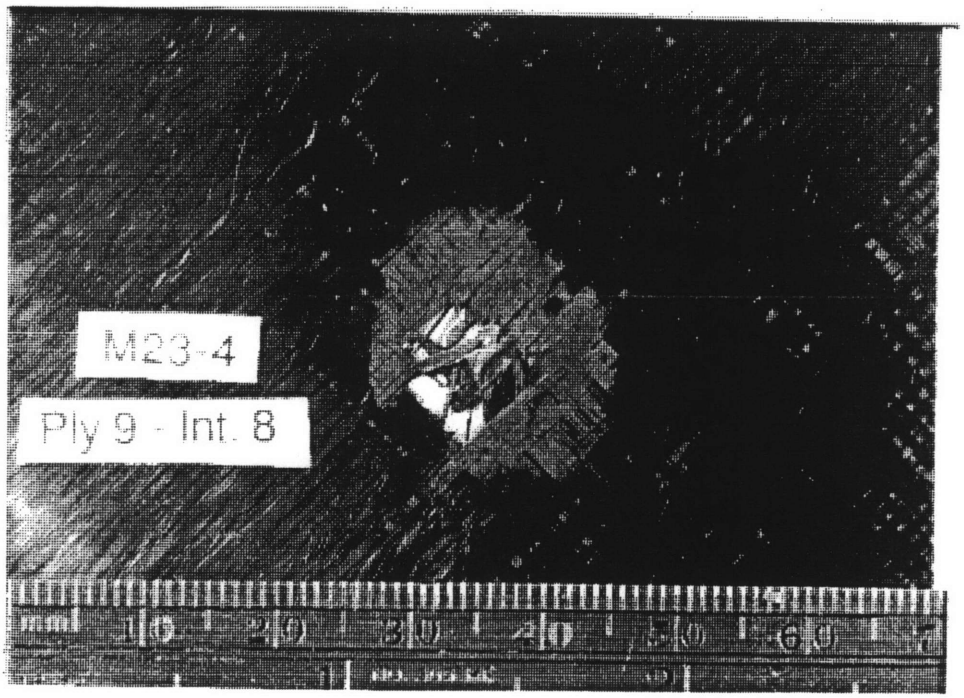

[45/-45/0/45/-45/0/0/-45/**/45**/0/-45/45] Impact Surface

Figure 4.100 Deply Photographs of Specimen M23-4 — Ply 10 and Ply 9 (Impacter Mass = 8.4 g, Velocity = 70 m/s).

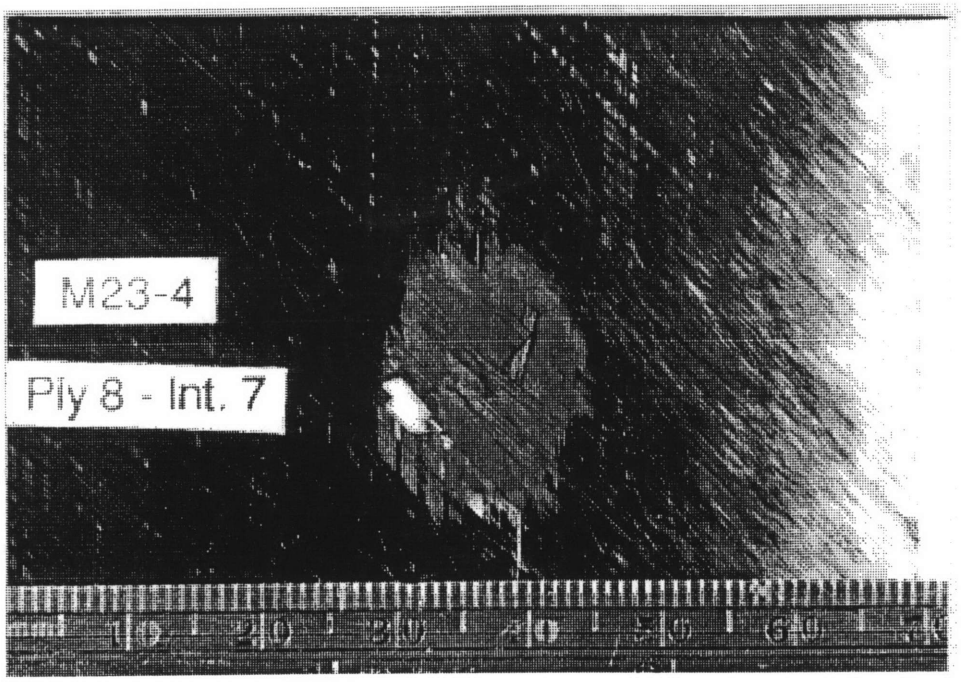

[45/-45/0/45/-45/0/0/<u>/**-45**</u>/45/0/-45/45] Impact Surface

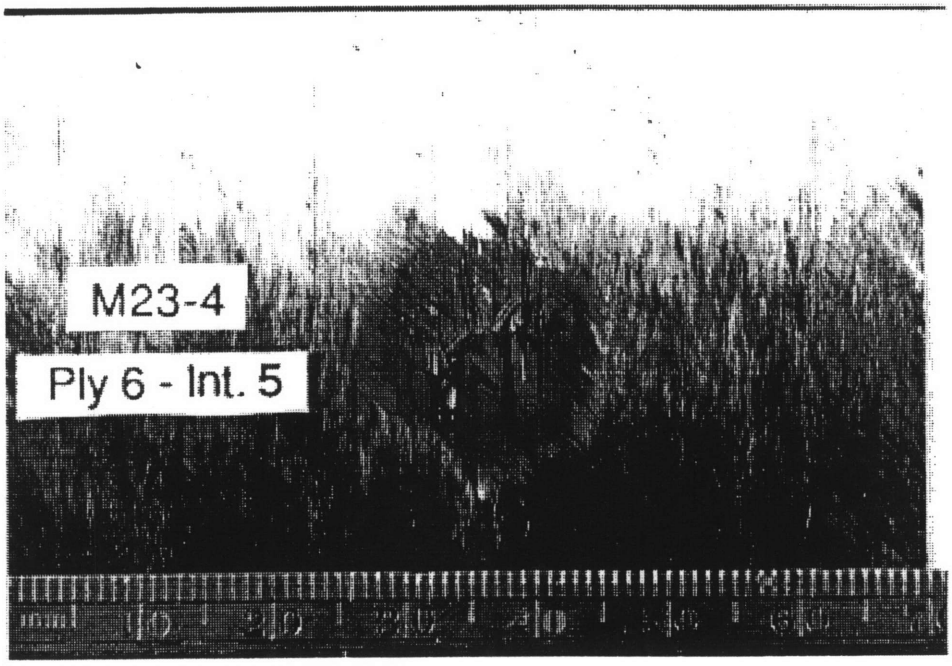

[45/-45/0/45/-45/<u>/**0**</u>/0/-45/45/0/-45/45] Impact Surface

Figure 4.101 Deply Photographs of Specimen M23-4 — Ply 8 and Ply 6 (Impacter Mass = 8.4 g, Velocity = 70 m/s).

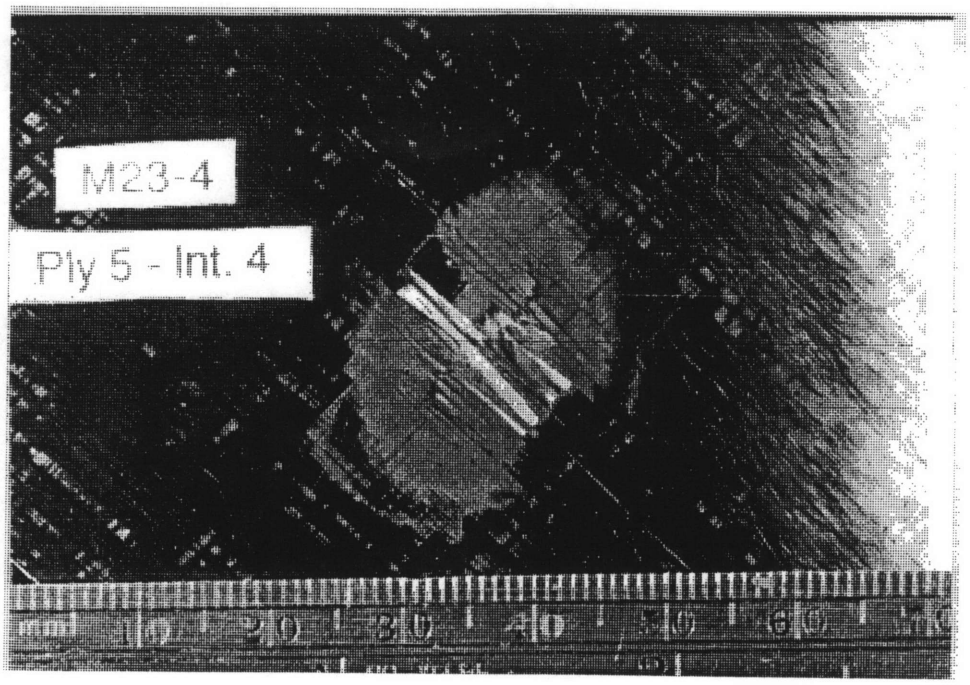

[45/-45/0/45/**/-45**/0/0/-45/45/0/-45/45] Impact Surface

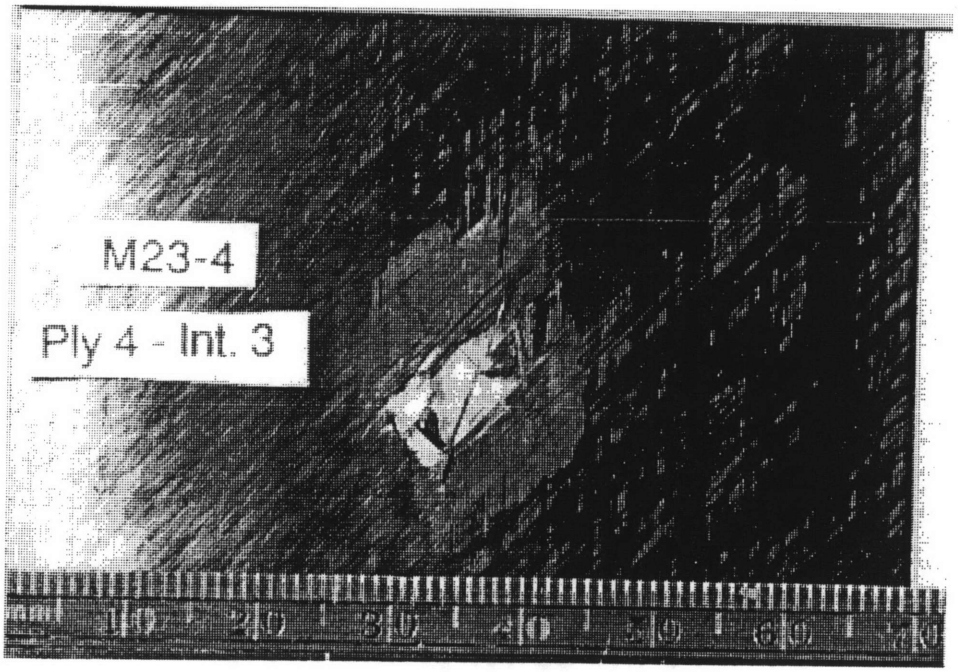

[45/-45/0/**/45**/-45/0/0/-45/45/0/-45/45] Impact Surface

Figure 4.102 Deply Photographs of Specimen M23-4 — Ply 5 and Ply 4 (Impacter Mass = 8.4 g, Velocity = 70 m/s).

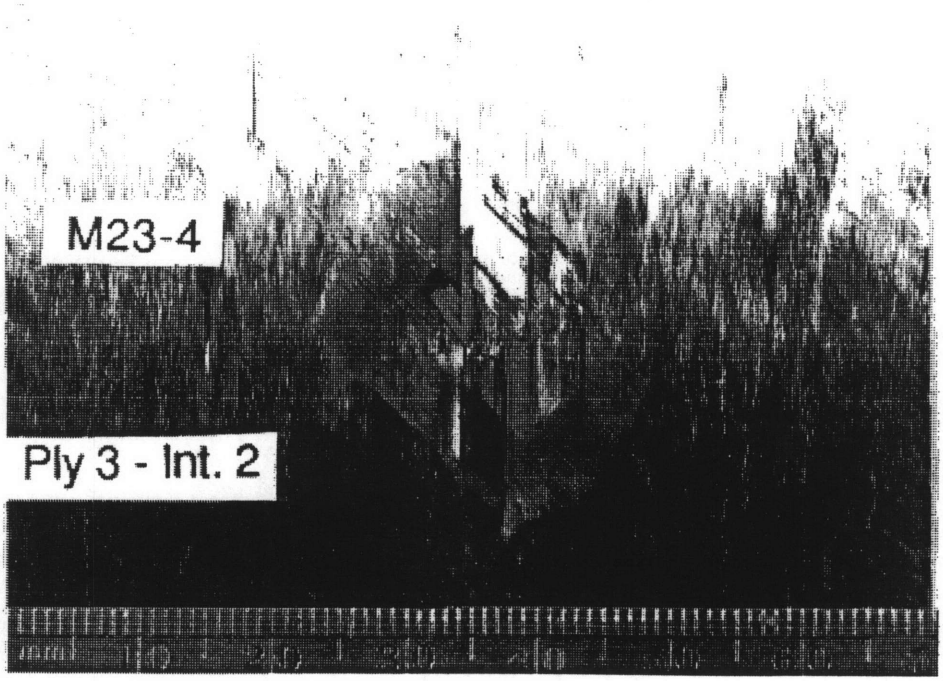

[45/-45/**/0**/45/-45/0/0/-45/45/0/-45/45] Impact Surface

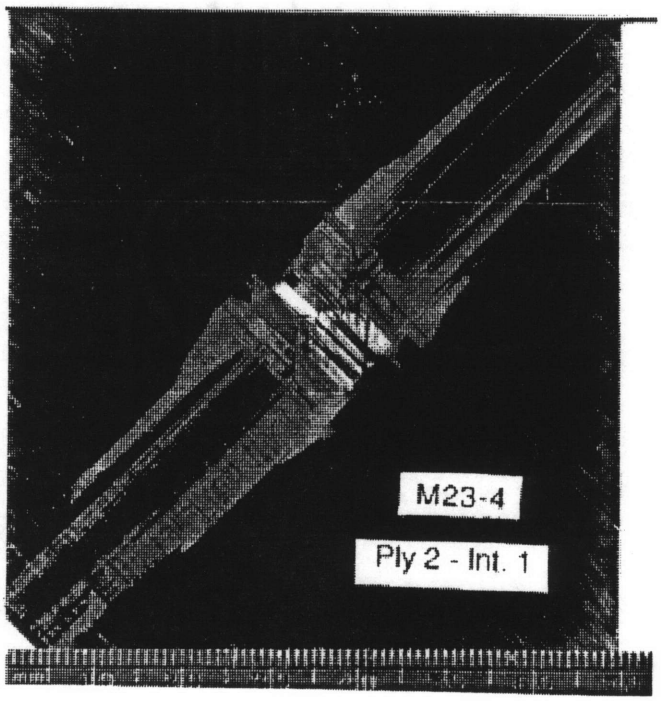

[45/**/-45**/0/45/-45/0/0/-45/45/0/-45/45] Impact Surface

Figure 4.103 Deply Photographs of Specimen M23-4 — Ply 3 and Ply 2 (Impacter Mass = 8.4 g, Velocity = 70 m/s).

impacted by an 8.4 g mass at 70 m/s, as with the previously examined photographs of coupons impacted at their respective MCRS-velocities for the 1523 g impacter mass (Figures 4.83) and the 578 g impacter mass (Figure 4.93), the back surface split and the fibers peeled towards the edge of the coupon between plies 1 and 2 as shown in Figure 103.

Damage evaluation by deply of the coupons provides valuable information on the three-dimensional damage state at the velocities investigated. A comparison of deply results at the respective MCRS-velocities for the three impacter masses used in this work is made in Section 4.5.

4.5 MCRS Damage State Definitions

It was previously shown in Section 4.3.2 that information provided by X-ray photographs on the damage state in a specimen after impact is not sufficient to relate to compressive residual strength. It is therefore not a good sole source of data for prediction of compressive residual strength. However, X-ray was the only nondestructive damage evaluation method used on all impact-damaged specimens in this work. Thus, the only "link" available for comparison of all impact-damaged specimens is by comparison of X-ray photographs.

The baseline for comparison of the damage state at MCRS is presented in Figure 4.104. There is no obvious explanation for the differences in compressive residual strength provided by the comparison of the X-ray photographs of specimens resulting in the same minimum compressive residual strength for the three impacter masses. (The X-ray

Mass = 8.4 g, Velocity = 70 m/s
CRS = 197 MPa (M30-1)

Mass = 578 g, Velocity = 9.2 m/s
CRS = 191 MPa (J1-2)

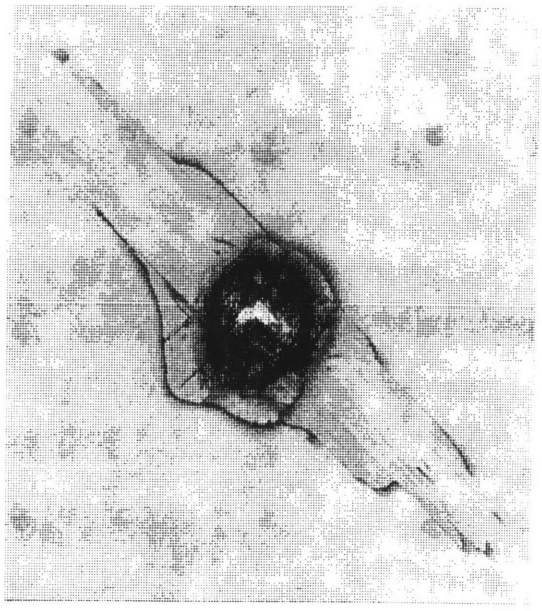

Mass = 1523 g, Velocity = 6.3 m/s
CRS = 184 MPa (M3-2)

(X-rays are to scale)

Figure 4.104 X-ray Photographs of Minimum Compressive Residual Strength Specimens for Three Impacter Masses.

photograph of M30-1, impacted at 70 m/s by an 8.4 g mass resulting in a residual strength of 197 MPa, is used for comparison as the X-ray photographs from the previous project [83] are not available and specimens impacted in this work at 57 m/s did not result in compressive residual strengths near the minimum.) The core damage size ranges from 17 to 23 mm. The minor axis of damage ranges from 21 to 27 mm. And the major axis of damage ranges from 69 to 80 mm. (The variation in damage orientation of Specimen J1-2 was due to impact on the ply 1 instead ply 12 as illustrated in Figure 3.12.)

In an attempt to accurately define the damage state by destructive evaluation, specimens selected for deply or cross-sectioning had similar damage as determined by X-ray to that of the minimum compressive residual strength specimen. The X-ray photographs of specimens selected for the MCRS damage state definition due to impact by the 1523 g mass are presented in Figure 4.105 with that of Specimen M3-2 which failed at 184 MPa.

The cross-section damage evaluation summary for the case of the 1523 g impacter mass at 6.3 m/s is presented in Figure 4.106. A summary of the damage evaluation by the time-of-flight ultrasonic C-Scan for the same coupon is presented in Figure 4.107. This summary was done by tracing outlines of damage indications observed in each time-of-flight ultrasonic C-Scan with the aid of a light table. Interpretations of time-of-flight ultrasonic C-Scans were checked by two individuals to verify similar observations. These damage indications are not necessarily centered for each ply in each summary. Thus, comparsion of one summary to another does not include exact location of ply damage within the window. The

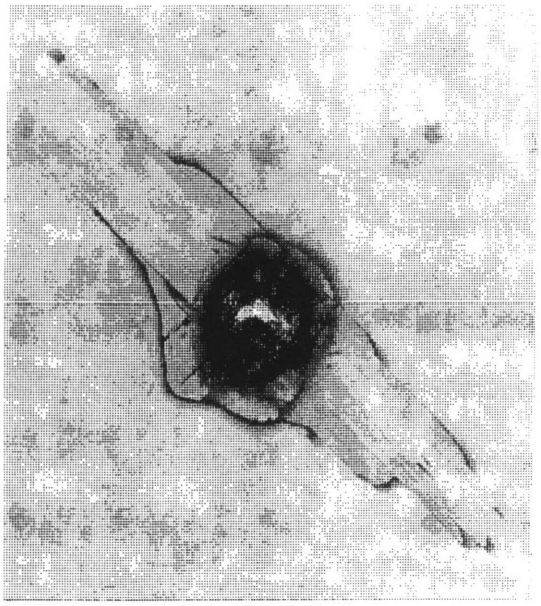

MCRS = 184 MPa (M3-2)

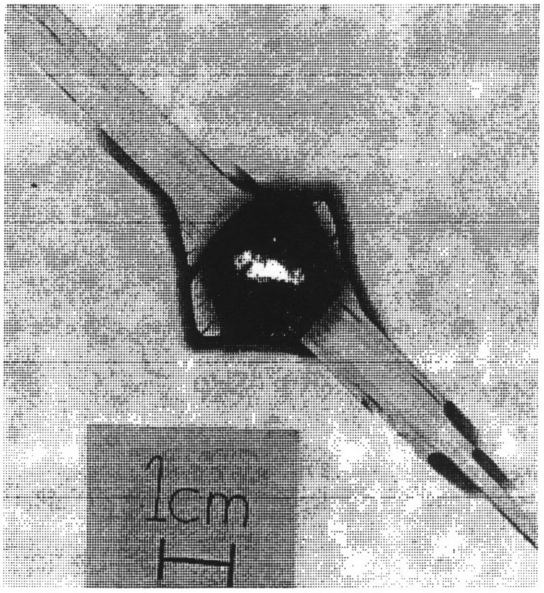

Cross-Section (T5-2)

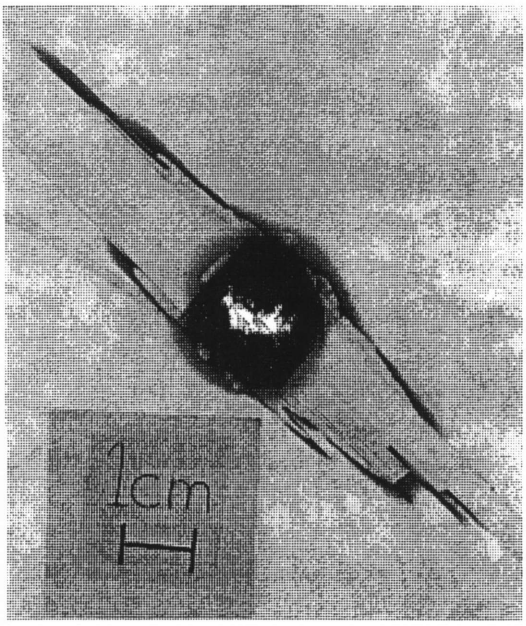

Deply (M8-2)

(X-rays are to scale)

Figure 4.105 X-ray Photographs of Three Specimens Impacted by the 1523 g Mass at the MCRS-Velocity of 6.3 m/s.

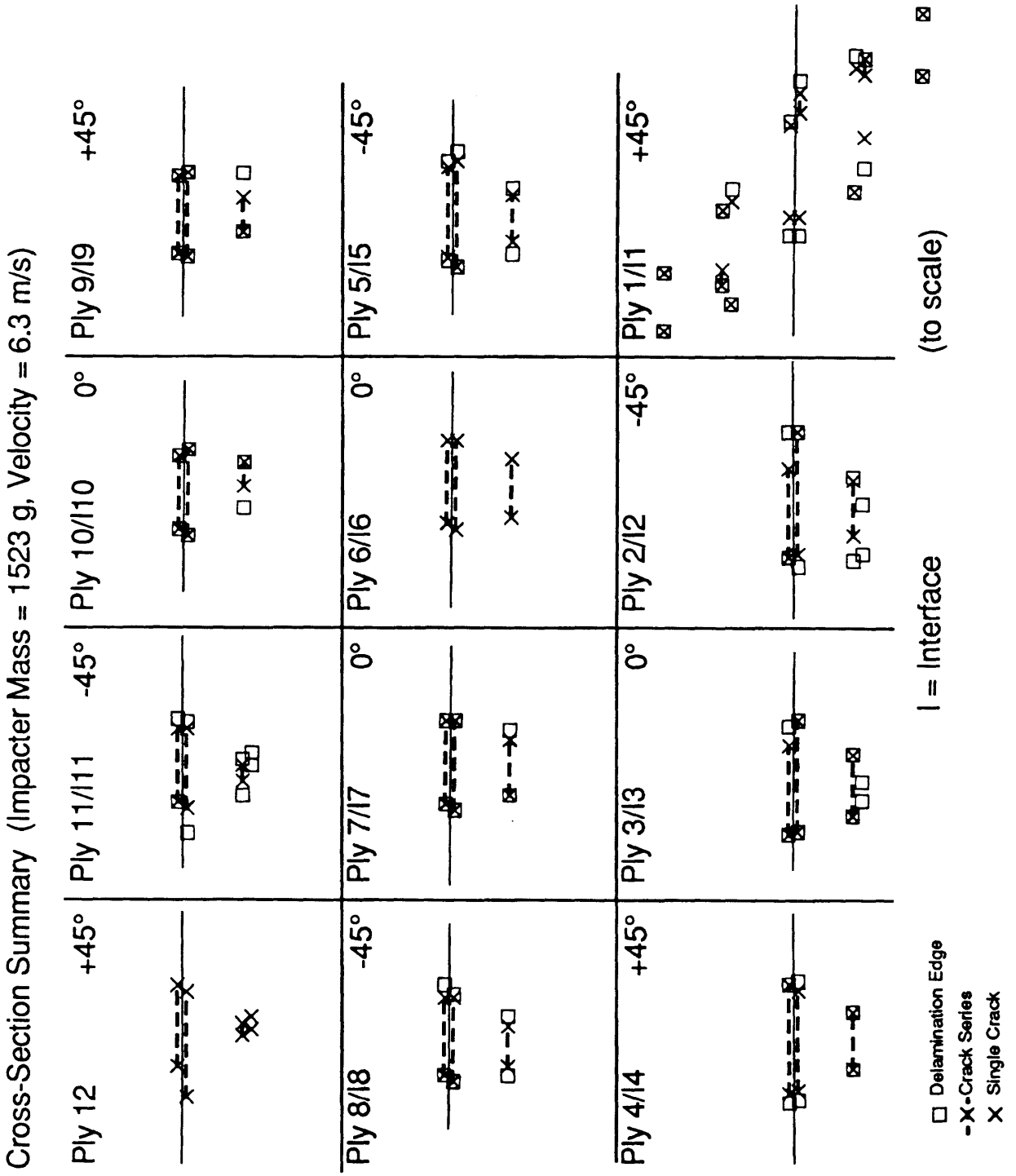

Figure 4.106 Summary of Damage Observed in Specimen T5-2 by Cross-Sectioning (Impacter Mass = 1523 g, Velocity = 6.3 m/s).

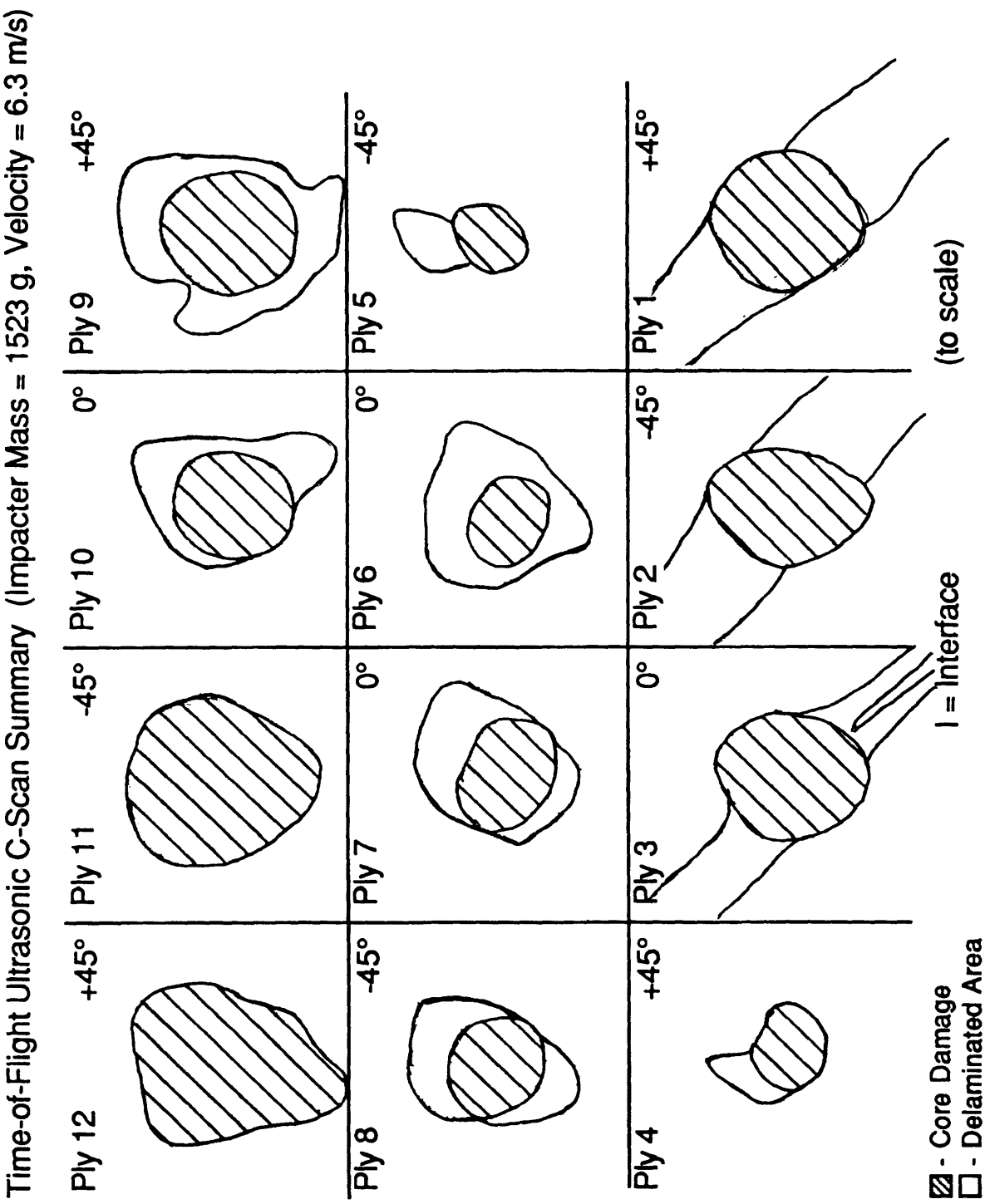

Figure 4.107 Summary of Damage Observed in Specimen T5-2 by Time-of-Flight Ultrasonic C-Scan (Impacter Mass = 1523 g, Velocity = 6.3 m/s).

immediate loss of the backwall reflection in the ultrasonic C-Scan due to penetration at this impacter velocity results in indications of significant core damage size in plies 11 and 12 in Figure 4.107. The core damage size indications in the ultrasonic C-Scans of plies 4 and 5 are small compared to the cross-section schematics. Core damage size indications in the remaining plies are similar by the two evaluation methods. Delamination indications, when present in the ultrasonic ply-by-ply C-Scans (Figure 4.107), do not appear representative of the size, shape, or orientation compared to those seen in the cross-section schematics (Figure 4.106) with the possible exceptions of plies 1, 7, and 8. The ultrasonic C-Scan of ply 6 shows evidence of delamination which does not agree with the cross-section summary for this specimen (nor was evidence of delamination at this interface seen by any destructive evaluation method at any of the tested velocities for any of the impacter masses used). The indications of delamination oriented in the 45° direction in the ultrasonic C-Scans of plies 2 and 3 in Figure 4.107 are believed to be a "preview" of the delamination that is observed by cross-section evaluation at interface 1 in Figure 4.106.

The deply damage evaluation summary for the case of the 1523 g impacter mass at 6.3 m/s is presented in Figure 4.108. A summary of the damage evaluation by the time-of-flight ultrasonic C-Scan for the same coupon is presented in Figure 4.109. (The same coupon cannot be cross-sectioned and deplied, thus, the need for two summaries of the damage by the time-of-flight ultrasonic C-Scans.) The summary of damage evaluation by deply was first done by tracing outlines of core damage from the ply (not the ply photograph) with the aid of a light table. Then observations on the major and minor axes of damage and delamination shape were transferred

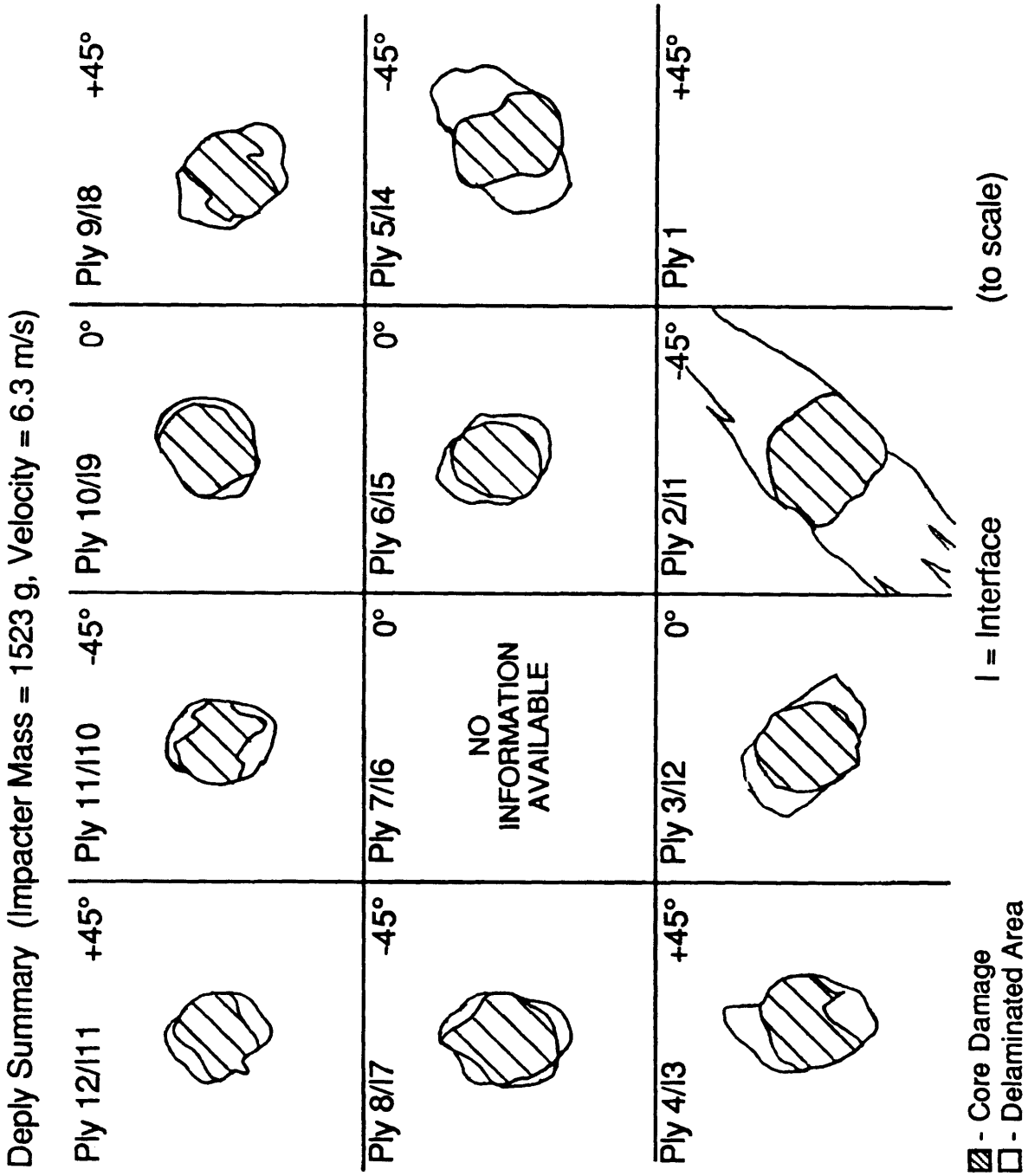

Figure 4.108 Summary of Damage Observed in Specimen M8-2 by Deply (Impacter Mass = 1523 g, Velocity = 6.3 m/s).

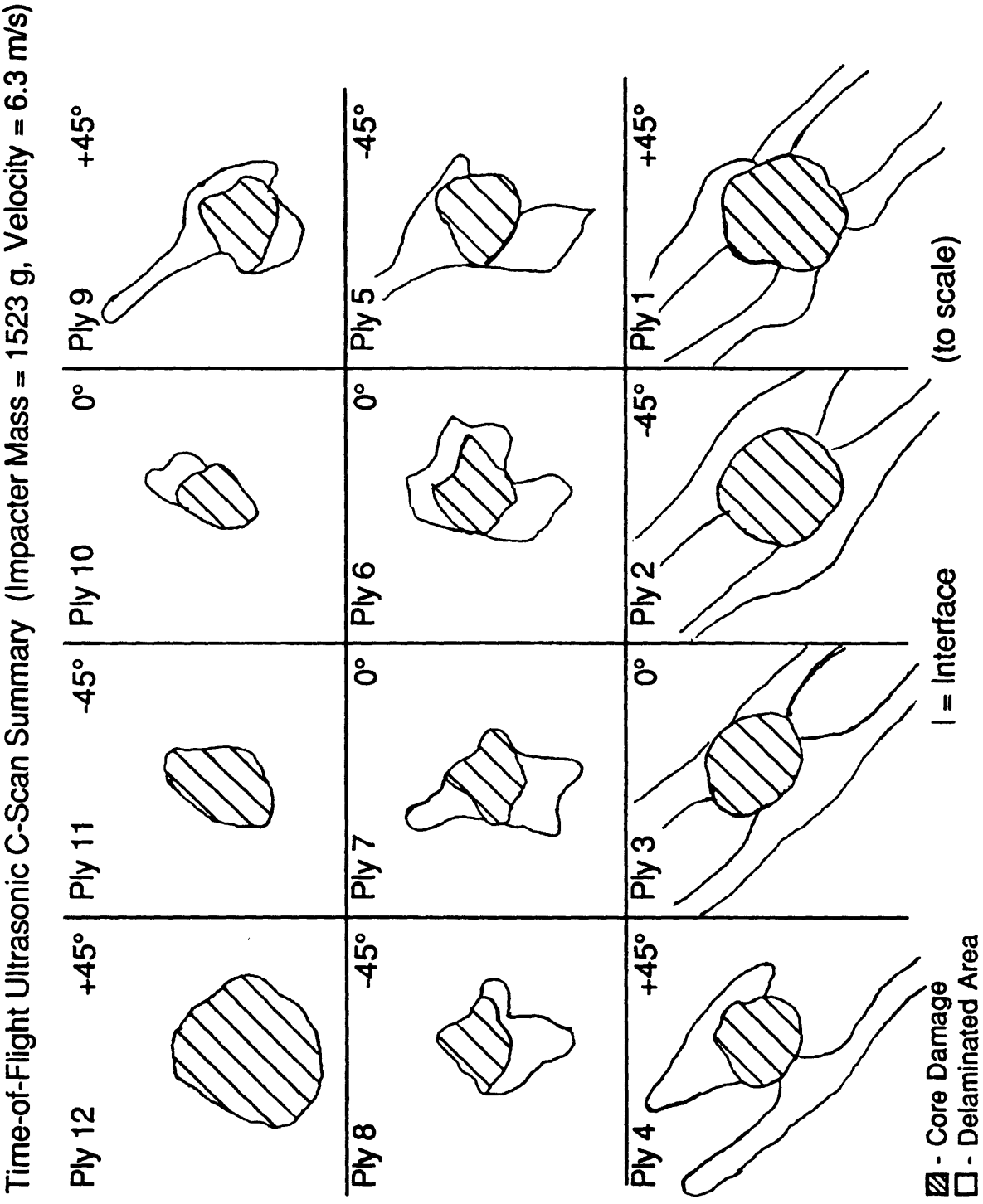

Figure 4.109 Summary of Damage Observed in Specimen M8-2 by Time-of-Flight Ultrasonic C-Scan (Impacter Mass = 1523 g, Velocity = 6.3 m/s).

to the drawing by free-hand. The deply summaries were checked by two individuals to verify similar observations. These damage indications are not necessarily centered for each ply in each summary. Thus, comparsion of one summary to another does not include exact location of ply damage within the window. The information provided on the core damage, the delamination size, and the delamination orientation by the deply method required no "interpretation". Thus, the information presented in Figure 4.108 is an accurate representation of the damage state which existed in this specimen due to impact by a 1523 g mass at a velocity of 6.3 m/s. The core damage sizes correlate better between these two evaluation methods than they did for the cross-section and time-of-flight summaries of a coupon with similar impact metrics. However, the delamination information provided by the time-of-flight ultrasonic C-Scan in Figure 4.109 is still an inaccurate representation of the actual damage shape and orientation. Damage size indications provided by the time-of-flight ultrasonic C-Scans is not consistently larger or smaller than the actual size determined by destructive evaluation.

The X-ray photographs of specimens selected for the MCRS damage state definition due to impact by the 578 g mass are presented in Figure 4.110 with that of Specimen J1-2 which failed at 191 MPa.

The cross-section damage evaluation summary for the case of the 578 g impacter mass at 9.2 m/s is presented in Figure 4.111. A summary of the damage evaluation by the time-of-flight ultrasonic C-Scan for the same coupon is presented in Figure 4.112. These damage indications are not necessarily centered for each ply in each summary. Thus, comparsion of one summary to another does not include exact location of ply damage

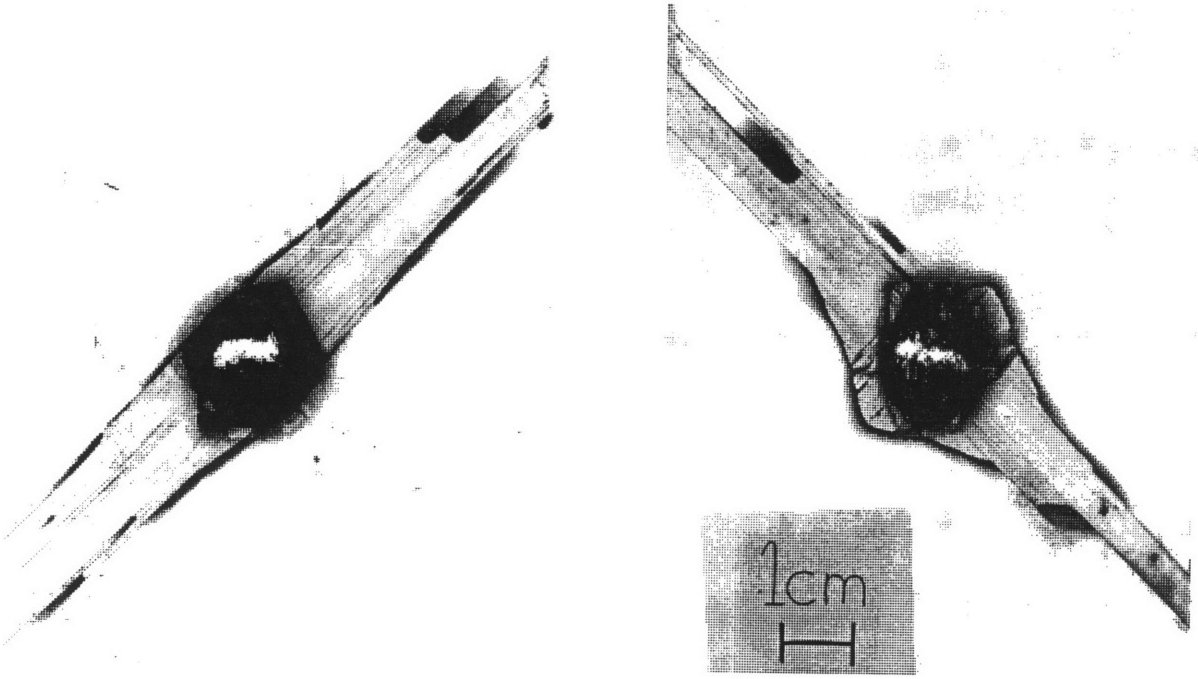

MCRS = 191 MPa (J1-2)
Velocity = 9.2 m/s

Cross-Section (J6-2)
Velocity = 9.2 m/s

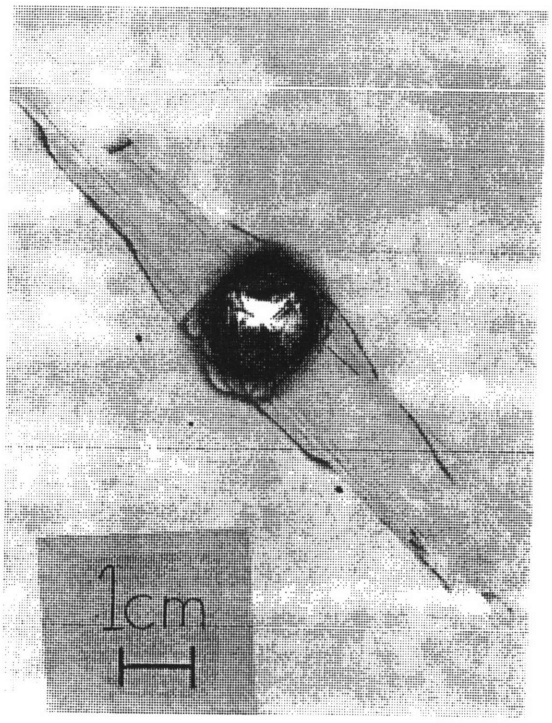

Deply (M10-4)
Velocity = 8.6 m/s

(X-rays are to scale)

Figure 4.110 X-ray Photographs of Three Specimens Impacted by the 578 g Mass Near the MCRS-Velocity of 9.2 m/s.

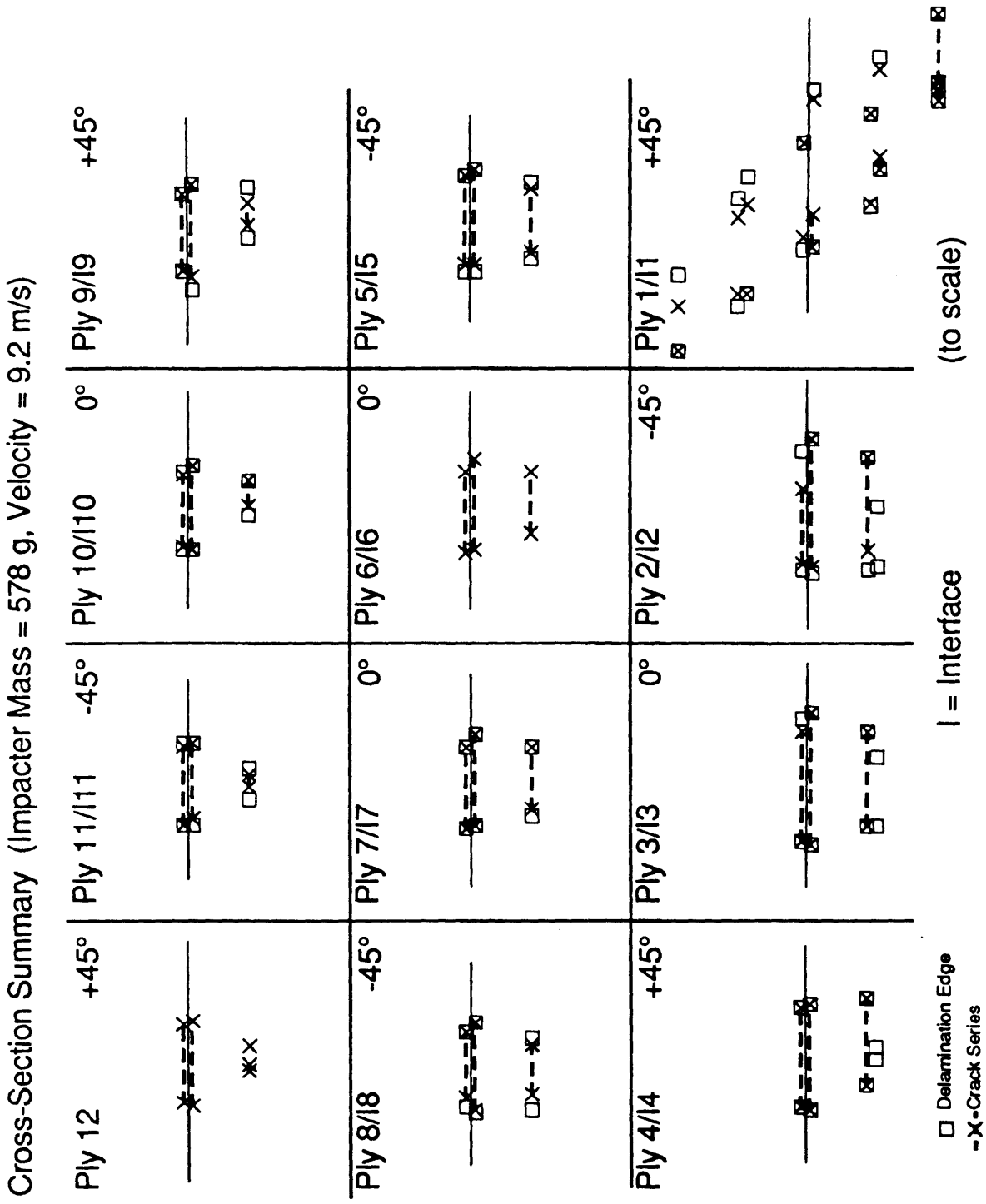

Figure 4.111 Summary of Damage Observed in Specimen J6-2 by Cross-Sectioning (Impacter Mass = 578 g, Velocity = 9.2 m/s).

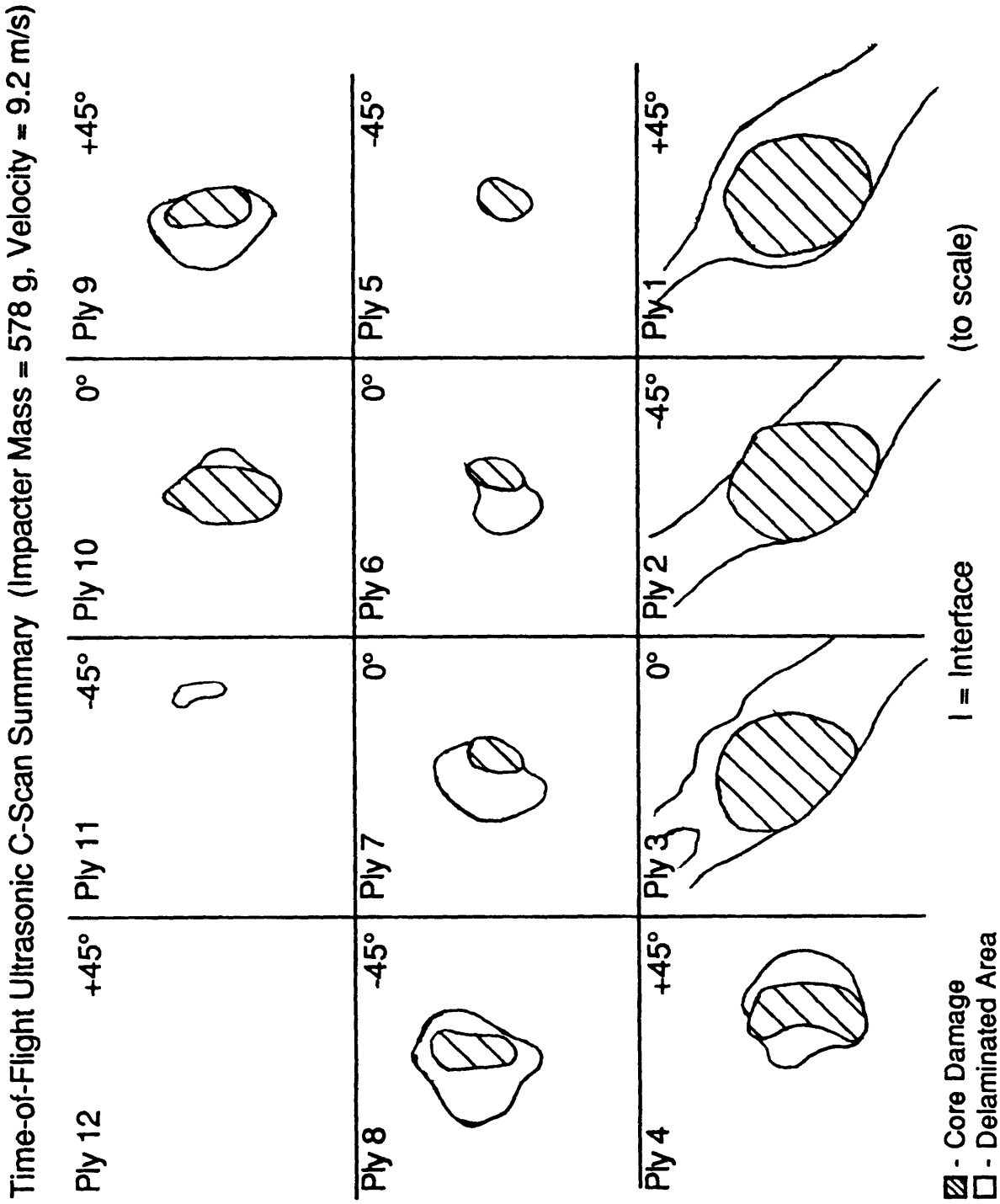

Figure 4.112 Summary of Damage Observed in Specimen J6-2 by Time-of-Flight Ultrasonic C-Scan (Impacter Mass = 578 g, Velocity = 9.2 m/s).

within the window. The correlation of core damage sizes, sizes of the major and minor axes of delamination, and delamination orientation between the two evaluation methods is perhaps more successful than that seen in the 1523 g impacter mass case. However, there are little to no indications of damage in the ultrasonic C-Scans of plies 11 and 12, respectively. The only core damage sizes and shapes that appear similar between the two methods are in plies 1 through 3, and ply 10 in Figure 4.112. The delamination indications that appear similar are seen in plies 1, 4, and 7 through 9.

The deply damage evaluation summary for the case of the 578 g impacter mass at 8.6 m/s is presented in Figure 4.113. The coupon impacted at 8.6 m/s was chosen for the deply summary of damage evaluation for the case of the 578 g impacter mass because the indications of additional damage in the photographs in Figures 4.84 through 4.88 in the coupon impacted at 9.6 m/s were not typical. A summary of the damage evaluation by the time-of-flight ultrasonic C-Scan is presented in Figure 4.114 for the coupon impacted at 8.6 m/s for which the deply summary is presented in Figure 4.113. These damage indications are not necessarily centered for each ply in each summary. Thus, comparsion of one summary to another does not include location of ply damage within the window. Again, the information provided on the core damage, the delamination size, the delamination orientation by the deply method required no "interpretation". Thus, the information presented in Figure 4.113 is an accurate representation of the damage state which existed in this specimen due to impact by a 578 g mass at a velocity of 8.6 m/s. The immediate loss of the backwall reflection in the ultrasonic C-Scan due to penetration at this impacter velocity results in indications of significant

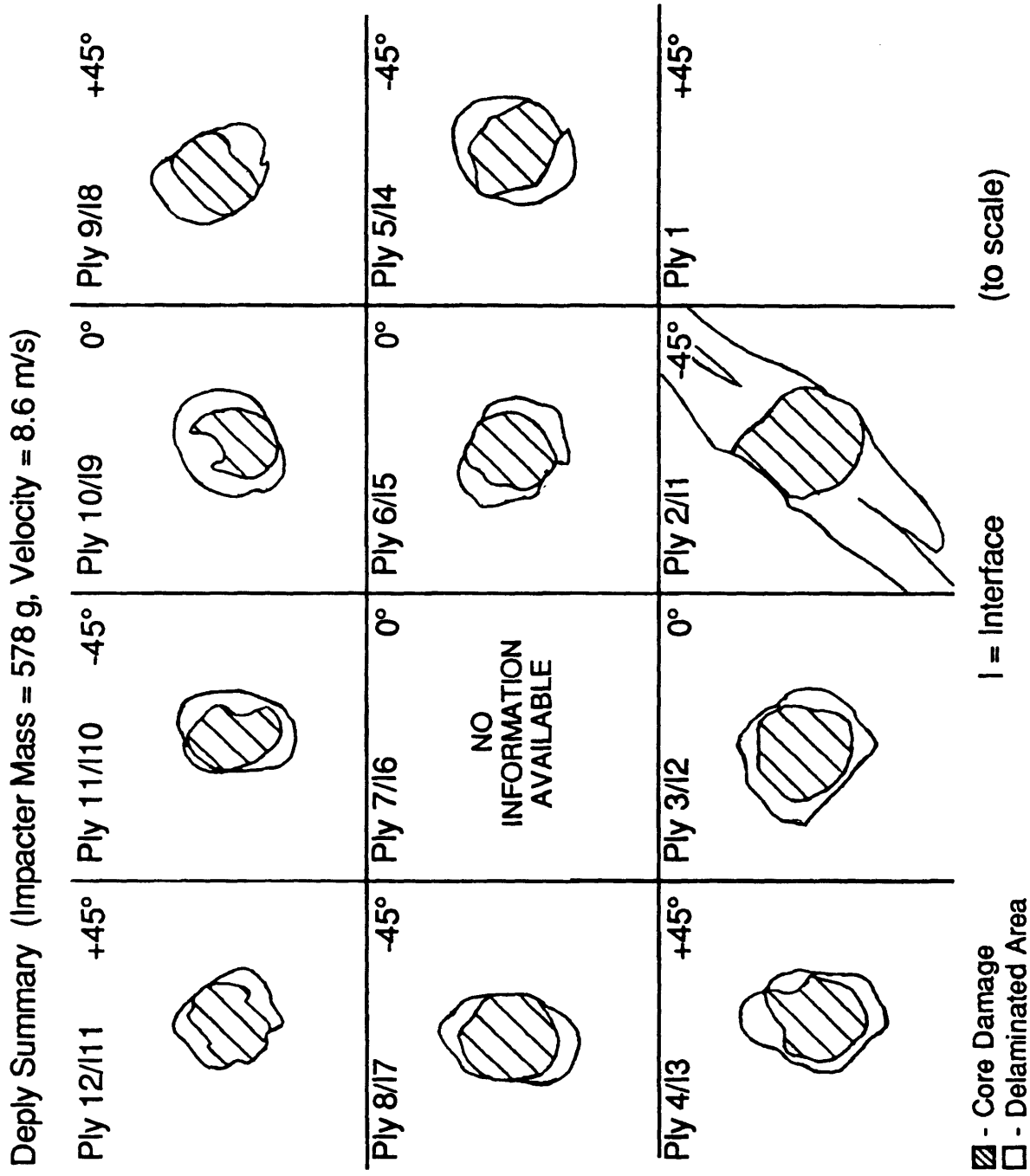

Figure 4.113 Summary of Damage Observed in Specimen M10-4 by Deply (Impacter Mass = 578 g, Velocity = 8.6 m/s).

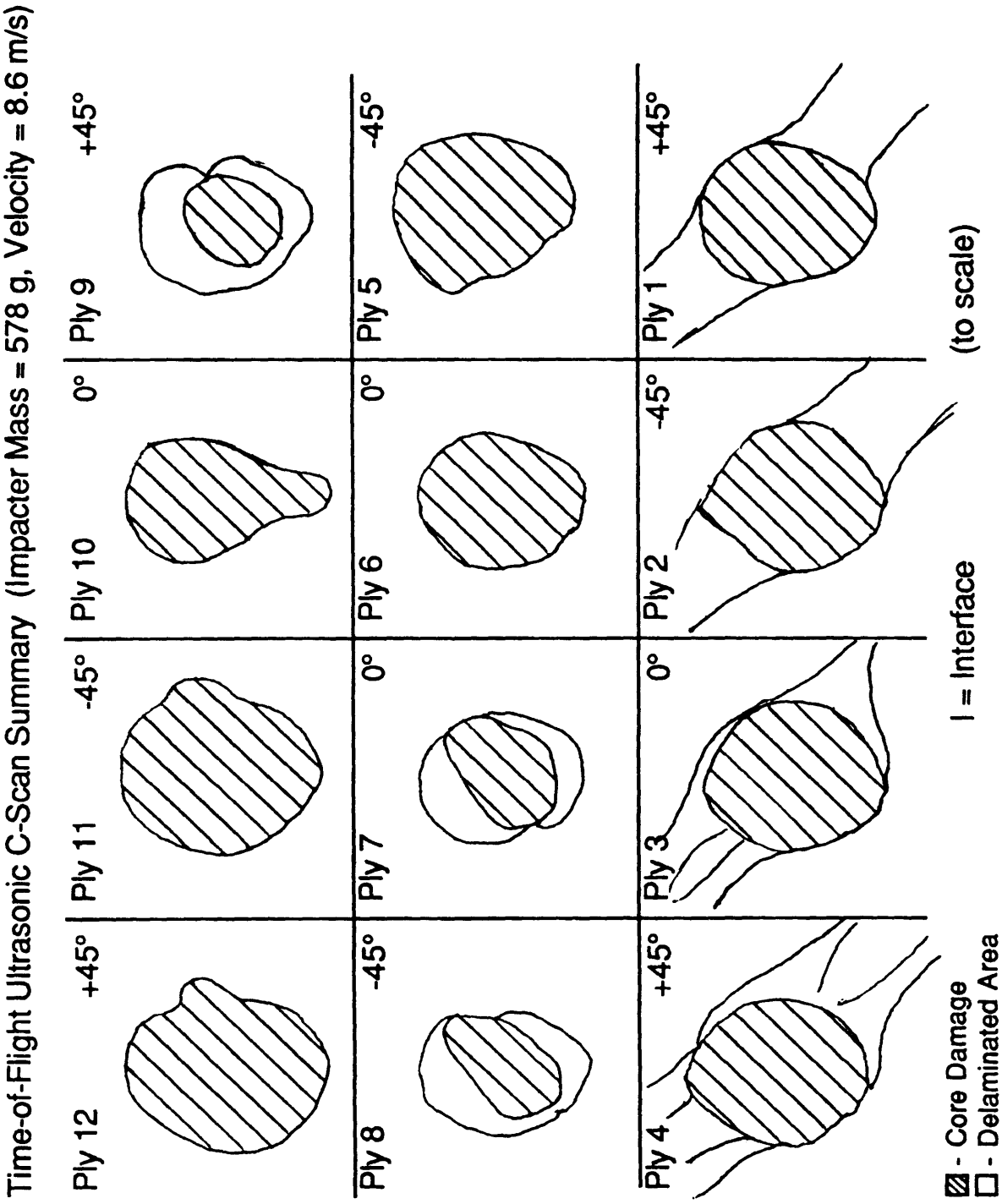

Figure 4.114 Summary of Damage Observed in Specimen M10-4 by Time-of-Flight Ultrasonic C-Scan (Impacter Mass = 578 g, Velocity = 8.6 m/s).

core damage size in every ply in Figure 4.114. The only core damage size indications that are similar between the two evaluation methods are seen in plies 8 and 9. Delamination indications, when present in the time-of-flight ultrasonic C-Scans (Figure 4.114), are significantly larger than those seen from the deply (Figure 4.113). The only representation of delamination in the time-of-flight summary that is corroborated by the deply summary is that seen at interface 1.

The X-ray photographs of specimens selected for the MCRS damage state definition due to impact by the 8.4 g mass are presented in Figure 4.115 with that of Specimen M30-1 which failed at 197 MPa.

The cross-section damage evaluation summary for the case of the 8.4 g impacter mass at 57 m/s is presented in Figure 4.116. There is no cross-section damage evaluation available for coupons impacted at 70 m/s by the 8.4 g mass otherwise that would have been used for damage state definition comparison as that impacter velocity resulted in a similar minimum compressive residual strength in the specimens tested in this work. A summary of the damage evaluation by the time-of-flight ultrasonic C-Scan is presented in Figure 4.117 for the coupon impacted at 57 m/s for which the cross-section summary is presented in Figure 4.116. These damage indications are not necessarily centered for each ply in each summary. Thus, comparsion of one summary to another does not include location of ply damage within the window. While the indications of core damage sizes are similar between the two evaluation methods, the correlation of the major and minor axes of delamination size, and delamination orientation between the two evaluation methods is less successful than that seen in the 1523 g impacter mass case. The only exception is ply 1 in which both

MCRS = 197 MPa (M30-1)
Velocity = 70 m/s

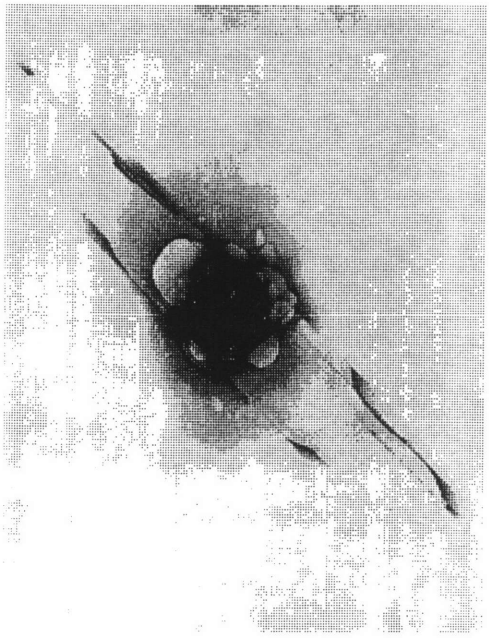

Cross-Section (M32-4)
Velocity = 57 m/s

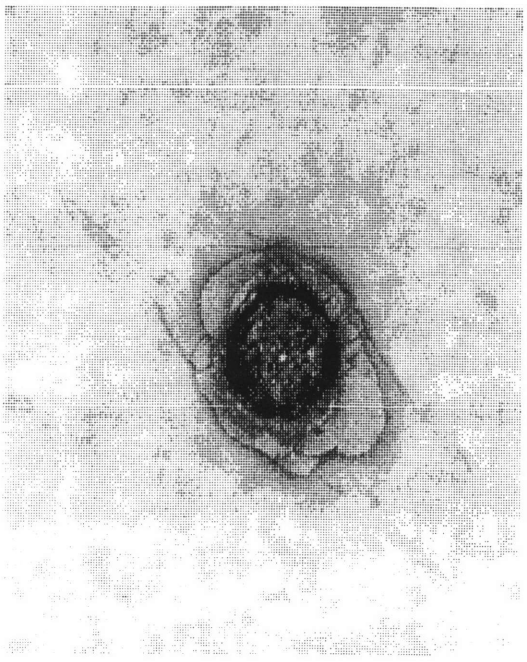

Deply (M23-4)
Velocity = 70 m/s

(X-rays are to scale)

Figure 4.115 X-ray Photographs of Three Specimens Impacted by the 8.4 g Mass at Velocities Known to Cause MCRS.

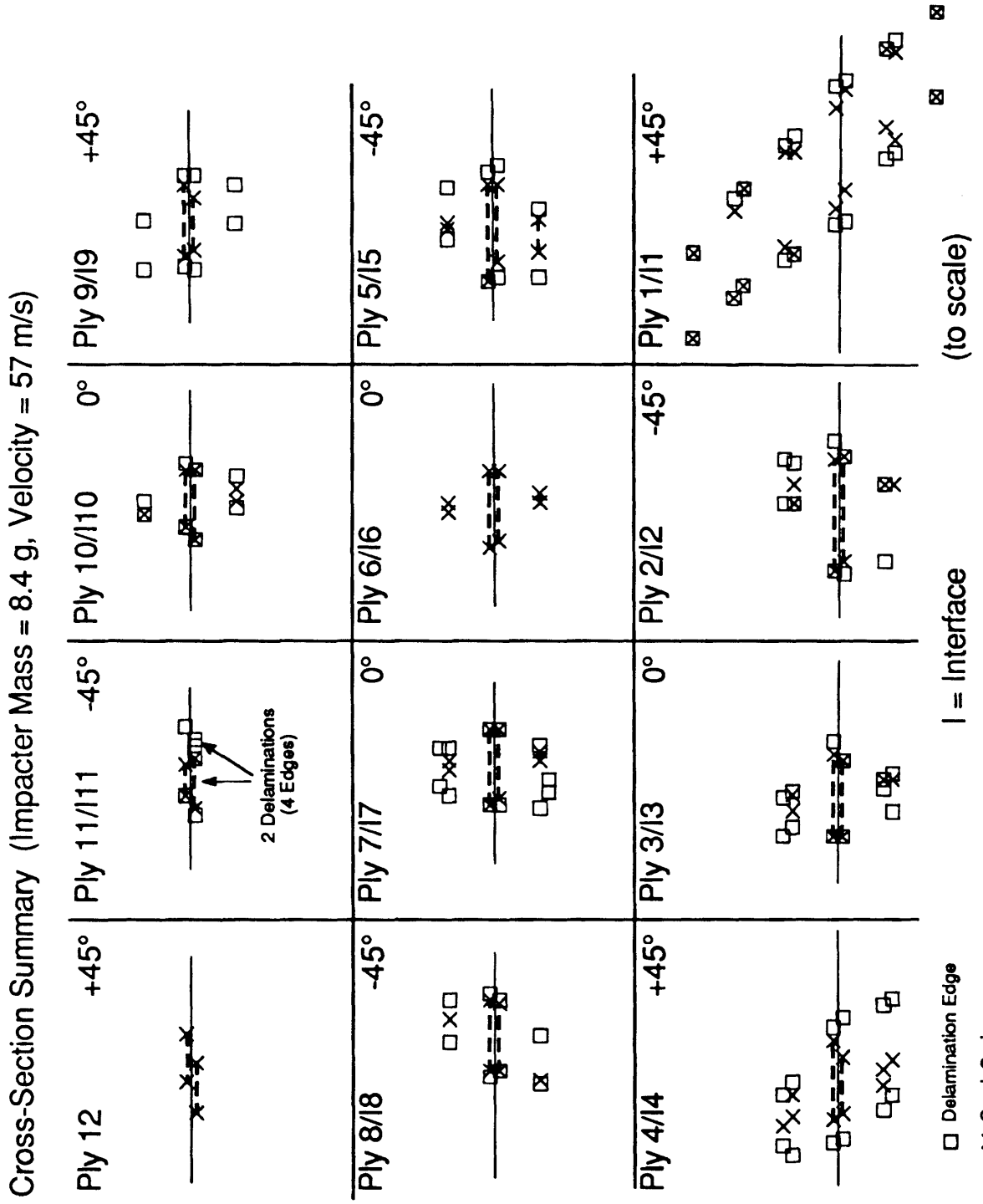

Figure 4.116 Summary of Damage Observed in Specimen M32-4 by Cross-Sectioning (Impacter Mass = 8.4 g, Velocity = 57 m/s).

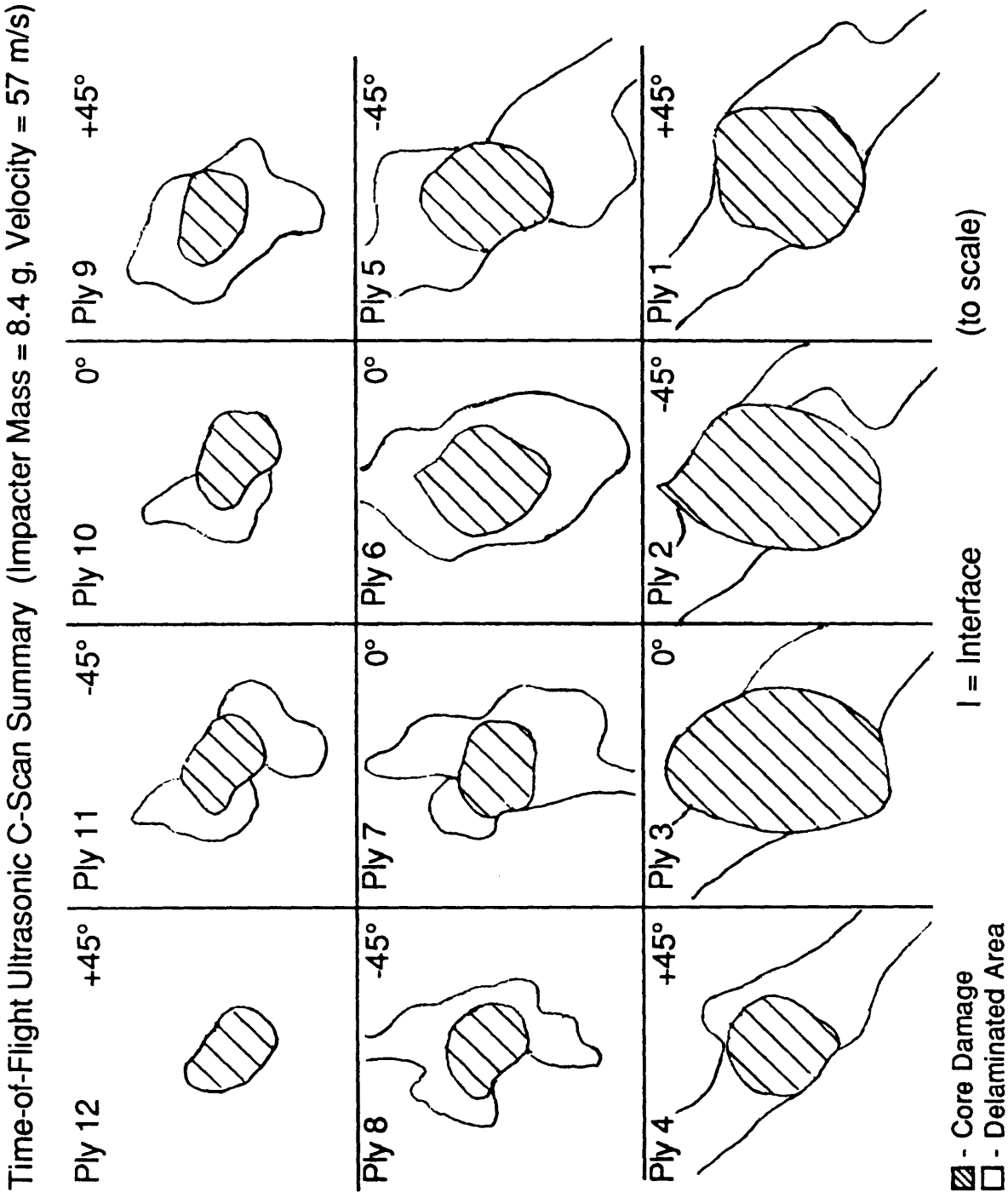

Figure 4.117 Summary of Damage Observed in Specimen M32-4 by Time-of-Flight Ultrasonic C-Scan (Impacter Mass = 8.4 g, Velocity = 57 m/s).

evaluation methods result in similar damage size measurements. And a significant indication of delamination is observed by the ultrasonic evaluation method in ply 6 which does not correspond to the lack of delamination observed at interface 6 by the cross-section evaluation method.

The deply damage evaluation summary for the case of the 8.4 g impacter mass at 70 m/s is presented in Figure 4.118. A summary of the damage evaluation by the time-of-flight ultrasonic C-Scan for the same coupon is presented in Figure 4.119. These damage indications are not necessarily centered for each ply in each summary. Thus, comparsion of one summary to another does not include location of ply damage within the window. Again, the information presented in Figure 4.118 is an accurate representation of the damage state which existed in this specimen due to impact by a 8.4 g mass at a velocity of 70 m/s. The core damage and delamination sizes seen in the time-of-flight summary in Figure 4.119 are consistently larger than those seen in Figure 4.118, though they are not as different in shape and orientation as the comparison provided in Figures 4.116 and 4.117 for the coupon impacted by the 578 g mass at 8.6 m/s.

The time-of-flight ultrasonic C-Scans do not compare well to the cross-section schematics of the same specimens. In fact, damage information provided by the ultrasonic C-Scans for plies 2 and 3 is typically grossly different from that observed by cross-sectioning. And because the impacter velocity used in the 1523 g case caused penetration, the immediate loss of the backwall signal resulted in a unusually large damage zone in the ultrasonic C-Scans of plies 11 and 12. However, the impacter velocity used in the 578 g case also resulted in penetration and there are virtually no damage indications in the ultrasonic C-Scans of plies 11 and 12.

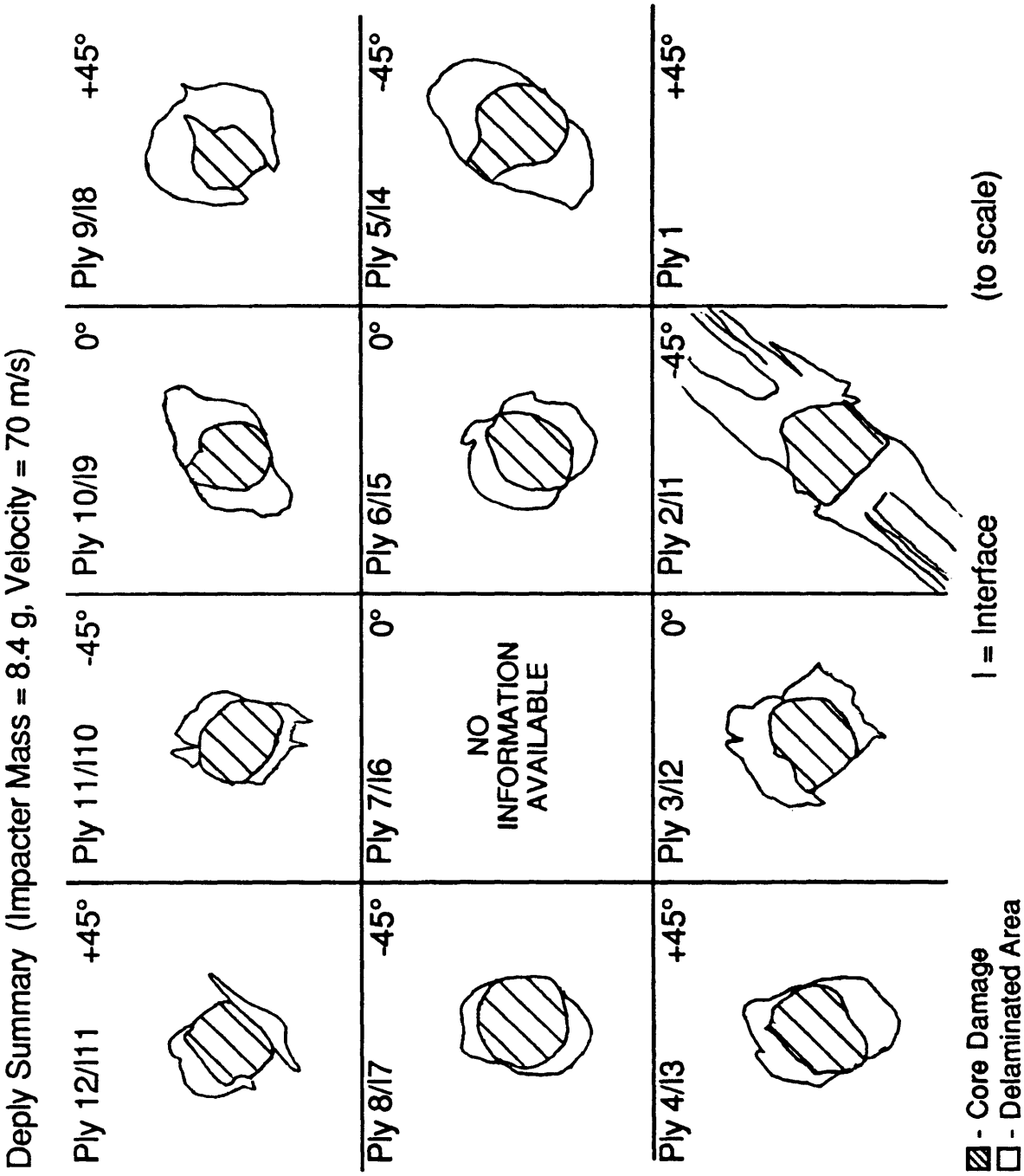

Figure 4.118 Summary of Damage Observed in Specimen M23-4 by Deply (Impacter Mass = 8.4 g, Velocity = 70 m/s).

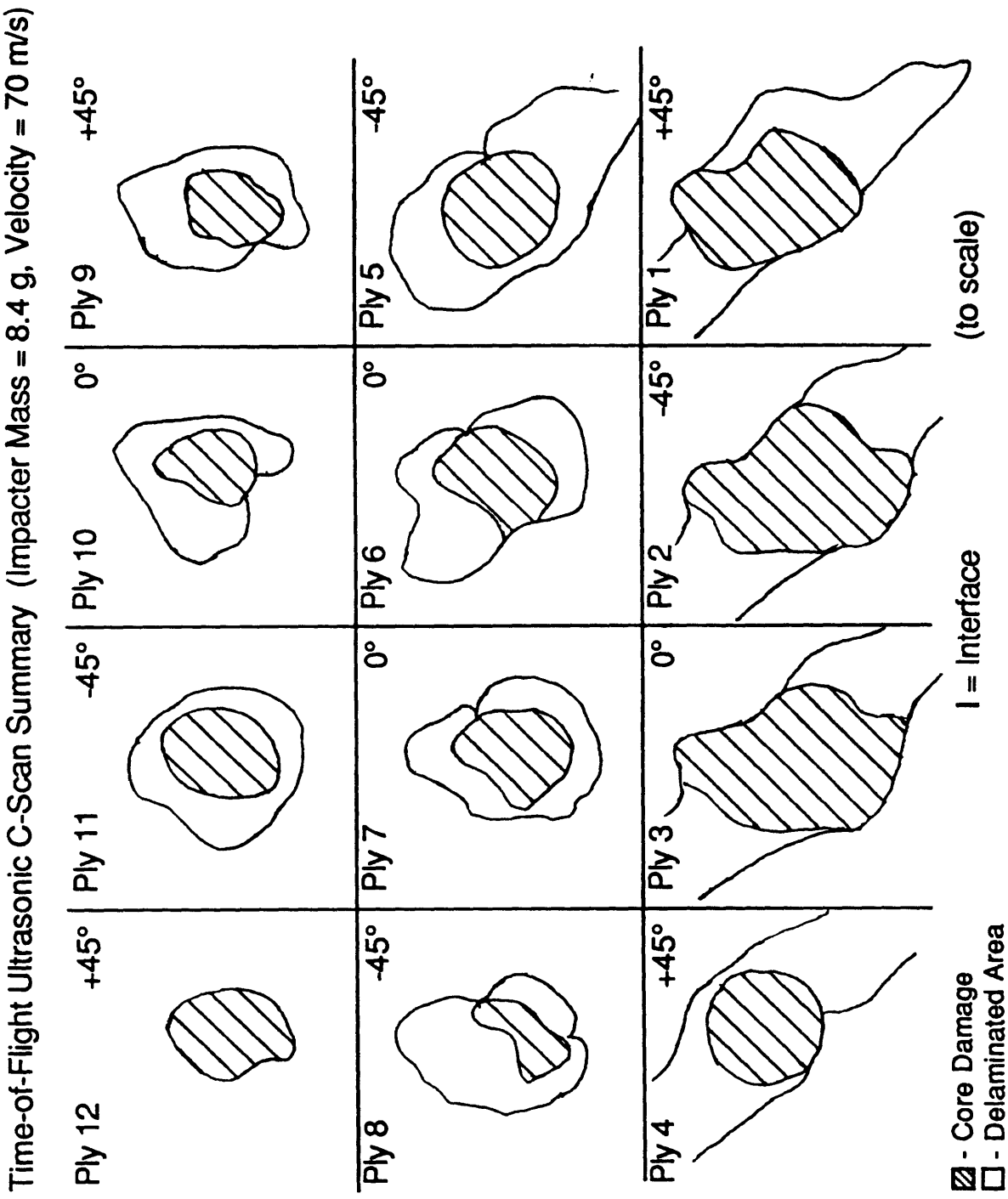

Figure 4.119 Summary of Damage Observed in Specimen M23-4 by Time-of-Flight Ultrasonic C-Scan (Impacter Mass = 8.4 g, Velocity = 70 m/s).

The time-of-flight ultrasonic C-Scans also do not compare well to the deply summaries of the same specimens. Again, damage information provided by the ultrasonic C-Scans for plies 2 and 3 is typically grossly different from that observed by deply. And because the impacter velocity used in the 578 g case caused penetration, the immediate loss of the backwall signal resulted in a unusually large damage zone in the ultrasonic C-Scans of plies 11 and 12. Indications of delaminations, when present in the ultrasonic C-Scans, are usually larger than those seen by deply and conclusions on major axis of damage orientation can not always be made.

The three-dimensional damage state definition of a coupon due to impact by a 1523 g mass at a velocity of 6.3 m/s is similar for both destructive evaluation methods as shown in Figures 4.106 and 4.108. The orientations of delaminations are easier to observe in the summary of the deply evaluation because damage information provided in the plane is continuous. The orientations of delaminations in the summary of the cross-section damage is difficult to observe due to the lack of information above the center of impact location (since the strip width dimension was too large). Both evaluation methods show delaminations existing at nearly every interface, with the exception of interface 6 between the two 0° plies. And delamination size increases towards the back surface. Delamination size and shape information that could be compared is similar between the two destructive evaluation methods.

The three-dimensional damage state definition by the cross-section technique of a coupon due to impact by a 578 g mass at a velocity of 9.2 m/s is compared to the deply technique of a coupon due to impact by a 578 g mass at a velocity of 8.6 m/s. As mentioned previously, the deply evaluation of the

coupon impacted at 9.2 m/s (photographs in Figures 4.84 through 4.88) is not used because of the indications of "additional" damage that was not seen by any of the nondestructive evaluation methods for this coupon. The results summarized in Figures 4.111 and 4.113 for comparison of the two destructive evaluation methods for impact by the 578 g mass are very similar. Again, the orientations of delaminations are easier to observe in the summary of the deply evaluation because damage information provided in the plane is continuous. The orientations of delaminations in the summary of the cross-section damage is difficult to observe due to the lack of information above the center of impact location (since the strip width dimension was, again, too large). Both evaluation methods show delaminations existing at nearly every interface, with the exception of interface 6 between the two 0° plies. And delamination size increases towards the back surface. Delamination size and shape information that could be compared is similar between the two destructive evaluation methods.

The three-dimensional damage state definition by cross-sectioning of a coupon due to impact by an 8.4 g mass at a velocity of 57 m/s and the definition by deply of a coupon due to impact by an 8.4 g mass at a velocity of 70 m/s is similar as shown in Figures 4.116 and 4.118. As mentioned previously, there was no specimen impacted at 70 m/s that underwent destructive damage evaluation by cross-sectioning. The orientations of delaminations are easy to observe in both the cross-section and deply technique summaries. Delamination orientation is identical to the orientation of the next ply further away from the impact surface. Both evaluation methods show delaminations existing at nearly every interface, with the exception of interface 6 between the two 0° plies. Delamination size

increases towards the back surface in both evaluation methods though the major and minor axes of damage sizes in the coupon impacted at 70 m/s are consistently slightly larger than in the coupon impacted at 57 m/s.

The comparison of the three-dimensional damage state definitions by cross-section are similar for the specimens impacted by the 1523 and 578 g masses as shown in Figures 4.106 and 4.111. The cross-section summary of the specimen impacted by the 8.4 g mass, in Figure 4.116, provides similar shape and orientation information compared to the cross-section summaries in Figures 4.106 and 4.111, though sizes are slightly reduced. Perhaps, if a cross-section summary of a coupon impacted at 70 m/s by the 8.4 g mass was available for comparison, the differences in damage size would no longer be apparent.

The three-dimensional damage state definitions at the minimum compressive residual strengths for the three impacter masses used in this work are best provided by the deply destructive damage evaluation method. The comparison of the three-dimensional damage state definitions by deply are similar for specimens impacted by all three masses as shown in Figures 4.108, 4.113, and 4.118. All three summaries exhibit similar damage type, size, shape, and orientation. Core damage remains fairly constant through the thickness due to impact at velocities in the penetration range. Delaminations exist between every interface with the exception of interface 6 (between the two 0° plies). Delamination shape is roughly elliptical with orientation in the direction of the next ply further away from the impact surface. Delamination size increases as ply distance from the impact surface increases. And, there is consistent evidence of the extensive delamination between plies 1 and 2 including indications of the back surface spalling.

Chapter 5

DISCUSSION

5.1 Overview

The purpose of this chapter is to discuss the experimental results presented in Chapter 4 as they pertain to the three questions raised by previous research results [83]. Those questions are, again: one, what is the three-dimensional damage state that governs minimum compressive residual strength behavior; two, is this minimum compressive residual strength value dependent upon impact method; and three, how is this minimum compressive residual strength value related to impacter mass and velocity?

The second and third questions were addressed by the compressive residual strength tests and the first question was addressed by an intense damage evaluation program, the results of which are discussed in Section 5.2. In the process of answering the first question, another important question was raised: once nondestructive damage evaluation is performed, how does one know that it is an accurate or adequate representation of the damage within the specimen? The destructive damage evaluation methods provide the necessary information to define the characteristic damage state for the specimens tested in this work. However, destructive evaluation is not always a viable option (e.g., production parts or specimens to be tested for residual strength). Often only visual inspection and a record of the damage state by a two-dimensional nondestructive damage evaluation method are available for determination of accept/reject of a part. Thus, the relative capabilities of the two-dimensional nondestructive evaluation

methods are discussed in Section 5.3. The relative capabilities of the nondestructive versus destructive damage evaluation methods used to determine the three-dimensional damage state in this work are also discussed in Section 5.3.

5.2 Compressive Residual Strength

All the results of compressive residual strength versus impacter velocity for the cases of the three impacter masses are summarized in Figure 5.1. The curves for the 1523 and 578 g impacter masses are condensed into the 0–14 m/s velocity range. The curve for the 8.4 g impacter mass extends to 70 m/s. The compressive residual strength test program resulted in the following minima: 184 MPa (1523 g, 6.3 m/s), 191 MPa (578 g, 9.2 m/s), and 187 MPa (8.4 g, 57 m/s). The three impacter masses, at their respective MCRS-velocities, resulted in virtually identical minimum compressive residual strengths. Thus, minimum compressive residual strength is apparently independent of impact method. Possible explanations for this phenomenon are explored comparing impacter energies, damage states in X-ray photographs, damage measurements from X-ray photographs, three-dimensional damage state definitions provided by both destructive and nondestructive evaluation methods, observed failure modes, and analytical predictions of maximum force due to a given impacter mass at the respective MCRS-velocity.

The compressive residual strength versus impacter energy curves for the three impacter masses are presented in Figure 5.2. The impacter energies are not equivalent at the minimum compressive residual

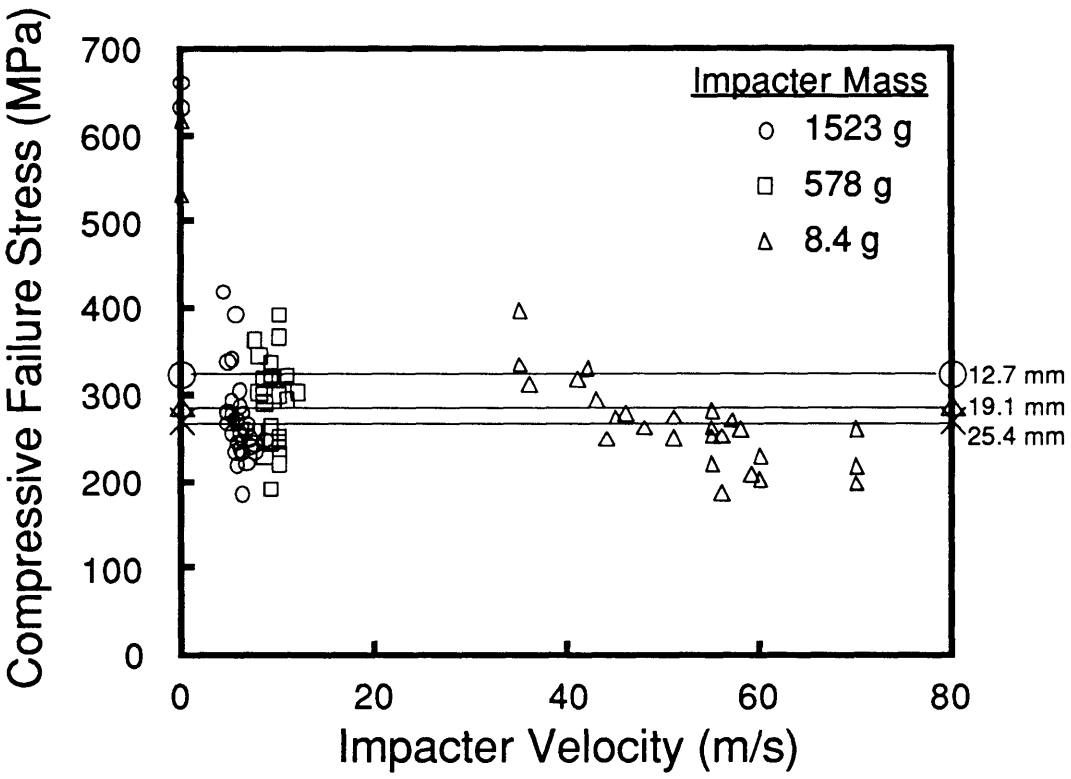

Figure 5.1 Summary of Compressive Residual Strength versus Impacter Velocity Data.

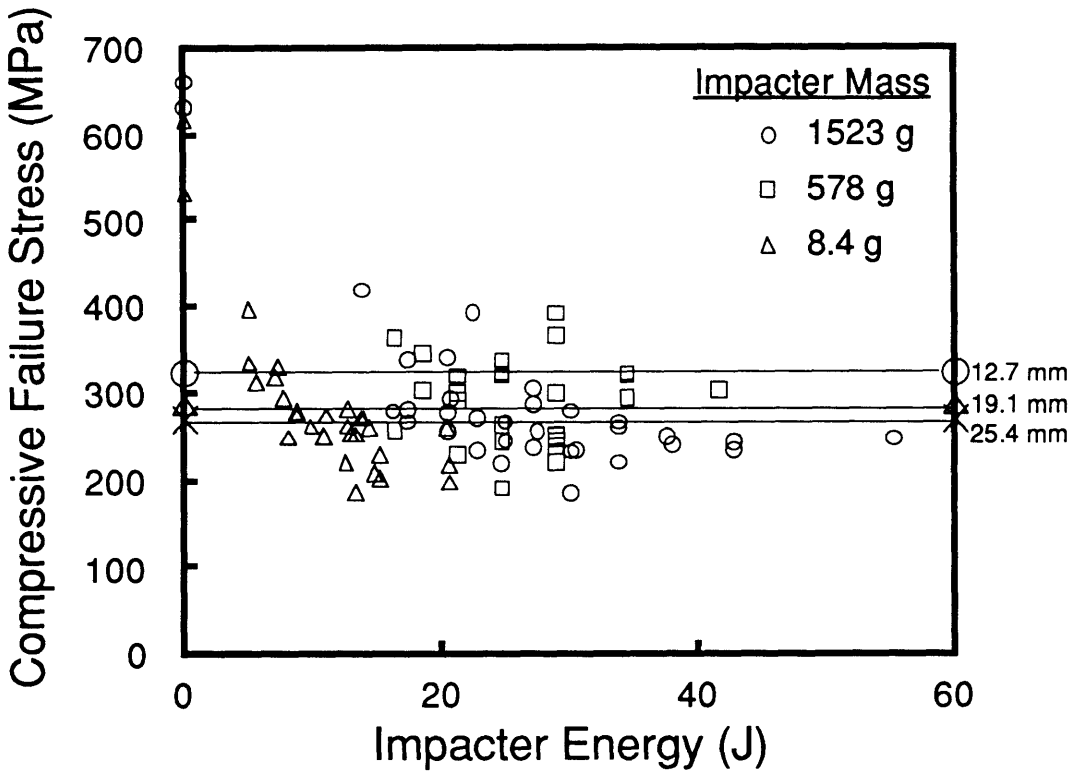

Figure 5.2 Summary of Compressive Residual Strength versus Impacter Energy Data.

strengths for the three impacter masses used in the test program. The impacter energies corresponding to these minima are: 30 J (1523 g), 25 J (578 g), and 13 J (8.4 g). However, the minimum compressive residual strength did not occur at a "point" on the impacter energy curve for the specimens impacted by an 8.4 g mass. At an impacter velocity of 70 m/s, a specimen impacted by the 8.4 g mass resulted in a compressive residual strength of 197 MPa. These impact metrics correspond to an impacter energy of 21 J. The use of this value as the MCRS-energy due to impact by the 8.4 g mass compared to those previously mentioned for the cases of impact by the 1523 and 578 g mass still results in a significant difference in impacter energies at MCRS.

Comparison of the compressive residual strength versus major axis of damage for the cases of the three impacter masses is presented in Figure 5.3. While compressive residual strength approaches the same minimum for all cases considered, the curve for the 8.4 g impacter mass approaches the minimum compressive residual strength at a much smaller major axis of damage size (approximately 40 mm) than the curves for the 1523 and 578 g impacter masses (approximately 70 mm). There is a significant amount of scatter among the three impacter masses. From the results presented in this curve, it would be inadvisable to predict compressive residual strength as a function of the major axis of damage.

Comparison of the compressive residual strength versus minor axis of damage for the cases of the three impacter masses is presented in Figure 5.4. There is less scatter in the minor axis data than the major axis data presented in Figure 5.3. Though the largest scatter band of data at 12 mm

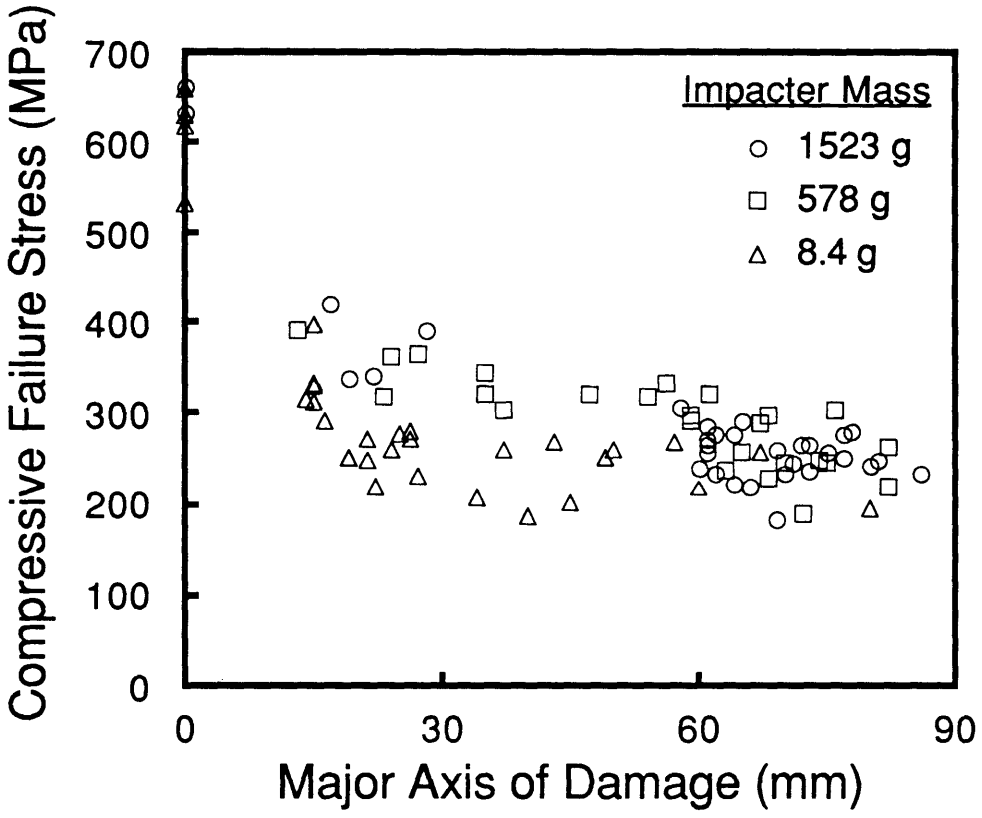

Figure 5.3 Summary of Compressive Residual Strength versus Major Axis of Damage Data.

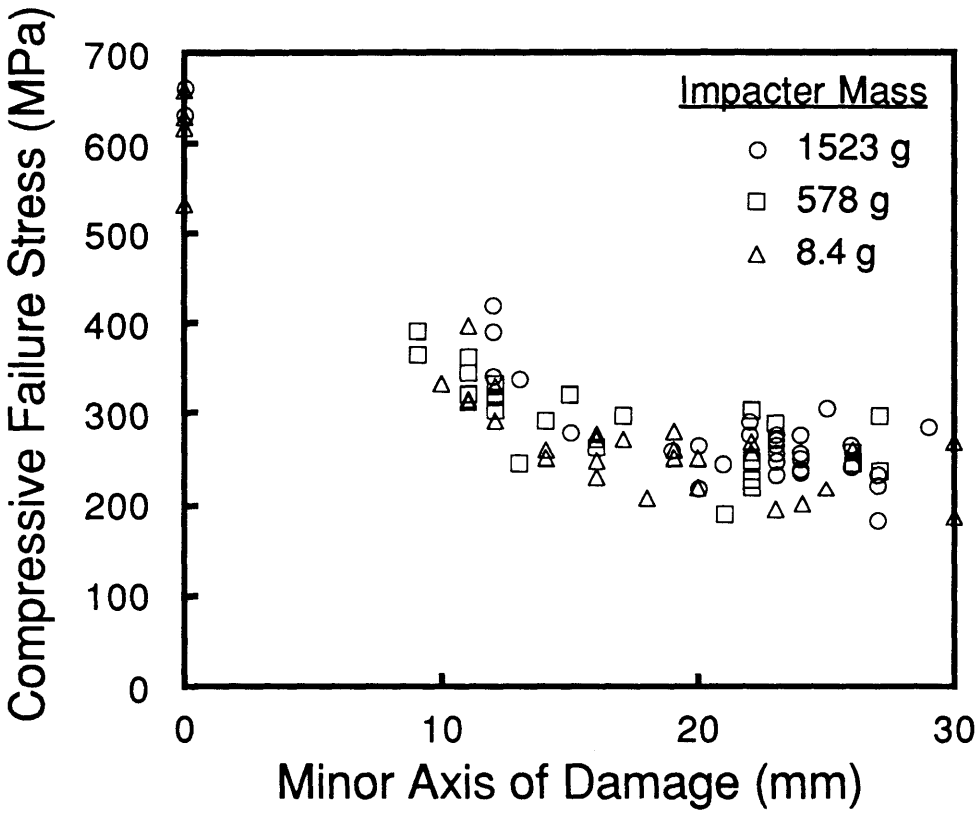

Figure 5.4 Summary of Compressive Residual Strength versus Minor Axis of Damage Data.

still represented a total difference of 33%, there is no obvious separation of data between the three impacter masses as there is in the case of the major axis.

Comparison of the compressive residual strength versus core damage size for the cases of the three impacter masses is presented in Figure 5.5. Again, the curve for the 8.4 g impacter mass approaches the minimum compressive residual strength at a smaller core damage size (13 mm) than the curves for the 1523 and 578 g impacter masses (23 and 19 mm respectively). There is again, a significant amount of scatter among the three impacter masses. From the results presented in this curve, similar to those presented in the major axis of damage curve, it would be inadvisable to predict compressive residual strength as a function of the core damage size.

As previously mentioned in Section 4.5, and shown in Figure 4.104, a comparison of the damage shown in the X-ray photographs of the specimens for the three impacter mass cases would indicate different compressive residual strengths for these specimens since the apparent type and extent of damages are not similar. However, the three specimens have the same compressive residual strengths. In addition, the two-dimensional damage information presented in Figures 5.3 through 5.5 does not correlate well with compressive residual strength. There is evidence of separation of impacter methods on these curves with the low mass/high velocity system consistently reaching the compressive residual strength asymptote at smaller damage measurements. Though the separation of data for the two impact methods is not as clear for the compressive residual

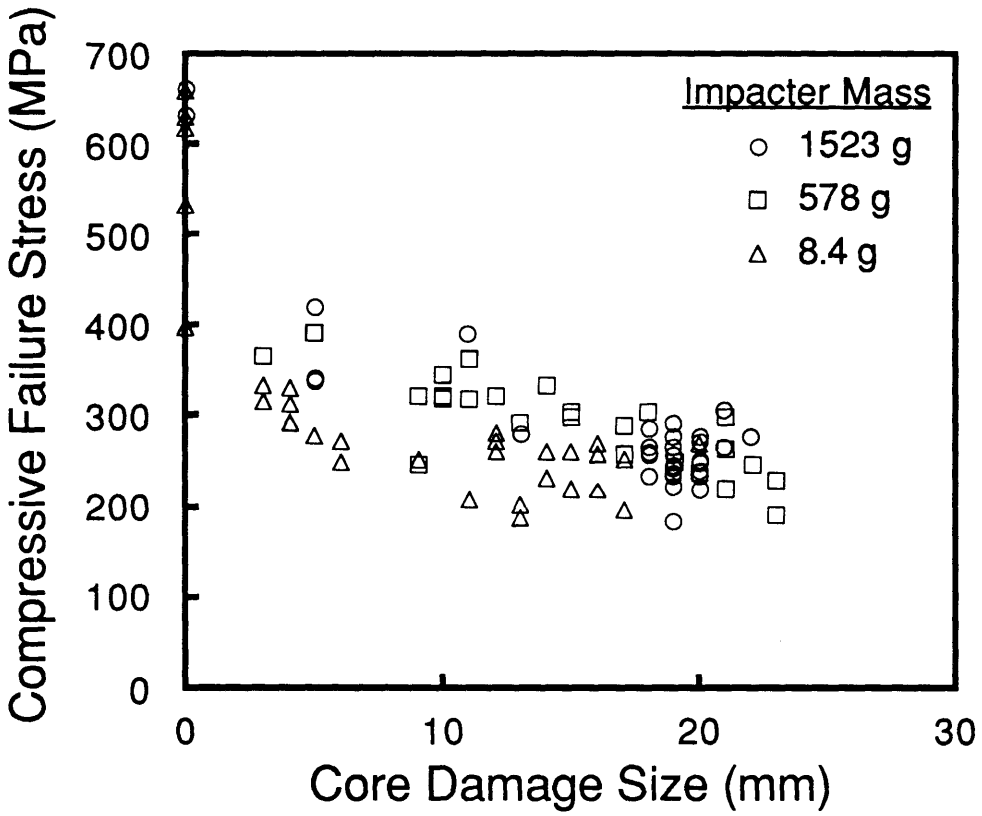

Figure 5.5 Summary of Compressive Residual Strength versus Core Damage Size Data.

strength curve versus the minor axis of damage, the same trend is observed. Thus, two-dimensional damage information is not sufficient for the prediction of compressive residual strength.

The three-dimensional damage states defined by the deply method in Figures 4.108, 4.113, and 4.118 for specimens impacted at MCRS-related impacter velocities for the three masses used in this work are similar. Thus, it would appear that a probable explanation for the similar minimum compressive residual strengths is the existence of similar three-dimensional damage states in these specimens. However, all three X-ray photographs from the same coupons are not similar (Figures 4.105, 4.110 and 4.115). The X-ray photograph of the specimen impacted at 70 m/s by the 8.4 g mass in Figure 4.115 shows evidence of major axis of delamination (not including the back surface spalling of fibers in ply 1) that is significantly larger than the indications for the specimens in Figures 4.105 and 4.110 even though the evaluation by deply results in similar damage sizes, types, and orientations for these specimens. Since two-dimensional damage data is an integration of the three-dimensional damage data, known similar three-dimensional damage states should result in similar two-dimensional damage states. It is possible that, for the specimens impacted by the 1523 and 578 g masses, the amount of dye penetrant used was not sufficient and/or all the interfaces where delamination occurred did not receive dye penetrant. The syringe was placed into as many ply interfaces in the core damage area as thought possible. However, it cannot be determined if all possible delamination interfaces had dye penetrant applied or if the quantity of dye penetrant was sufficient.

Since the evidence of the damage state definition provided by the two-dimensional nondestructive evaluation methods cannot be successfully

compared to known similarities provided by the destructive three-dimensional damage state definitions, it is impossible to compare damage states of compressive residual strength specimens with any confidence. Specimens that undergo destructive evaluation cannot be tested for compressive residual strength. And after specimens have been tested for compressive residual strength, the comparison of damage states by destructive evaluation is impossible, since it cannot be determined which damage is due to impact and which is due to the residual strength test.

The three-dimensional damage states determined by destructive evaluation are similar for specimens impacted by the three impacter masses at velocities known to cause minimum compressive residual strength. However, since these specimens were destructively evaluated, they could not be tested for compressive residual strength. Thus, a postmortem examination of the specimens that failed at the minimum compressive residual strengths for the three impacter mass cases was conducted to determine if the failure modes were the same. These specimens, after failure, are shown in Figures 4.13, 4.22, and 4.31. The postmortem examination of these minimum compressive residual strength specimens showed the extensive core damage due to impacter penetration, sublaminate buckling of ply 1, fiber failure in the remaining plies, and extensive back side spalling of ply 1. Although from the postmortem examination it is not possible to determine which damage mode or combination of damage modes are controlling the compressive residual strength, it is clear that the failure modes are similar if not the same.

If the damage states causing minimum compressive residual strength for specimens impacted by the three impacter masses are similar

for different impacter metrics, the explanation must lie with the mechanics of the impact event.

Though the focus of this work was on compressive residual strength, analytical predictions of maximum force due to impact using the metrics of three MCRS-impact events may provide an explanation for the similar damage states. A series of analytical models developed by Cairns [25] is capable of predicting the maximum force, displacement, and acceleration due to impact by a given mass at a given velocity. A brief description of the models follows.

Impact behavior of the laminate is divided into local and global levels of response. The local level is assumed to control the development of damage and is modeled as a lateral Hertzian contact problem [92]. This information is used for the contact law in a global model that also includes the influence of such variables as boundary conditions, specimen geometry, and laminate properties [93]. The global analytical model to predict the force, acceleration, and displacement histories in this work has been adapted and modified by Tsang [89] based on the analysis methods developed by Cairns [25] with further modifications by Kraft [90] and Ryan [29]. The force history provided by the global model is representative of the force of the impacter. To determine the force in the coupon the d'Alembert corrections due to acceleration of the coupon need to be included [91]. This resulting force is then fed into another model which determines stress and strain used to predict the resulting damage state.

Several assumptions made in the global model should be mentioned here. The impacter is rigid and hemispherical and the plate is rectangular, monoclinic, and undamaged. Stretching in the plate is assumed to be negligible but bending-twisting coupling and shear

deformation is included. The maximum forces with the d'Alembert corrections predicted for the three impacter masses used in this work at velocities known to result in the minimum compressive residual strength can be compared and a relative nature established.

The ply properties for the AS4/3501-6 graphite/epoxy material are presented in Table 5.1 [29]. The resulting $[\pm 45/0]_{2S}$ laminate properties used in this analysis are presented in Table 5.2 [29]. As mentioned previously, this laminate was chosen due to the prior data base generated in damage resistance and damage tolerance studies in TELAC [e.g., 25, 29]. Previous damage resistance studies comparing analysis to experiment were done using high velocity/low mass [25] and low velocity/high mass [29] impact methods. Thus, force histories generated by the analytical models for the three masses and two impact methods used in this work can be compared to those presented in References 25 and 29.

The predicted force history for the AS4/3501-6 $[\pm 45/0]_{2S}$ laminate impacted by a 1523 g mass at 6.3 m/s is presented in Figure 5.6. The time step used in the analysis is 5 μs. The analysis used 17 by 17 modes to reach a converged solution. This predicted force history is almost identical to the one predicted in Reference 29 for the same mass at a velocity of 1.46 m/s using a time step of 1 μs and 17 by 17 modes. The total time of the impact event in Reference 29 is also 0.0225 s. The maximum force predicted for the undamaged laminate impacted by a 1523 g mass at 6.3 m/s is 1834 N. The corresponding predicted acceleration history is presented in Figure 5.7. The maximum acceleration does not occur at the same time as the maximum force. The acceleration at the time of maximum force is on the order of -0.5×10^6 m/s^2.

Table 5.1 AS4/3501-6 Graphite/Epoxy Ply Properties [29]

E_{11}	142.0 GPa
$E_{22} = E_{33}$	9.81 GPa
$G_{12} = G_{13}$	6.0 GPa
G_{23}	3.77 GPa
$\nu_{12} = \nu_{13}$	0.30
ν_{23}	0.34
t_{ply}	0.134 mm
ρ	1540 kg/m^3

Table 5.2 AS4/3501-6 $[\pm 45/0]_{2S}$ Graphite/Epoxy Laminate Properties [29]

Bending	Shear
D_{11} = 21.75 Nm	A_{44} = 6.92 MN/m
D_{12} = 9.79 Nm	A_{45} = 0.00 MN/m
D_{22} = 13.64 Nm	A_{55} = 8.06 MN/m
D_{66} = 10.85 Nm	
D_{16} = 2.24 Nm	
D_{26} = 2.24 Nm	

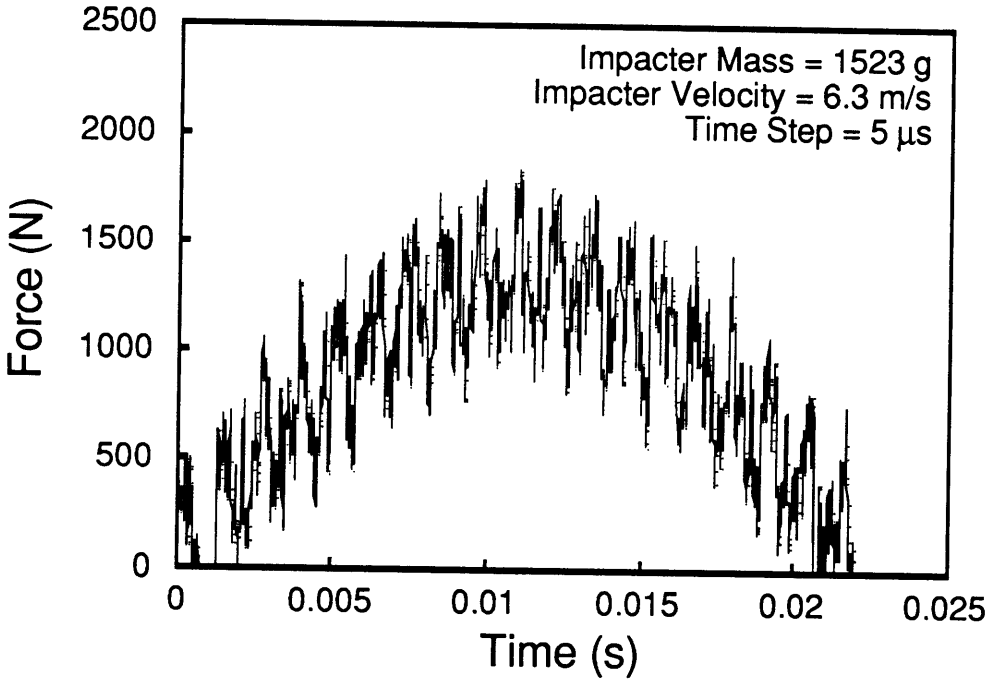

Figure 5.6 Predicted Force History of $[\pm 45/0]_{2S}$ Graphite/Epoxy Laminate (Impacter Mass = 1523 g, Velocity = 6.3 m/s).

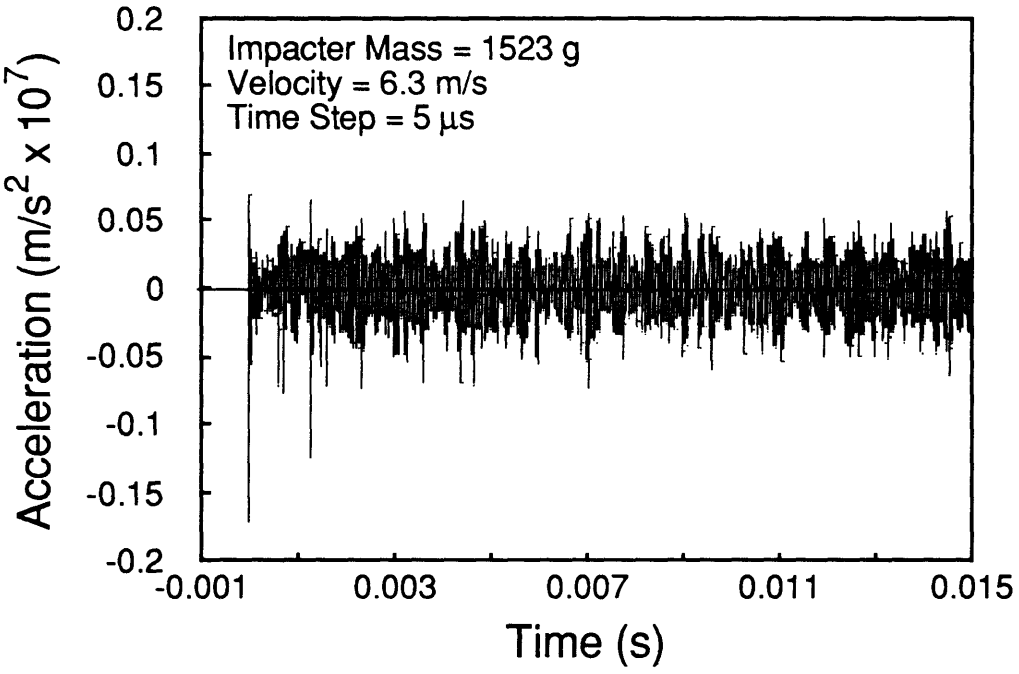

Figure 5.7 Predicted Acceleration History of $[\pm 45/0]_{2S}$ Graphite/Epoxy Laminate (Impacter Mass = 1523 g, Velocity = 6.3 m/s).

The predicted force history for the AS4/3501-6 $[\pm 45/0]_{2S}$ laminate impacted by a 578 g mass at 9.2 m/s is presented in Figure 5.8. The time step used in the analysis is 5 μs. Again, 17 by 17 modes were required to reach a converged solution. This predicted force history is very similar to the one in Figure 5.6, although the total time of the impact event in this case is only 0.014 s. The maximum force predicted for the undamaged laminate impacted by a 578 g mass at 9.2 m/s is 1869 N. The corresponding predicted acceleration history is presented in Figure 5.9. Again, the maximum acceleration does not occur at the same time as the maximum force. The acceleration at the time of maximum force is on the order of -1.0×10^6 m/s^2.

The predicted force history for the AS4/3501-6 $[\pm 45/0]_{2S}$ laminate impacted by an 8.4 g mass at 57 m/s is presented in Figure 5.10. The time step used in the analysis was 1 μs. The analysis also used 17 by 17 modes to reach a converged solution. This predicted force history is very similar to those predicted in Reference 25 for the same mass at velocities of 49 and 69 m/s. The maximum force predicted for the undamaged laminate impacted by a 8.4 g mass at 57 m/s is 4266 N. The corresponding predicted acceleration history is presented in Figure 5.11. In this case, the maximum acceleration occurs at the same time as the maximum force. The maximum acceleration predicted for the undamaged laminate impacted by a 578 g mass at 9.2 m/s is -2.71×10^7 m/s^2.

The fact that the analysis predicted virtually identical maximum force for the 578 and 1523 g masses and maximum acceleration on the same order of magnitude is significant. The similar output results from the global model for these two impacter masses, when fed into the damage prediction model, should result in similar damage states and thus,

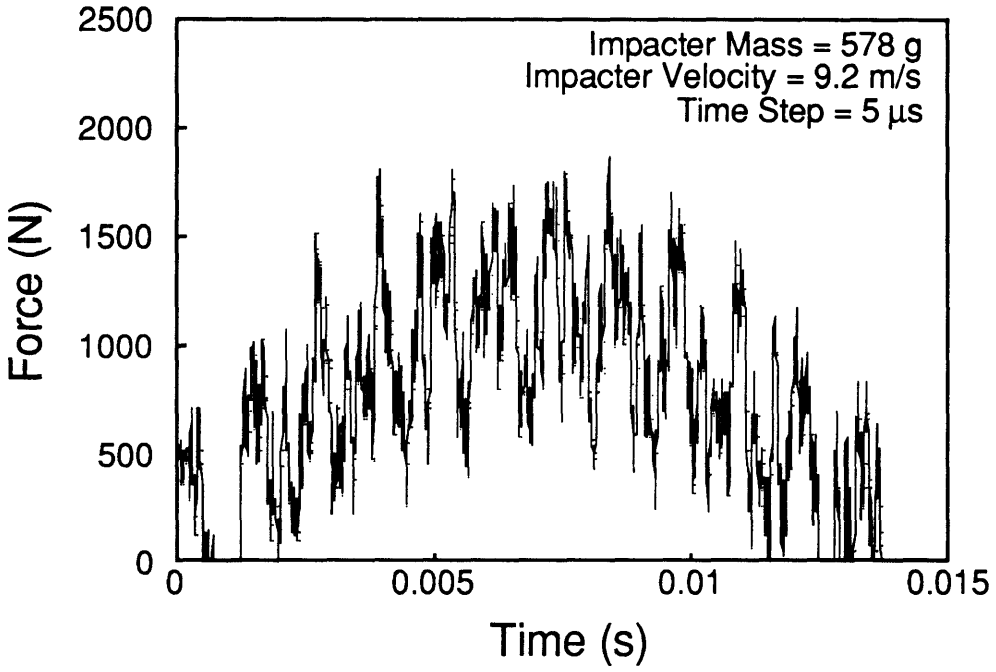

Figure 5.8 Predicted Force History of $[\pm 45/0]_{2S}$ Graphite/Epoxy Laminate (Impacter Mass = 578 g, Velocity = 9.2 m/s).

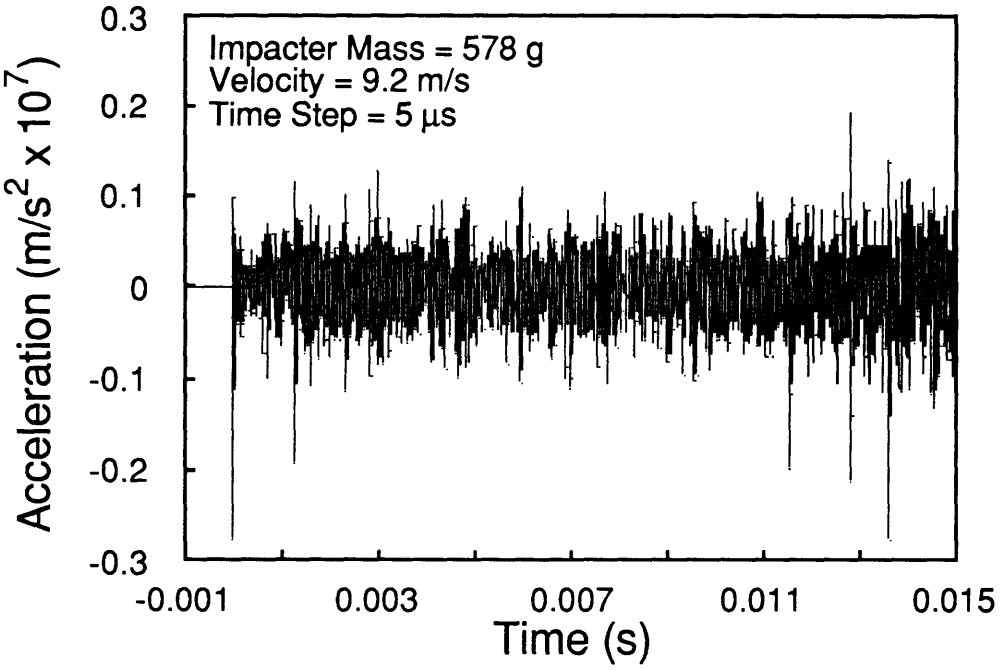

Figure 5.9 Predicted Acceleration History of $[\pm 45/0]_{2S}$ Graphite/Epoxy Laminate (Impacter Mass = 578 g, Velocity = 9.2 m/s).

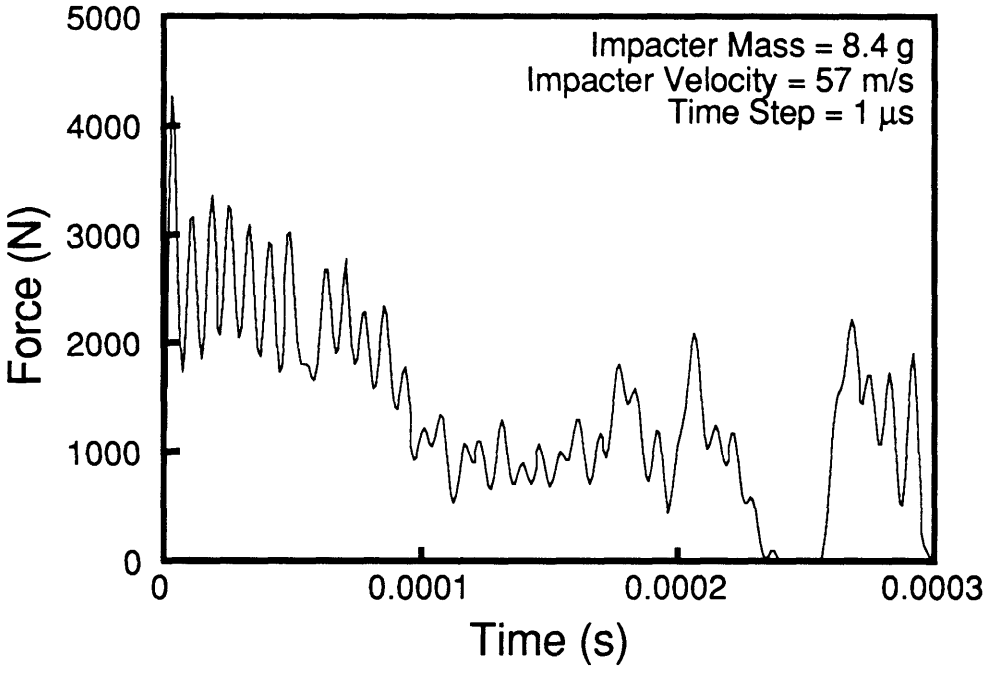

Figure 5.10 Predicted Force History of $[\pm 45/0]_{2S}$ Graphite/Epoxy Laminate (Impacter Mass = 8.4 g, Velocity = 57 m/s).

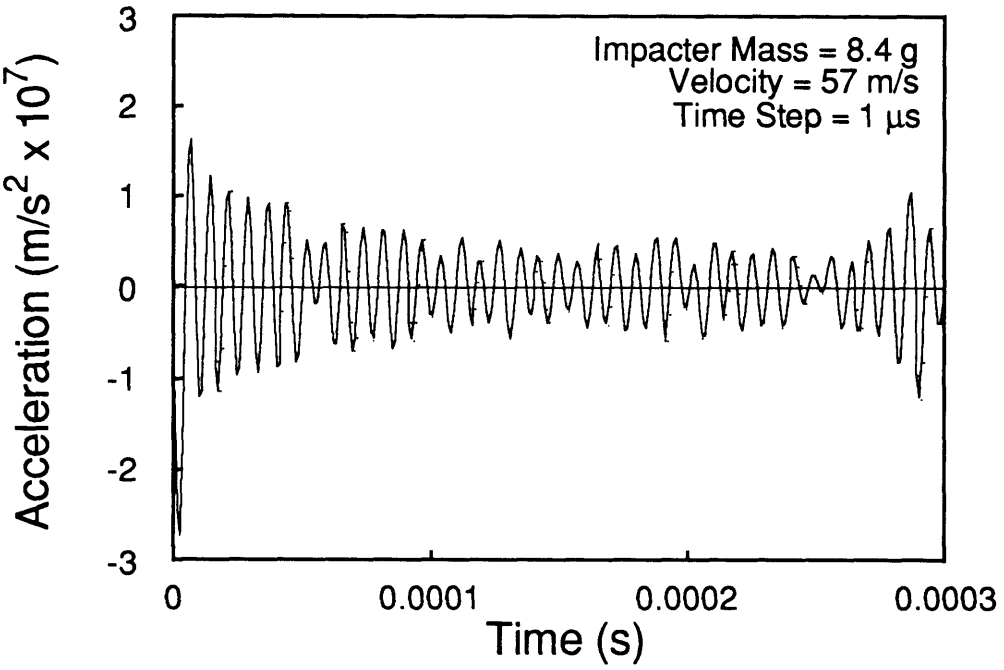

Figure 5.11 Predicted Acceleration History of $[\pm 45/0]_{2S}$ Graphite/Epoxy Laminate (Impacter Mass = 8.4 g, Velocity = 57 m/s).

presumably similar residual strengths. This analysis suggests that the minimum compressive residual strengths of 184 and 191 MPa caused by similar damage states, are a result of a similar maximum force at their respective MCRS-velocities. Thus, the use of this methodology has merit for the prediction of damage states and possible extension to compressive residual strength.

The maximum force and acceleration predicted for the 8.4 g mass at the related MCRS-velocity is on the order of two times the maximum force predicted for the 1523 and 578 g masses at their MCRS-velocities. From the results in Reference 25, an increase in velocity for the 8.4 g mass would just produce an increase in the maximum force. Thus, if the 70 m/s velocity was selected for analysis (also a velocity known to cause MCRS due to impact by an 8.4 g mass), the disparity between predicted maximum forces for the two impact methods would just increase as well as the maximum accelerations. When the d'Alembert forces are considered, however, the resulting force in the coupon at impact will be reduced.

The acceleration history predicted by this model results in the acceleration at the point of contact. However, the acceleration of surrounding points in the plate is a function of this maximum, but it is not equivalent to it. Thus, the application of this acceleration history to an amount of mass, other than that corresponding to the point of impact, is not an accurate approach in calculation of the d'Alembert correction force. From the information provided at this time, the amount of reduction to the predicted force due to the predicted acceleration at the point of contact cannot be assessed. As the resulting forces due to the maximum predicted force combined with the d'Alembert correction factors cannot be predicted in this work, the comparison of possible predicted damage states from the

predicted force and acceleration of the three impact masses is not possible. Thus, it is not known whether the similarity in compressive residual strengths between the specimens impacted by the low mass/high velocity system and the high mass/low velocity system caused by similar damage states can be explained by similar impact events despite different metrics. The prediction of damage states from predicted force and acceleration histories needs to be addressed further.

The assumption of the plate being undamaged for the calculation of force and acceleration histories is not exactly correct as damage occurs during the event. The existence of damage has been shown to affect the resulting force history through the local contact law [94]. As the velocities used for the three impacter mass cases resulted in significant damage (i.e., penetration), the presence of damage needs to be included to more accurately predict the force and acceleration histories. However, the predicted force and acceleration histories presented in this work are a good first approximation of potential similarities in the mechanics of the three impact events of interest.

5.3 Damage Evaluation Methods

From previous work discussed in Chapter 2, the correlation of compressive residual strength based on damage area in the plane of the nondestructive evaluation record has met with limited success [8, 16, 27, 30, 45, 49, 82]. These results included comparison of damage due to open holes, imbedded delaminations, and impact damage. In Chapter 4 (Figures 4.34, 4.35, 4.38, and 4.50), specimens with apparently identical two-dimensional damage indications due to impact also did not always result in similar

compressive residual strengths. In practice, often only two-dimensional nondestructive damage evaluation techniques are available for use on a particular item. Thus, a comparison of X-ray and two-dimensional ultrasonic C-Scan is made to provide information on relative capabilities of these two two-dimensional damage evaluation methods.

There were over fifty specimens impacted by the three different masses that were ultrasonically inspected at Hercules, Inc. Comparison of damage in the X-ray photographs to the corresponding ultrasonic C-Scans did not consistently result in similar observations. Selections from the X-ray photographs and two-dimensional ultrasonic C-Scans presented in Chapter 4 were chosen for comparison to demonstrate the inconsistent observations between the two nondestructive two-dimensional methods.

In an example of a "worst" case comparison, the X-ray photograph in Figure 4.38 of Specimen M15-2 and the corresponding ultrasonic C-Scan in Figure 4.46 show the difference in resolution of the two methods. The core area is very dark in the ultrasonic C-Scan as expected due to the immediate loss of backwall reflection. However, there is no indication in the ultrasonic C-Scan of the additional delamination around the core or the back surface ply split and delamination between plies 1 and 2 that is apparent in the X-ray photograph.

The comparison of damage due to impact by the 8.4 g mass at all velocities used in this work resulted in better correlation of damage state definitions from the two evaluation methods than those done for specimens impacted by the 1523 and 578 g masses. Evidence of this was shown in Figures 4.40 and 4.47 of the X-ray photograph and ultrasonic C-Scan respectively of Specimen J16-4 which was impacted at 55 m/s. And for the 70 m/s case, the X-ray photograph in Figure 4.43 compares well with the

ultrasonic C-Scan in Figure 4.50 of Specimen M30-1. There is more detail about fiber breakage in the immediate vicinity of the core damage in the X-ray photographs than the ultrasonic C-Scans. However, the ultrasonic C-Scans and X-ray photographs have equal indications of the significant delamination around the core damage area, the back surface ply split, and delamination between plies 1 and 2.

The two-dimensional ultrasonic C-Scan evaluation method is inconsistent in providing reasonably good damage state definition results for the specimens impacted by the 1523 and 578 g masses. For the specimens impacted by the 8.4 g mass, the ultrasonic C-Scan evaluation method consistently identifies the core damage area, surrounding delaminations, back ply splitting, and the delamination between plies 1 and 2. The X-ray photographs are typically easier to evaluate and even give hints at possible three-dimensional damage states. The wicking nature of the dye penetrant often results in several outlines of delaminations that, by the nature of their shape, had to occur at different ply interfaces. The specimens impacted by the 8.4 g mass typically did not experience the physical location of the impacter on the back side of the coupon. Perhaps, ultrasonic C-Scan evaluation is not appropriate for specimens that experience penetration by the impacter. Even for those specimens that did not experience penetration, X-ray provided better detailed information on the extent of core damage and evidence of multiple delaminations than the ultrasonic C-Scans (e.g., Figures 4.51 compared to 4.50).

The damage evaluation data from the cross-sectioning and deply methods provides an accurate three-dimensional characteristic damage state definition for the AS4/3501-6 $[\pm 45/0]_{2S}$ graphite/epoxy laminate. Comparison of these destructive damage evaluation methods to the time-of-

flight ultrasonic C-Scans is made to provide information on relative capabilities of these three three-dimensional damage evaluation methods. Looking at the relative capabilites of the three three-dimensional damage evaluation methods involves comparison of the damage evaluation summaries presented in Figures 4.106 through 4.109, 4.111 through 4.114, and 4.116 through 4.119.

Cross-sectioning of impact coupons gives through-the-thickness damage information that is converted to ply-by-ply damage schematics. Once this transformation is accomplished, the results are comparable to the time-of-flight ultrasonic C-scans. The summaries of damage evaluation by cross-section compared to the time-of-flight ultrasonic C-Scans are presented in Figures 4.106, 4.107, 4.111, 4.112, 4.116, and 4.117 for the cases of the three impacter masses used in this work. The time-of-flight ultrasonic C-Scans did not provide accurate information on damage type or extent when compared to the cross-section schematics of the same specimens. Damage extent in the ultrasonic C-Scans was not typically larger or smaller than that determined by cross-sectioning. For example, damage information provided by the ultrasonic C-Scans for plies 2 and 3 is typically grossly different from that observed by cross-sectioning. And because the impacter velocity used in the case of the 1523 g impacter caused penetration, the immediate loss of the backwall signal resulted in a very large damage zone in the ultrasonic C-Scans of plies 11 and 12. However, the impacter velocity used in the 578 g impacter case also resulted in penetration and there are no damage indications in plies 11 and 12 in this case.

The deply technique provides the damage definition directly. Thus, deply damage definition results are immediately comparable to time-of-

flight C-scan results. The summaries of damage evaluation by deply compared to the time-of-flight ultrasonic C-Scans are presented in Figures 4.108, 4.109, 4.113, 4.114, 4.118, and 4.119 for the cases of the three impacter masses used in this work. (Reminder: the deply coupons are different from the cross-section coupons since two destructive evaluation methods cannot be applied to the same coupon.) The interpretations of the time-of-flight ultrasonic C-Scans also did not provide accurate information on damage type or extent when compared to the deply damage evaluations. Damage extent in the ultrasonic C-Scans was not typically larger or smaller than that determined by deply. For example, "previews" of damage in the following plies could cause significant misinterpretations of damage in the ply of interest, especially if no corresponding physical evidence was available to corroborate the ultrasonic C-Scans.

Since the two-dimensional damage evaluation methods provide an integrated through-the-thickness summary of the three-dimensional damage state, comparisons of the two- and three-dimensional damage evaluation methods is also made. The comparison of the two-dimensional damage state to the three-dimensional damage state is made using X-ray photographs and the deply damage evaluation summaries as these are the best representations available. The three-dimensional damage state definitions by deply for the three impacter masses tested at or near their "MCRS-velocity" are very similar, as shown in Figures 4.108, 4.113, and 4.118. However, the X-ray photograph of the specimen impacted by the 8.4 g mass, shown in Figure 4.115, has a different major axis of damage indication than for the specimens impacted by the 1523 and 578 g masses shown in Figures 4.105 and 4.110, respectively. Thus, the two-dimensional integrated through-the-thickness summary of the damage state is not

necessarily an accurate representation of the actual three-dimensional damage state.

The results from the damage evaluation program indicate that the three-dimensional damage state currently cannot be determined by any method other than a destructive one. Results from the compressive residual strength test program show the need for an accurate assessment of the three-dimesional damage state. However, destructive evaluation is not an option for specimens to be tested for residual strength or for production parts. The state-of-the-art in nondestructive damage evaluation methods as presented in this work is not capable of providing the necessary information for an accurate assessment of the three-dimensional damage state as needed.

Chapter 6

CONCLUSIONS AND RECOMMENDATIONS

The damage states and compressive residual strength behavior of AS4/3501-6 $[\pm 45/0]_{2S}$ graphite/epoxy laminates after impact has been experimentally studied in this research effort. The original purpose of the experimental program was twofold: to provide data for correlation to a preliminary predictive analysis method to be developed for compressive residual strength; and to answer the questions raised by the results of a previous research project concerning the existence of a minimum compressive residual strength [83]. As to the first purpose of the experimental program, assessment of the state-of-the-art in predictive capabilities indicated that the need for basic understanding of the damage mechanisms governing compressive failure behavior still existed. Thus, the focus of the experimental program shifted to answering the questions on minimum compressive residual strength which were: one, what is the three-dimensional damage state that governs minimum compressive residual strength behavior; two, is this minimum compressive residual strength value dependent upon impact method; and three, how is this minimum compressive residual strength value related to impacter mass and velocity?

The first question raised from the previous research results [83] motivated the intensive damage evaluation program conducted in this research effort. Three two-dimensional nondestructive damage evaluation methods were studied: visual inspection, inspection by X-ray, and inspection by ultrasonic C-Scan. Three three-dimensional damage

evaluation methods were also studied: nondestructive evaluation by time-of-flight ultrasonic C-Scan, destructive evaluation by cross-sectioning, and destructive evaluation by deply.

In the process of answering the first question, another important question was raised: once nondestructive evaluation is performed, how does one know that it is an accurate or adequate representation of the damage within the specimen? The destructive damage evaluation methods used in this work provide the necessary information to define the damage state. However, destructive evaluation is not always a viable option (e.g., production parts or specimens to be tested for residual strength). Often only visual inspection and a record of the damage state by a two-dimensional nondestructive damage evaluation method are available for determination of accept/reject of a part. Thus, the two-dimensional damage information provided by X-ray and ultrasonic C-Scan were compared to the damage state definition provided by the destructive evaluation methods. The two-dimensional damage evaluation methods are integrated through-the-thickness summaries of the three-dimensional damage state and, if accurate, should represent the same damage types, sizes, shapes, and orientations.

The answers to the questions raised are provided in the order they were addressed in the experimental program:

1. *Is the minimum compressive residual strength value dependent upon impact method?*

   The three impacter masses used in this work resulted in virtually identical minimum compressive residual strengths (approximately

187 MPa ± 3 MPa). Thus, minimum compressive residual strength is apparently independent of impacter mass and impact method.

2. *How is the minimum compressive residual strength value related to impacter mass and velocity?*

The parameter typically used to compare the effects of different impacter masses and associated velocities is impacter energy. The impacter energies are not equivalent for the specimens that failed at the same minimum compressive residual strength for the three impacter masses used in the test program (nor, obviously, are the velocities).

3. *What is the three-dimensional damage state that governs minimum compressive residual strength behavior?*

The three-dimensional damage states due to impact by the three masses used in this work were similar at velocities known to cause minimum compressive residual strength. This damage state consists of core damage and delamination. Core damage remains fairly constant through the thickness due to impact at velocities in the penetration range. Delaminations exist between every interface with the exception of the interface between the two 0° plies. Delamination shape is roughly elliptical with orientation in the direction of the next ply further away from the impact surface. Delamination size increases as ply distance from the impact surface increases. And, there is consistent evidence of the extensive delamination between plies 1 and 2 including indications of back surface spalling.

In answering the aforementioned questions, the compressive residual strength test program and the intensive damage evaluation investigation resulted in the following additional conclusions:

1. Two-dimensional damage information, such as major axis of damage, minor axis of damage, and core damage size, is not sufficient for prediction of compressive residual strength.

2. The damage state definition provided by the two-dimensional nondestructive evaluation methods does not represent the integrated through-the-thickness summary of the destructively-determined three-dimensional damage state.

3. The state-of-the-art in nondestructive three-dimensional damage evaluation, as presented in this work, is not capable of providing the necessary information for an accurate assessment of the three-dimensional damage state. Currently, the three-dimensional damage state can only be determined accurately by destructive methods.

4. The postmortem evaluation of the minimum compressive residual strength specimens showed the extensive core damage due to impacter penetration, sublaminate buckling of ply 1, fiber failure in the remaining plies, and extensive back side spalling of ply 1. Although it is not possible to determine which damage mode or combination of damage modes are controlling the compressive residual strength, it is clear that failure modes are similar if not the same.

5. It is the resulting three-dimensional damage state, not the impact metrics, that is important in determining the residual performance capabilities.

6. Though it is important to understand the separation of damage tolerance and damage resistance, the two issues are linked through the damage state caused by the impact event. The use of the calculated force and acceleration histories from the impact metrics has merit for the prediction of damage states and subsequent prediction of residual performance.

As a result of this work, a number of items arise which are worthy of further research:

1. A prediction methodology for compressive residual strength should be developed using the common three-dimensional damage state known to result in minimum compressive residual strength.

2. Parametric studies (experimental and analytical) should be performed to determine the relative effects of the different damage types and locations on compressive residual strength.

3. Further work needs to be done on accurately addressing the combination of predicted impacter force with inertia of the plate resulting in the force needed to predict stresses and strains in the plate and, thus, damage states.

4. All the compressive residual strength specimens in this work were fabricated with the impact surface bonded to the honeycomb sandwich. Tests should be conducted to determine if bonding the back surface to

the honeycomb sandwich results in lower, higher, or identical compressive residual strength, thus, providing experimental evidence as to the importance of the ply 1 sublaminate buckling in the resulting compressive residual strength.

5. Improvements in three-dimensional nondestructive evaluation methods need to be made to accurately assess the three-dimensional damage state since two-dimensional nondestructive evaluation may may inaccurately represent the extent and type of damage.

Further research in these areas is justified to provide analysis models and experimental evidence that will aid engineers in the design of composite structures and increase the level of confidence in analytical prediction methodologies.

REFERENCES

1. Demuts, E., R. S. Whitehead, and R. B. Deo, "Assessment of Damage Tolerance in Composites," Composite Structures, Vol. 4, No. 1, 1985, pp. 45–58.

2. Potter, R. T., "The Significance of Defects and Damage in Composite Structures," Characterization, Analysis and Significance of Defects in Composite Materials, AGARD-CP-355, 1983, pp. 17-1 through 17-10.

3. Baker, A. A., R. Jones, and R. J. Callinan, "Damage Tolerance of Graphite/Epoxy Composites," Composite Structures, Vol. 4, No. 1, 1985, pp. 15–44.

4. Garg, A. C., "Delamination—A Damage Mode in Composite Structures," Engineering Fracture Mechanics, Vol. 29, No. 5, 1988, pp. 557–584.

5. Sollars, T. A., "Shuttle/Centaur G-Prime Composite Adapters Damage Tolerance/Repair Test Program," Proceedings of the 28th AIAA/ASME/ASCE/AHS Structures, Structural Dynamics and Materials Conference, Monterey, California, April, 1987, pp. 362–375.

6. Whitehead, R. S., "Certification of Primary Composite Aircraft Structures," New Materials and Fatigue Resistant Aircraft Design, Proceedings of the 14th ICAF Symposium, Ottawa, Canada, June, 1987, pp. 585–617.

7. O'Brien, T. K., "Toward a Damage Tolerance Philosophy for Composite Materials and Structures," Composite Materials: Testing and Design, Vol. 9, ASTM STP 1059, 1990, pp. 7–33.

8. Challenger, K. D., "The Damage Tolerance of Carbon Fiber Reinforced Composites—A Workshop Summary," Composite Structures, Vol. 6, No. 4, 1986, pp. 295–318.

9. Rhodes, M. D., and J. G. Williams, "Concept for Improving the Damage Tolerance of Composite Compression Panels," NASA-TM-85748, 1984.

10. Ghasemi Nejhad, M. N., and A. Parvizi-Majidi, "Impact Behaviour and Damage Tolerance of Woven Carbon Fibre-Reinforced Thermoplastic Composites," Composites, Vol. 21, No. 2, March, 1990, pp. 155–168.

11. Shaw, D., and M. Y. Tsai, "Analysis of Delamination in Compressively Loaded Laminates," Composites Science and Technology, Vol. 34, No. 1, 1989, pp. 1–17.

12. Wilkins, D. J., "The Engineering Significance of Defects in Composite Structures," Characterization, Analysis and Significance of Defects in Composite Materials, AGARD-CP-355, 1983, pp. 20-1 through 20-11.

13. Gurdal, Z., R. T. Haftka, and J. H. Starnes, Jr., "The Effect of Slots on the Buckling and Postbuckling Behavior of Laminated Plates," Journal of Composites Technology and Research, Vol. 7, No. 3, Fall, 1985, pp. 82–87.

14. Porter, T. R., "Compression and Compression Fatigue Testing of Composite Laminates," NASA-CR-168023, July, 1982.

15. Rhodes, M. D., J. G. Williams, and J. H. Starnes Jr., "Effect of Low-Velocity Impact Damage on the Compressive Strength of Graphite-Epoxy Hat-Stiffened Panels," NASA TN D-8411, April, 1977.

16. Byers, B. A., "Behavior of Damaged Graphite/Epoxy Laminates Under Compression Loading," NASA-CR-159293, August, 1980.

17. Flanagan, G., "Two-Dimensional Delamination Growth in Composite Laminates Under Compression Loading," Composite Materials: Testing and Design, ASTM STP 972, 1988, pp. 180–190.

18. Pavier, M. J., and W. T. Chester, "Compression Failure of Carbon Fibre-Reinforced Coupons Containing Central Delaminations," Composites, Vol. 21, No. 1, January, 1990, pp. 23–31.

19. Garrett, R. A., "Effect of Defects on Aircraft Composite Structures," McAir No. 83-010, Presented at AGARD Structures and Material Panel, London, England, April, 1983.

20. Starnes, J. H., Jr., M. D. Rhodes, and J. G. Williams, "Effect of Impact Damage and Holes on the Compressive Strength of a Graphite/Epoxy Laminate," Nondestructive Evaluation and Flaw Criticality for Composite Materials, ASTM STP 696, 1979, pp. 145–171.

21. Cantwell, W. J., and J. Morton, "Impact Perforation of Carbon Fibre Reinforced Plastic," Composites Science and Technology, Vol. 38, No. 2, 1990, pp. 119–141.

22. Jones, R., and R. J. Callinan, "Analysis of Compression Failures in Composite Materials," Proceedings of International Conference on Composite Materials IV, Vol. 1, Tokyo, Japan, 1982, pp. 447–454.

23. Ishai, O., and A. Shragai, "Effect of Impact Loading on Damage and Residual Compressive Strength of CFRP Laminated Beams," Composite Structures, Vol. 14, No. 4, 1990, pp. 319–337.

24. Structures Analysis Manual, General Dynamics Convair and Space Systems Divisions, Vol. 2, 1988, p. 20.2.1.

25. Cairns, D. S., "Impact and Post-Impact Response of Graphite/Epoxy and Kevlar/Epoxy Structures," TELAC Report No. 87-15, Massachusetts Institute of Technology, August, 1987.

26. Sjoblom, P., and H. W. Hwang, "Compression After Impact, the $5000 Data Point," Tomorrow's Materials: Today, 34th International SAMPE Symposium & Exhibition, Reno, Nevada, May, 1989, pp. 1411–1421.

27. Ilcewicz, L. B., E. F. Dost, and R. L. Coggeshall, "A Model for Compression After Impact Strength Evaluation," Advanced Materials: The Big Payoff, 21st International SAMPE Technical Conference, Atlantic City, New Jersey, September, 1989, pp. 130–147.

28. Cairns, D. S., and P. A. Lagace, "Residual Tensile Strength of Graphite/Epoxy and Kevlar/Epoxy Laminates with Impact Damage," Composite Materials: Testing and Design, Vol. 9, ASTM STP 1059, 1990, pp. 48–63.

29. Ryan, K. F., "Dynamic Response of Graphite/Epoxy Plates Subjected to Impact Loading," TELAC Report No. 89-13, Massachusetts Institute of Technology, September 1989.

30. Williams, J. G., "Effect of Impact Damage and Open Holes on the Compression Strength of Tough Resin/High Strain Fiber Laminates," Tough Composite Materials, NASA-CP-2334, May, 1983, pp. 61–79.

31. Manders, P. W., and W. C. Harris, "A Parametric Study of Composite Performance in Compression-After-Impact Testing," SAMPE Journal, Vol. 22, November/December, 1986, pp. 47–51.

32. Williams, J. G., T. K. O'Brien, and A.J. Chapman III, "Comparison of Toughened Composite Laminates Using NASA Standard Damage Tolerance Tests," ACEE Composite Structures Technology, NASA-CP-2321, Seattle, Washington, August , 1984, pp. 51–73.

33. Dorey, G., S. M. Bishop, and P. T. Curtis, "On the Impact Performance of Carbon Fibre Laminates with Epoxy and PEEK Matrices," Composites Science and Technology, Vol. 23, No. 3, 1985, pp. 221–237.

34. Bishop, S. M., and G. Dorey, "The Effect of Damage on the Tensile and Compressive Performance of Carbon Fibre Laminates," Characterization, Analysis and Significance of Defects in Composite Materials, AGARD-CP-355, London, England, April, 1983, pp. 10-1 through 10-10.

35. Hong, S., and D. Liu, "On the Relationship Between Impact Energy and Delamination Area," Experimental Mechanics, Vol. 29, No. 2, June, 1989, pp. 115–120.

36. Marshall, R. D., P. E. Sandorff, and K. N. Lauraitis, "Buckling of a Damaged Sublaminate in an Impacted Laminate," Journal of Composites Technology and Research, Vol. 10, No. 3, Fall, 1988, pp. 107–113.

37. Liu, D., L. S. Lillycrop, L. E. Malvern, and C. T. Sun, "The Evaluation of Delamination—An Edge Replication Study," Experimental Techniques, Vol. 11, No. 5, May, 1987, pp. 20–25.

38. Avery, J. G., Design Manual for Impact Damage Tolerant Aircraft Structure, AGARDograph No. 238, AGARD/NATO, Paris, France, October, 1981.

39. Cantwell, W. J., and J. Morton, "Comparison on the Low and High Velocity Impact Response of CFRP," Composites, Vol. 20, No. 6, November, 1989, pp. 545–551.

40. Rhodes, M. D., J. G. Williams, and J. H. Starnes, "Low-Velocity Impact Damage in Graphite-Fiber Reinforced Epoxy Laminates," Polymer Composites, Vol. 2, January, 1981, pp. 36–44.

41. Chai, H., C. D. Babcock, and W. G. Knauss, "One Dimensional Modelling of Failure in Laminated Plates by Delamination Buckling," International Journal of Solid Structures, Vol. 17, No. 11, 1981, pp. 1069–1083.

42. Chai, H., W. G. Knauss, and C. D. Babcock, "Observation of Damage Growth in Compressively Loaded Laminates," Experimental Mechanics, Vol. 23, No. 3, September, 1983, pp. 329–337.

43. Sharma Avva, V., "Effect of Specimen Size on the Buckling Behavior of Laminated Composites Subjected to Low-Velocity Impact," Compression Testing of Homogeneous Materials and Composites, ASTM STP 808, 1982, pp. 140–154.

44. Cantwell, W. J., P. T. Curtis, and J. Morton, "An Assessment of the Impact Performance of CFRP Reinforced with High-Strain Carbon Fibres," Composites Science and Technology, Vol. 25, No. 2, 1986, pp. 133–148.

45. Levin, K., "Effect of Low-Velocity Impact on Compressive Strength of Quasi-Isotropic Laminate," Proceedings of the American Society of Composites, First Technical Conference, Dayton, Ohio, October, 1986, pp. 313–326.

46. Elber, W., "The Effect of Matrix and Fiber Properties on Impact Resistance," Tough Composite Materials, NASA-CP-2334, May, 1988, pp. 99–121.

47. Husman, G. E., J. M. Whitney, and J. C. Halpin, "Residual Strength Characterization of Laminated Composites Subjected to Impact Loading," Foreign Object Impact Damage to Composites, ASTM STP 568, 1975, pp. 92–113.

48. Wu, H. Y. T., and G. S. Springer, "Measurements of Matrix Cracking and Delamination Caused by Impact on Composite Plates," Journal of Composite Materials, Vol. 22, June, 1988, pp. 518–532.

49. Guynn, E. G., and T. K. O'Brien, "The Influence of Lay-Up and Thickness on Composite Impact Damage and Compression Strength," Proceedings of the 26th AIAA/ASME/ASCE/AHS Structures, Structural Dynamics and Materials Conference, Orlando, Florida, April, 1985, pp. 187–196.

50. Whitney, J. M., and R. J. Nuismer, "Stress Fracture Criteria for Laminated Composites Containing Stress Concentrations," Journal of Composite Materials, Vol. 8, July, 1974, pp. 253–265.

51. Nuismer, R. J., and J. D. Labor, "Application of the Average Stress Failure Criterion: Part II—Compression," Journal of Composite Materials, Vol. 13, January, 1979, pp. 49–60.

52. Tan, S. C., "Effective Stress Fracture Models for Unnotched and Notched Multidirectional Laminates," Journal of Composite Materials, Vol. 22, April, 1988, pp. 322–340.

53. Chang, F. K., L. Lessard, and J. M. Tang, "Compression Response of Laminated Composites Containing an Open Hole," SAMPE Quarterly, Vol. 19, No. 4, July, 1988, pp. 46–51.

54. Whitcomb, J. D., "Finite Element Analysis of Instability Related Delamination Growth," Journal of Composite Materials, Vol. 15, September, 1981, pp. 403–426.

55. Whitcomb, J. D., "Parametric Analytical Study of Instability-Related Delamination Growth," Composites Science and Technology, Vol. 25, No. 1, 1986, pp. 19–48.

56. Donaldson, S. L., "The Effect of Interlaminar Fracture Properties on the Delamination Buckling of Composites," Composites Science and Technology, Vol. 28, No. 1, 1987, pp. 33–44.

57. Rothschilds, R. J., J. W. Gillispie, Jr., and L. A. Carlsson, "Instability-Related Delamination Growth in Thermoset and Thermoplastic Composites," Composite Materials: Testing and Design, ASTM STP 972, 1988, pp. 161–179.

58. Ramkumar, R. L., "Performance of a Quantitative Study of Instability-Related Delamination Growth," NASA-CR-166046, March, 1983.

59. Vizzini, A. J., and P. A. Lagace, "An Elastic Foundation Model to Predict the Growth of Delamination," Journal of Composites Technology and Research, Vol. 11, No. 3, Fall, 1989, pp. 81–86.

60. Wang, A. S. D., M. Slomiana, and R. B. Bucinell, "Delamination Crack Growth in Composite Laminates," Delamination and Debonding of Materials, ASTM STP 876, 1985, pp. 135–167.

61. Kutlu, Z., and F. K. Chang, "Compression Strength of Laminated Composites Containing Multiple Delaminations," Proceedings of the American Society for Composites, Fifth Technical Conference, East Lansing, Michigan, June, 1990, pp. 839–848.

62. Gillespie, J. W. Jr., and R. B. Pipes, "Compressive Strength of Composite Laminates with Interlaminar Defects," Composite Structures, Vol. 2, No. 1, 1984, pp. 49–69.

63. Sallam, S., and G. J. Simitses, "Delamination Buckling and Growth of Flat, Cross-Ply Laminates," Composite Structures, Vol. 4, No. 4, 1985, pp. 361–381.

64. Sheinman, I., M. Bass, and O. Ishai, "Effect of Delamination on Stability of Laminated Composite Strip," Composite Structures, Vol. 11, No. 3, 1989, pp. 227–242.

65. Yin, W. L., S. N. Sallam, and G. J. Simitses, "Ultimate Axial Load Capacity of a Delaminated Beam-Plate," AIAA Journal, Vol. 24, No. 1, January, 1986, pp. 123–128.

66. Shivakumar, K. N., and J. D. Whitcomb, "Buckling of a Sublaminate in a Quasi-Isotropic Composite Laminate," Journal of Composite Materials, Vol.19, January, 1985, pp. 2–18.

67. Kardomateas, G. A., "Large Deformation Effects in the Postbuckling Behavior of Composites with Thin Delaminations," AIAA Journal, Vol. 27, No. 5, May, 1989, pp. 624–631.

68. Kardomateas, G. A., "End Fixity Effects on the Buckling and Post-buckling of Delaminated Composites," Composites Science and Technology, Vol. 34, No. 2, 1989, pp. 113–128.

69. Jones, R., J. Paul, and W. Broughton, "On the Effects of Delamination Damage in Fibre Composite Laminates," Structures Report 403, DSTO Aeronautical Research Laboratories, Melbourne, Australia, 1984.

70. Williams, J. F., D. C. Stouffer, S. Illic, and R. Jones, "An Analysis of Delamination Behavior," Composite Structures, Vol. 5, No. 3, 1986, pp. 203–216.

71. Whitcomb, J. D., "Mechanics of Instability-Related Delamination Growth," Composite Materials: Testing and Design, Vol. 9, ASTM STP 1059, 1990, pp. 215–230.

72. Whitcomb, J. D., "Three-Dimensional Analysis of a Postbuckled Embedded Delamination," NASA-TP-2823, 1988.

73. Whitcomb, J. D., and K. N. Shivakumar, "Strain-Energy Release Rate Analysis of a Laminate With a Postbuckled Delamination," NASA TM-89091, February, 1987.

74. Chai, H., and C. D. Babcock, "Two-Dimensional Modelling of Compressive Failure in Delaminated Composites," Journal of Composite Materials, Vol. 19, January, 1985, pp. 67–98.

75. Kardomateas, G. A., and D. W. Schmueser, "Buckling and Postbuckling of Delaminated Composites Under Compressive Loads Including Transverse Shear Effects," AIAA Journal, Vol. 26, No. 3, March, 1988, pp. 337–343.

76. Bottega, W. J., and A. Maewal, "Delamination Buckling and Growth in Laminates," Journal of Applied Mechanics, Vol. 50, No. 1, March, 1983, pp. 184–189.

77. Yin, W. L., "Axisymmetric Buckling and Growth of a Circular Delamination in a Compressed Laminate," International Journal of Solids and Structures, Vol. 21, No. 5, 1985, pp. 503–514.

78. Yin, W. L., and Z. Fei, "Delamination Buckling and Growth in a Clamped Circular Plate," AIAA Journal, Vol. 26, No. 4, April, 1988, pp. 438–445.

79. Webster, J. D., "Flaw Criticality of Circular Disbond Defects in Compressive Laminates," NASA-CR-164830, March, 1981.

80. Kassapoglou, C., "Buckling, Post-Buckling and Failure of Elliptical Delaminations in Laminates under Compression," Composite Structures, Vol. 9, No. 2, 1988, pp. 139–159.

81. Geier, W., J. Vilismeier, and D. Weiserver, "Experimental Investigation of Delaminations in Carbon," Characterization, Analysis and Significance of Defects in Composite Materials, AGARD-CP-355, 1983, pp. 6-1 through 6-11.

82. Clark, G., and T. J. van Blaricum, "Carbon Fibre Composite Coupons - Static and Fatigue Behavior After Impact Damage," Structures Report 422, DSTO Aeronautical Research Laboratories, Melbourne, Australia, 1986.

83. Martin, R. C., and C. Poelman, "Compressive Residual Strength of Composite Laminates After Impact," 16.622 Final Report, Department of Aeronautics and Astronautics, Massachusetts Institute of Technology, December 12, 1989.

84. Dost, Ernest F., Larry B. Ilcewicz, and J. H. Gosse, "Sublaminate Stability Based Modeling of Impact-Damaged Composite Laminates," Proceedings of the American Society for Composites, Third Technical Conference, Seattle, Washington, September, 1988, pp. 354–363.

85. Lagace, P. A., and A. J. Vizzini, "The Sandwich Column as a Compressive Characterization Specimen for Thin Laminates," Composite Materials: Testing and Design, ASTM STP 972, Philadelphia, Pennsylvania, 1988, pp. 143–160.

86. Lagace, P. A., J. C. Brewer, and C. F. Varnerin, " TELAC Manufacturing Course Class Notes," TELAC Report No. 88-4, Massachusetts Institute of Technology, 1988.

87. Lie, S. C., "Damage Resistance and Damage Tolerance of Thin Composite Facesheet Honeycomb Panels," TELAC Report No. 89-3, Massachusetts Institute of Technology, March, 1989.

88. Freeman, S. M., "Characterization of Lamina and Interlaminar Damage in Graphite/Epoxy Composites by the Deply Technique," Composite Materials: Testing and Design, ASTM STP 787, 1982, pp. 50–62.

89. Tsang, P. H. W., "Impact Resistance of Graphite/Epoxy Sandwich Panels," TELAC Report No. 89-12, Massachusetts Institute of Technology, April, 1989.

90. Kraft, M. J., "Impact Damage Response of Graphite/Epoxy Fabric Structures," TELAC Report No. 88-9, Massachusetts Institute of Technology, July, 1988.

91. Cairns, D. S., and P. A. Lagace, "A Consistent Engineering Methodology for the Treatment of Impact in Composite Materials," Proceedings of the American Society for Composites, Fifth Technical Conference, East Lansing, Michigan, June, 1990, pp. 589–599.

92. Cairns, D. S., and P. A. Lagace, "Thick Composite Plates Subjected to Lateral Loadings," Journal of Applied Mechanics, Vol. 54, No. 3, September, 1987, pp. 611–616.

93. Cairns, D. S., and P. A. Lagace, "Transient Response of Graphite/Epoxy and Kevlar/Epoxy Laminates Subjected to Impact," AIAA Journal, Vol. 27, No. 11, November, 1989, pp. 1590–1596.

94. Lagace, P. A., K. F. Ryan, and M. J. Graves, "Effect of Damage in the Impact Response of Composite Laminates," Proceedings of the 32nd AIAA/ASME/ASCE/AHS Structures, Structural Dynamics and Materials Conference, Baltimore, Maryland, April, 1991, pp. 1137–1143.

Appendix A

MATERIAL AND MANUFACTURING DATA

The AS4/3501-6 graphite/epoxy material system supplied by Hercules, Inc. is manufactured in lots and provided to the user in rolls. Each roll has identification information including: lot number, spool number, areal weight, resin content, and date of manufacture. This information is recorded here for traceability of material consistency from laminate to laminate.

Eleven cure cycles were completed in the manufacturing of laminates for impact testing and subsequent manufacturing into compressive residual strength specimens. The third cure cycle was not nominal, as discussed in Chapter 3. Thus, cure cycle numbers for all laminates fabricated in this study are referenced herein.

The measured thickness for each coupon is determined by the average of nine measurements while the measured width is determined by the average of three measurements. As the measured thickness and width as manufactured are used for stress calculations, they are listed herein.

Table A.1 AS4/3501-6 Graphite/Epoxy Material Identification Data

Material	Lot Number	Spool Number	Resin Content	Areal Weight (g/m2)	Manufacture Date
1	5874-2	10	0.43	148	5/18/89
2	6075-2	50	0.42	150	10/18/89
3	6137-2	15	0.41	151	12/11/89
4	6253-2	7	0.40	152	4/3/90
5	6253-2	5	0.42	152	4/3/90

Table A.2 Coupon Manufacturing Data

Specimen No.	Cure Number	0 ply Material	+45 ply Material	-45 ply Material	Thickness (mm)	Width (mm)
J1-1	6	3	3	4	1.54	70.39
J1-2	6	3	3	4	1.56	70.45
J1-3	6	3	3	4	1.58	70.42
J1-4	6	3	3	4	1.54	70.40
J2-1	6	3	3	4	1.55	70.43
J2-2	6	3	3	4	1.56	70.45
J2-3	6	3	3	4	1.56	70.47
J2-4	6	3	3	4	1.56	70.44
J3-1	7	4	4	4	1.60	71.81
J3-2	7	4	4	4	1.60	70.15
J3-3	7	4	4	4	1.61	70.19
J3-4	7	4	4	4	1.58	69.61
J4-1	7	4	4	4	1.58	71.37
J4-2	7	4	4	4	1.60	70.11
J4-3	7	4	4	4	1.60	69.94
J4-4	7	4	4	4	1.55	70.14
J5-1	7	4	4	4	1.59	71.29
J5-2	7	4	4	4	1.63	70.18
J5-3	7	4	4	4	1.62	70.18
J5-4	7	4	4	4	1.61	70.19
J6-1	8	4	4	4	1.60	69.86
J6-2	8	4	4	4	1.62	69.78
J6-3	8	4	4	4	1.61	69.45
J6-4	8	4	4	4	1.61	69.78
J7-1	8	4	4	4	1.64	69.84
J7-2	8	4	4	4	1.65	69.49
J7-3	8	4	4	4	1.68	69.76
J7-4	8	4	4	4	1.64	69.77
J8-1	8	4	4	4	1.57	69.76
J8-2	8	4	4	4	1.61	69.65
J8-3	8	4	4	4	1.58	69.76
J8-4	8	4	4	4	1.57	69.77
J9-1	9	5	5	5	1.59	70.07
J9-2	9	5	5	5	1.63	70.06
J9-3	9	5	5	5	1.63	69.67
J9-4	9	5	5	5	1.62	70.07

Table A.2 Coupon Manufacturing Data (continued)

Specimen No.	Cure Number	0 ply Material	+45 ply Material	-45 ply Material	Thickness (mm)	Width (mm)
J10-1	9	5	5	5	1.57	70.03
J10-2	9	5	5	5	1.60	70.10
J10-3	9	5	5	5	1.60	70.07
J10-4	9	5	5	5	1.57	70.15
J11-1	9	5	5	5	1.59	70.06
J11-2	9	5	5	5	1.65	70.09
J11-3	9	5	5	5	1.63	70.13
J11-4	9	5	5	5	1.60	70.11
J12-1	10	5	5	5	1.59	69.70
J12-2	10	5	5	5	1.64	70.03
J12-3	10	5	5	5	1.63	70.05
J12-4	10	5	5	5	1.59	70.06
J13-1	10	5	5	5	1.58	70.03
J13-2	10	5	5	5	1.62	70.10
J13-3	10	5	5	5	1.62	70.05
J13-4	10	5	5	5	1.60	70.09
J14-1	10	5	5	5	1.59	70.03
J14-2	10	5	5	5	1.63	69.65
J14-3	10	5	5	5	1.64	70.09
J14-4	10	5	5	5	1.60	70.09
J15-1	11	5	5	5	1.59	70.17
J15-2	11	5	5	5	1.64	69.90
J15-3	11	5	5	5	1.65	69.36
J15-4	11	5	5	5	1.61	70.14
J16-1	11	5	5	5	1.60	70.21
J16-2	11	5	5	5	1.64	69.89
J16-3	11	5	5	5	1.64	70.11
J16-4	11	5	5	5	1.59	70.18
J17-1	11	5	5	5	1.60	70.19
J17-2	11	5	5	5	1.63	70.11
J17-3	11	5	5	5	1.63	70.14
J17-4	11	5	5	5	1.59	70.11
M1-1	1	1	1	1	1.57	70.23
M1-2	1	1	1	1	1.57	70.05
M1-3	1	1	1	1	1.58	69.85
M1-4	1	1	1	1	1.56	70.07

Table A.2 Coupon Manufacturing Data (Continued)

Specimen No.	Cure Number	0 ply Material	+45 ply Material	-45 ply Material	Thickness (mm)	Width (mm)
M2-1	1	1	1	1	1.58	70.21
M2-2	1	1	1	1	1.58	69.89
M2-3	1	1	1	1	1.59	70.22
M2-4	1	1	1	1	1.59	70.17
M3-1	1	1	1	1	1.61	70.23
M3-2	1	1	1	1	1.59	70.23
M3-3	1	1	1	1	1.60	70.09
M3-4	1	1	1	1	1.57	70.23
M4-1	1	1	1	1	1.60	70.21
M4-2	1	1	1	1	1.58	70.13
M4-3	1	1	1	1	1.57	70.06
M4-4	1	1	1	1	1.56	70.15
M5-1	2	1	2	2	1.58	70.23
M5-2	2	1	2	2	1.61	70.19
M5-3	2	1	2	2	1.59	70.21
M5-4	2	1	2	2	1.63	70.20
M6-1	2	1	2	1	1.60	70.19
M6-2	2	1	2	1	1.64	70.20
M6-3	2	1	2	1	1.63	70.21
M6-4	2	1	2	1	1.62	70.21
M7-1	2	1	2	1	1.61	70.20
M7-2	2	1	2	1	1.62	70.14
M7-3	2	1	2	1	1.61	70.23
M7-4	2	1	2	1	1.61	70.11
M8-1	3	2	2	2	1.61	69.93
M8-2	3	2	2	2	1.65	69.90
M8-3	3	2	2	2	1.62	69.93
M8-4	3	2	2	2	1.61	69.85
M10-1	3	2	2	2	1.60	69.93
M10-2	3	2	2	2	1.63	69.92
M10-3	3	2	2	2	1.62	69.95
M10-4	3	2	2	2	1.59	69.87
M11-1	3	2	2	2	1.56	69.97
M11-2	3	2	2	2	1.61	69.69
M11-3	3	2	2	2	1.62	69.91
M11-4	3	2	2	2	1.58	69.90

Table A.2 Coupon Manufacturing Data (Continued)

Specimen No.	Cure Number	0 ply Material	+45 ply Material	-45 ply Material	Thickness (mm)	Width (mm)
M12-1	3	2	2	2	1.60	69.80
M12-2	3	2	2	2	1.63	69.97
M12-3	3	2	2	2	1.65	69.77
M12-4	3	2	2	2	1.60	69.17
M13-1	3	2	2	2	1.59	69.63
M13-2	3	2	2	2	1.64	70.17
M13-3	3	2	2	2	1.62	69.63
M13-4	3	2	2	2	1.57	69.91
M14-1	6	3	4	4	1.57	70.42
M14-2	6	3	4	4	1.58	70.38
M14-3	6	3	4	4	1.56	70.42
M14-4	6	3	4	4	1.57	70.40
M15-1	6	3	4	4	1.56	70.41
M15-2	6	3	4	4	1.58	70.41
M15-3	6	3	4	4	1.59	70.38
M15-4	6	3	4	4	1.60	70.39
M16-1	6	3	3	4	1.58	70.42
M16-2	6	3	3	4	1.58	70.31
M16-3	6	3	3	4	1.58	70.33
M16-4	6	3	3	4	1.59	70.36
M17-1	6	3	3	4	1.54	70.45
M17-2	6	3	3	4	1.55	70.39
M17-3	6	3	3	4	1.56	70.15
M17-4	6	3	3	4	1.56	70.29
M18-1	7	4	4	4	1.56	70.57
M18-2	7	4	4	4	1.62	70.17
M18-3	7	4	4	4	1.60	70.21
M18-4	7	4	4	4	1.57	70.18
M19-1	7	4	4	4	1.59	71.91
M19-2	7	4	4	4	1.63	70.17
M19-3	7	4	4	4	1.60	70.20
M19-4	7	4	4	4	1.55	70.17
M20-1	7	4	4	4	1.59	71.81
M20-2	7	4	4	4	1.64	70.18
M20-3	7	4	4	4	1.63	70.19
M20-4	7	4	4	4	1.59	70.21

Table A.2 Coupon Manufacturing Data (Continued)

Specimen No.	Cure Number	0 ply Material	+45 ply Material	-45 ply Material	Thickness (mm)	Width (mm)
M21-1	8	4	4	4	1.60	69.89
M21-2	8	4	4	4	1.66	69.85
M21-3	8	4	4	4	1.64	69.77
M21-4	8	4	4	4	1.63	69.81
M22-1	8	4	4	4	1.61	69.77
M22-2	8	4	4	4	1.63	69.79
M22-3	8	4	4	4	1.64	69.78
M22-4	8	4	4	4	1.63	69.80
M23-1	8	4	4	4	1.59	69.82
M23-2	8	4	4	4	1.62	69.82
M23-3	8	4	4	4	1.62	69.80
M23-4	8	4	4	4	1.60	69.79
M24-1	9	5	5	5	1.59	65.36
M24-2	9	5	5	5	1.65	70.13
M24-3	9	5	5	5	1.63	70.09
M24-4	9	5	5	5	1.57	70.07
M25-1	9	5	5	5	1.58	70.00
M25-2	9	5	5	5	1.62	70.13
M25-3	9	5	5	5	1.62	69.87
M25-4	9	5	5	5	1.59	70.11
M26-1	9	5	5	5	1.60	70.06
M26-2	9	5	5	5	1.64	70.09
M26-3	9	5	5	5	1.63	70.08
M26-4	9	5	5	5	1.62	70.09
M27-1	10	5	5	5	1.56	70.07
M27-2	10	5	5	5	1.66	70.08
M27-3	10	5	5	5	1.63	70.11
M27-4	10	5	5	5	1.58	70.05
M28-1	10	5	5	5	1.61	70.08
M28-2	10	5	5	5	1.63	70.06
M28-3	10	5	5	5	1.63	69.59
M28-4	10	5	5	5	1.61	70.05
M29-1	10	5	5	5	1.61	70.07
M29-2	10	5	5	5	1.65	69.83
M29-3	10	5	5	5	1.64	70.12
M29-4	10	5	5	5	1.56	69.78

Table A.2 Coupon Manufacturing Data (Continued)

Specimen No.	Cure Number	0 ply Material	+45 ply Material	-45 ply Material	Thickness (mm)	Width (mm)
M30-1	11	5	5	5	1.60	70.17
M30-2	11	5	5	5	1.63	70.25
M30-3	11	5	5	5	1.61	70.19
M30-4	11	5	5	5	1.58	70.18
M31-1	11	5	5	5	1.56	70.21
M31-2	11	5	5	5	1.63	70.13
M31-3	11	5	5	5	1.62	70.17
M31-4	11	5	5	5	1.61	70.10
M32-1	11	5	5	5	1.57	70.11
M32-2	11	5	5	5	1.63	70.01
M32-3	11	5	5	5	1.62	70.25
M32-4	11	5	5	5	1.60	70.11
C1-1	4	3	2	2	1.60	69.85
C1-2	4	3	2	2	1.63	69.84
C1-3	4	3	2	2	1.61	69.77
C1-4	4	3	2	2	1.62	69.83
C2-1	4	3	2	2	1.60	69.97
C2-2	4	3	2	2	1.63	69.69
C2-3	4	3	2	2	1.61	69.91
C2-4	4	3	2	2	1.62	69.91
C3-1	4	3	2	2	1.60	70.40
C3-2	4	3	2	2	1.62	69.97
C3-3	4	3	2	2	1.59	69.91
C3-4	4	3	2	2	1.62	69.93
C4-1	4	3	2	2	1.61	69.77
C4-2	4	3	2	2	1.64	69.98
C4-3	4	3	2	2	1.61	69.75
C4-4	4	3	2	2	1.65	69.93
C5-1	4	3	2	2	1.62	69.89
C5-2	4	3	2	2	1.67	69.78
C5-3	4	3	2	2	1.64	69.58
C5-4	4	3	2	2	1.64	69.93
C6-1	4	3	2	2	1.60	69.78
C6-2	4	3	2	2	1.61	69.87
C6-3	4	3	2	2	1.55	69.89
C6-4	4	3	2	2	1.62	69.90

Table A.2 Coupon Manufacturing Data (continued)

Specimen No.	Cure Number	0 ply Material	+45 ply Material	-45 ply Material	Thickness (mm)	Width (mm)
C7-1	5	3	2	2	1.59	69.75
C7-2	5	3	2	2	1.61	69.93
C7-3	5	3	2	2	1.59	69.85
C7-4	5	3	2	2	1.62	69.92
T1-1	1	1	1	1	1.56	69.93
T1-2	1	1	1	1	1.59	70.23
T1-3	1	1	1	1	1.58	70.21
T1-4	1	1	1	1	1.56	70.23
T2-1	1	1	1	1	1.59	70.21
T2-2	1	1	1	1	1.59	70.02
T2-3	1	1	1	1	1.57	70.08
T2-4	1	1	1	1	1.58	70.21
T3-1	2	1	2	2	1.64	69.95
T3-2	2	1	2	2	1.63	70.17
T3-3	2	1	2	2	1.62	70.24
T3-4	2	1	2	2	1.61	70.15
T4-1	2	1	2	1	1.63	70.17
T4-2	2	1	2	1	1.64	69.93
T4-3	2	1	2	1	1.62	70.22
T4-4	2	1	2	1	1.61	70.21
T5-1	2	1	2	1	1.64	70.25
T5-2	2	1	2	1	1.66	70.25
T5-3	2	1	2	1	1.63	70.24
T5-4	2	1	2	1	1.63	70.20
T6-1	5	3	2	2	1.61	69.91
T6-2	5	3	2	2	1.65	69.61
T6-3	5	3	2	2	1.64	69.91
T6-4	5	3	2	2	1.62	69.77

Appendix B

IMPACT AND COMPRESSIVE RESIDUAL STRENGTH DATA

The undamaged, open hole, impact and compressive residual strength figures and tables in the main body of the text are based on data herein. The listing includes: specimen number (which can be used to cross-reference material and cure information provided in Appendix A); measured geometry (i.e., thickness and width); impacter velocity and energy; damage measurements provided by X-ray of the major axis, minor axis, and core (or hole) size; and, the compressive residual failure stress of the damaged facesheet. The above information is divided into tables by impacter mass.

Table B.1 Compressive Residual Strength Data of Undamaged and Open Hole Specimens

Specimen Number	Average Thickness (mm)	Average Width (mm)	Hole Diameter (mm)	Failure Stress (MPa)
C1-3	1.61	69.8	0	630
M5-2	1.61	70.2	0	660
T6-2	1.65	69.6	12.7	344
M2-2	1.58	69.9	12.7	324
C2-2	1.63	69.7	12.7	329
T5-3	1.63	70.2	19.1	279
M19-2	1.63	70.2	19.1	278
C6-2	1.61	69.9	19.1	299
M7-2	1.62	70.1	25.4	240
C5-3	1.64	69.6	25.4	294
T2-2	1.59	70.0	25.4	268

Table B.2 Compressive Residual Strength Data and Damage Size Determined by X-ray of Specimens Impacted by a 1523 g Mass

Specimen Number	Average Thickness (mm)	Average Width (mm)	Impacter Velocity (m/s)	Impacter Energy (J)	Major Axis (mm)	Minor Axis (mm)	Core Damage (mm)	Failure Stress (MPa)
T1-2	1.59	70.2	4.3	13.8*	17	12	5	419
T2-3	1.57	70.1	4.6	16.2	62	23	19	278
M4-3	1.57	70.1	4.8	17.3*	19	13	5	337
C4-3	1.61	69.8	4.8	17.3*	61	20	18	266
T3-2	1.63	70.2	4.8	17.3*	78	15	13	279
M2-3	1.59	70.2	5.2	20.5*	22	12	5	341
C2-3	1.61	69.9	5.2	20.5*	64	22	22	276
M5-1	1.58	70.2	5.2	20.5*	61	23	19	255
M10-3	1.62	70.0	5.2	20.7	65	22	19	291
M6-2	1.64	70.2	5.5	22.4*	28	12	11	392
M17-2	1.55	70.4	5.5	22.7	61	23	20	270
M23-3	1.62	69.8	5.5	22.7	62	23	20	234
C1-4	1.62	69.8	5.7	24.6*	66	20	20	219
M21-2	1.66	69.9	5.7	24.9	71	21	19	244
J6-3	1.61	69.5	5.7	24.9	73	23	19	266
J3-3	1.61	70.2	6.0	27.1*	61	29	18	285
J4-2	1.60	70.1	6.0	27.1*	58	25	21	305
M1-4	1.56	70.1	6.0	27.1*	73	24	19	236
M18-2	1.62	70.2	6.0	27.4	75	24	18	255
M3-2	1.59	70.2	6.3	30.0*	69	27	19	184
C6-3	1.55	69.9	6.3	30.0*	77	24	20	278
T3-3	1.62	70.2	6.3	30.0*	86	23	20	232
J17-2	1.63	70.1	6.3	30.4	70	27	19	234
J5-2	1.63	70.2	6.7	33.8	72	26	21	266
J8-2	1.61	69.7	6.7	33.8	64	27	19	220
M19-3	1.60	70.2	6.7	33.8	69	19	18	260
M7-3	1.61	70.2	7.1	37.5*	77	24	20	250
M20-3	1.63	70.2	7.1	37.9	60	24	20	240
J7-3	1.68	69.8	7.5	42.8	70	27	18	233
M14-3	1.56	70.4	7.5	42.8	80	26	19	243
C3-2	1.62	70.0	8.6	55.3*	81	23	20	247

* Impacter Mass = 1505 g

Table B.3 Damage Size Determined by X-ray of Specimens Impacted by a 1523 g Mass and Selected for Destructive Evaluation

Specimen Number	Average Thickness (mm)	Average Width (mm)	Impacter Velocity (m/s)	Impacter Energy (J)	Major Axis (mm)	Minor Axis (mm)	Core Damage (mm)	Test Type
M11-2	1.61	69.7	5.5	22.7	55	23	18	Section
M25-2	1.62	70.1	5.7	24.9	84	24	18	Section
J13-3	1.62	70.1	5.7	24.9	72	19	21	Section
J15-2	1.64	69.9	5.7	24.9	81	23	16	Section
M29-3	1.64	70.1	5.7	24.9	67	23	20	Deply
T4-2	1.64	69.9	5.7	24.5*	65	24	25	CRS**
J11-2	1.65	70.1	6.0	27.4	88	28	21	Section
J16-3	1.64	70.1	6.0	27.4	65	22	18	Section
C3-3	1.59	69.9	6.0	27.1*	55	22	18	CRS**
T1-3	1.58	70.2	6.0	27.1*	60	23	20	CRS**
T5-2	1.66	70.3	6.3	30.4	72	30	19	Section
M12-3	1.65	69.8	6.3	30.4	77	22	18	Section
M13-2	1.64	70.2	6.3	30.4	76	22	20	Section
M8-2	1.65	69.9	6.3	30.4	61	24	19	Deply
C4-2	1.64	70.0	6.3	30.1*	67	27	19	CRS**
M3-3	1.60	70.1	6.3	30.1*	70	22	16	CRS**
M32-2	1.63	70.0	6.7	33.8	62	25	20	Section
C7-3	1.59	69.9	6.7	33.8	63	20	19	Section
M4-2	1.58	70.1	6.7	33.5*	70	20	19	CRS**
M6-3	1.63	70.2	7.1	37.5*	60	22	18	CRS**
M10-2	1.63	69.9	7.5	42.8	81	26	22	Section

* Impacter Mass = 1505 g

** Compressive residual strength tests stopped due to facesheet disbond from the honeycomb core

Table B.4 Compressive Residual Strength Data and Damage Size Determined by X-ray of Specimens Impacted by a 578 g Mass

Specimen Number	Average Thickness (mm)	Average Width (mm)	Impacter Velocity (m/s)	Impacter Energy (J)	Major Axis (mm)	Minor Axis (mm)	Core Damage (mm)	Failure Stress (MPa)
J1-3	1.58	70.4	7.5	16.3	24	11	11	364
J15-3	1.65	69.4	7.5	16.3	65	26	17	257
J17-3	1.63	70.1	8.0	18.5	37	12	15	303
C7-2	1.61	69.9	8.0	18.5	35	11	10	345
J9-3	1.63	69.7	8.6	21.2	59	17	15	299
J10-2	1.60	70.1	8.6	21.2	23	12	11	319
M15-3	1.59	70.4	8.6	21.2	68	22	23	228
M12-2	1.63	70.0	8.6	21.2	67	23	17	291
M24-3	1.63	70.1	9.2	24.6	47	11	10	322
M26-3	1.63	70.1	9.2	24.6	61	15	12	321
M30-2	1.63	70.3	9.2	24.6	70	13	9	245
J14-2	1.63	69.7	9.2	24.6	82	16	21	262
M20-4	1.59	70.2	9.2	24.6	56	12	14	335
J1-2	1.56	70.5	9.2	24.6	72	21	23	191
M27-3	1.63	70.1	10.0	28.9	13	9	5	392
M28-2	1.63	70.1	10.0	28.9	27	9	3	367
J2-2	1.56	70.5	10.0	28.9	74	22	19	250
J5-3	1.62	70.2	10.0	28.9	68	27	21	299
M26-2	1.64	70.1	10.0	28.9	75	26	22	246
M14-2	1.58	70.4	10.0	28.9	82	22	21	220
M22-3	1.64	69.8	10.0	28.9	63	27	20	238
J3-2	1.60	70.2	10.9	34.4	54	12	10	320
J4-3	1.60	69.9	10.9	34.4	35	11	9	322
M31-2	1.63	70.1	10.9	34.4	59	14	13	293
M15-2	1.58	70.4	12.0	41.6	76	22	18	303

Table B.5 Damage Size Determined by X-ray of Specimens Impacted by a 578 g Mass and Selected for Destructive Evaluation

Specimen Number	Average Thickness (mm)	Average Width (mm)	Impacter Velocity (m/s)	Impacter Energy (J)	Major Axis (mm)	Minor Axis (mm)	Core Damage (mm)	Test Type
M28-3	1.63	69.6	8.0	18.5	49	23	18	Section
J12-3	1.63	70.1	8.0	18.5	39	10	14	Section
J16-2	1.64	69.9	8.0	18.5	43	11	12	Section
M13-3	1.62	69.6	8.6	21.2	70	22	18	Section
M27-2	1.66	70.1	8.6	21.2	15	10	13	Section
M23-2	1.62	69.8	8.6	21.2	82	16	8	Section
M10-4	1.59	69.9	8.6	21.2	63	22	19	Deply
M8-4	1.61	69.9	9.2	24.6	68	14	16	Section
M11-4	1.58	69.9	9.2	24.6	85	17	14	Section
J6-2	1.62	69.8	9.2	24.6	63	27	18	Section
M30-3	1.61	70.2	9.2	24.6	70	21	17	Deply
J2-3	1.56	70.5	10.0	28.9	76	21	18	Section
J9-2	1.63	70.1	10.0	28.9	75	21	19	Section
M32-3	1.62	70.3	10.9	34.4	58	19	15	Section
J10-3	1.60	70.1	12.0	41.6	60	22	19	Section

Table B.6 Compressive Residual Strength Data and Damage Size Determined by X-ray of Specimens Impacted by an 8.4 g Mass

Specimen Number	Average Thickness (mm)	Average Width (mm)	Impacter Velocity (m/s)	Impacter Energy (J)	Major Axis (mm)	Minor Axis (mm)	Core Damage (mm)	Failure Stress (MPa)
J16-4	1.59	70.2	55	12.8	49	19	17	252
M12-1	1.60	69.8	55	12.8	37	26	12	261
J9-4	1.62	70.1	56	13.3	49	20	17	252
J7-2	1.65	69.5	57	13.8	43	22	16	270
M31-3	1.62	70.2	57	13.8	57	30	20	270
M22-2	1.63	69.8	58	14.3	50	19	15	260
M28-1	1.61	70.1	70	20.6	67	22	16	259
M30-1	1.60	70.2	70	20.6	80	23	17	197
M24-2	1.65	70.1	70	20.6	60	25	16	218

Table B.7 Damage Size Determined by X-ray of Specimens Impacted by an 8.4 g Mass and Selected for Destructive Evaluation

Specimen Number	Average Thickness (mm)	Average Width (mm)	Impacter Velocity (m/s)	Impacter Energy (J)	Major Axis (mm)	Minor Axis (mm)	Core Damage (mm)	Test Type
M29-1	1.61	70.1	55	12.7	43	16	16	Section
M13-1	1.59	69.6	55	12.7	38	25	14	Section
M13-4	1.57	69.9	55	12.7	39	18	15	Section
M25-4	1.59	70.1	55	12.7	38	22	17	Deply
J13-1	1.58	70.0	56	13.2	44	20	14	Section
M29-2	1.65	69.8	57	13.6	45	24	12	Section
M32-4	1.60	70.1	57	13.6	52	16	14	Section
J11-4	1.60	70.1	57	13.6	54	25	15	Deply
J13-2	1.62	70.1	58	14.1	43	27	15	Section
J11-3	1.63	70.1	58	14.1	56	20	15	Section
M25-3	1.62	69.9	58	14.1	42	22	16	Section
M16-2	1.58	70.3	58	14.1	39	22	14	Deply
M23-4	1.60	69.8	70	20.6	68	23	16	Deply